Shape Resonances as a Probe of an Evolving Nuclear and Electronic Structure in Molecules

im Fachbereich Physik
der Freien Universität Berlin
zur Erlangung des Grades eines

doctor rerum naturalium (Dr. rer. nat.)

eingereichte

Dissertation

vorgelegt von

Felix Brauße

Berlin
September 2018

Erstgutachter:	Prof. Marc Vrakking, Ph. D.
Zweitgutachter:	Prof. Markus Gühr, Ph. D.
Drittgutachter:	Prof. Robert Lucchese, Ph. D.

Tag der Verteidigung: 14. Februar 2019

11. 5. [2018] Heute taucht zwischen Kohl- und Blaumeisen, Buch- und Grünfinken, Sperlingen, Amseln, Goldammern auch ein Gimpel auf, ein starenartiger, großer bunter Vogel, den ich für einen Kreuzschnabel hielt. Bei näherer Betrachtung aber wurde ich unsicher. War es nicht ein Kirschkernbeißer? Beide Arten gehören zu den Finkenvögeln. Man weiß zu wenig. Was müßte man noch alles lernen?

Heinz Strunk, *Intimschatulle* (39).

Für Margarethe

Abstract

Shape resonances are a ubiquitous phenomenon in electron–molecule scattering, in which the impinging electron is resonantly captured in a pseudo-bound state that is supported by the molecular potential. To study the electron scattering dynamics, we use time- and angle-resolved photoelectron spectroscopy here. With this technique, the transient evolution of the photoelectron angular distributions (PADs) from the ionization of an excited-state species can be measured. In the PADs, the electron–molecular-ion scattering dynamics are contained because the photoelectron necessarily interacts with the potential of the parent molecule as it escapes. The aim of this thesis is to investigate to what extent molecular dynamics, which are triggered by a pump laser pulse, are reflected in the PADs of the photoelectron spectra generated by an ionizing probe pulse, and how these effects can be rationalized in a photoelectron-scattering picture.

Three experimental studies are covered in this thesis: In the first experiment, CF_3I molecules are impulsively aligned in space by a short near-infrared pulse, which creates a rotational wave packet. During the revival of the rotational wave packet, PADs are measured for different molecular-axes distributions by photoionization with an ultrashort XUV pulse generated through high-order harmonic generation (HHG). Comparing the PADs thus obtained to the results of quantum-scattering calculations carried out with the ePolyScat suite of programs, we show that the alignment-dependent change in the PADs can be largely explained by two prominent shape resonances that contribute to the PADs in a distinctly different way geometrically.

In the second experiment, we investigate the laser-assisted photoelectron recollisions that occur in strong-field ionization of atoms and molecules. We show how the differential scattering cross sections (DCSs) for the electron–molecular-ion collision process can be extracted from the resulting photoelectron spectrum. Then, we apply this approach to the investigation of the excited-state dynamics of I_2 molecules that are prepared in the A or B state, leading to photodissociation and the creation of a vibrational wave packet, respectively. Again, by comparing to calculations carried out with ePolyScat, we conclude that the observed modulations in the DCSs of the rescattered electrons can be very well explained by considering two prominent shape resonances involved, the $l = 6$ resonance of the diatomic molecular ion and the $l = 3$ resonance of the free iodine atomic ion.

In the third study, the time-resolved core-shell photoionization of dissociating halomethane molecules, namely CH_3I and CH_2ICl, is investigated employing ultrashort soft x-ray pulses provided by the free-electron laser FLASH in Hamburg, which are able to ionize the $4d$ shell of iodine close to the well-known “giant” photoionization resonance (again related to the $l = 3$ shape resonance). We find that the dissociation clearly manifests as a shift of the $4d$ core-level binding energy, and that the time scale and temporal onset of this effect is distinctly different from that of the photoion measurements, which are commonly exploited to quantify the dissociation dynamics.

Zusammenfassung

In der Elektronenstreuung an Molekülen sind Formresonanzen ein allgegenwärtiges Phänomen, in dem das einschlagende Elektron resonant in einem pseudogebundenen Zustand eingefangen wird, den das Molekülpotential ermöglicht. Um die Dynamik der Elektronenstreuung zu untersuchen, bedienen wir uns der zeit- und winkelaufgelösten Photoelektronenspektroskopie. Mit dieser Technik kann die transiente Entwicklung der Photoelektronenwinkelverteilungen (engl. *photoelectron angular distributions*, PADs), die in der Photoionisation angeregter Molekülspezies auftritt, untersucht werden. In den PADs ist die Streudynamik der Elektron–Molekülionen-Wechselwirkung enthalten, weil das Photoelektron beim Verlassen des Moleküls notwendigerweise an dessen Rumpfpotential gestreut wird. Das Ziel der vorliegenden Arbeit ist es zu untersuchen, inwieweit Moleküldynamiken, die durch einen Anregungslaserpuls ausgelöst werden, die PADs der Photoelektronenspektren prägen, die durch einen abfragenden Ionisationspuls erzeugt werden, und wie die beobachteten Effekte im Modell der Photoelektronenstreuung verstanden werden können.

Die vorliegende Arbeit trägt die Ergebnisse dreier Experimente zusammen: Im ersten Experiment werden CF_3I-Moleküle durch einen kurzen Laserpuls im Nahinfrarot impulsiv im Raum ausgerichtet. Das heißt, dass ein Rotationswellenpaket präpariert wird und während des Wiederauflebens dieses Wellenpakets werden die PADs für verschiedene Molekülachsenverteilungen durch einen XUV-Laserpuls vermessen, der durch Höhere-Harmonischenerzeugung (HHG) gewonnen wurde. Durch den Vergleich der gemessenen PADs mit den Ergebnissen von Quantenstreuungsrechnungen, die mit dem ePolyScat-Programmpaket durchgeführt wurden, können wir zeigen, dass die ausrichtungsabhängigen Veränderungen der PADs im Wesentlichen durch zwei ausgeprägte Formresonanzen erklärt werden können, die ihrerseits räumlich auf signifikant unterschiedliche Weise zu den PADs beitragen.

Im zweiten Experiment untersuchen wir die laservermittelten Elektronenrekollisionen, die in der Starkfeldionisation von Atomen und Molekülen auftreten. Wir zeigen, wie sich die differentiellen Wirkungsquerschnitte für die Elektronen–Molekülionenstreuung aus den gewonnenen Photoelektronenspektren extrahieren lassen. Dann wenden wir diesen Ansatz auf die Untersuchung von angeregten I_2-Molekülen an, die entweder in ihrem *A*- oder *B*-Zustand präpariert wurden, was im einen Fall zur Photodissoziation und im andern zu einem Vibrationswellenpaket führt. Durch den Vergleich mit Rechnungen, die wieder mit ePolyScat durchgeführt wurden, können wir zeigen, dass sich die zeitabhängigen Veränderungen der Wirkungsquerschnitte durch die Beteiligung einer molekularen ($l = 6$) und einer atomaren ($l = 3$) Formresonanz erklären lassen.

In der dritten Studie wird die zeitaufgelöste Kernschalenphotoionisation in den Halomethanen CH_3I und CH_2ICl durch kurze Laserpulse im Bereich weicher Röntgenstrahlung untersucht, die durch den Freie-Elektronenlaser FLASH in Hamburg bereitgestellt wurden. Mit Licht dieser Wellenlänge kann die $4d$-Schale von Iod im Bereich der gut untersuchten "gigantischen" Photoionisationsresonanz, die eng mit der ($l = 3$)-Resonanz verwandt ist, ionisiert werden. Wir können zeigen, dass sich die Photodissoziation in einer Verschiebung der Kernschalenbindungsenergie manifestiert, und zwar auf Zeitskalen und mit zeitlichen Verzögerungen, die sich signifikant von denen unterscheiden, die in den ionischen Fragmenten beobachtet werden, die ihrerseits gewöhnlich genutzt werden, um die Dissoziationsdynamik zu charakterisieren.

Contents

Introduction

At the heart of molecular physics lies the question of what constitutes a chemical bond, or, more explicitly, what laws govern the diverse phenomena of electronic structure and molecular dynamics, that show an extraordinarily rich and intricate structure, even for the most simple of molecular systems like diatomics.[1] The understanding of chemical bonding is of such central importance, that it can hardly be overstated: Not only does the chemical bond form the basis of the structure and properties of all stable matter that surrounds us, but, obviously, it is also key to all reactivity, the formation and dissolution of bonds and the molecular rearrangements that go along with them. What drives chemical reactions and determines their outcome among various reaction paths is the delicate balance between the energetic stabilization of the chemical products that are formed and the kinetic favor of such a path, which can be understood as the facility of a rearrangement. Many systems of practical interest, like the catalysis that happens in the active centers of enzymes or man-made catalytic materials, but in particular reactions that are initiated by light, like photosynthesis and the spatial motion of photoswitches, can only be described to a satisfactory degree on a quantum-mechanical level, as these processes often involve exotic, highly excited species and energy transfer through non-adiabatic processes. It is here that the toolbox of modern molecular physics is applied to unveil the details of the underlying elementary processes.

To characterize and elucidate the microscopic structure of matter in an experiment, we expose a sample of it to an external stimulus and carefully observe its response. Without doubt, the most prolific source of what we know about atoms and molecules is their interaction with electromagnetic radiation. In fact, there are numerous ways radiation can interact with the bound electrons in an atom or molecule, giving rise to an entire array of spectroscopic techniques. For instance, the light could be scattered off, but it could also be absorbed, which would either trigger a photochemical reaction or lead to the re-emission of light at a different wavelength. This thesis is entirely devoted to photoelectron spectroscopy, a technique in which the absorption of a photon causes the ejection of an electron, and it is this photoelectron that is in the end measured and whose properties reveal all the details about the circumstances of its birth.

Historically,[2] it was Heinrich Hertz who, in 1887, first observed that metals emit electrons when ultraviolet radiation (UV) is shining on them. This phenomenon was called photoelectric effect, but there remained some confusion about the correct explanation of it, in particular with respect to its dependence on the light's intensity. Hertz and his contemporaries expected that increasing the intensity of the light would accelerate the electrons, as if the beam of light was hitting the bulk material like water from a hose: When the water pressure is increased, the electron will be pushed out more vigorously. What they found, instead, was that it only increased the number of electrons that were emitted per time interval, but that all of them had the same, well-defined velocity. In 1905, Albert Einstein was able to describe this finding correctly: He proposed that one should picture the light as a stream of particles, the

photons, and that increasing the intensity corresponds to increasing the density of particles in the photon stream. Every photon carries a characteristic photon energy and only if that energy exceeds the energy required to remove an electron entirely from the irradiated sample, emission can occur, and the emitted electron will fly away with exactly the amount of energy it had in excess. When considering molecules, not only one, but several ionic final states of the molecule may be accessible that are excited in the electronic, vibrational and rotational degrees of freedom. As every of these states has a well-defined total energy, which is independent of the probing radiation, the photoelectrons are emitted at a series of discrete energies, each of which can be related to a final state through energy conservation. This constitutes what Carlson[3] calls the "beauty of photoelectron spectroscopy". If for the moment we consider an independent-particle picture, in which the electrons move in shell-like, spatially and energetically well-defined orbitals, the incident radiation can create a hole in one of the orbitals that it can energetically access, and therefore the resulting photoelectron spectrum immediately reflects the electronic structure of the system under investigation.

In traditional photoelectron spectroscopy, the main observables of interest were the total photoionization cross section and the partial cross sections for the different ionization channels, and their dependence on the incident radiation's wavelength. This rather rudimentary information already can reveal insight into the potential that the leaving electron interacts with. Among the phenomena that can be observed and studied this way are potential-barrier trapping of the photoelectron, closely related to the frequently encountered "shape resonances", and inflection of the dipole matrix elements, the so-called Cooper minimum.[4] Ideally, this requires a light source that is tunable over a wide wavelength range above the ionization potential of the target systems. For a long time, however, elemental photoemission lines were the only sources of narrow-band vacuum ultraviolet and x-ray radiation. Especially the emission lines of helium, He I at 21.2 eV and He II at 40.8 eV were a popular (and suitable) choice to characterize the valence band structure of many molecules,[5] but clearly they come with the drawback of not being tunable. This situation changed drastically when synchrotrons were set up as tunable photon sources. Throughout the seventies, the literature on wavelength-dependent photoelectron spectroscopy in atoms and molecules grew enormously, and the state of the field is covered in some comprehensive monographs from the second half of that decade.[3,4]

Forty years later, research in photoelectron spectroscopy is still a thriving field owing to the progress in the development of new light sources and detection schemes that constantly push the boundaries of what experiments are feasible and at what level of detail electronic structure can be investigated. In this regard, the thrust of this thesis is twofold: First, with pulsed light sources in the extreme ultraviolet (XUV, which we define here as covering a photon-energy range of roughly 10 to 100 eV) and soft x-ray (from approx. 100 to 5000 eV) regime not only molecules in the ground state, but also excited-state species and their nuclear and electronic relaxation can be investigated. This is achieved by pumping the molecule first with a short light pulse, e. g., in the visible or ultraviolet region, into an excited state and probing it after some well-defined time delay by a pulse of ionizing radiation. To this end, both table-top sources that are based on high-order harmonic generation in gases as well as free-electron lasers, that generate XUV and soft x-ray pulses with pulse durations of a few tens of femtoseconds – which is what is required to resolve the nuclear motion of molecules – have been applied during the course of this thesis work. The second direction in modern

photoelectron spectroscopy we are following is the application of spectrometers that not only resolve the absolute velocity of a charged particle, but also its direction of emission. Most notable here is the construction of the so-called velocity-map-imaging spectrometer (VMI) by Eppink and Parker[6] in 1997 that is designed to project the three-dimensional velocity distribution of the escaping electrons onto a two-dimensional plane where it is recorded with a position-sensitive detector. This allows not only to record the photoelectron spectrum itself, but also the angular probability distribution for every photoemission line, the so-called photoelectron angular distribution (PAD).

What, maybe, sets this thesis apart from others in this field is that it is not focused on a single technique or a specific system that is explored in great depth, but instead it rather orbits around a central concept, that is, measuring and rationalizing photoelectron angular distributions to elucidate molecular dynamics, to which end a variety of techniques, sources and physical phenomena were employed. In total, three different experimental studies are covered in the thesis, each of which makes use of photoionization of a different flavor: valence-shell ionization, core-shell ionization, and electron rescattering after strong-field ionization. What all of them have in common is that they can be considered essentially instantaneous ionization events, at least on the time scale of molecular motion. Actually, photoionization is always *implied* to be sudden when proposing an experiment in time-resolved photoelectron spectroscopy, where the aim is to interrogate the evolution of an excited state by an immediate response of some sort.[a]

Let us first turn to the crucial question what additional information can be retrieved from measuring the photoelectron angular distributions? As the electron leaves the molecule, it scatters off the molecular potential and this encounter, in turn, is imprinted on the leaving electron's wave function as an angular intensity modulation. These angular distributions show an intricate richness and vary widely as the wavelength of the incident radiation is tuned. This was observed already in the earliest studies carried out by Dill, Siegel, and Dehmer.[7] Even though it might be tempting, the angular distributions cannot be *directly* identified with the shape of the orbital or the chemical surrounding they are originating from, and a great deal of modeling is typically involved in their interpretation. This is not to say that the photoionization process cannot be rationalized in any way. We like to think of it as being composed of three contributing factors that are deeply interrelated, but can conceptually be separated: First, there is the overlap between the initial (neutral) and final (ionic) states' wave functions of the molecule, which accounts for the electronic relaxation in the charged species and captures phenomena that can only be explained through electron correlation, like shake-up transitions, in which not only one electron is ejected, but a second one is promoted into an unoccupied orbital. Second, as already mentioned, electron scattering plays a crucial role in shaping the angular distribution. In particular, shape resonances, which are a commonly encountered phenomenon in scattering experiments, can also be observed through photoionization. In a shape resonance, the impinging electron – instead of being deflected right away – is transiently captured by the molecular potential where it forms a pseudo-bound state. It turns out that these resonances are extremely sensitive to the smallest distortions in the shape of the molecular potential (hence the name), which can be exploited to trace the motion of the nuclei in the molecule. The third ingredient is the dipole selection rule in

a It is, however, not necessarily always justified; when, for example, bound states in the continuum are excited, as in autoionization, they can be considerably long-lived.[4]

single-photon ionization that, together with the shape of the orbital, acts as a kind of spatial filter that selects only a small part of the continuum. The consequences of this filtering are often hard to predict: sometimes it hides underlying photoelectron dynamics and sometimes it strongly enhances them.

This thesis is organized as follows: after an introductory chapter on the theory of photoemission and photoelectron angular distributions, Chapter 1, the results of three experimental studies are presented that were carried out in the course of this thesis. In Chapter 2, the XUV ionization of CF_3I molecules, which are spatially aligned by a laser-induced alignment technique is investigated. The problem that is addressed here is the following: what is peculiar about molecules is the fact that, in contrast to atoms, they are obviously not spherically symmetric, and, what is more, in gas-phase experiments they tumble in space freely. As a consequence, many details of the photoelectron angular distributions are washed out, but not all. In the photoionization of atoms, the angular distribution is related to the interference of the outgoing photoelectron's partial-wave components. In rotating molecules these relations are much more complicated. By aligning the molecules in some way, additional details can be extracted, and we will, in particular, show how two shape resonances that are obfuscated in the ionization of the randomly oriented molecule, can be clearly identified in the aligned ensemble.

The investigation of aligned molecules is still considered a static experiment because no electronic excitations are involved. In Chapter 3 we extend our approach of studying photoelectron scattering dynamics to experiments that involve excited-state I_2 molecules undergoing nuclear rearrangements. However, the experimental concept of Chapter 3 seems very different at first: instead of working with ionizing radiation, the molecules are ionized by a strong mid-infrared laser field. As will be shown, closer inspection of the strong-field photoionization process reveals that some of the photoelectrons that are driven forth and back in the oscillating laser field recollide with the parent molecule. Based on a semiclassical model, the electron-scattering angular distributions can be extracted from the experimental data (which can be seen as the "unfiltered" form of the PAD, with respect to the third ingredient in the intuitive picture outlined above). We will demonstrate that along the stretching of the molecular bond, a prominent molecular shape resonance is detuned and a well-known atomic shape resonance appears, which can be seen as an immediate probe of the molecular potential evolving into an atomic one.

In Chapter 4, we will try to go even one step further: photoelectron scattering at low energies (say, <20 eV) can typically only be modeled and understood on a quantum-mechanical level of treatment. At higher photoelectron kinetic energies, when the de-Broglie wavelength[b] of the electrons becomes as small as the interatomic dimensions, a much simpler picture can be used to interpret the PADs. This is particularly true when photoionization occurs in a core shell, where the bound electrons are highly localized at an atomic site: then, this specific atom can be pictured as a point emitter of an outgoing photoelectron wave, and the photoelectron scattering reduces to spherical scattering at the positions of the other atoms, so that in total a classical wave-interference model can be used to predict the PADs. To reach the photon energies required for this so-called time-resolved core-shell photoelectron spectroscopy (>100 eV) we make use of the soft x-ray radiation from a free-electron laser. With

b The de-Broglie wavelength λ is the wavelength of the matter wave that is associated with a moving particle. It is defined as $\lambda = h/p$, where h is the Planck constant and p is the particle's momentum.

this radiation the excited-state dynamics of two halomethanes are investigated in Chapter 4. It turns out that the electronic relaxation manifests on significantly different time scales for photoelectrons as opposed to -ions, which emphasizes the great potential that time-resolved core-shell photoelectron spectroscopy shows for investigating ultrafast dynamics in molecules.

Overall, we will show in Chapters 2 and 3 that shape resonances largely determine the photoelectron scattering dynamics at low photoelectron energies, and that these resonances, properly taken into account, can reveal a lot of insight into the shape of the molecular potential. In Chapter 4, we will demonstrate what progress has been made in bringing together time-resolved photoelectron spectroscopy with core-shell photoionization, both of which are well established fields of research in their own rights, after which we will give a perspective upon what remains to be done.

References

1. Herzberg, G. & Spinks, J. W. T. *Molecular Spectra and Molecular Structure: Diatomic Molecules* (Van Nostrand, New York, 1950).
2. Bonzel, H. & Kleint, C. "On the History of Photoemission". *Prog. Surf. Sci.* **49,** 107–153 (1995).
3. Carlson, T. A. *Photoelectron and Auger Spectroscopy* (Springer, Boston, 1975).
4. Berkowitz, J. *Photoabsorption, Photoionization, and Photoelectron Spectroscopy* (Academic Press, New York, 1979).
5. Kimura, K. *Handbook of He I Photoelectron Spectra of Fundamental Organic Molecules: Ionization Energies, Ab-Initio Assignments, and Valence Electronic Structure for 200 Molecules* (Japan Scientific Societies Press, Tokyo, 1981).
6. Eppink, A. T. J. B. & Parker, D. H. "Velocity Map Imaging of Ions and Electrons Using Electrostatic Lenses: Application in Photoelectron and Photofragment Ion Imaging of Molecular Oxygen". *Rev. Sci. Instrum.* **68,** 3477–3484 (1997).
7. Dill, D., Siegel, J. & Dehmer, J. L. "Spectral Variation of Fixed-molecule Photoelectron Angular Distributions". *J. Chem. Phys.* **65,** 3158–3160 (1976).

Chapter 1

Fundamentals

In this chapter, the central concepts and quantities are introduced that are necessary to follow the discussion of angle-resolved photoionization experiments, here and in the literature. In the first section on photoelectron spectroscopy with ionizing radiation, Section 1.1, we follow Berkowitz[1] in his presentation of the material, who certainly has to be credited with giving one of the most comprehensive treatments of the subject. We then continue by presenting a very brief introduction to scattering theory, Section 1.2, which is a key ingredient to interpreting the angular distributions of photoelectrons. When dealing with molecules as opposed to single atoms, another such ingredient is the relation between the photoemission from a molecule that is fixed in space (which is the most natural way to think about this process) to that in an ensemble of molecules that rotate in space (which is what they always do). As soon as this relation is established at the end of Section 1.3, most of what is required to rationalize the angular distributions of photoelectrons in the single-photon ionization of molecules is covered. When, instead, an atom or a molecule is exposed to a slowly varying, intense laser field, single-photon ionization is impossible as the radiation frequency is too low, but photoionization can still proceed through multi-photon ionization, which leads to a number of features in the photoelectron spectra unknown in single-photon ionization. By taking into account the electron–laser-field interactions explicitly, characteristic features in the photoelectron spectra from this so-called strong-field ionization can be understood. The two central processes that lead to these features, above-threshold ionization and the presence of high-energy, elastically rescattered electrons, are discussed in Section 1.4.

1.1 Photoelectron spectroscopy

As a starting point, we introduce photoelectron spectroscopy as the photoionization of a gaseous sample by ionizing vacuum UV or x-ray radiation, where the absorption of a single photon at a time dominates, which is the simplest case conceptually. In such a photoionization experiment, two observables are of fundamental importance: the kinetic energies of the ejected photoelectrons, which encode the energy-level structure of the ionized target, and the photoionization cross sections associated with these energy levels. Formally, we can write such a single-photon photoionization event as

$$\mathrm{M} \xrightarrow{\hbar\omega} \mathrm{M}_f{}^+ + \mathrm{e}^- \left(\epsilon_f\right), \tag{1.1}$$

where M denotes the molecule in some initial, neutral state and $\hbar\omega$ is the photon energy of light with angular frequency ω. Through the ionization, the molecule can – in principle – end up in any of the molecular ionic states $\mathrm{M}_f{}^+$ that are energetically accessible, ejecting

a photoelectron with kinetic energy ϵ_f. In *direct* photoemission,[a] the photoelectron kinetic energy ϵ_f is simply determined through conservation of energy as the difference between the binding energy of the bound electron V_f and the photon energy, i. e.,

$$\epsilon_f = \hbar\omega - V_f \,. \tag{1.2}$$

Here we use the terms "binding energy" and "ionization potential" interchangeably. Strictly, V_f is the difference between the total energies of the final (ionic) and the initial (neutral) states. If, however, the final state can be reasonably well described by only eliminating one electron from one of the molecular orbitals, V_f can be identified with the energy that is required to remove an electron from that orbital, namely the binding energy. This simplified way of conceiving photoionization is referred to as the single-particle picture, and we will describe photoionization processes in terms of this picture wherever possible. From Eq. (1.2) it is also clear that, for a final state to be energetically accessible for photoionization, its associated V_f must be smaller than the photon energy.

To see the significance of the cross section, consider an attenuation experiment, in which a beam of monochromatic light with angular frequency ω and incoming intensity I_0 propagates through an isotropic, gaseous medium along the z axis. Within every infinitely thin slice dz along the propagation, the impinging intensity I is reduced through absorption by a fraction dI that is proportional to I, i. e.,

$$-\,\mathrm{d}I = \sigma_{\mathrm{tot}}(\omega)\, N_0\, I\, \mathrm{d}z \;, \tag{1.3}$$

where N_0 is the number density of atoms or molecules per volume and $\sigma_{tot}(\omega)$ is the total cross section at frequency ω. Solving the above differential equation readily yields the celebrated Lambert–Beer formula,

$$I(z) = I_0\, \mathrm{e}^{-\sigma_{\mathrm{tot}}(\omega)\, N_0\, z} \,, \tag{1.4}$$

which states that the intensity of the penetrating light beam decays exponentially with penetration depth. From Eq. (1.4) it is also clear that the units in the exponent need to cancel each other to equate an intensity on the left with an intensity on the right-hand side. As z has the dimension of a length and N_0 the dimension of an inverse volume, the cross section *must* be an area. It is common to report photoionization cross sections in units of "barn", where $1\,\mathrm{b} = 1 \times 10^{-24}\,\mathrm{cm}^2$. Typical valence-shell cross sections are on the order of a few megabarn.

Even though the above derivations were made for a continuous light source, they are still valid when working with ultrashort XUV pulses. For such a pulse, we first assume that the spatio-temporal shape of its electric-field component $\mathbf{E}(\mathbf{x}, t)$ along the laser propagation vector $\mathbf{k}_L$ can be written as[2]

$$\mathbf{E}(\mathbf{x}, t) = E_0\, \hat{\mathbf{n}}\, F(\omega t - \mathbf{k}_L{\cdot}\mathbf{x})\, \cos(\omega t - \mathbf{k}_L{\cdot}\mathbf{x} + \phi) \,, \tag{1.5}$$

where ω is now referred to as the carrier angular frequency, $\hat{\mathbf{n}}$ is the polarization vector of the electric field, $\mathbf{x} = \begin{pmatrix} x & y & z \end{pmatrix}$ is a position vector, and $F(\omega t - \mathbf{k}_L{\cdot}\mathbf{x})$ is a non-negative envelope function whose maximum value is normalized to unity, so that E_0 is the peak electric field strength. The additional phase ϕ is referred to as the carrier-envelope phase (CEP) that plays

a As opposed to sequential multi-electron emission processes, like Auger ionization, in which a second photoelectron is emitted from the highly excited core-hole state that is formed in direct photoemission.

an important role when working with few-cycle laser pulses. As we have not employed such short pulses, we typically ignore the CEP. Note that a pulse of the form in Eq. (1.5) is spatially uniform in the plane perpendicular to the laser propagation axis. Then, the cycle-averaged intensity profile $I(\mathbf{x}, t)$ of $\mathbf{E}(\mathbf{x}, t)$ along the propagation direction is given by[3]

$$I(\mathbf{x}, t) = \frac{1}{2} c\, \varepsilon_0\, E_0^2\, F^2(\omega t - \mathbf{k_L} \cdot \mathbf{x})\,, \tag{1.6}$$

where c is the speed of light and ε_0 is the vacuum permittivity. Introducing a function $G(\mathbf{x})$ that describes the beam profile of the laser pulse, the total pulse energy is given by

$$W = \int_{-\infty}^{\infty} \int_P G(\mathbf{x})\, I(\mathbf{x}, t)\, \mathrm{d}\mathbf{x}\, \mathrm{d}t\ , \tag{1.7}$$

where the spatial integration is carried out over a cross-sectional plane P perpendicular to the propagation direction.

If the spectrum of the pulse is sufficiently monochromatic, the number of photons in a laser pulse is just the pulse energy W divided by $\hbar\omega$ (when it is not monochromatic, as in a higher-harmonics comb, which is introduced in Section 1.4, we have to determine the fraction of spectral energy in a narrow wavelength band first). Further, if the intensity $I(\mathbf{x}, t)$ is low enough to only enable light–matter interactions that are linear in I, then, in Eq. (1.4), I_0 and I can be replaced by the incident and transmitted number of photons, respectively. When we assume that one photon absorbed leads to one electron emitted, the difference between incoming and transmitted photons is the number of photoelectrons generated from a single pulse, and the photoelectron count rate is that number times the repetition rate.

Strictly, the total cross section σ_{tot} is the sum of a number of *partial* cross sections σ_f, i. e.,

$$\sigma_{\mathrm{tot}}(\omega) = \sum_f \sigma_f(\omega)\,, \tag{1.8}$$

where the sum runs over all final states that are accessible at the given photon energy, as discussed above. At the same time, the partial cross sections determine the count rates of each of the discrete photoemission transitions at the energies ϵ_f in the same way as shown above, which is how the photoelectron spectrum takes its shape.

Microscopically, the partial cross section is proportional to the absolute square of the dipole transition matrix element between the N-electron initial state $|i\rangle$ and the total final state $\left|f\ \epsilon_f\right\rangle$, which is the product of the $(N-1)$-electron ion state and the wave function of the electron escaping with kinetic energy ϵ_f, i. e.,

$$\sigma_f(\omega) = \frac{4\pi^2 e^2 \omega}{c} \sum_{j=1}^{N} \left| \left\langle f\ \epsilon_f \middle| \hat{\mathbf{n}} \cdot \mathbf{x}_j \middle| i \right\rangle \right|^2 , \tag{1.9}$$

where e is the elementary charge. Further, $\mathbf{x}_j = \begin{pmatrix} x_j & y_j & z_j \end{pmatrix}$ is the position of the j-th electron, and the sum runs over all N electrons in the molecule. The derivation of Eq. (1.9) is a little involved and we only want to give a very brief account of it here as it may help in understanding the generalization from the single-photon to the multi-photon ionization regime, which is introduced later in Section 1.4. For details, we refer the interested reader to the literature.[4,5] Consider an electron at position $\mathbf{x}$ moving with momentum $\mathbf{p}$. In the absence of any radiation

field, its kinetic energy is just $T = \mathbf{p}^2/2m_e$, where m_e is the electron mass. If the radiation can be described by a plane wave with wave vector $\mathbf{k}_L$ and frequency ω, the electron is accelerated in the electric field, and this acceleration can be described by the instantaneous vector potential $\mathbf{A}(\mathbf{x}, t) = A_0\,\hat{\mathbf{n}}\,\mathrm{e}^{\mathrm{i}(\mathbf{k}_L\cdot\mathbf{x}-\omega t)}$ of the wave, which is defined such that $\mathbf{E} = -\frac{\mathrm{d}\mathbf{A}}{\mathrm{d}t}$. Consequently, in the expression for the kinetic energy, the canonical momentum $\mathbf{p}$ has to be replaced with the kinematic (or kinetic) momentum $\boldsymbol{\pi} = \mathbf{p} + \frac{|e|}{c}\mathbf{A}$,[b] so that, in the presence of an electromagnetic field, the kinetic energy reads

$$T = \frac{\boldsymbol{\pi}^2}{2m_e} = \frac{1}{2m_e}\left[\mathbf{p}^2 + \frac{2|e|}{c}\mathbf{A}\cdot\mathbf{p} + \left(\frac{e}{c}\mathbf{A}\right)^2\right] = K + H_{\mathrm{int}}\,. \tag{1.10}$$

The first term in Eq. (1.10) is just the field-free (and, hence, *interaction-free*) kinetic energy, which we denote from here on as $K = \mathbf{p}^2/2m_e$. The other two terms together are referred to as the interaction Hamiltonian H_{int}. The third term is of second order in $\mathbf{A}$, which means that – in the weak-field, single-photon regime – we can safely neglect it (which will not be the case in the strong-field regime). Consequently, the interaction between the initial and final states must be governed by the second term. Now – according to first-order, time-dependent perturbation theory – the transition rate between the two states turns out to be *independent* of time and to be proportional to $\left|\left\langle f\epsilon_f\middle|\mathbf{p}\cdot\hat{\mathbf{n}}\,A_0\,\mathrm{e}^{\mathrm{i}(\mathbf{k}_L\cdot\mathbf{x})}\middle|i\right\rangle\right|^2$. Now, in the last – and maybe most important step – $\mathrm{e}^{\mathrm{i}(\mathbf{k}_L\cdot\mathbf{x})}$ is expanded around $\mathbf{x} = \begin{pmatrix}0 & 0 & 0\end{pmatrix}$, which yields the series

$$\mathrm{e}^{\mathrm{i}(\mathbf{k}_L\cdot\mathbf{x})} = 1 + \mathrm{i}(\mathbf{k}_L\cdot\mathbf{x}) - \frac{1}{2}(\mathbf{k}_L\cdot\mathbf{x})^2\ldots\,, \tag{1.11}$$

which shows that, as long as $\mathbf{k}_L\cdot\mathbf{x} \ll 1$, the exponential term can be replaced by unity. This is known as the dipole approximation, and the resulting interaction matrix element $\left|\left\langle f\epsilon_f\middle|\mathbf{p}\cdot\hat{\mathbf{n}}\middle|i\right\rangle\right|^2$ is said to contain only electric dipole (E1) transitions. For the photoionization of molecules with XUV and soft x-ray radiation, applying the dipole approximation is typically well justified, and, throughout this thesis, we will always assume that it does hold. To support this, note that, for the valence-shell molecular orbital of a small molecule, $\mathbf{x}$ will be, at most, on the order of a few Ångstrom, whereas the wave vector of an 100 eV photon, for instance, is roughly $0.05\,\text{Å}^{-1}$. If, however, $\mathbf{x}$ becomes very large (as in Rydberg states) or $\mathbf{k}_L$ increases (as with photons in the keV range), the dipole approximation breaks down, and then electric quadrupole (E2) and magnetic dipole (M1) transitions may contribute significantly, which are contained in the $\mathbf{k}_L\cdot\mathbf{x}$ term of Eq. (1.11).

Eventually, applying the derivation outlined above properly to an N-electron system, we obtain an expression for the partial cross section σ_f, which is

$$\sigma_f(\omega) = \frac{4\pi^2e^2}{m_e^2c\omega}\sum_{j=1}^{N}\left|\left\langle f\,\epsilon_f\middle|\hat{\mathbf{n}}\cdot\mathbf{p}_j\middle|i\right\rangle\right|^2\,. \tag{1.12}$$

Note the difference between the above equation and Eq. (1.9): one contains the matrix element of the position operator $\mathbf{x}_j$ and the other one that of the canonical momentum $\mathbf{p}_j$. These

b The difference between the canonical and kinematic momentum is that the latter describes the *instantaneous* momentum of the electron, whereas the former is a conserved quantity in the electron–laser interaction because the time integral of $\mathbf{A}(\mathbf{x}, t)$ over an integer number of optical cycles is zero.

forms are referred to as length gauge (LG) and velocity gauge (VG), respectively. Formally, one can prove that the cross sections in the length and velocity form are identical,[6] given that the initial and final state wave functions are *exact* eigenfunctions of an *exact* molecular Hamiltonian; then, the cross sections in these two gauges take the same value. Practically, however, one will have to resort to various approximations for both the Hamiltonians *as well as* their respective eigenfunctions. Under these circumstances, the results in the two gauges will typically (but not always!)[5] differ, and the magnitude of the difference can be seen as an estimate of the minimum error in a photoionization calculation.[7]

What is rather formidable about the expressions for the partial cross sections, Eq. (1.9) and Eq. (1.12), is that they involve all N electrons. There is, however, a straightforward way to approximate the dipole transition of an electron into the continuum through an effective single-electron expression,[8] using the generalized overlap amplitude between the initial and final state $g(\mathbf{x})$, which is also known as a Dyson orbital, i. e.,

$$g(\mathbf{x}) = \sqrt{N} \int \mathrm{d}\mathbf{x_2} \ldots \mathrm{d}\mathbf{x_N}\ \Psi^{N-1}(\mathbf{x_2}, \ldots \mathbf{x_N})^*\, \Psi^{N}(\mathbf{x_1}, \mathbf{x_2}, \ldots \mathbf{x_N})\,, \tag{1.13}$$

where Ψ^{N-1} and Ψ^{N} denote the wave functions of the ionic and neutral states, respectively. In this approximation, the partial cross section is given by a one-electron integral, namely

$$\sigma^r \propto |\, \langle \psi_{\mathbf{k}}(\mathbf{x}) | \hat{\mathbf{n}} \cdot \mathbf{x} | g(\mathbf{x}) \rangle |^2\,, \tag{1.14}$$

where the superscript r denotes the length gauge,[c] but the velocity gauge could have been used, as well. The other single-particle wave function, $\psi_{\mathbf{k}}(\mathbf{x})$, is the solution for an electron moving in the potential of the $(N-1)$-electron ion with (canonical) momentum $k = \sqrt{2m\epsilon_f}/\hbar$. This is where the connection between photoionization and electron scattering is revealed because, unless $\psi_{\mathbf{k}}(\mathbf{x})$ is just assumed to be a plane wave, the Schrödinger equation for an electron scattering off the parent ion has to be solved in some way, which will be the subject of the next section.

The most straightforward way to obtain an approximation to the Dyson orbital $g(\mathbf{x})$ is the so-called frozen-orbital approximation, which we will always use in this thesis. If the same orbitals are used for the neutral and ionic states, $g(\mathbf{x})$ is just identical to the orbital that the electron is ejected from, which establishes the correspondence between the intuitive, single-particle picture of photoionization introduced above and the most straightforward theoretical description of it.

The observables that have been introduced up to this point are all angle-integrated quantities. A closer look at Eq. (1.14) reveals that, depending on the exact shape of the outgoing photoelectron's wave function $\psi_{\mathbf{k}}(\mathbf{x})$, we can – in general – *not* expect the cross section σ to be spherically isotropic, which means that it depends on the emission direction of the photoelectron. Furthermore, an important difference between molecules and atoms is that, in molecules, also $g(\mathbf{x})$ is typically not spherically symmetric, so that σ must also explicitly depend on the angle between the polarization axis $\hat{\mathbf{n}}$ and the principal molecular axis. To be able to describe the shape of $\psi_{\mathbf{k}}(\mathbf{x})$, we will introduce some basic concepts from scattering theory in the next section, before we return to the problem of photoelectron angular distributions in molecules in Section 1.3.

c Here, r stands for radius because later the cross sections will be rewritten in terms of radial integrals.

1.2 Elements of scattering theory

Here, we try to give a very brief account of the central concepts of scattering theory that are key to understanding the most prominent phenomena in (photo-)electron scattering, like shape resonances. As a first step, consider the prototypical, text-book scattering experiment where a particle scatters off a short-range potential $V(\mathbf{x})$ that is located at the origin of the coordinate system. Formally, a potential is defined as being short-ranged if it falls off faster than $1/r$ at infinity, with r being the radial distance from the origin. The conceptually simplest scattering event is the totally elastic collision, in which only the direction, but not the absolute value of the scattered particle's momentum changes, and we will restrict the discussion to this case, only. In a classical picture of (elastic) scattering, the impinging particle flies in from the negative z direction with momentum k and is deflected through the interaction with the potential $V(\mathbf{x})$, after which it flies away under some angle, but still with momentum k. Now, in the quantum-mechanical treatment, it is not a discrete particle that collides, but an incoming matter wave, and one has to find the wave function $\psi_{\mathbf{k}}(\mathbf{x})$ that satisfies the Schrödinger equation of the scattered particle (setting $\hbar = 1$ from here on),

$$\left[-\frac{\Delta}{2m} + V(\mathbf{x})\right]\psi_{\mathbf{k}}(\mathbf{x}) = \epsilon\,\psi_{\mathbf{k}}(\mathbf{x})\,, \tag{1.15}$$

where Δ is the Laplace operator and $k = \sqrt{2m\epsilon}$. It turns out that one can find a stationary solution[9] for $\psi_{\mathbf{k}}(\mathbf{x})$, which *asymptotically* behaves like

$$\psi_{\mathbf{k}}(\mathbf{x}) \underset{r\to\infty}{\sim} \mathrm{e}^{\mathrm{i}\,\mathbf{k}\cdot\mathbf{x}} + f(\theta,\phi)\,\frac{\mathrm{e}^{\mathrm{i}\,k\,r}}{r}\,, \tag{1.16}$$

with θ and ϕ being the polar and the azimuthal angles of the polar coordinate system, whose polar axis we conveniently define to be parallel to the Cartesian z axis and, therefore, also to be parallel to $\mathbf{k}$. The asymptotic form shown in Eq. (1.16) has an appealing, intuitive interpretation: asymptotically, $\psi_{\mathbf{k}}(\mathbf{x})$ is just the sum of a plane wave, which is incoming *and* outgoing, plus an outgoing spherical wave, which results from the scattering process and which is modulated in its angular distribution by the so-called scattering amplitude $f(\theta,\phi)$. What is most important is that $f(\theta,\phi)$ entirely determines the probability for an incoming particle to be scattered into the solid angle $\mathrm{d}\mathbf{\Omega} = \mathrm{d}\phi\sin\theta\,\mathrm{d}\theta$, and this probability is referred to as the differential cross section $\mathrm{d}\sigma/\mathrm{d}\mathbf{\Omega} = |f(\theta,\phi)|^2$, often abbreviated as DCS.[d]

Certainly, the most common and most powerful way to solve the Schrödinger equation Eq. (1.15) is to rewrite it in spherical coordinates, which, in general, yields a set of coupled differential equations. The reasoning behind this is that $\psi_{\mathbf{k}}(\mathbf{x})$ can always be expanded in a series of functions, which are themselves products of a radial function $f_l^m(r)$ and an angular function $Y_l^m(\theta,\phi)$, i. e.,

$$\psi_{\mathbf{k}}(\mathbf{x}) = \sum_{l=0}^{\infty}\sum_{m=-l}^{l} a_l^m f_l^m(r) Y_l^m(\theta,\phi)\,, \tag{1.17}$$

d Note that the *scattering* cross section is different from the *photoionization* cross section, even when both are typically denoted as σ. We found this convention too iconic to break with it, and hope that, the way the material is organized, the two can never be confused.

an approach that is known as the partial-wave expansion of the scattering wave function. The functions $Y_l^m(\theta,\phi)$ in Eq. (1.17) are the so-called spherical harmonics that form a complete set of orthonormal functions, which means that they can be used to expand an arbitrary function of θ and ϕ as

$$F(\theta,\phi) = \sum_{l=0}^{\infty} \sum_{m=-l}^{l} f_{lm} Y_l^m(\theta,\phi)\,, \tag{1.18}$$

where both l and m take integer values and for every l there are $(2l+1)$ allowed values for m, running from $-l$ to $+l$. Formally, the spherical harmonics are defined as the product of a θ-dependent, associated Legendre polynomial $P_l^m(\cos\theta)$ and a ϕ-dependent complex exponential term,[10] like

$$Y_l^m(\theta,\phi) = (-1)^m \sqrt{\frac{(2l+1)}{4\pi}\frac{(l-m)!}{(l+m)!}}\, P_l^m(\cos\theta)\, \mathrm{e}^{\mathrm{i}\phi m}\,. \tag{1.19}$$

The associated Legendre polynomials $P_l^m(x)$, in turn, are derived from the *ordinary* Legendre polynomials $P_l(x)$ (for details, we refer to the monograph by Edmonds[10]). Here, we only want to point out that the ordinary Legendre polynomials $P_l(\cos\theta)$ themselves from a complete set of orthonormal functions, a property that we will use later several times. In that sense, the spherical harmonics can be understood as a generalization of the Legendre series from one into two angles, or – more generally – two degrees of freedom. When a problem is studied that is of rotational symmetry around the principal axis of the spherical coordinate system, all terms with $m \neq 0$ vanish on the right-hand side of Eq. (1.18), which then collapses to an ordinary Legendre expansion because $P_l^0(x) = P_l(x)$.

Coming back to the partial-wave expansion of the Schrödinger equation for the scattered electron, let us first consider the free solution, where $V(\mathbf{x}) = 0$. The set of equations for the radial functions $y_{l,k}(r)$ then reads[9]

$$\left[\frac{\mathrm{d}^2}{\mathrm{d}r^2} - \frac{l(l+1)}{r^2} + k^2\right] y_{l,k}(r) = 0\,, \tag{1.20}$$

for any integer $l \geq 0$ and again $k = \sqrt{2m\epsilon}$. The second, l-dependent term is referred to as the centrifugal potential for an angular momentum of l. It can be shown[11] that the Riccati–Bessel functions $\hat{j}_l(kr)$ are solutions of Eq. (1.20). Not very surprisingly, the complete solution of the free partial-wave Schrödinger equation is just a partial-wave expansion similar to Eq. (1.17) of a plane wave (which is a solution of the same Schrödinger equation in Cartesian coordinates),[9]

$$\sqrt{\frac{2}{\pi}}\frac{1}{kr} \sum_{l=0}^{\infty} \sum_{m=-l}^{l} \mathrm{i}^l\, \hat{j}_l(kr)\, Y_l^m(\hat{\mathbf{k}})^*\, Y_l^m(\hat{\mathbf{x}}) = \mathrm{e}^{\mathrm{i}\mathbf{k}\cdot\mathbf{x}}\,, \tag{1.21}$$

where $\hat{\mathbf{k}}$ and $\hat{\mathbf{x}}$ denote the directions of $\mathbf{k}$ and $\mathbf{x}$, respectively. While the exact form of the functions $\hat{j}_l(kr)$ is not so important for our purpose, it is important to see how they behave asymptotically. From Eq. (1.20) it is clear that the centrifugal term vanishes for large r, so that the function must then behave like an ordinary sine wave. In fact, one finds that[9]

$$\hat{j}_l(kr) \underset{r\to\infty}{\sim} \sin\left(kr - \frac{1}{2}l\pi\right). \tag{1.22}$$

In the next step, consider an electron scattering off a central potential, which is one that is spherically symmetric, so that the potential can be written as $V(r)$. For a central potential, the radial equations are still decoupled, which makes their treatment a lot easier. Then, the radial Schrödinger equation becomes

$$\left[\frac{\mathrm{d}^2}{\mathrm{d}r^2} - \frac{l(l+1)}{r^2} - 2\,m\,V(r) + k^2\right]\psi_{l,k}(r) = 0\,. \tag{1.23}$$

The radial eigenfunctions $\psi_{l,k}(r)$ that solve the above equation will, again, take the form of a sine wave at large radii because $V(r)$ quickly vanishes (which is what we *demanded*, in the first place). More precisely, it can be shown that their asymptotic form is[11]

$$\psi_{l,k}(r) \underset{r\to\infty}{\sim} a_l \sin\!\left(k\,r - \frac{1}{2}l\,\pi + \delta_l(k)\right), \tag{1.24}$$

where a_l is some constant. The striking difference between Eq. (1.22) and Eq. (1.24) is the *additional* phase shift $\delta_l(k)$. One can intuitively picture the action of the potential from the sign of the phase shift: a (net) repulsive potential pushes the partial wave out, which corresponds to a negative phase shift, and a (net) attractive potential sucks the partial wave in, which corresponds to a positive phase shift. What is most striking about the phase shifts $\delta_l(k)$ is that the scattering amplitude $f(\theta,\phi)$ that was introduced above can be obtained from these phase shifts alone, as will be shown below.

In the example of a central potential, the scattering amplitude is cylindrically symmetric and – for simplicity – we denote it as $f(\theta)$, which is given by[9]

$$f(\theta) = \sum_l (2l+1) f_l(k)\,P_l(\cos\theta) \tag{1.25}$$

where $f_l(k)$ is the so-called partial-wave amplitude that is defined as

$$f_l(k) = \frac{\mathrm{e}^{\mathrm{i}\delta_l(k)}\sin\delta_l(k)}{k}\,. \tag{1.26}$$

What is striking about $f_l(k)$ is that it is entirely determined by the phase shift $\delta_l(k)$ and that the amplitude a_l from Eq. (1.24) does not *seem* to appear in the definition of the partial-wave amplitude. To understand this, recall that in the formal description of the stationary scattering process, according to Eq. (1.16), the incoming *and* transmitted matter wave of the scattering particle is written as a plane wave. The partial-wave components of this plane wave are defined according to Eq. (1.21), by which also its partial-wave amplitudes are determined. Through the scattering process a fraction of this amplitude (or, at most, all of it) is transferred into the scattered spherical wave, and it is the *phase shift* between the transmitted and the scattered wave that determines this fraction.

From the partial-wave amplitude, one readily obtains the angle-integrated partial-wave cross section, σ_l, which is just

$$\sigma_l(k) = 4\,\pi\,(2l+1)\,\frac{\sin^2\delta_l(k)}{k^2}\,, \tag{1.27}$$

from which it is clear that $\sigma_l(k)$ reaches its maximum value for values of k that are half-integer multiples of π. In other words, for $\delta_l = 0 \pm n\,\pi$ (with integer n), the partial wave is completely

transmitted, and for $\delta_l = \frac{1}{2}\pi \pm n\,\pi$, it is completely scattered. Finally, the total cross section is just the sum of the partial-wave cross sections,

$$\sigma_{\text{tot}}(k) = \sum_l \sigma_l(k)\,. \tag{1.28}$$

In the beginning of this section, we have introduced a short-range potential as one that falls off *faster* than $1/r$ at infinity. Now, it is an unfortunate fact of life that this condition does not hold for any of the problems that are to be discussed in this thesis because both in photoionization and laser-assisted electron recollisions the electrons interact with the parent *ion*, which means that a net charge is involved, and the Coulomb potential that this charge creates falls off just as $1/r$. This means that, instead of Eq. (1.23), we have to find the solution to the equivalent Schrödinger equation, in which $V(r)$ can be written as the sum of a short-range potential $V_{sr}(r)$ and the Coulomb potential Z/r for an integer net charge Z.

The solution to this problem is to define the scattering phase shifts not relative to the partial-wave expansion of a plane wave, but relative to that of a so-called Coulomb wave, which is the continuum wave function for an electron moving in the presence of a point charge with charge Z. Introducing the strength parameter $\gamma = -(Z\,e^2\,m)/k$, the corresponding partial-wave expansion is[12]

$$\psi_c = \sqrt{\frac{2}{\pi}}\,\frac{1}{k\,r}\sum_{l=0}^{\infty}\sum_{m=-l}^{l} \mathrm{i}^l\,\mathrm{e}^{\mathrm{i}\eta_l} F_l(\gamma, k\,r)\,Y_l^m(\hat{\mathbf{k}})^*\,Y_l^m(\hat{\mathbf{x}})\,, \tag{1.29}$$

which differs from Eq. (1.21) only by the radial functions, which are the so-called Coulomb functions $F_l(\gamma, k\,r)$, and the phase factor containing η_l, which is the Coulomb phase shift. This phase shift is defined as

$$\eta_l(k) = \arg\Gamma(l + 1 + \mathrm{i}\gamma) \tag{1.30}$$

where $\Gamma(x)$ is the gamma function and $\arg(z)$ denotes the argument of a complex number. The asymptotic form of the Coulomb functions is now

$$F_l(\gamma, k\,r) \underset{r\to\infty}{\sim} \sin\!\left(k\,r - \gamma\,\ln 2k\,r - \frac{1}{2}l\,\pi + \eta_l\right), \tag{1.31}$$

which emphasizes that these functions never stop to accumulate phase through the logarithmic term, which is a consequence of the fact that the Coulomb potential does not vanish at infinity. Now, when an *additional* short range potential is introduced, an *additional* phase shift $\nu_l(k)$ appears in the asymptotic form of the radial solution function, completely analogous to the case without a net charge that was discussed above. Just as the potential $V(r)$ is decomposed in the Coulomb-plus-short-range case, so is the scattering amplitude, which can be written as the sum of the scattering amplitude for the short-range potential, f_{sr}, and the Coulomb amplitude, f_c. The former is given as[9]

$$f_{\text{sr}}(\theta) = \frac{1}{2\mathrm{i}k}\sum_l (2l + 1)\,\mathrm{e}^{2\mathrm{i}\eta_l}\,(\mathrm{e}^{2\mathrm{i}\nu_l} - 1)\,P_l(\cos\theta)\,, \tag{1.32}$$

from which it is clear that the Coulomb phase shift always has to be taken into account when dealing with the scattering on charged targets. The differential cross section for electron–ion

scattering is consequently determined by the coherent sum of f_{sr} and f_c, i. e.,

$$\frac{\mathrm{d}\sigma}{\mathrm{d}\mathbf{\Omega}} = |f_c + f_{\mathrm{sr}}|^2 \,, \tag{1.33}$$

where

$$f_c = \frac{2Zm}{(2k\sin\frac{\theta}{2})^2} \exp\left[2\mathrm{i}\left(\eta_0 - \gamma\,\ln\sin\frac{\theta}{2}\right)\right], \tag{1.34}$$

and η_0 is the Coulomb phase shift for an s wave. Note that, the way f_c is written, the summation over l was carried out analytically, rendering f_c independent of l. What is remarkable about Eq. (1.34) is that the associated Coulomb-only cross section, given by

$$|f_c|^2 = \frac{m^2Z^2}{4k^4\sin^4\frac{\theta}{2}} \,, \tag{1.35}$$

is identical to the Rutherford formula, which is the result for classical scattering of two charged particles.

We now continue this section with a short introduction to one of the most prominent resonance phenomena in scattering, the so-called shape resonances, which we will discuss in several contexts in this thesis. In a shape resonance, the scattering electron is thought to be transiently captured by the potential in an intermediate state that is not a real bound state, but that has a finite lifetime, during which the captured electron gradually escapes. Such a pseudo-bound state is, under certain circumstances, supported by the scattering target through the delicate interplay of an attractive short-range potential and the centrifugal potential $l(l+1)/r^2$. For a specific value of l, it may happen that an inner potential well is formed behind an angular-momentum barrier. To see his, consider the prototypical example of a square well potential,

$$V(r) = \begin{cases} -V_0 & \text{if } r \le a \\ 0 & \text{if } r > a \end{cases} . \tag{1.36}$$

For the parameters[e] $a = 2\,a_0$ and $V_0 = 3\,E_\mathrm{h}$ it is known that the resulting square-well potential $V(r)$ supports a shape resonance in the $l = 3$ channel at a resonance energy of $E_R \approx 18\,\mathrm{eV}$.[9] In Fig. 1.1a, the effective potential, which is the sum of $V(r)$ and the centrifugal potential, is shown for the four lowest possible values for l. Note how the angular-momentum barrier builds up at $r = a$ with increasing l.

To illustrate the barrier-penetration mechanism, we show the radial wave function[f] in Fig. 1.1b, for three different energies in the $l = 3$ channel: below, right at, and above the resonance energy E_R. Clearly, for $\epsilon = E_R$, the wave-function value is strongly increased inside the inner potential well, whereas at lower energies, the wave function cannot penetrate the angular-momentum barrier, and at energies higher than E_R, the wave-function value inside the well is just as high as outside of it.

e To simplify the notation, we work in atomic units from here on, in which $m_e = e = \hbar = a_0 = 1$. Here, a_0 is the so-called Bohr radius, which corresponds to the radius of the electron orbit in the ground state of hydrogen according to the classical Bohr model of the atom. In atomic units, energy is measured in Hartrees, with $1\,\mathrm{Ha} = 1\,E_\mathrm{h} = 27.2114\,\mathrm{eV}$.

f The results of this section were obtained with a modified version of the potential scattering code written by Bartschat,[13] which is distributed with every copy of this text book.

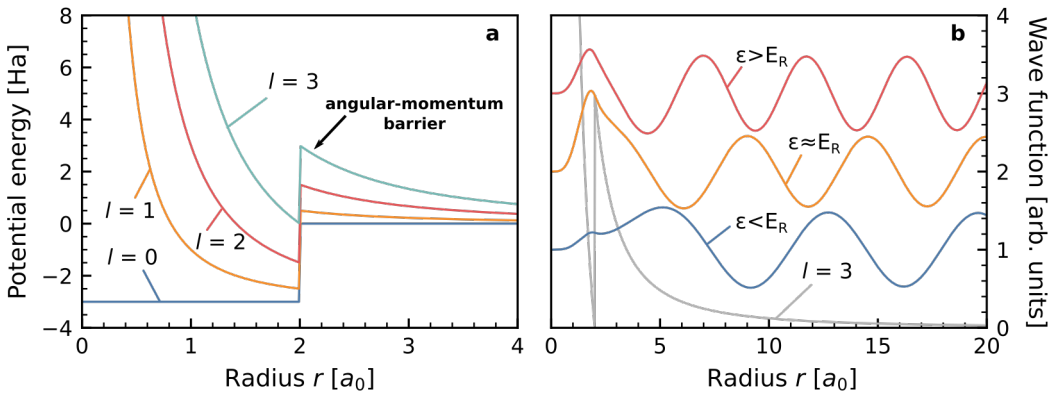

Figure 1.1 Potential scattering at a square-well potential. **a)** Effective, l-dependent potential for the square-well $V(r)$. **b)** Radial wave functions for $l = 3$ and three different energies: One below (blue), one closely at (orange), and one above (red) the resonance energy E_R. The effective potential for $l = 3$ is shown in light gray, as well. Note that the abscissas of **a** and **b** are scaled differently.

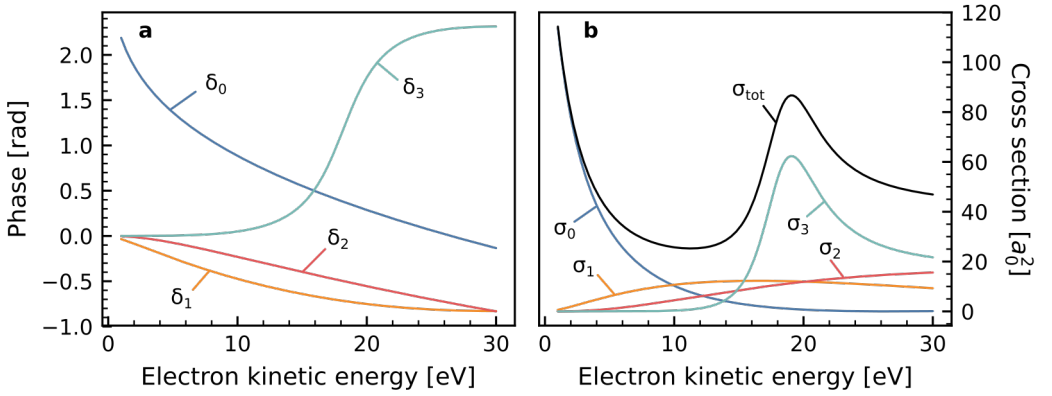

Figure 1.2 Scattering phase shifts δ_l **(a)** and cross sections σ_l **(b)** for scattering on the effective potentials of Fig. 1.1a, as a function of scattering kinetic energy.

To verify the presence of a shape resonance, one has to investigate the energy dependence of the scattering phase shifts. It turns out that such a resonance always manifests itself as a sudden energy-dependent, *positive*[g] phase jump of $\approx \pi$. This is exactly what is found for δ_3, as can be seen from Fig. 1.2a, where the energy dependence of the scattering phase shifts is shown for the angular momenta 0 through 3.

From the fact that the partial-wave cross sections in Eq. (1.27) exhibit a periodicity of π with respect to variations in k, one can derive that, at the resonance, the cross section must vary rapidly. The exact shape depends on the interference of the resonance with the background phase shift,[9] which is the scattering phase shift that one would obtain if the resonance was absent. From Fig. 1.2a it is clear that δ_3 is essentially zero before the phase jump, which is why the resonance shows up as a pronounced maximum in the scattering cross section, which

g This must be the case because the inner potential well is an attractive potential that sucks the partial wave in, which, in turn, leads to a positive phase shift, as discussed above.

can also be clearly distinguished in the total cross section, as demonstrated in Fig. 1.2b.

Concluding this section, we want to briefly outline what happens, when one is faced with treating the scattering of electrons on actual molecules as opposed to spherically symmetric model potentials: the biggest difference is that the Schrödinger equations of Eq. (1.23) are not decoupled anymore, so that the angular momentum l is not conserved during scattering. We note, however, that this angular-momentum coupling is not completely arbitrary and that, if the target is of high symmetry, which is often the case with small molecules, a symmetry-adapted basis set can be devised, in which only partial waves of like symmetry couple.[14] As a consequence of this coupling, the scattering phase shifts δ_l alone are not sufficient to describe the scattering amplitude and hence the cross section. Instead, the scattering S matrix is introduced, which connects the incoming partial waves of angular momentum l to all outgoing partial waves of angular momentum l'. In that sense, the S matrix for the scattering on a central potential just takes a special form: it becomes diagonal, with diagonal entries[9]

$$s_l(k) = \mathrm{e}^{2\mathrm{i}\delta_l(k)} \,. \tag{1.37}$$

Shape resonances can be observed in molecules as well,[15] but from the S matrix itself it is not clear, how they can be uniquely identified. To achieve this, the S matrix is first diagonalized,

$$\mathbf{S} = \mathbf{U}\mathrm{e}^{2\mathrm{i}\boldsymbol{\delta}}\,\mathbf{U}^{\dagger} \tag{1.38}$$

where $\mathbf{U}$ is a unitary matrix, and $\tilde{\boldsymbol{\delta}}$ is the diagonal matrix with matrix elements $\tilde{\delta}_l$, which are referred to as *eigenphases*. Now, while the individual eigenphases tend to show a very complicated behavior,[16] the *eigenphase sum*, i. e., the sum of eigenphases associated with the same continuum symmetry, often reveals a phase jump similar to the one shown in Fig. 1.2a, a fact that we will make use of later.

A powerful way to rationalize what shape resonances are and how they can be characterized, is to see how they can be described as poles of the S matrix in the complex energy plane. In general, the S matrix is clearly a function of the scattering energy E, and when one allows E to take complex values, S may go to infinity at certain points in the lower imaginary half plane.[9] These points can be written as $E_R - \mathrm{i}\Gamma/2$, where E_R is again the resonance position on the real energy axis and Γ is the width of the resonance. To see how such a pole affects the behavior of the phase along the real energy axis, consider the phase portrait $\arg f(E)$ of the function $f(E) = 1/(E-(E_R-\mathrm{i}\Gamma/2))$, shown in Fig. 1.3a, with the shape-resonance parameters of the above square-well example.[h] According to Cauchy's integral formula, a total phase of 2π is accumulated on a closed line that contains the pole. Qualitatively speaking, going from $-\infty$ to ∞ on the real energy axis, only half a circle surrounds the pole, which corresponds to half the phase accumulated, which is just π. This is the reason for the characteristic phase shift of $\approx \pi$ observed at shape resonances. Furthermore, once the exact pole position of the resonance is found, the scattering wave function can be evaluated at that complex-valued energy, which is the *pure* resonance wave function without interference with the background phase shift. This can be helpful in analyzing the effect that the shape resonance may have on the (photo-)electron angular distributions.

h For $f(E)$ this particular form is chosen because it represents the simplest function that has a single, *simple* pole at the complex-valued resonance energy $E_R - \mathrm{i}\Gamma/2$.

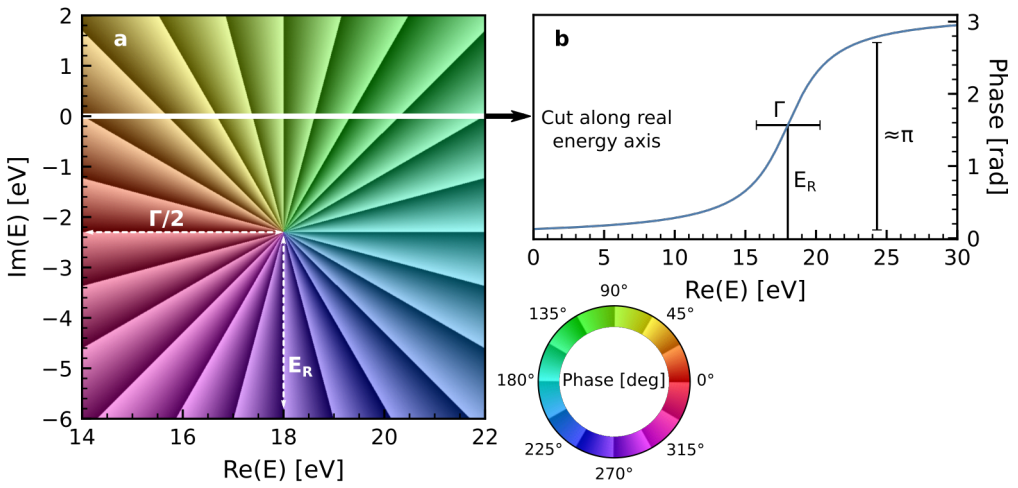

Figure 1.3 Illustration of a pole of the S matrix in the complex energy plane. **a)** Phase portrait of the function with a simple pole, $f(E) = 1/(E - (E_R - \mathrm{i}\Gamma/2))$, where $E_R = 18\,\mathrm{eV}$ and $\Gamma = 4.6\,\mathrm{eV}$. The shading that is superimposed onto the color scale is intended to emphasize the circular phase accumulation that the pole introduces. In particular, it helps illustrating that the phase jump as seen from the real energy axis is the steeper, the closer the pole is located to this axis (and, hence, the smaller Γ is). **b** Effect of the pole on the phase behavior along the real energy axis.

1.3 Photoelectron angular distributions in molecules

After the discussion of the scattering angular distributions in the previous section, it would be very surprising if the differential cross sections for photoionization, which are often called photoelectron angular distributions (PADs), were always isotropic. Experimentally, one observes that the PADs always exhibit cylindrical symmetry when linearly polarized light is used, and therefore the differential cross sections for *photoionization* are written in terms of the Legendre series of the so-called beta parameters β_l,

$$\frac{\mathrm{d}\sigma}{\mathrm{d}\theta} = \frac{\sigma_f}{4\pi}\left(1 + \sum_l \beta_l P_l(\cos\theta)\right). \tag{1.39}$$

What is remarkable about the single-photon ionization of atoms is that all β_l vanish except for $l = 2$ (which is why β_2 is commonly referred to as *the* beta parameter, only). What is even more remarkable – and not at all obvious – is that this is *also* true for molecules that are randomly oriented in the gas phase.

To explain and generalize this finding, we proceed in two steps: First, consider again the dipole matrix element for photoionization,

$$\langle \psi_{\mathbf{k}}(\mathbf{x}) | \mathbf{d} | g(\mathbf{x}) \rangle \ , \tag{1.40}$$

where $\psi_{\mathbf{k}}$ is the continuum wave function for the electron–molecular-ion scattering problem discussed above,[i] $\mathbf{d}$ is a dipole operator (in length or velocity gauge) and $g(\mathbf{x})$ is some overlap

i We note that, strictly, the continuum wave functions in electron–ion scattering on one side, and in photoionization on the other, have different asymptotic boundary conditions,[17] a technical detail that need not worry us here.

amplitude or Dyson orbital that the photoelectron is ejected from. To systematically treat the spectroscopic observables of rotating molecules, we need to distinguish two frames of reference: the molecular frame (MF) and the laboratory frame (LF). The molecular (or body-fixed) frame is defined such that all observables, like the PAD, are given with respect to a coordinate system that has a fixed relation to the internal coordinates of the molecule, and this frame of reference does not need to coincide with the laboratory (or space-fixed) frame, in which the photoelectron is detected. To distinguish these two frames, we will use primed variables to denote quantities in the LF and unprimed variables for the MF from here on. Moreover, we follow the convention to take the Cartesian z axis in the MF to be aligned along the principal molecular axis.

In the previous section, we have introduced the partial-wave decomposition of the continuum wave function, and now we can proceed to decompose the photoionization dipole matrix element in just the same way.[18] Writing the usual photoionization dipole matrix elements as

$$I^r = \sqrt{k}\,\langle \psi_{\mathbf{k}}(\mathbf{x}) | \hat{\mathbf{n}} \cdot \mathbf{x} | g(\mathbf{x}) \rangle \tag{1.41a}$$

and

$$I^\nabla = \frac{\sqrt{k}}{\omega}\,\langle \psi_{\mathbf{k}}(\mathbf{x}) | \hat{\mathbf{n}} \cdot \mathbf{p} | g(\mathbf{x}) \rangle \tag{1.41b}$$

with the superscripts r and ∇ denoting the length and velocity form, respectively, and ω being the radiation frequency, the partial-wave decomposition is just

$$I^{r,\nabla} = \sqrt{\frac{4\pi}{3}} \sum_{lm\mu} I^{r,\nabla}_{lm\mu}\, Y_l^m(\hat{\mathbf{k}})^*\, Y_1^\mu(\hat{\mathbf{n}})^* \,. \tag{1.42}$$

In this equation, $\hat{\mathbf{k}}$ is the direction of the emitted photoelectron and $\hat{\mathbf{n}}$ is the orientation of the polarization axis in the molecular frame. The partial-wave photoionization matrix elements $I^{r,\nabla}_{lm\mu}$ are then given by[18]

$$I^r_{lm\mu} = \sqrt{k}\,\left\langle \psi_{lm,\mathbf{k}} \middle| \mathbf{r}_\mu \middle| g \right\rangle \tag{1.43a}$$

and

$$I^\nabla_{lm\mu} = \frac{\sqrt{k}}{\omega}\,\left\langle \psi_{lm,\mathbf{k}} \middle| \boldsymbol{\nabla}_\mu \middle| g \right\rangle \tag{1.43b}$$

both of which are now *radial* integrals between the partial-wave radial functions of the continuum and the bound-state wave functions (where the latter has to be expanded into such a representation first, of course), and the $\mathbf{r}_\mu$ as well as the $\boldsymbol{\nabla}_\mu$ are so-called vector spherical harmonics,[10] which are used to represent the (Cartesian) dipole operator in spherical coordinates. The index μ denotes the Cartesian axis that is projected, where $\mu = 0$ represents the dipole along the z axis, and $\mu = +1, -1$ correspond to the x and y axes, respectively (all in the MF).

Now that we know how the photoionization process is formally described in the molecular frame, the question remains what happens, when the molecule is being rotated with respect to the laboratory frame (LF) in which we measure the emitted photoelectron,[j] which is the

j The laboratory frame is also referred to as the photon frame[19] because the polarization axis is defined in the laboratory frame.

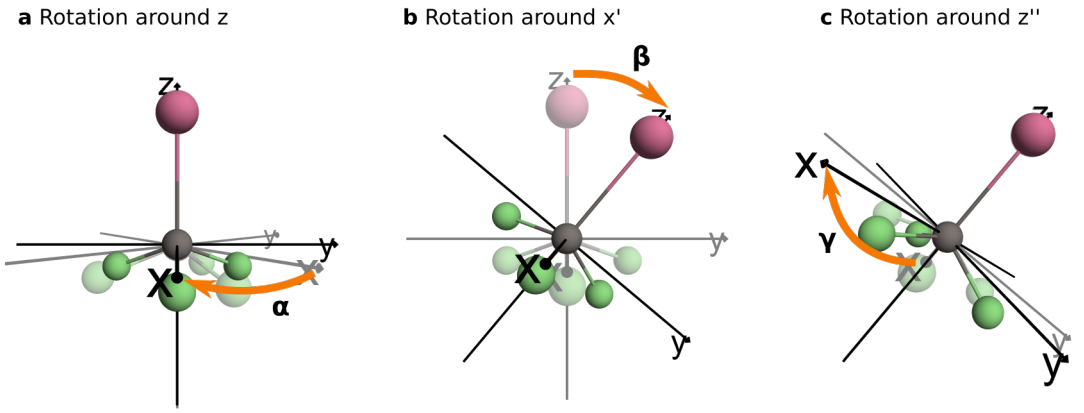

Figure 1.4 Rotations of a molecule under the Euler angles to realize any possible orientation of it in the laboratory frame. First, the molecule is rotated around the space-fixed polar axis by the angle α **(a)**. Then this polar axis is tilted by the angle β **(b)**. Third, the molecule is rotated around the body-fixed polar axis by the angle γ **(c)**.

second step. In general, a non-linear molecule has three degrees of rotational freedom: the two external rotations around the polar and azimuthal angles in the LF, and the internal rotation around its principal molecular axis. (A linear molecule only has two such degrees of freedom because there is no internal rotation possible.)

Consequently, we need to define three angles to describe any possible orientation of the molecule in the LF. These angles are called the Euler angles, and we denote them as $\mathbf{R} = (\alpha\ \beta\ \gamma)$. In Cartesian coordinates, rotations under the Euler angles are expressed by the threefold application of the rotation matrices around the Cartesian axes z—x'—z'' (see Fig. 1.4), written as[10]

$$\begin{aligned}\begin{pmatrix}\cos\gamma & -\sin\gamma & 0\\ \sin\gamma & \cos\gamma & 0\\ 0 & 0 & 1\end{pmatrix}\begin{pmatrix}1 & 0 & 0\\ 0 & \cos\beta & -\sin\beta\\ 0 & \sin\beta & \cos\beta\end{pmatrix}\begin{pmatrix}\cos\alpha & -\sin\alpha & 0\\ \sin\alpha & \cos\alpha & 0\\ 0 & 0 & 1\end{pmatrix}\begin{pmatrix}x\\ y\\ z\end{pmatrix} &= \mathbf{D}(0\,0\,\gamma)\,\mathbf{D}(0\,\beta\,0)\,\mathbf{D}(\alpha\,0\,0)\,\mathbf{x}\\ &= \mathbf{D}(\mathbf{R})\,\mathbf{x} = \mathbf{x}'\,. \end{aligned} \tag{1.44}$$

The application of these matrices transfers a point $\mathbf{x} = (x\ y\ z)$ to the point $\mathbf{x}' = (x'\ y'\ z')$ within a coordinate system rotated by the Euler angles. Moreover, we can use the rotation matrices to express the rotation of spherical harmonics between different coordinate systems. To this end, we need the matrix elements of the rotation operator $\mathbf{D}(\mathbf{R})$ in the angular momentum basis,[10]

$$\langle lm|\mathbf{D}(\mathbf{R})|lm'\rangle = \mathfrak{D}^{l}_{m'm}(\mathbf{R})\,, \tag{1.45}$$

where $|lm\rangle$ is the spherical harmonic $Y^m_l(\theta,\phi)$ in the more general vector-space notation, and $\mathfrak{D}^{l}_{m'm}(\mathbf{R})$ is a matrix element of the so-called Wigner D matrix. We find the following interpretation of the Wigner D matrix most intuitive: Just as the spherical harmonics can be understood as a generalization of Legendre series from one into two dimensions, the Wigner D matrix can be seen as a generalization of the spherical harmonics from two into three dimensions, namely the three Euler angles. As mentioned above, the Wigner D matrix can be used to express the rotation of the spherical harmonic of angular momentum l as a linear

combination of the $(2l+1)$ spherical harmonics of like l and all allowed values for m, as[19]

$$Y_l^m(\hat{\mathbf{x}}') = \sum_{m'} \mathcal{D}^l_{m'm}(\mathbf{R})\, Y_l^{m'}(\hat{\mathbf{x}})\,, \tag{1.46}$$

where $\hat{\mathbf{x}}'$ and $\hat{\mathbf{x}}$ denote again the directions of $\mathbf{x}'$ and $\mathbf{x}$.

Finally, to be able to average over all possible orientations of a molecule in the LF we need to know how to integrate over these rotations. Analytically, this can be done with the help of the so-called vector-coupling coefficients, for which there are – unfortunately – numerous definitions and conventions[10] in the literature. The two most commonly encountered coupling coefficients are the Clebsch–Gordan coefficients and the Wigner $3j$ symbols, which are related to each other through a phase factor and a normalization constant. Here we will work with the $3j$ symbols, which are written as

$$\begin{pmatrix} l_1 & l_2 & L \\ m_1 & m_2 & M \end{pmatrix}$$

, which suggests that the sum of two angular momenta, $|l_1 m_1\rangle$ and $|l_2 m_2\rangle$, is expressed in the basis of a total angular momentum, namely $|LM\rangle$. An intuitive way to understand the meaning of the coupling coefficients is to see that they arise as integrals between three Wigner D matrices,[10]

$$\int_0^{2\pi}\int_0^{\pi}\int_0^{2\pi} \mathcal{D}^{l_1}_{m_1' m_1}(\mathbf{R})\, \mathcal{D}^{l_2}_{m_2' m_2}(\mathbf{R})\, \mathcal{D}^{l_3}_{m_3' m_3}(\mathbf{R})\, \mathrm{d}\alpha \sin\beta\, \mathrm{d}\beta\, \mathrm{d}\gamma = 8\pi^2 \begin{pmatrix} l_1 & l_2 & l_3 \\ m_1' & m_2' & m_3' \end{pmatrix} \begin{pmatrix} l_1 & l_2 & l_3 \\ m_1 & m_2 & m_3 \end{pmatrix}. \tag{1.47}$$

Equivalently, the vector-coupling coefficients can be used to re-express the product of two Wigner D matrices in a coupled angular-momentum basis (hence the name), which is, for example, vital to describe the interaction between a space-fixed polarization axis and the rotating molecular axis in the LF. This re-expansion is then

$$\mathcal{D}^{l_1}_{m_1' m_1}(\mathbf{R})\, \mathcal{D}^{l_2}_{m_2' m_2}(\mathbf{R}) = \sum_{LM'M} (2L+1) \begin{pmatrix} l_1 & l_2 & L \\ m_1' & m_2' & M' \end{pmatrix} \mathcal{D}^{L*}_{M'M}(\mathbf{R}) \begin{pmatrix} l_1 & l_2 & L \\ m_1 & m_2 & M \end{pmatrix}. \tag{1.48}$$

To be able to draw *some* conclusion from the formidable vector-coupling equations that one encounters in the literature, one has to know the conditions for which the angular-momentum coupling coefficients can be nonzero. The first one is known as the triangular condition,

$$|l_1 - l_2| \le L \le l_1 + l_2\,. \tag{1.49}$$

Second, the projection onto the z axis must be conserved, which implies,

$$m_1 + m_2 = -M\,. \tag{1.50}$$

A third condition, which only applies to the special case $m_1 = m_2 = M = 0$, is that the sum $l_1 + l_2 + L$ be *even* for the coefficient not to vanish. Clearly, all three conditions have to be met (the third one only if it applies), for a $3j$ symbol to be possibly nonzero.

With all this in mind, we can now turn to the expressions for the photoelectron angular distributions. First, we consider photoemission from a molecule that is fixed in space. In this case, the differential cross section is actually *doubly* differential because it is parametrized by **R**, which describes the relative orientation between the polarization axis and the (fixed) principal molecular axis in terms of the Euler angles. The respective PAD can be written – and that should be not surprising – as a series of spherical harmonics,[19] i. e.,

$$\frac{\mathrm{d}\sigma(\mathbf{R})}{\mathrm{d}\mathbf{\Omega}} = \frac{4\pi^2\omega}{c} \sum_{L=0}^{2l} \sum_{M=-L}^{L} A_{LM}(\mathbf{R})\, Y_L^M(\mathbf{\Omega}) \tag{1.51a}$$

where

$$\begin{aligned} A_{LM}(\mathbf{R}) = \sum_{\substack{lm\mu \\ l'm'\mu'}} & (-\mathrm{i})^{l-l'}\, \mathrm{e}^{\mathrm{i}(\eta_l - \eta_{l'})} (-1)^{m+\mu} \sqrt{(2l+1)(2l'+1)(2L+1)} \\ & \times \begin{pmatrix} l & l' & L \\ 0 & 0 & 0 \end{pmatrix} \begin{pmatrix} l & l' & L \\ -m & m' & M \end{pmatrix} I^{r,\nabla}_{lm\mu}\, I^{r,\nabla}_{l'm'\mu'} \\ & \times \sum_{L_\mu} (2L_\mu + 1) \begin{pmatrix} 1 & 1 & L_\mu \\ -m_\mu & m'_\mu & 0 \end{pmatrix} \begin{pmatrix} 1 & 1 & L_\mu \\ -\mu & \mu' & \mu - \mu' \end{pmatrix} \mathfrak{D}^{L_\mu}_{\mu-\mu',0}(\mathbf{R})\,. \end{aligned} \tag{1.51b}$$

What can be seen from Eq. (1.51) is that the highest-order partial wave that can contribute to the PAD is that of $L = 2l$ (with the limiting coefficients being those on the second line of the expression for $A_{LM}(\mathbf{R})$). This is, in turn, a consequence of condition (1.49), and a fact that already Dill[20] has discussed.

Now, by integrating Eq. (1.51a) over all molecular orientations **R** analytically, one arrives at the following expression

$$\frac{\mathrm{d}\sigma}{\mathrm{d}\theta'} = \frac{\pi\omega}{3c} \sum_L A_L\, P_L(\cos\theta') \tag{1.52a}$$

with

$$\begin{aligned} A_L = (2L+1) \begin{pmatrix} 1 & 1 & L \\ 0 & 0 & 0 \end{pmatrix} \sum_{\substack{lm\mu \\ l'm'\mu'}} & (-\mathrm{i})^{l-l'}\, \mathrm{e}^{\mathrm{i}(\eta_l - \eta_{l'})} (-1)^{m+\mu} \\ & \times \sqrt{(2l+1)(2l'+1)} \begin{pmatrix} l & l' & L \\ 0 & 0 & 0 \end{pmatrix} \begin{pmatrix} l & l' & L \\ -m & m' & m - m' \end{pmatrix} \\ & \times \begin{pmatrix} 1 & 1 & L \\ -\mu & \mu' & \mu - \mu' \end{pmatrix} I^{r,\nabla}_{lm\mu}\, I^{r,\nabla}_{l'm'\mu'}\,, \end{aligned} \tag{1.52b}$$

where θ' denotes the polar angle in the *laboratory* frame. Here, right from the first $3j$ symbol, together with conditions (1.49) and (1.50), it is clear that the only values of L for which A_L does not vanish are zero and two. In other words, it is the angular momentum of the photon ($l = 1$) that is coupled with itself (through the square) to the LF, which gives rise to

the observation that the PAD for a randomly oriented ensemble is completely characterized by $\sigma \propto A_0$ and $\beta_2 = A_2/A_0$.

Underwood & Reid[21] have investigated the situation where the molecular axis distribution $P_{\mathrm{MA}}(\mathbf{R})$ is not uniform, which is the case when the molecules are aligned or oriented by some technique. The straightforward approach to dealing with this situation is to integrate $\mathrm{d}\sigma(\mathbf{R})/\mathrm{d}\mathbf{\Omega}$ numerically over $P_{\mathrm{MA}}(\mathbf{R})$.[k] However, from the equations that Underwood & Reid[21] have derived, one can estimate what the maximum l is that one would expect to be sensitive to when measuring the PADs for an aligned ensemble. If we assume that the internal rotation of the molecule (related to the angle γ in Fig. 1.4) is unconstrained, the molecular axis distribution P_{MA} can be expanded in spherical harmonics, just like in Eq. (1.18), i. e.,

$$P_{\mathrm{MA}}(\alpha,\beta) = \sum_{K=0}^{\infty} \sum_{Q=-K}^{K} B_{KQ} Y_K^Q(\alpha,\beta)\,, \tag{1.53}$$

and then, if K_{max} is the highest coefficient that gives a significant contribution to the above expansion (what "significant" in this context means certainly depends on the sensitivity of the experiment, but say $B_{K_{max}Q} \approx 1$), the maximum β_l that can *in principle* be observed is β_{K+2}.

1.4 Photoionization in strong laser fields

Up to this point we have only discussed photoionization with a single photon of ionizing radiation. However, atoms and molecules can also be ionized by radiation in the visible and infrared region if the intensities are high enough, which becomes possible with ultrashort laser pulses. Then the linear regime of light–matter interactions that was introduced in Eq. (1.3) is completely overthrown and N-photon processes dominate. In general, two pictures are commonly used to think about these multiphoton processes: in a photon picture, where the laser pulse is viewed as a packed bunch of photons, a high intensity corresponds to a high photon flux which implies a high spatial density of photons. Consequently, the probability for "finding more than one photon" at a molecule at the same time increases with intensity, making the interactions with more than one photon possible. Now, if the sum of photon energies absorbed exceeds the ionization potential, multiphoton ionization can occur. When, instead, the light pulse is pictured as an electromagnetic wave, the peak electric field strength of this wave increases with intensity to a point, where it becomes comparable to the electric fields that hold together electrons and nuclei. In this field picture, the atomic potential is distorted by the radiation to a point where electrons can escape by tunneling through – or passing directly over – the barrier. To get an estimate of what intensities are required to impose such vigorous conditions, consider the electric field that an electron in a hydrogen atom experiences at the first Bohr radius a_0, namely[2]

$$E_a = \frac{e}{4\pi\epsilon_0 a_0^2} \approx 5.1 \times 10^9\,\mathrm{V\,cm^{-1}}\,, \tag{1.54}$$

k Which is what we do later in this thesis. Note however that, in order to do so, one more rotation has to be applied to Eq. (1.51) such that the polarization axis is fixed in space and that it is the molecule that rotates under **R**.

where ϵ_0 is the vacuum permittivity. Calculating the intensity that corresponds to such a field strength, it turns out that this "atomic intensity" is

$$I_a = \frac{1}{2}\,\epsilon_0\, c\, E_a^2 \approx 3.5 \times 10^{16}\,\mathrm{W/cm^2}\,. \tag{1.55}$$

Practically, one will find that multiphoton ionization sets in already a few orders of magnitude below I_a, typically around 10^{11} to $10^{12}\,\mathrm{W/cm^2}$, depending on the ionization potential of the target.

In the strong-field ionization of matter, many new phenomena can be observed that have no correspondence in single-photon ionization. Among these, the three most prominent are above-threshold ionization (ATI), laser-assisted electron recollisions, and high-order harmonic generation (HHG), all of which will play a role at some point in this thesis. Another striking difference between single- and multiphoton processes is that, in the former, the electromagnetic radiation is thought to interact *only* with the bound electrons and not at all with the photoelectron after its liberation. In strong-field processes, this situation is reversed: here, often the interactions between the light field and the photoelectron are the *dominant* effects. One quantity that is particularly important in this context is the ponderomotive potential,

$$U_p = \frac{e^2 E_0^2}{4m\omega^2} \tag{1.56}$$

where E_0 is the peak electric field strength. The ponderomotive potential is an effective quiver energy that the photoelectron gains during its periodic acceleration in the light field.

Above-threshold ionization is the name for the observation that in strong-field ionization with light of the frequency ω typically not a single photoelectron line appears, but rather a series of lines that are spaced by $\hbar\omega$. Then, the equation for the photoelectron kinetic energy, Eq. (1.2), has to be generalized, such that now[22]

$$\epsilon_f^{(s)} = (n_0 + s)\cdot\hbar\omega - V_f - U_p\,, \tag{1.57}$$

where n_0 is the minimum number of photons that are required to overcome V_f and s is the number of photons absorbed "above threshold". The reason that U_p appears in Eq. (1.57) can be qualitatively understood as follows: In the presence of the oscillating laser field, the energy levels of the Rydberg and continuum states of an atom or molecule are increased by the Stark shift, which is approximately equal to U_p. As the electronic ground state is much less affected by the Stark shift, the effective ionization potential of the atom (or molecule) becomes $V_f + U_p$, which is accounted for in Eq. (1.57).

Over the years, many approaches were developed to treat the photoionization of atoms and molecules in strong laser fields. The most obvious, but often computationally prohibitive, idea is to solve the time-dependent Schrödinger equation for the electron–laser-field interaction numerically. Especially when wavelengths in the infrared region are considered, the quasi-static tunneling-rate equations, known as the ADK theory after Ammosov, Delone & Krainov,[23] and the strong-field approximation (SFA) are particularly popular. In Chapter 3 we will work with the SFA as developed by Faisal[24] and Reiss[25] because it has the especially attractive property that the expressions for the photoionization cross sections can be solved analytically. The central idea behind the SFA is that the interactions between the photoelectron and the

parent ion are either neglected completely or incorporated perturbatively, so that only the photoelectron–laser-electric-field problem has to be solved. Also, the SFA can be applied to molecules in a straightforward fashion, a variant known as molecular-orbital SFA, from which the complete, angle-resolved photoelectron spectrum and differential ionization rates can be obtained as a function of the angle between the laser polarization and the principal molecular axis.

To see how this works, we first need to consider the most formal way to describe the properties of a photoelectron spectrum, that is by viewing it as a spectrum of transition probabilities P_{fi} for the projection of an electron bound in the initial state $|\psi_i(t)\rangle$ onto a final state $\left|\psi_f(t)\right\rangle$ of the free electron through the action of the time-dependent laser field. For simplicity, we introduce the single active electron (SAE) approximation, in which only a single electron moving in the potential V of the parent molecular ion is taken into account. Then $|\psi_i(t)\rangle$ and $\left|\psi_f(t)\right\rangle$ are just solutions of the time-dependent Schrödinger equation in the absence of the laser field, which reads

$$\mathrm{i}\frac{\mathrm{d}}{\mathrm{d}t}\psi = H_0\psi\,, \tag{1.58}$$

where $H_0 = T + V$ is the laser-field-free Hamiltonian. As H_0 is not time-dependent, $|\psi_i(t)\rangle$ and $\left|\psi_f(t)\right\rangle$ can be written as products of stationary solutions of H_0 times a time-dependent phase factor, namely $\left|\psi_{i,f}(t)\right\rangle = \left|\phi_{i,f}\right\rangle \exp\{-\mathrm{i}\epsilon_{i,f}\,t\}$, where $|\epsilon_i| = V_i$ is just the ionization potential of the bound electron and ϵ_f is the final kinetic energy of the free electron. Formally, the transition probability for such a process is

$$P_{fi} = \left|T_{fi}\right|^2\,, \tag{1.59}$$

where the transition amplitude T_{fi} is given by,[2]

$$T_{fi} = \left\langle\psi_f(t)\middle|U(t,t_0)\middle|\psi_i(t_0)\right\rangle\,. \tag{1.60}$$

Here, $U(t,t_0)$ is a so-called time-evolution operator that propagates the system from t_0 to t, which is now also including the interaction with the laser field. In principle, the evolution operator is a solution of the equation

$$\mathrm{i}\frac{\mathrm{d}}{\mathrm{d}t}U(t,t_0) = H_{\mathrm{tot}}\,U(t,t_0)\,, \tag{1.61}$$

where the total Hamiltonian is now $H_{\mathrm{tot}} = H_0 + H_{\mathrm{int}}$. We recall that the interaction Hamiltonian H_{int} is obtained by taking into account that, in the presence of an electromagnetic wave, the electrons are accelerated by the instantaneous vector potential $\mathbf{A}(\mathbf{x},t)$. Using the same arguments that we presented for the single-photon case above in Section 1.1, we now – again – assume that the dipole approximation holds, which implies that the vector potential is independent of the position $\mathbf{x}$. Just as in Eq. (1.10) (but now in atomic units) the kinetic energy associated with the kinematic momentum $\boldsymbol{\pi} = \mathbf{p} + \mathbf{A}(t)$ is given by,[2]

$$\frac{\boldsymbol{\pi}^2}{2} = \frac{\mathbf{p}^2}{2} + \mathbf{A}(t)\cdot\mathbf{p} + \frac{\mathbf{A}^2(t)}{2} = K + H_{\mathrm{int}}(t) = H_F(t)\,, \tag{1.62}$$

where H_F denotes the "field Hamiltonian", i. e., the one that only takes into account the motion of a free electron in the presence of the laser field, and K is the kinetic energy of the photoelectron in the absence of the laser field.

In general, one cannot hope to find an explicit solution for the time-evolution operator $U(t, t_0)$ of the total Hamiltonian, and this is why a perturbative treatment is introduced. In the standard perturbation approach, H_{int} would be treated as the small perturbation to refine the (known) eigenfunctions of H_0 (as was done in Section 1.1 with single-photon ionization). The SFA, however, is based on the idea that the laser–electron interactions are much stronger than the influence of the molecular potential V on the electron, so that solutions for the field Hamiltonian H_F are sought, and V is introduced as the perturbation (if at all).

This means that in the first step we have to find the wave functions $\chi_{\mathbf{k}}(\mathbf{x}, t)$ that solve the time-dependent Schrödinger equation for the field Hamiltonian, i. e.,

$$\mathrm{i}\frac{\mathrm{d}}{\mathrm{d}t}\,\chi_{\mathbf{k}}(\mathbf{x}, t) = H_F(t)\,\chi_{\mathbf{k}}(\mathbf{x}, t)\,. \tag{1.63}$$

The solutions of this equation are explicitly time-dependent because $H_F(t)$ is a time-dependent quantity, and are formally found to be[2]

$$\chi_{\mathbf{k}}(\mathbf{x}, t) = (2\pi)^{-3/2}\exp\left\{\mathrm{i}\mathbf{k}\cdot\left[\mathbf{x} - \int_{-\infty}^{t}\mathbf{A}(\tau)\,\mathrm{d}\tau\right] - \mathrm{i}\epsilon_k\,t - \frac{\mathrm{i}}{2}\int_{-\infty}^{t}\mathbf{A}^2(\tau)\,\mathrm{d}\tau\right\}. \tag{1.64}$$

These time-dependent solutions, which can be understood as plane waves that are distorted by the vector potential, are known as Gordon–Volkov states. In particular, when $\mathbf{A}$ is zero, the Gordon–Volkov states collapse to ordinary plane waves (up to a phase factor). Using these Gordon–Volkov states, we can now write the time-evolution operator $U_F(t, t_0)$ for an electron moving in an oscillating laser field,[2] i. e.,

$$U_F(t, t_0) = \int \mathrm{d}\mathbf{k}\,|\chi_{\mathbf{k}}(t)\rangle\,\langle\chi_{\mathbf{k}}(t_0)|\ . \tag{1.65}$$

Starting from $U_F(t, t_0)$, the time-evolution operator of the total Hamiltonian $U(t, t_0)$, can formally be obtained by solving the integral equation

$$U(t, t') = U_F(t, t') - \mathrm{i}\int_{t'}^{t} U(t, \tau)\,V\,U_F(\tau, t')\ \mathrm{d}\tau\ . \tag{1.66}$$

Without going into the details of the derivation, we just want to remark that an integral equation like Eq. (1.66) can always be solved by developing $U(t, t_0)$ into an infinite series of perturbation terms $u^{(n)}(t, t')$, each of which contains n times an interaction with V. In particular, $u^{(0)}(t, t') = U_F(t, t_0)$, so that a qualitative way of understanding these terms is that $u^{(0)}(t, t')$ describes only the *direct* photoionization, whereas for $n \geq 1$, the electron has rescattered n times on the molecular potential.

In the most basic formulation of the SFA (which is the one that we adopt), all terms with $n \geq 1$ are ignored, and the photoionization amplitude is written as[2]

$$\begin{aligned} T_{f0}^{\text{SFA}} &= -\mathrm{i}\int_{t_0}^{t_1}\left\langle\phi_f(t_1)\middle|U_F(t_1, \tau)\,H_{\text{int}}(\tau)\middle|\phi_i(\tau)\right\rangle\mathrm{d}\tau \\ &= -\mathrm{i}\int_{t_0}^{t_1}\langle\chi_{\mathbf{k}}(\tau)|H_{\text{int}}(\tau)|\phi_i(\tau)\rangle\,\mathrm{d}\tau\ , \end{aligned} \tag{1.67}$$

where t_0 and t_1 are the times corresponding to the beginning and the end of the laser pulse, respectively. To find an analytical expression for the matrix elements in Eq. (1.67) we need to know that the overlap between the initial state $|\psi_i(t)\rangle$ and the Gordon–Volkov state $|\chi_{\mathbf{k}}(t)\rangle$ is given by[2]

$$\langle\chi_{\mathbf{k}}(t)|\psi_i(t)\rangle = \exp\{\mathrm{i}S(\mathbf{k}_f, t, t_0)\}\,\langle\mathbf{k}_f|\phi_i\rangle\,, \tag{1.68}$$

where $\langle\mathbf{k}_f|\phi_i\rangle$ is just the momentum-space representation of the molecular orbital ϕ_i and $S(\mathbf{k}_f, t, t_0)$ is the so-called modified action, defined as

$$S(\mathbf{k}_f, t, t_0) = \frac{1}{2}\int_{t_0}^{t}\left[\boldsymbol{\pi}(\mathbf{k}_f, \tau)\right]^2 \mathrm{d}\tau + V_i(t - t_0)\,, \tag{1.69}$$

where we recall that V_i is the ionization potential of the bound electron. In the next step, we make a drastically simplifying assumption about the shape of the laser pulse: we assume that the field envelope is square and that it encompasses exactly N laser cycles, so that the total duration of the laser pulse is $\tau_p = 2\pi N/\omega = N\,T$. After some algebraic manipulations, one arrives at the central expression for the photoionization probability,

$$P^{\mathrm{SFA}}(\mathbf{k}_f) = k_f|M_{f0}|^2\frac{\sin^2(NS_c/2)}{\sin^2(S_c/2)}\,\mathrm{d}\hat{\mathbf{k}}_f\,, \tag{1.70}$$

where M_{f0} is an angle-dependent photoionization amplitude that we will come back to in a moment, and $S_c = S(\mathbf{k}_f, T, 0)$ is the modified action *per cycle* (which is identical for every cycle due to the periodicity of the field and the square shape of the pulse), and which can be given explicitly[2] as $S_c = (\epsilon_f + U_p + V_i)(2\pi/\omega)$. The fraction of the $\sin^2$ terms in Eq. (1.70) is peaked around values of $S_c/2$ that are integer multiples of π, and as N grows larger (and with it the pulse duration), these peaks become infinitely narrow. From the expression for S_c, one can derive that these peaks occur when

$$\epsilon_n = n\omega - V_i - U_p\,, \tag{1.71}$$

which is just the position of the ATI peaks introduced in Eq. (1.57).

The angular dependence of the photoionization probability is introduced through the amplitude M_{f0} in Eq. (1.70), which is given by

$$M_{f0} = \mathrm{i}\,\langle\mathbf{k}_f|\phi_i\rangle\,(\epsilon_f + V_i)\int_0^T \exp\{\mathrm{i}S(\mathbf{k}_f, \tau, 0)\}\,\mathrm{d}\tau\,. \tag{1.72}$$

The only unknown quantity that is left is the integral involving the modified action in Eq. (1.72). Reiss[25] has shown that it can be solved analytically in terms of a series of Bessel functions $J_l(x)$, namely

$$\begin{aligned}\int_0^T \exp\{\mathrm{i}S(\mathbf{k}_f, \tau, 0)\}\,\mathrm{d}\tau &= (-1)^n\,T\sum_{l=-\infty}^{\infty} J_{2l+n}\left(\frac{\mathbf{k}_f\cdot\mathbf{A_0}}{\omega}\right)J_l\left(\frac{U_p}{2\omega}\right)\\ &= J_{-n}\left(\frac{\mathbf{k}_f\cdot\mathbf{A_0}}{\omega}, \frac{U_p}{2\omega}\right),\end{aligned} \tag{1.73}$$

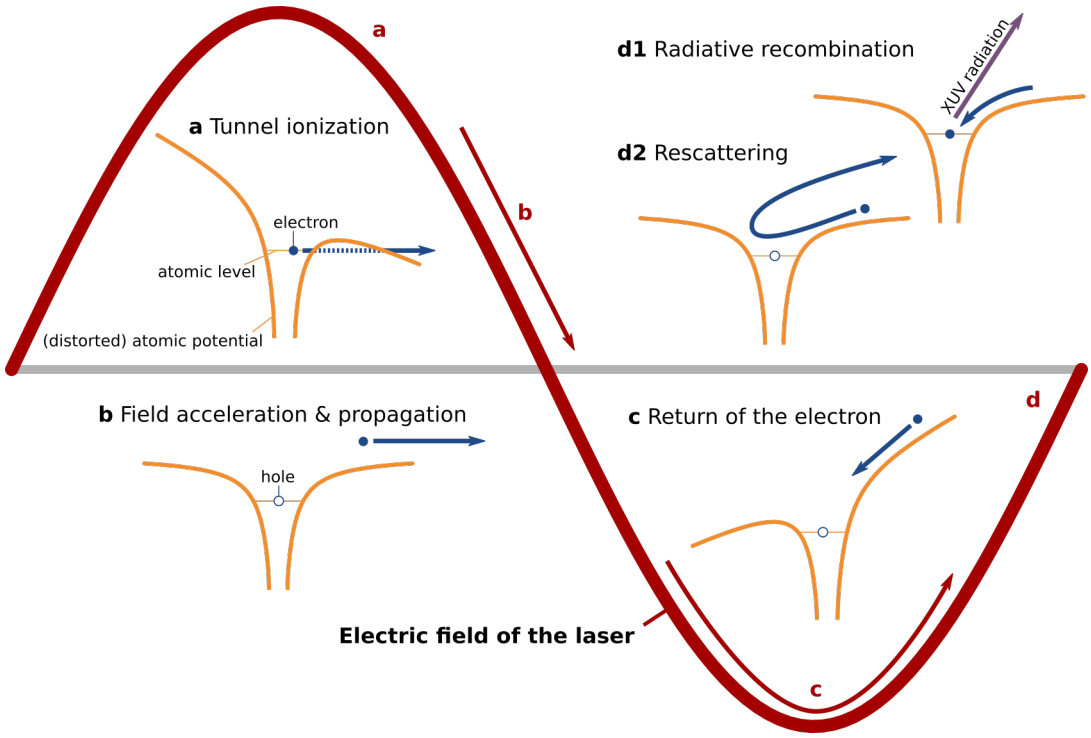

Figure 1.5 Illustration of the three-step model. **a)** In the presence of the laser field, the atomic (or molecular) potential is distorted such that a valence electron can escape by tunnel ionization. **b, c)** The liberated electron is accelerated in the laser field, first away from the parent ion **(b)** and then back to it **(c)**. **d)** Upon recollision, the electron either recombines with the parent ion, as in **d1**, under the emission of XUV radiation, or the electron scatters off the parent ion, as in **d2**. (Adapted from Fig. 1 in the paper of Eikema[26]).

in which $J_n(a, b)$ is referred to as a "generalized Bessel function" by Reiss,[25] and $\mathbf{A_0}$ is the peak vector potential.

Even though we have found a way to rationalize and predict the *direct* photoionization in strong laser fields, many of the fascinating phenomena in strong-field ionization can only be understood in terms of electron recollisions after photoionization. To see this, a classical picture of the electron propagating in the field is most intuitive, which has become known as the three-step model.

In this model, a photoelectron is born *via* tunnel ionization close to the peak of the electric field with a zero (or very small) initial kinetic energy (Fig. 1.5a). From that point on, again, only the acceleration of the electron in the laser field is considered. In this classical picture, the electron is accelerated away from the parent ion, until the electric field changes sign (Fig. 1.5b). Then, under a field with an opposite sign, the electron is driven back to the parent ion (Fig. 1.5c), where the two collide. This collision can have two possible outcomes: firstly, the electron may recombine with the parent ion to form the neutral species, a process during which the excess kinetic energy that the electron has gained during acceleration in the field is emitted as a burst of XUV light (Fig. 1.5d1). In principle, this burst is of attosecond duration and it has a broad frequency spectrum that extends well into the XUV.[1] When laser

[1] As a rule of thumb, the maximum photon energy is $\hbar\omega = V_i + 3U_p$.

pulses are used that encompass many optical cycles, a train of these attosecond pulses is formed, and they interfere with each other in the frequency domain, which gives rise to a characteristic comb of higher-order harmonics, at frequencies $\omega_h = (2h + 1)\,\omega$, with ω being the driving laser's frequency and integer $h \geq 1$. Therefore this process is referred to as high-order harmonic generation (HHG). The observation that only odd harmonics are generated can be explained by the fact that *two* attosecond bursts are emitted per cycle, which gives rise to *half* the frequency of the intensity modulation in the spectral domain.

Second, another outcome of the recollision could be that the electron scatters off the parent ion and is deflected under some angle (Fig. 1.5d2). Although, in principle, the scattering can occur elastically and inelastically – the latter of which is accompanied by an excitation or even ionization of the molecular ion – we consider only the totally elastic scattering as discussed in Section 1.2, as it is the dominant process at low scattering energies (say, < 20 eV). The details of how the rescattered electron can be extracted from the photoelectron spectra and how the connection to the differential cross sections of scattering theory is made, are discussed in Chapter 3 in connection with the actual experimental data.

An important difference between – on the one hand – the electron rescattering just described and the rotational averaging of photoelectron angular distributions described in Section 1.3, and – on the other hand – the high-order harmonic generation process introduced above is that, for the former, the observables can always be generalized from the single-molecule level to the molecular ensemble by an *incoherent* summation, which means that the response of the individual molecule is directly reflected (after averaging over all possible realizations) in the measurement of the target sample. In HHG, understanding the single-molecule response alone is not sufficient. Only if the radiation bursts of all the individual emitters add up *coherently*, a net emission of radiation is produced. The tuning of the experimental conditions, like gas pressure and focus geometry, such as to enforce a constructive interference between the emission events is referred to as "phase matching".

1.5 Connection to the experimental chapters

The material presented in this chapter will be applied in various contexts to the analysis of the experimental results that follow. In Chapter 2, we will present results on the XUV ionization of spatially aligned CF_3I molecules. The ionizing XUV radiation is generated in the HHG process just described at the end of Section 1.4. To interpret the measured photoelectron spectra, we make extensive use of the independent-particle picture of photoionization introduced in Section 1.1, by which we connect the observed photoionization transitions to the valence-shell electronic structure of CF_3I.

In Sections 1.1 and 1.2, it was stressed that, in order to predict the PADs, the continuum wave functions for the photoelectron would have to be obtained in some way. To this end, we use the ePolyScat suite programs that was written by Lucchese, Sanna, Natalense, and Gianturco[27,28] here. With ePolyScat, the general, elastic electron-scattering problem for polyatomic molecules is solved in the static–exchange approximation. This means that, based on a Hartree–Fock reference wave function that is precomputed for the molecule in a given geometry by a standard electronic-structure program (like "GAMESS" or "Gaussian"), the electrostatic repulsion and exchange interaction between the impinging electron and the bound molecular electrons are

treated exactly for a single electronic state of the molecule, which is referred to as a single-channel calculation. The quantitative treatment of correlation and polarization effects would require the expansion of the target state into a series of electronically excited states (the so-called close-coupling expansion), which is beyond the scope of the solution method employed by ePolyScat. Therefore, correlation and polarization effects are accounted for by model potentials that parametrically depend on the electron density and the polarizability tensor of the target molecule, respectively. As soon as the continuum wave function is calculated, its dipole overlap with respect to the ionized molecular orbital is calculated in the frozen-core approximation introduced in Section 1.1. The photoionization dipole matrix elements are reported in both length and velocity gauge in the form of the partial-wave expansion shown in Eq. (1.42). Based on this representation, the effect of molecular alignment on the resulting photoelectron angular distributions can be studied by the theoretical framework presented in Section 1.3.

Besides calculating photoionization dipole matrix elements, one can also investigate the results of scattering calculations in their own right to characterize the underlying photoelectron scattering dynamics. Based on the eigenphase sums and the structure of the S matrix as function of a complex-valued scattering energy, which were introduced at the end of Section 1.2, shape resonances can be identified and their associated resonance wave functions can be calculated.

The experimental concept of Chapter 3 seems very different at first: Instead of working with ionizing radiation, the molecules are ionized in a strong, slowly varying laser field. However, as we have discussed in Section 1.4, the electrons that leave the molecule do not immediately leave the interaction region, but are accelerated forth and back in the oscillating laser field. During this propagation, they can recollide with the parent molecular ion, as shown in Fig. 1.5d2. To find a way to rationalize the angular distributions of the photoelectrons that have undergone such a recollision it is particularly helpful if the frequency of the laser field is low, as this leads to a large excursion length of the electrons. In the so-called quantitative rescattering approximation (QRS),[29,30] it is assumed that the propagation over this excursion length washes out the details of the photoelectron wave packet, so that, when it returns, it can be reasonably well approximated by an incoming plane wave. According to Eq. (1.16), this situation then corresponds to a prototypical electron-scattering experiment, and therefore the differential scattering cross sections (DCSs) for this process must be imprinted onto the angular distributions of the photoelectrons. In Chapter 3, we will demonstrate how the DCSs can be extracted from the photoelectron spectra, which we then compare again to calculations carried out with ePolyScat, this time working with the continuum wave functions directly without the dipole transition. Of course, the same analysis of the involved shape resonances in terms of the eigenphase sums and the poles of the S matrix in the complex energy plane can be applied that was introduced above.

With the work that is presented in Chapter 4, we will try to go beyond what has been covered up to this point, in that we intend to *overcome* the need for involved quantum-scattering calculations by using ionizing radiation it the soft x-ray regime. If the photoelectron kinetic energies are high enough (at least >50 eV), photoelectron scattering can be treated classically, which would offer a particularly intuitive interpretation of the experimental findings. Therefore, only a fraction of the theoretical apparatus presented in this chapter is needed for rationalizing experiments such as the ones discussed in Chapter 4, namely only

the fundamental equations of photoelectron spectroscopy from Section 1.1.

References

1. Berkowitz, J. *Photoabsorption, Photoionization, and Photoelectron Spectroscopy* (Academic Press, New York, 1979).
2. Joachain, C. J., Kylstra, N. J. & Potvliege, R. M. *Atoms in Intense Laser Fields* (Cambridge University Press, Cambridge, 2011).
3. Diels, J.-C. & Rudolph, W. *Ultrashort Laser Pulse Phenomena: Fundamentals, Techniques, and Applications on a Femtosecond Time Scale* 2nd ed. (Academic Press, Burlington, 2006).
4. Sakurai, J. J. *Advanced Quantum Mechanics* 1st ed. (Addison-Wesley, Reading, 1967).
5. Starace, A. in *Springer Handbook of Atomic, Molecular, and Optical Physics* (ed Drake, G.) 379–390 (Springer, New York, 2006).
6. Bethe, H. A. & Salpeter, E. E. *Quantum Mechanics of One- and Two-Electron Atoms* (Springer, Boston, 1977).
7. Lucchese, R. R., Takatsuka, K. & McKoy, V. "Applications of the Schwinger Variational Principle to Electron-Molecule Collisions and Molecular Photoionization". *Phys. Rep.* **131,** 147–221 (1986).
8. Pickup, B. T. "On the Theory of Fast Photoionization Processes". *Chem. Phys.* **19,** 193–208 (1977).
9. Taylor, J. R. *Scattering Theory: The Quantum Theory of Nonrelativistic Collisions* (Wiley, New York, 1972).
10. Edmonds, A. R. *Angular Momentum in Quantum Mechanics* (Princeton University Press, Princeton, 1974).
11. Messiah, A. *Quantum Mechanics* 1st ed. (North Holland, Amsterdam, 1961).
12. Lucchese, R. & McKoy, V. "Application of the Schwinger Variational Principle to Electron-Ion Scattering in the Static-Exchange Approximation". *Phys. Rev. A* **21,** 112–123 (1980).
13. *Computational Atomic Physics: Electron and Positron Collisions with Atoms and Ions* (ed Bartschat, K.) (Springer, Heidelberg, 1996).
14. Gianturco, F. A. & Jain, A. "The Theory of Electron Scattering from Polyatomic Molecules". *Phys. Rep.* **143,** 347–425 (1986).
15. Gianturco, F. A. & Lucchese, R. R. "Resonant Capture of Low-Energy Electrons by Gas-Phase Glycine: A Quantum Dynamics Calculation". *J. Phys. Chem. A* **108,** 7056–7062 (2004).
16. Lee, C.-W. "Identification of the Beutler-Fano Formula in Eigenphase Shifts and Eigentime Delays near a Resonance". *Phys. Rev. A* **58,** 4581–4592 (1998).
17. Sommerfeld, A. *Atombau und Spektrallinien* 4th ed. (Verlag Harri Deutsch, Frankfurt am Main, 1978).
18. Lucchese, R. R., Raseev, G. & McKoy, V. "Studies of Differential and Total Photoionization Cross Sections of Molecular Nitrogen". *Phys. Rev. A* **25,** 2572–2587 (1982).
19. Chandra, N. "Photoelectron Spectroscopic Studies of Polyatomic Molecules. I. Theory". *J. Phys. B: At. Mol. Phys.* **20,** 3405 (1987).
20. Dill, D. "Fixed-molecule Photoelectron Angular Distributions". *J. Chem. Phys.* **65,** 1130–1133 (1976).

21. Underwood, J. G. & Reid, K. L. “Time-Resolved Photoelectron Angular Distributions as a Probe of Intramolecular Dynamics: Connecting the Molecular Frame and the Laboratory Frame”. *J. Chem. Phys.* **113,** 1067 (2000).

22. Agostini, P. & DiMauro, L. F. “Atoms in High Intensity Mid-Infrared Pulses”. *Contemp. Phys.* **49,** 179–197 (2008).

23. Ammosov, M. V., Delone, N. B. & Krainov, V. P. “Tunnel Ionization of Complex Atoms and of Atomic Ions in an Alternating Electromagnetic Field”. *Sov. Phys. JETP* **64,** 1191 (1986).

24. Faisal, F. H. M. “Multiple Absorption of Laser Photons by Atoms”. *J. Phys. B: At. Mol. Phys.* **6,** L89 (1973).

25. Reiss, H. R. “Effect of an Intense Electromagnetic Field on a Weakly Bound System”. *Phys. Rev. A* **22,** 1786–1813 (1980).

26. Eikema, K. S. E. “Nonlinear Optics: Twisted High-Harmonic Generation”. *Nat. Photonics* **9,** 710–712 (2015).

27. Gianturco, F. A., Lucchese, R. R. & Sanna, N. “Calculation of Low-energy Elastic Cross Sections for Electron-CF_4 Scattering”. *J. Chem. Phys.* **100,** 6464 (1994).

28. Natalense, A. P. P. & Lucchese, R. R. “Cross Section and Asymmetry Parameter Calculation for Sulfur 1*s* Photoionization of SF_6”. *J. Chem. Phys.* **111,** 5344 (1999).

29. Chen, Z., Le, A.-T., Morishita, T. & Lin, C. D. “Quantitative Rescattering Theory for Laser-Induced High-Energy Plateau Photoelectron Spectra”. *Phys. Rev. A* **79,** 033409 (2009).

30. Lin, C. D., Le, A.-T., Chen, Z., Morishita, T. & Lucchese, R. “Strong-Field Rescattering Physics—Self-Imaging of a Molecule by Its Own Electrons”. *J. Phys. B: At., Mol. Opt. Phys.* **43,** 122001 (2010).

Chapter 2

Photoelectron Angular Distributions from XUV Ionization of Aligned CF_3I Molecules

2.1 Introduction

Photoelectron spectroscopy is a powerful technique to investigate the electronic structure of quantum-mechanical systems, be it of solids, of atoms and molecules in the gas phase, or even in solution. In particular, when dealing with molecules, much can be learned from the ionization of the valence levels in a photon energy range from the first ionization potential of the system (typically >10 eV) up to ~40 eV above the ionization threshold, which we will refer to as valence-shell photoelectron spectroscopy. The investigation of the valence electronic structure is particularly insightful since the valence electrons directly participate in chemical bonding, so that the key observables, such as binding energies and partial cross sections, are very sensitive to changes in bond strength and the shape of the molecular potential. In particular, the photoelectron angular distributions and their wavelength dependence show a different behavior for every final state of the ion, which is a manifestation of the different shapes and symmetries of the molecular orbitals.[1] In general, the angular distributions will contain the maximum amount of information when they are observed in a frame of reference, in which both the molecule and the polarization vector of the light are fixed in space, which we will call the molecular frame (MF).[2]

However, for gas-phase molecules that rotate freely in space, most of the information content of the molecular-frame photoemission is washed out. There are only few techniques to experimentally access the molecular-frame photoelectron angular distribution (MF-PAD). Certainly the most successful approach is to detect photoelectrons and -ions in coincidence and then to correlate the emission direction of a photoelectron to the flight direction of a molecular fragment ion. In doing so, the photoelectron angular distribution with respect to the recoil axis of the dissociation can be recovered, which is referred to as the recoil-frame (RF-)PAD. Most notably, this concept is put to work in a technique known as "cold target recoil ion momentum spectroscopy" (COLTRIMS).[3] However, a necessary condition for COLTRIMS is that the molecule does dissociate after ionization and that this dissociation is fast compared to the molecular vibration and rotation, which is limiting the general applicability of this technique. In contrast, experimental schemes, in which the gas-phase molecular ensemble is spatially aligned by a laser pulse, can be applied more universally.[a] Fundamentally, the alignment is caused by the induced dipole moments that the oscillating laser electric field creates, mediated

a Here we restrict the discussion to laser-based techniques. Note, however, that molecules can also be aligned or oriented along strong, static electric fields,[4] by molecular-beam techniques,[5] and through adsorption onto surfaces.[6]

by the polarizability of the molecule. The torque that results from the interaction of the induced dipole moment with the laser field forces the molecules to align themselves along the laser polarization axis. Laser-induced alignment is generally divided into adiabatic and non-adiabatic (also *field-free* or *impulsive*) alignment. In both cases, intense infrared light pulses are used that are tuned off-resonance with respect to any vibrational or electronic transitions. The essential difference between the two is the pulse length employed: If the pulse duration is larger than the rotational period of the molecule, the degree of alignment will adiabatically follow the intensity envelope of the pulse, hence the name "adiabatic alignment". Therefore, the alignment can only be exploited while the alignment laser is present, which may interfere with the photoionization process one wants to characterize. In contrast, for a pulse duration that is significantly shorter than the rotational period of the molecule, a rotational wave packet is prepared by the laser pulse, i. e., a coherent superposition of molecules in rotationally excited states. After the pulse has ended, this wave packet evolves freely and revives periodically at well-defined time intervals. At a revival, the probability distribution of the molecular axes rapidly alternates between a distribution that is peaked along the polarization axis of the laser pulse and one that is concentrated in the equatorial plane perpendicular to the laser polarization axis, which is often referred to as *planar delocalization* or *anti-alignment*. Consequently, the molecules can be probed in various alignment distributions, given that the probe pulse duration is significantly shorter than that of the alignment dynamics.

There are numerous examples of photoionization studies in aligned molecules aiming to uncover details about the photoionization dynamics itself. Among them, one major research direction is to quantify the molecular axis distribution[7] and the differential photoionization yield as a function of the angle between the molecular axis and the laser polarization, which are – in such a measurement – intimately related.[8,9] Beyond that, different groups have attempted to extract the photoionization dipole matrix elements by studying the ionization behavior of molecules with varying degrees of alignment, either directly through resonantly enhanced multiphoton ionization (REMPI)[10] or indirectly through the radiative recombination in high-order harmonic generation (HHG).[11,12]

As discussed in Section 1.4, high-order harmonic generation is one of many phenomena that can occur in the strong-field ionization of matter by intense infrared pulses, and is typically rationalized in the celebrated three-step model:[13] We recall that, in this model, the generation of XUV light in strong laser fields is explained by the recombination of high-energy photoelectrons with the parent ion. This process is repeated at every half cycle of the laser field, so that, when a multi-cycle pulse is employed, an attosecond pulse train (APT) is formed. In the frequency domain, this repetitive sequence in time structures the broad spectrum into a comb of discrete harmonics, all of which are of odd order and are thus separated by 2ω, with ω being the driving laser frequency.

In addition to being the subject of scientific investigations, high-order harmonic generation has matured over the last three decades into an attractive light source for ultrashort pulses in the XUV[14,15,16] and soft x-ray[17,18] regime. In particular, such a source can be used to investigate the valence electronic structure of molecules by photoelectron spectroscopy. Compared to synchrotron radiation, it comes with the advantage that it can be employed in pump–probe studies because it is a pulsed light source. Combined with an alignment laser excitation, for instance, PADs for the single-photon ionization of an aligned ensemble can be measured. This approach has recently been applied in our group to the first valence-shell photoionization

experiments in impulsively aligned, linear molecules.[19,20] In these studies, the entire high-harmonic comb was used, ionizing molecules at a series of photon energies simultaneously, which bears the risk of having photoelectrons originating from different orbitals (and produced by different harmonics) overlap on the detector. For the investigated molecules, like N_2 and CO_2, the accessible final ion states are, however, few in number and widely spaced in energy, so that the different contributions to the photoelectron spectra could still be disentangled. In this first study, the shape and symmetry of the ionized orbitals could be assigned based on the change in photoelectron angular distributions with molecular alignment, supported by involved photoionization calculations.

In the experiments presented in this chapter, we have applied this technique to a more complex molecular target, namely CF_3I, which is a polyatomic, symmetric-top molecule containing a heavy atom, and which displays a richer and more dense valence level structure. Ultimately, this choice was motivated by the work of Bisgaard *et al.*,[21] in which the authors not only impulsively aligned CS_2 molecules, but, in addition, triggered a photochemical dissociation reaction with a second pump pulse at the alignment peak. In this regard, CF_3I is appealing because it is known to undergo photodissociation when excited into the *A* band, which can be accessed by single-photon transitions in a range from 220 to 320 nm.[22] This investigation, therefore, is the first step towards resolving the electronic structure of dissociating CF_3I in a time-resolved MF-PAD experiment.

By comparing the MF-PAD recorded in CF_3I to extensive photoionization calculations performed using the ePolyScat package that allows to predict the change in the angular distributions of the emitted photoelectrons, we are able to relate observed modulations in the PADs to the interplay between the shapes of the involved molecular orbitals and two prominent shape resonances in the photoelectron scattering process.

2.2 Electronic Structure of CF_3I

The valence-shell photoionization dynamics of CF_3I has been the subject of several studies. Sutcliffe & Walsh[23] have investigated a series of Rydberg states converging to the ionization continuum of the ionic ground state by vacuum ultraviolet absorption. From the extrapolation of this series, they obtained an ionization potential (IP) of 10.41 eV. The entire set of valence-shell ion states were first studied with He I (21.2 eV) and He II (40.8 eV) radiation by Cvitaš *et al.*,[24] who found an IP of 10.45 eV and assigned most of the ion states to removal of a photoelectron from specific molecular orbitals, based on an independent-particle picture. These findings were later confirmed and extended by Yates *et al.*,[25] who recorded photoelectron spectra with synchrotron radiation, varying the photon energy between 21 and 100 eV. This remains the most comprehensive collection of photoionization data on this molecule to date. Comparing the branching ratios of the experimentally observed ion states to multiple-scattering calculations, the authors made a definitive assignment of these ion states to the molecular orbitals of CF_3I. We briefly review the shapes and bonding characters of these molecular orbitals, which are presented in Fig. 2.1 together with the experimental binding energies, as we will refer to these orbitals several times throughout this chapter. In doing so, we anticipate the results of a Hartree–Fock calculation for CF_3I that is not introduced until Section 2.5.2, and that confirms and complements the results of Yates *et al.*[25] with respect

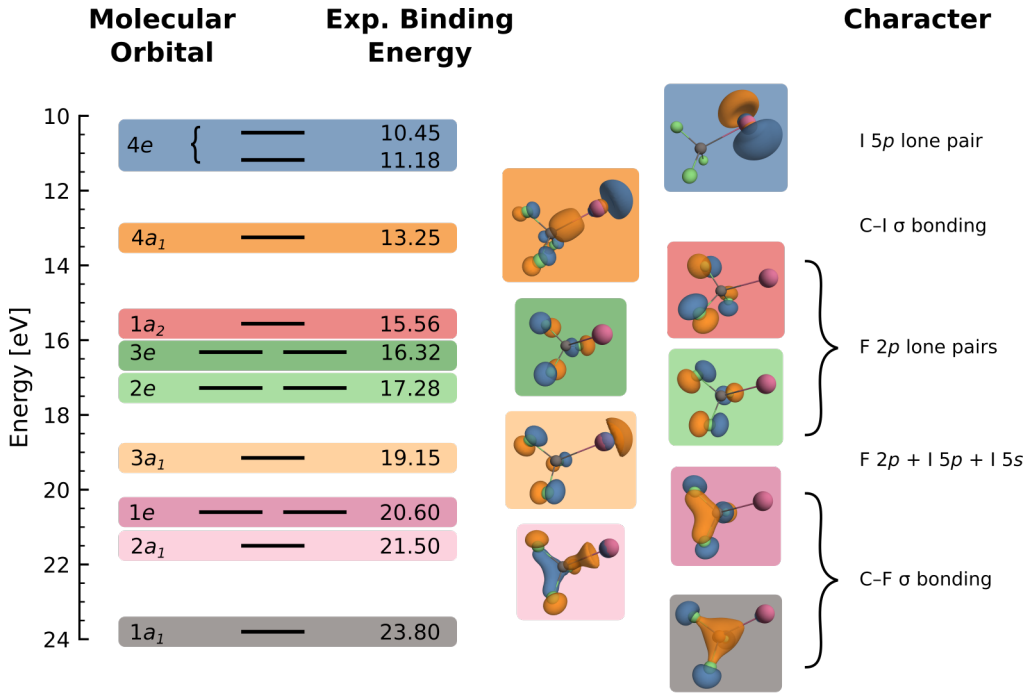

Figure 2.1 Overview of the electronic structure of CF_3I. The binding energies and molecular-orbital assignments are taken from Yates *et al.*[25] The visualized wave functions are the Hartree–Fock orbitals from the corresponding calculations described in detail in Section 2.5.2, shown as isocontour surfaces at a wave function value of $\pm 0.1\, a_0^{-3/2}$.

to the orbitals' shape and ordering, which is why we present it at this point as "established knowledge".

The highest occupied molecular orbital (HOMO) of CF_3I is the degenerate $4e$ set, which is essentially made up of the p_x and p_y orbitals of iodine, making it a lone-pair orbital. Consequently, it exhibits photoionization dynamics that closely resemble that of the $5p$ valence shell of atomic iodine; also, similar to the iodine atom, the ionic ground state of CF_3I is spin-orbit split by 0.73 eV. The $4a_1$ orbital mainly constitutes the C–I bond through constructive overlap of the p_z orbitals of carbon and iodine, but also carbon $2s$ and fluorine p_z orbitals are involved. Next is a group of three states that are closely spaced in energy: the $1a_2$, $3e$ and $2e$ states. All of them can be considered fluorine $2p$ lone pair orbitals. The $1a_2$ state, in particular, is exclusively made up of fluorine p_x and p_y orbitals, which is required by point group symmetry. According to Yates *et al.*[25], the $3a_1$ and $2a_1$ orbitals are the result of a mixing of the iodine $5s$ with the $2p$ orbitals of fluorine. We find, however, that they also contain a significant contribution from the iodine p_z orbitals, and that the $2a_1$ has a strong C–F bonding character, similar to the $1e$ and $1a_1$ orbitals. The binding energy of the deepest inner-valence orbital, the $1a_1$ level, amounts to 23.8 eV, although the authors caution that the assignment of a discrete binding energy is problematic because the independent-particle picture breaks down for the inner-valence levels and satellite states make a significant contribution to photoionization, which can only be described by the additional excitation of an electron (other than the photoelectron) in the molecular ion.

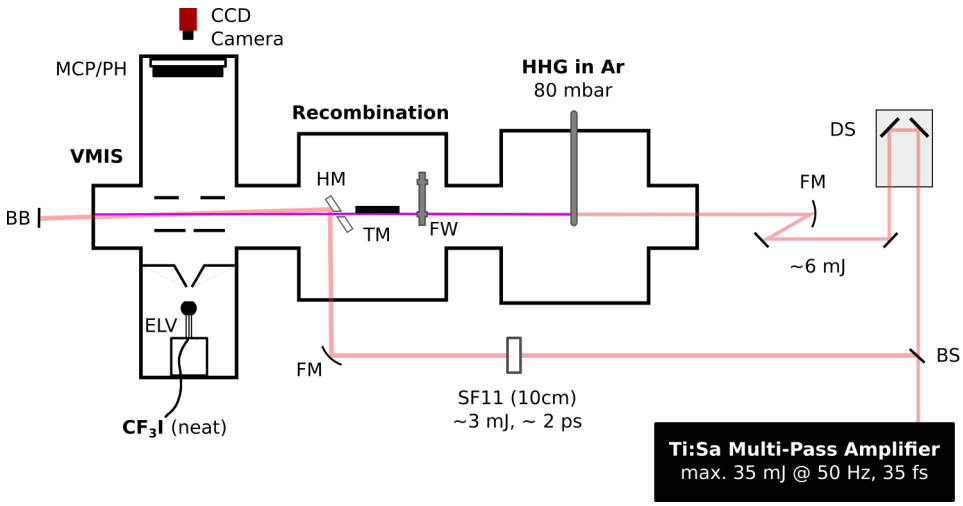

Figure 2.2 Sketch of the experimental setup. BS: beam splitter; BB: beam block; FM: focusing mirror; DS: opto-mechanical delay stage; FW: filter wheel; TM: toroidal mirror; HM: drilled mirror; HHG: high-order harmonic generation; VMIS: velocity map imaging spectrometer; MCP/PH: multi-channel plate–phosphor screen assembly; CCD: charge-coupled device; ELV: Even-Lavie valve.

2.3 Experiment

As discussed above, the valence-shell binding energies of CF_3I range from 10.45 to 23.8 eV. To generate photon energies in this range and beyond, we make use of the HHG process. The setup that was used for the present experiments is introduced in the following section. We then proceed to give details on the characterization of both the XUV and NIR light pulses in the sections that follow.

2.3.1 Setup

The experimental setup used for this experiment is shown in Fig. 2.2. The experiment was performed using a two-stage Ti:Sa laser amplifier. In the first stage, the output of a Ti:Sa laser oscillator ("Griffith", KMLabs) was amplified by a commercial multi-pass laser amplifier ("Dragon", KMLabs) delivering 3 mJ, 25 fs pulses, centered at 785 nm at a 1.5 kHz repetition rate. Pulses were then picked at a repetition rate of 50 Hz with a pulse picker to seed a home-built, butterfly multi-pass amplifier,[26] delivering up to 35 mJ, 35 fs pulses after pulse compression.

The output energy was split into two arms: Up to 3 mJ of pulse energy were used to impulsively align the molecules, whereas up to 6 mJ were used to generate an XUV pulse using the well-known high-order harmonic process in a gas cell containing argon, maintaining a constant pressure of 80 mbar. A high-order harmonic comb was generated in argon by directly focusing the NIR laser pulses inside the gas cell with a 75 cm focusing mirror. An aperture was installed in the beam path to adjust the NIR intensity for maximum HHG conversion efficiency. A 200 nm thick Al foil was used to filter out the intense fundamental from the XUV pulse. Using a 40 cm focal distance toroidal mirror, the XUV pulse was focused onto a molecular beam of CF_3I inside a velocity map imaging spectrometer[27] (VMI). The

molecular beam was obtained by expanding neat CF_3I, maintained at a pressure of 1 bar, through an Even–Lavie valve mounted at the side opposite to the detector of the VMI.

The 785 nm alignment pulse was stretched to ~2 ps with a 10 cm long piece of SF11 glass before it was recombined with the XUV pulse using a drilled mirror. The intensity envelope of the stretched IR pulse was characterized by monitoring the appearance of sidebands in the XUV ionization of helium in the presence of the IR field, which is discussed in Section 2.3.2. The polarization axes of both the alignment and the XUV pulse were aligned parallel to the detector plane.[b] At the center of the velocity map imaging spectrometer, charged particles, created upon ionization by the XUV pulse, were accelerated towards a field-free flight tube terminated by a double stack microchannel plate and phosphor screen assembly (MCP/PH). The luminescence light from the phosphor screen was recorded with a charge-coupled device (CCD) camera. The delay between the 785 nm and XUV pulses was controlled by a motorized delay stage. Additionally, a voltage gate in the form of a 200 ns square pulse was applied to the MCP/PH assembly to selectively detect ions with specific mass-over-charge ratios.

Fundamentally, when a gaseous target is photoionized, the photoelectrons and -ions are ejected as an expanding particle cloud with a specific distribution of (radial) velocities and angular probabilities into all solid angles. Therefore, the photoionization outcome is completely characterized by capturing this three-dimensional (3D) velocity distribution, an example of which is shown in the central panel of Fig. 2.3 for a single photoionization transition. Clearly, what is a narrow line in the angle-integrated photoelectron spectrum becomes a thin spherical shell in the 3D momentum distribution. Furthermore, if the 3D distribution is cylindrically symmetric, it can be completely characterized by only considering a slice through it that contains the cylindrical symmetry axis, as shown in Fig. 2.3a.

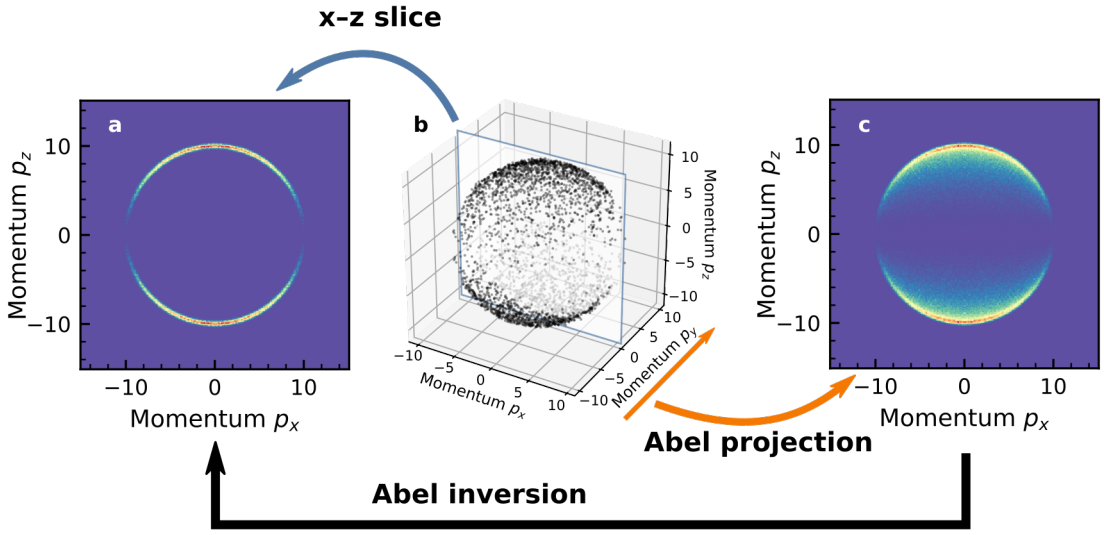

Figure 2.3 Illustration of the 3D momentum distribution of a photoionization event **(b)**, its Abel projection **(a)** and Abel inversion **(c)**.

With a VMI, the 3D velocity distribution is translated into a two-dimensional (2D) spatial

b This guarantees that the resulting photoelectron or -ion momentum distribution is cylindrically symmetric with respect to an axis parallel to the detector plane, which is a necessary requirement for the recorded detector distributions to correspond to the Abel projection of that momentum distribution, as explained in Appendix A.

distribution, by focusing particles with the same velocity components parallel to the detector plane, even with different positions of birth within the interaction volume, onto the same spot on the position-sensitive detector. However, the image that is recorded on the detector is a "projection" of the original velocity distribution in that the information about the velocity component perpendicular to the detector plane is lost, which is illustrated in Fig. 2.3c.[c] For the special case of a cylindrically symmetric velocity distribution, this projection is called an Abel projection, and a special inversion routine is necessary to recover the slice through the momentum distribution – the Abel inversion – because only from the inverted data the observables of the angle-resolved photoelectron spectrum can be extracted.[d] If we express the slice through the momentum distribution in polar coordinates as $f(v, \theta)$, where v is the radial coordinate that is proportional to the particle's momentum and θ is the angle between the polarization axis and the direction of the momentum, we can rewrite $f(v, \theta)$ in terms of the key observables of the angle-resolved photoelectron spectrum, which are the (angle-integrated) radial intensity distribution $Q_0(v)$ and the radial distributions of the beta parameters $\beta_l(v)$ – in complete analogy to Eq. (1.39) – as

$$f(v, \theta) = \frac{Q_0(v)}{v^2}\left(1 + \sum_{l=1}^{L} \beta_l(v)\, P_l(\cos\theta)\right), \tag{2.1}$$

The details of the Abel-inversion routine and the treatment of the VMI data are discussed in Appendix A. In essence, the inverted image that the Abel-inversion routine yields, and that corresponds to the aforementioned slice through the 3D velocity distribution, is transformed into polar coordinates, and an angular integration is carried out to obtain the radial intensity distribution $Q_0(v)$. If the image in polar coordinates is multiplied with one of the $P_l(\cos\theta)$ before the angular integration, each of the radial distributions of the higher angular moments, which we call $Q_l(v)$, can be recovered. Then the beta parameters of Eq. (2.1) are given by $\beta_l(v) = Q_l(v)/Q_0(v)$.

2.3.2 Higher-order harmonics spectra and characterization

To calibrate the detector and characterize the harmonics spectrum, photoelectron spectra were recorded in helium. In the photon energy range considered here, only one final state is accessible, i. e., the ^{2}S ground state of the ion. However, due to helium's high ionization potential of 24.587 eV,[29] only harmonics of order 17 and above are able to photoionize the atom.

A typical, two-dimensional (2D) detector distribution recorded upon photoionization of helium with the 785 nm harmonics comb is displayed in the left half of Fig. 2.4a, in which the high-order harmonics spectrum manifests as a series of concentric rings. To recover the three-dimensional momentum distribution of the photoelectrons, the MEM Abel-inversion routine (see Appendix A was applied to the detector image and the slice through that distribution is shown in the right half of Fig. 2.4a. From this slice, the radial intensity distribution was extracted as described in Appendix A, which was used for the detector calibration.

c This is strictly true for the standard setup with a CCD camera. If a detector is employed that records the time of impact for every particle as well, this projection can be avoided, e. g., by so-called "slicing" techniques.[28]

d This becomes immediately clear, when one imagines a momentum distribution with more than one photoline because then the one with lower absolute momentum will overlap with the projection of the other line.

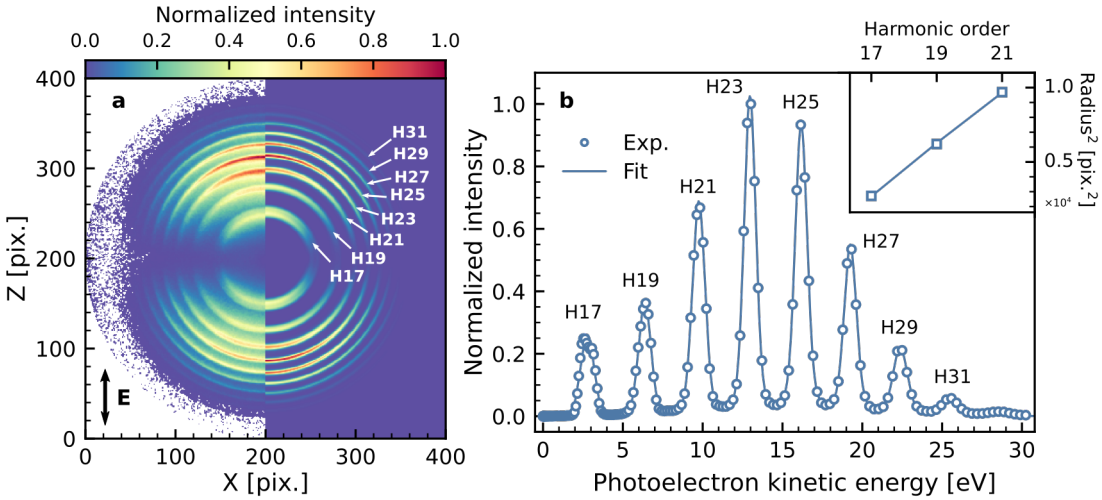

Figure 2.4 Characterization of the 785 nm harmonics by photoelectron spectroscopy in helium. Here and throughout, the labels H*N* indicate the harmonic order *N* of the driving laser frequency. **a)** Raw image (left half) and slice through the 3D momentum distribution (right half) of photoelectrons recorded upon photoionization of helium with 785 nm harmonics generated in argon, filtered by the Al foil. **b)** Angle-integrated photoelectron spectrum obtained from the Abel-inverted momentum distribution after energy calibration. The inset shows the calibration curve according to Eq. (2.2).

In the HHG process, the harmonics are spaced by $2\hbar\omega$, which is a consequence of the half-cycle symmetry of the harmonic-generation process. Practically, one often finds that the spacing does not scale *exactly* with ω, but rather with an *effective* frequency ω_{eff}. If, for instance, the laser pulse is slightly chirped, its wavelength differs between the leading and the trailing part of the pulse, and, depending on the details of the phase matching, only a specific part of the pulse may contribute to harmonic generation, efficiently, which results in an apparent detuning of the fundamental. Keeping this in mind, the energy scale can be calibrated by fitting the photoelectron kinetic energy spectrum according to

$$R_N^2 = c\,(N \cdot \hbar\omega_{\text{eff}} - \text{IP}_{\text{He}})\ , \tag{2.2}$$

where R_N is the radius of the photoelectron line's maximum in pixels, c is the calibration constant, and N is the harmonic order. From Eq. (2.2), it is clear that the squared radii of the photolines should all fall onto a straight line. We find however, that this is *rigorously* true only for the photolines corresponding to harmonics 17 through 21, after which the spacing between the peaks decreases monotonically by 5 to 10 %. For the calibration, we have therefore fitted the expression of Eq. (2.2) to squared radii of the first three photolines only, treating both c and ω_{eff} as free parameters, and using the well-known IP of helium, $\text{IP}_{\text{He}} = 24.587\,\text{eV}$.[29] As a result of this procedure, we retrieve a calibration constant of $c = (1050 \pm 20)\,\text{pix}^2/\text{eV}$, corresponding to an uncertainty of roughly ±2 % in the energy scale calibration (see inset of Fig. 2.4), and an *effective* photon energy $\hbar\omega_{\text{eff}} = (1.59 \pm 0.01)\,\text{eV}$, which corresponds to a wavelength of 780 nm.

To fully characterize the spectrum of the harmonics, we need to retrieve their spectral width and relative intensities. The spectral width of the harmonics can, however, not be directly inferred from the photoelectron lines because of the finite energy resolution of the

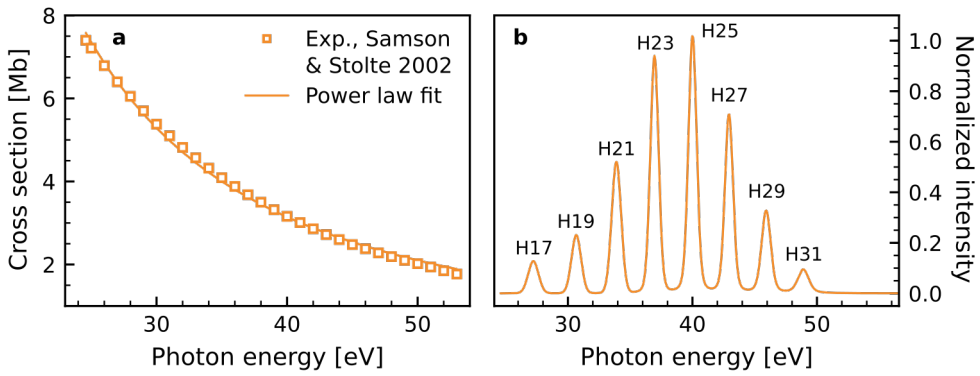

Figure 2.5 Reconstruction of the harmonics spectrum using the photoionization cross sections of helium reported by Samson & Stolte.[30] **a)** Absolute, total photoionization cross sections of helium in the photon energy range from the IP to ~55 eV (squares). A power-law fit for that energy range, yielding a photon-energy dependence of $(\hbar\omega)^{-1.8}$ is shown as well (solid line). **b)** High-order harmonics spectrum determined by dividing the photoelectron peak areas of Fig. 2.4b by the interpolated cross sections of **a**.

VMIS, which is, moreover, not uniform across the detector. The relative intensities of the harmonics, on the other hand, can be recovered if the photoionization cross section is taken into account.[e] Here we make use of the absolute photoionization cross sections reported by Samson & Stolte,[30] shown in Fig. 2.5a. The photoionization cross section drops by a factor of 4 over the energy range between harmonics 17 to 31 and follows a power law given by $(\hbar\omega)^{-1.8}$. Assuming that the cross section is approximately constant over the bandwidth of a harmonic, the high-order harmonic spectrum can be recovered by dividing the peak area of every photoelectron line by the photoionization cross section at the central photon energy of the corresponding harmonic, giving rise to the reconstructed HHG spectrum shown in Fig. 2.5b.

2.3.3 Characterization of the pump–probe setup

When describing the experimental setup in Section 2.3.1, it was stated that the alignment pulses were stretched by sending them through a piece of SF11 glass to add dispersion. Stretching the pulse[f] is advantageous because the limiting factor in impulsive alignment is the peak field strength, which is adjusted such that the rate of field ionization is kept at a minimum. As – in first approximation — the strength of the alignment effect depends only on the area under the field envelope, increasing the pulse width – while keeping the peak field strength close to the threshold of strong-field ionization – is a common strategy to optimize the degree of alignment in the ensemble.

e We further have to assume that the detection efficiency is uniform across the detector, which is a condition always implicit to any Abel-inversion routine.

f Note that this pulse stretching is limited by the requirement that the pulse duration be short compared to the rotational period of the molecule. In the present experiment, the laser pulses are roughly four orders of magnitude shorter than the rotational period before stretching, and still two order of magnitude shorter after stretching, as will be shown later in this section.

To characterize the precise shape of the laser envelope, we have repeated the photoionization experiment of Section 2.3.2 in a time-resolved fashion, temporally and spatially overlapping the XUV pulse and the stretched NIR pulse. Having extracted the angle-integrated photoelectron spectrum for each delay, the time dependence of the photoelectron signal can be cast into a 2D map, shown in Fig. 2.6a. When the two pulses overlap, additional features appear in the photoelectron spectrum in the form of fringes between the photolines, which are referred to as "sidebands".[31,32] Formally, these are photoelectrons that have absorbed or emitted one NIR photon. As the high-order harmonics are of odd order only, as explained in Section 2.1, the sidebands resemble photoelectron peaks of "quasi-even" order, appearing exactly between the photolines of two adjacent harmonics.

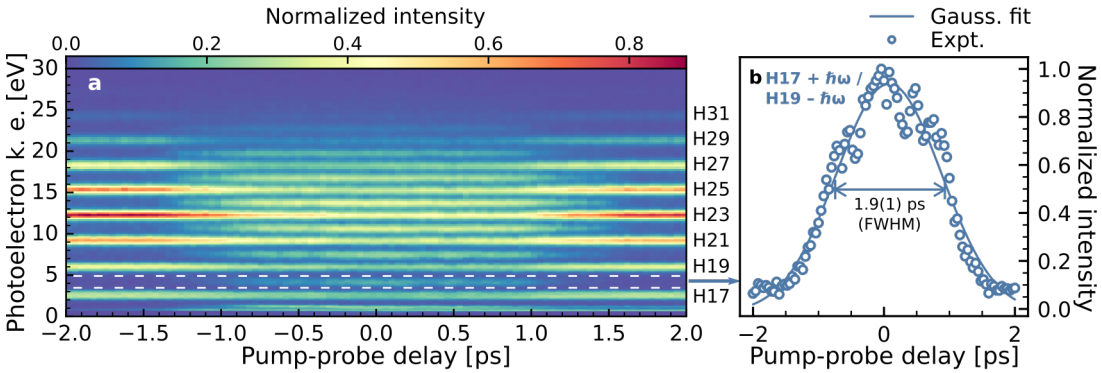

Figure 2.6 Appearance of sidebands in the XUV photoionization of helium in the presence of the NIR field. **a)** Time-dependent photoelectron spectra recorded in helium, varying the time delay around the temporal overlap of the two pulses. All spectra were normalized to the *overall* maximum signal of this sequence of measurements. The dashed lines indicate the integration region for the sideband between harmonics 17 and 19. The integrated yield of this region is displayed in **b**, together with the result of fitting a Gaussian function to it.

Within second-order perturbation theory, the intensity of the sidebands scales linearly with the (cycle-averaged) intensity of the NIR light.[32] Therefore, the shape of the pulse envelope can be measured by monitoring the integrated yield of a sideband contribution as a function of pump–probe delay.[g] The problem that is apparent from Fig. 2.6a is, however, that, close to time zero, most of the sidebands are comparable to the harmonic peaks in terms of their intensity, under which condition second-order perturbation theory does not apply. To obtain an estimate of the NIR pulse duration, we have chosen to monitor the time-dependent intensity of the sideband between harmonics 17 and 19, as for this feature the requirement that it be less intense than the surrounding photolines is *approximately* fulfilled. In Fig. 2.6b, the yield of this sideband – integrated over its peak width – is displayed, and we find that the outline of this trace can be reasonably well approximated by fitting a Gaussian function to it, which is shown as well. From optimum fit parameters thus obtained, we recover a pulse duration (FWHM) of (1.9 ± 0.1) ps. We note that this pulse duration is still significantly shorter than the rotational period of CF_3I ($\tau \approx 300$ ps), which means that the molecular alignment will still proceed in the non-adiabatic regime.

g Strictly, what is measured is the cross correlation between the envelopes of the XUV and NIR pulses. As the NIR pulse, however, is stretched in duration by almost two orders of magnitude, the finite width of the XUV pulse is neglected here.

2.4 Characterization of the molecular alignment

One way to characterize the evolving molecular axis distribution of an impulsively aligned molecular ensemble is to measure the change of the angular distribution of the charged fragments that result from ionization of the aligned molecules by the XUV pulse. In the axial recoil approximation, i. e., if the dissociation of the molecular ion is fast with respect to the vibrational and rotational motion,[33] the molecular axis distribution of the molecule at the time of ionization is directly imprinted onto the angular distribution of the charged fragments. Then, the ion momentum distribution $I(p,\theta)$, which is a function of the ionic fragment's drift momentum p and the angle θ between the polarization axis of the incident radiation and the direction the drift momentum, $\hat{\mathbf{p}}$, can be written as

$$I(p,\theta) = P_{\mathrm{MA}}(\theta) \cdot P_{\mathrm{ion}}(p,\theta)\,, \tag{2.3}$$

where $P_{\mathrm{MA}}(\theta)$ is the molecular axis distribution before ionization and $P_{\mathrm{ion}}(p,\theta)$ is the differential ion yield for a given ionization channel.[h] The influence of the last factor can, in principle, be strongly suppressed by turning the polarization axis of the ionizing probe pulse such that it is perpendicular to both that of the alignment pulse and to the detector plane, a technique that was introduced by Stapelfeldt and co-workers.[34] For the setup that was used for this experiment this was, however, not possible because turning the polarization of the XUV pulse would result in severe losses on the toroidal mirror whose reflectivity is optimized for p polarization. Therefore, we will make use of Eq. (2.3) to extract the evolving molecular axis distribution of the impulsively aligned CF_3I molecules in the following sections.

To this end, we first discuss the photofragmentation dynamics of CF_3I based on static photoion measurements in the next section, before we present the results of the alignment experiments, which we then try to model with alignment simulations to unambiguously recover the molecular axis distribution $P_{\mathrm{MA}}(\theta)$.

2.4.1 Static photoion spectroscopy

In the photon energy range between 10 and 25 eV, the photoionization of CF_3I leads to the formation of CF_3I^+, I^+, $CF_3{}^+$, and CF_2I^+,[35] the latter of which is formed through C – F bond fission upon ionization of a fluorine 2p lone-pair orbital. Of these fragments, we would expect that in particular the I^+ fragments can be used to characterize the molecular alignment since previous experiments[36] have demonstrated that I^+ is formed through prompt dissociation of the molecule via a strongly repulsive, excited state of the parent molecular ion, and this dissociation likely occurs along the principal molecular axis.

h Note that Eq. (2.3) takes a particularly simple form because all three distributions are written as functions of the angle θ. In general, this is not possible because the polar angles in P_{ion}, P_{MA} are distinctly different. In writing Eq. (2.3), two assumptions are made: First, the distributions P_{ion} and P_{MA} are only depending on the angle between the laser polarization and the principal molecular axis, and these distributions are translated into photoion directions by a mapping transformation. Zare[33] has shown, however, that in the axial recoil approximation this mapping takes the form of a delta function, so that there is a one-to-one correspondence between the orientation of the molecule and the direction of the photoion. Second, P_{ion} and P_{MA} are measured relative to the XUV and NIR pulses' polarization axes, respectively. Only when the polarization axes of the two pulses are aligned parallel to each other, these two frames of reference coincide.

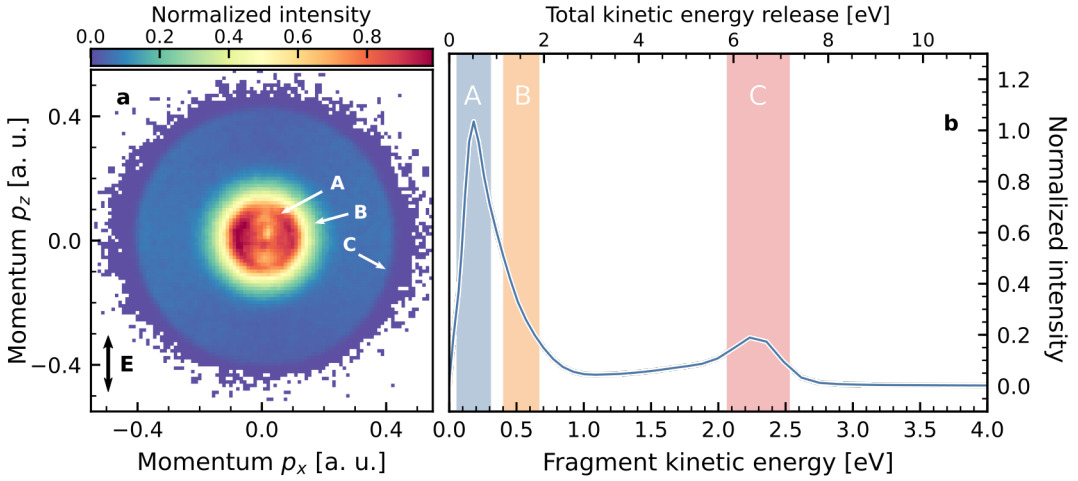

Figure 2.7 Static photoion spectroscopy of the I^+ fragment upon ionization of CF_3I with 785 nm high-order harmonics. **a)** Normalized VMI detector image of the I^+ signal. The polarization axis is oriented parallel to the vertical axis of the image. **A:** Fragments resulting from the dissociation of low-lying ionic states of CF_3I^+; **B:** Fragments associated with the dissociation of highly excited states of CF_3I^+; **C:** Coulomb explosion fragments from the dissociation of CF_3I^{2+} into $CF_3{}^+ + I^+$ **b)** Corresponding kinetic energy distribution of the I^+ fragments. The shaded regions correspond to the features as labeled in **a**. The top scale indicates the total kinetic energy release corresponding to the dissociation into $CF_3 + I^+$.

A typical 2D I^+ momentum distribution that results from ionization of CF_3I by the XUV pulse, generated by the 785 nm laser, is shown in Fig. 2.7a. Several features are apparent: an intense, peaked feature in the center of the distribution (labeled A in Fig. 2.7a) that lies on top of a broad rim that falls off slowly (B), and a faint, concentric ring (C) at a momentum of ~0.4 a. u. After Abel-inversion and extraction of the radial velocity distribution, the fragment kinetic energy spectrum is recovered using the calibration obtained in the previous section.[i] The dominant feature in this spectrum, shown in Fig. 2.7b, is a broad distribution of fragments with low kinetic energies, ranging from 0.1 to 1.0 eV. According to previous work by Powis *et al.*[35] on dissociative photoionization of CF_3I at a photon energy of 21.2 eV, this contribution can be further divided into the peaked region A with a mean fragment kinetic energy of 0.15 eV and a high energy tail, B, with a mean fragment kinetic energy of 0.47 eV. By virtue of momentum conservation, these fragment kinetic energies correspond to total kinetic energy releases of 0.43 and 1.33 eV, respectively. In the work of Powis *et al.*, the I^+ fragment distribution with a mean KER of 0.4 eV was assigned to dissociative photoionization of CF_3I through the $\tilde{A}$ state, which corresponds to ionization from the $4a_1$ orbital. We therefore assign region A in our measurement to this state, as well. The next state that leads to formation of I^+ is the $\tilde{E}$ band, which is associated with ionization from the $3a_1$ orbital at a binding energy of ~19 eV. Low, Hampton & Powis[36] and Powis *et al.*[35] reported an average KER of 0.6 eV and 0.69 eV for this channel, respectively, which is certainly lower than what we observe in region B. Considering that the ions in the $\tilde{E}$ state have, depending on the dissociation limit, up to 7 eV of total energy in excess, and assuming that only 25 % of this excess energy is converted into translational

i The magnification of the VMI only depends on the charge, not on the particle's mass. Therefore, the same calibration applies to electrons and singly-charged ions alike.

energy, which is what is typically found for other dissociation channels,[36] the kinetic energy release could be as high as 1.7 eV. We therefore assign contribution B in our measurement to dominantly originate from the dissociative ionization of the molecule through the $\tilde{E}$ state of the molecular ion. Still, it appears that there is a large discrepancy between the literature values cited above and our findings. We speculate that one reason for this discrepancy could be that, in these publications, not the entire fragment kinetic energy distributions, but only single, average values are reported for measurements with monochromatized radiation. As we are measuring here the sum of – probably overlapping – contributions from the ionization by several harmonics, it is not straightforward to disentangle the different fragmentation channels in order to determine their average fragment energies.

In the fragment kinetic energy distribution shown in Fig. 2.7b, also a weaker contribution, labeled C, with a mean kinetic energy of 2.2 eV is observed. By virtue of momentum conservation, the fragment kinetic energy we observe corresponds to a total kinetic energy release of 6.3 eV, or 93 % of the Coulomb energy. The kinetic energy of these fragments is close to the Coulomb repulsion energy $E_C = (q_1\, q_2)/R_e = 6.72$ eV of two point charges with charge $q_1 = q_2 = +1$, separated by the equilibrium C–I bond length of CF_3I, $R_e = 2.144$ Å. Comparing our results to the work of Eland, Feifel & Hochlaf,[37] who investigated the double photoionization of CF_3I in the XUV regime, we find that the photon energies of the high harmonics comb in the present experiment exceed the double ionization threshold those authors report for CF_3I at 28.89 eV,[38] as well as the appearance threshold for the $CF_3{}^+ + I^+$ channel, estimated to be at 31 eV,[37] which supports our observation and assignment of the Coulomb channel.

2.4.2 Time-resolved photoion spectroscopy

As previously stated, the alignment dynamics that is induced by the short NIR pulse can be extracted from the change of the angular distribution of the I^+ fragments as a function of the delay between the NIR and the XUV pulse. It is well known that the rotational wave packet that is formed by the NIR laser excitation revives at integer and half-integer multiples of the rotational period τ of the molecule, which are referred to as full and half revivals, respectively. The rotational period is related to the rotational constant of the molecule B as $\tau = 1/2B$. For CF_3I, whose rotational constant, $B = 1523$ MHz, is known with great precision from microwave spectroscopy,[39] this implies a rotational period of $\tau = 328$ ps. In our measurement, 2D I^+ momentum distributions were recorded as a function of the pump–probe time delay around the first half revival at 164 ps, where the maximum degree of alignment was expected.[40] For each time delay, the recorded images were subjected to the Abel-inversion routine to reconstruct a slice through the 3D ion momentum distribution, $I(p, \theta)$, which we already introduced above. Here, the polar angle θ is defined with respect to the polarization axis of the ionizing radiation and p represents the absolute momentum.

Examples of 2D momentum distributions recorded at 162.5 ps and 165.5 ps are shown in Fig. 2.8a and b, respectively. A clear modification of the angular distribution is observed for all detected fragmentation channels. At 162.5 ps, the momentum distribution is peaked along the laser polarization, whereas at 165.5 ps, the angular distribution is peaked in the direction perpendicular to the laser polarization axis. To describe the changing fragment ion angular

distribution by a single figure, the $\cos^2\theta$ moment, or expectation value, given by

$$\left\langle \cos^2\theta \right\rangle_{\text{ion}}(p) = \frac{\int_0^\pi I(p,\theta)\cos^2\theta\sin\theta\,\mathrm{d}\theta}{\int_0^\pi I(p,\theta)\sin\theta\,\mathrm{d}\theta}, \tag{2.4}$$

is evaluated at each time delay by numerical integration. Then $\left\langle \cos^2\theta \right\rangle_{\text{ion}}(p)$, which is a continuous function of the momentum p, is averaged over the regions shown as shaded areas in Fig. 2.7b to obtain a single, average value for each of the three fragmentation channels.

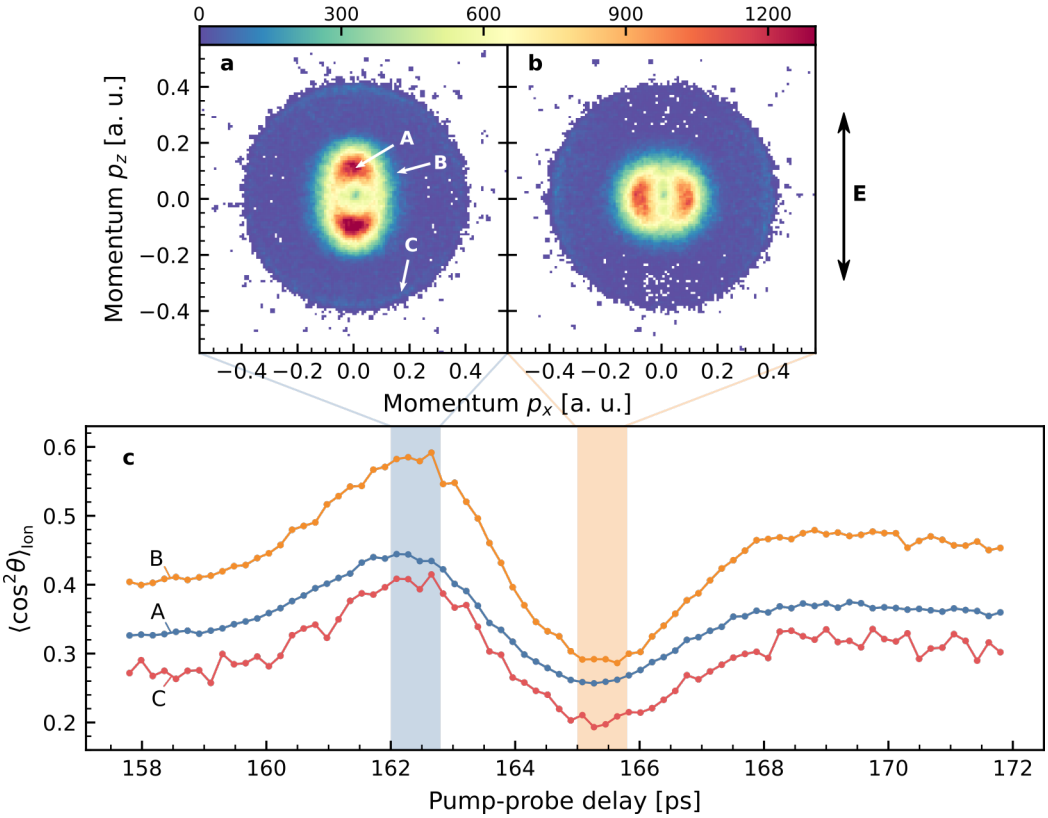

Figure 2.8 Effect of molecular alignment on the I^+-fragment momentum distributions. **a, b)** Detector momentum distributions taken at the alignment peak **(a)** and the planar-delocalization peak **(b)**. The labels A–C are identical to those in Fig. 2.7. The double-headed arrow indicates the orientation of the polarization axis in the images **a** and **b**. **c)** Evolution of the expectation value $\left\langle \cos^2\theta \right\rangle_{\text{ion}}$ of the reconstructed, three-dimensional ion momentum distributions as a function of the pump–probe delay. The three traces are obtained by averaging $\left\langle \cos^2\theta \right\rangle_{\text{ion}}(p)$ over the respective regions indicated in Fig. 2.7b.

The resulting time-dependent evolutions are displayed in Fig. 2.8c. Overall, the three traces show the same revival structure, going through a maximum around 162.5 ps and a minimum around 165.5 ps. However, the modulation depth is different for the three channels and the traces are vertically offset by different amounts.

As we have discussed above, a breakdown of the axial recoil approximation will weaken the correspondence between the molecular axis distribution and the fragment ion distribution. We

therefore assume that the fragments that show the greatest modulation depth (which is region B here) should reflect the change in molecular axis distribution closest and have decided to take region B as the reference for making the comparison to the alignment simulations.

2.4.3 Extraction of the molecular axis distributions

Basically, our strategy to retrieve the molecular axis distribution P_{MA} is to perform numerical simulations of the laser-induced molecular alignments that are described below to model the dynamics of the rotational wave packet and, using Eq. (2.3) and Eq. (2.4), to predict the time-dependent evolution of $\left\langle \cos^2\theta \right\rangle_{\mathrm{ion}}$. To this end, also a particular form for P_{ion} has to be proposed, which will be introduced in the beginning of Section 2.4.3. Then, the parameters that go into the simulation, namely the rotational temperature of the ensemble T and the peak electric field strength of the laser pulse E_0, and the parameter that describes the shape of the differential photofragmentation yield a^{diss} are varied until the best agreement with the experiment is achieved in a least-squares sense.

Molecular alignment simulation

To predict the evolution of the molecular axis distribution, the time-dependent Schrödinger equation (TDSE) is solved for the rotational wave function Ψ,

$$\mathrm{i}\hbar\frac{\partial}{\partial t}\Psi(t) = H_{\mathrm{tot}}(t)\Psi(t)\,, \tag{2.5}$$

of a symmetric top rotor in the presence of a non-perturbative field interaction. The total Hamiltonian H_{tot} can be approximately written as the sum $H_{\mathrm{tot}}(t) = H_{\mathrm{rot}} + H_{\mathrm{ind}}(t)$. Here, H_{rot} is the field-free rotational Hamiltonian of the molecule, that is independent of time and whose eigenfunctions correspond to the rotational states of the molecule, which we denote $|JKM\rangle$, with associated eigenenergies $\mathscr{E}_{JK}$, according to the Schrödinger equation

$$H_{\mathrm{rot}}\,|JKM\rangle = \mathscr{E}_{JK}\,|JKM\rangle\ . \tag{2.6}$$

It can be shown[41] that, if the molecular rotations are parametrized by the set of Euler angles $\mathbf{R}$ (as introduced in Section 1.3), the rotational eigenfunctions of the symmetric top (those that solve Eq. (2.6)) are – up to a normalization constant – the Wigner D matrices (also introduced in Section 1.3), i. e.,

$$\langle \mathbf{R}|JKM\rangle = \sqrt{\frac{2J+1}{8\pi^2}}\mathscr{D}^{J*}_{MK}(\mathbf{R})\,. \tag{2.7}$$

On the other hand, the induced Hamiltonian, H_{ind}, describes the interaction between the instantaneous electric field envelope of the laser pulse, $E(t)$ at time t, and the anisotropy of the dipole polarizability, $\Delta\alpha$, of the molecule, as a function of the angle θ between the principal molecular axis and the polarization vector of the light, given by

$$H_{\mathrm{ind}} = -\frac{1}{4}E^2(t)\Delta\alpha\cos^2\theta\,. \tag{2.8}$$

The anisotropy of the polarizability, $\Delta\alpha$, is simply defined as the difference between $\alpha_{\parallel}$ and $\alpha_{\perp}$, which are the polarizabilities parallel and perpendicular to the principal molecular axis, respectively.

We assume the field envelope $E(t)$ to be of sine-squared shape, that is for a pulse of a duration τ_{FWHM}, full-width half-maximum,

$$E(t) = E_0 \left(\sin \frac{\pi t}{2\tau_{\mathrm{FWHM}}} \right)^2 . \tag{2.9}$$

For every $|JKM\rangle$ state of the symmetric top, the TDSE is propagated for the duration of the alignment laser pulse, using a simple first-order integration scheme for partial differential equations, commonly known as Crank–Nicolson method.[42]

After the passing of the pulse, the superposition of rotational states that was created through rotational excitation evolves freely, as

$$|\Psi(t)\rangle = \sum_{JKM} C_{JKM}\, \mathrm{e}^{-\frac{\mathrm{i}}{\hbar}\mathscr{E}_{JK}t}\, |JKM\rangle \ , \tag{2.10}$$

where C_{JKM} are the complex-valued state-vector coefficients at the time the field interaction vanishes.

Eventually, a weighted average of the wave-packet evolution, starting from every initially populated $|JKM\rangle$ state, is formed with weighting factors w_{JK}, reflecting the thermal population of the states at temperature T, according to the Boltzmann distribution,

$$w_{JK} = (2J+1) \frac{\mathrm{e}^{-\mathscr{E}_{JK}/kT}}{\sum_{JK} \mathrm{e}^{-\mathscr{E}_{JK}/kT}} . \tag{2.11}$$

where k is the Boltzmann constant and the factor $2J+1$ accounts for the degeneracy of rotational states in the quantum number M. From this weighted average all required observables, like the probability distribution of the molecular axes, $P_{\mathrm{MA}}(t) = |\langle \mathbf{R}|\Psi(t)\rangle|^2$, and its $\cos^2\theta$ expectation value $\left\langle \cos^2\theta \right\rangle_{\mathrm{MA}}(t) = \langle \Psi(t)|\cos^2\theta|\Psi(t)\rangle$ are calculated.

Fitting procedure and comparison to the experiment

To establish the connection to the experiment according to Eq. (2.3), we still have to propose a form for the differential photofragmentation yield, $P_{\mathrm{ion}}(p,\theta)$. For single-photon ionization it is well known that the angular distribution of the photofragmentation yield can be described by a single parameter, similar to the famous β parameter in photoelectron spectroscopy. In a way that is entirely equivalent to introducing the β parameter,[41] but somewhat more intuitive, and that avoids confusion with the photoelectron angular distributions, we describe the normalized angular distribution of the fragmentation yield as the sum of a cosine-squared and a sine-squared component,

$$P_{\mathrm{ion}}^{a^{\mathrm{diss}}}(\theta) = \frac{3}{2} \left(a^{\mathrm{diss}} \cos^2\theta + \frac{1 - a^{\mathrm{diss}}}{2} \sin^2\theta \right) . \tag{2.12}$$

Obviously, the limiting cases are $a^{\mathrm{diss}} = 1$, which corresponds to a parallel transition, and $a^{\mathrm{diss}} = 0$, describing a perpendicular one. As we do not know a^{diss} for all the involved ion

Table 2.1 Molecular constants of CF_3I required for the alignment simulations. $\alpha_\parallel$ and $\alpha_\perp$ are the polarizabilities parallel and perpendicular to the principal molecular axis, respectively.

Rotational constants[a]				Static polarizability[b]	
A	B	D_J	D_{JK}	$\alpha_\parallel$	$\alpha_\perp$
5750 MHz	1523 MHz	0.164 kHz	0.992 kHz	9.04 Å^3	6.67 Å^3

[a] From Walters & Whiffen.[43]
[b] This work. See Appendix B.

channels in the experiment and we further have to assume that we are measuring a weighted average of different dissociation channels due to the wide range of photon energies, we treat a^{diss} as a free parameter in the least-squares fitting procedure. Note that a^{diss} is a single parameter (and not a continuous distribution) because we fit the simulation only to the average photoion angular distribution of region B in Fig. 2.7.

The other two free parameters that we have to determine are the peak field strength E_0 and the ensemble rotational temperature, T. Strictly speaking, also the pulse duration τ_{FWHM} could be varied, but here we make use of the fact that – in first approximation – it is the area under the field envelope alone that determines the strength of the alignment effect. Consequently, we have to explore a three-dimensional parameter space, which for the field strength and temperature we did by scanning a range of values on an equidistant grid.

For this series of simulations, we assumed a pulse duration of $\tau_{\text{FWHM}} = 1.9$ ps and integrated the TDSE with a time step of $\Delta t = 6.7$ fs. The rotational constants of CF_3I were taken from the microwave spectroscopy results of Cox *et al.*,[39] and Walters & Whiffen[43] which are summarized in Table 2.1. For completeness, we have also included the effect of centrifugal distortion to first order, even though it probably has a negligible effect at the first half revival. To the best of our knowledge, no values for the anisotropy of the dipole polarizability, $\Delta\alpha$, are reported for CF_3I in the literature. Therefore, we obtained the polarizability tensor from an *ab initio* calculation, the details of which are given in Appendix B. The maximum rotational quantum number included was $J_{max} = 50$, which should support ensemble rotational temperatures up to 30 K.

For every distinct set of (T, E_0) values, the complete evolution of the molecular axis distribution, P_{MA}, was calculated at the same pump–probe delay values as those in the experiment. Then the ion distribution parameter a^{diss} was tuned – for every one of the (T, E_0) pairs individually – to give the minimum sum of squared residuals, $\sum_i e_i^2$, where the residual e_i is just the differences between the measured and the calculated value for $\langle \cos^2\theta \rangle_{\text{ion}}$ at data point i.

In Fig. 2.9a, the dependence of $\sum_i e_i^2$ on the parameter sets $[T, E_0, a_{opt}^{\text{diss}}(T, E_0)]$ is shown, which resembles a two-dimensional minimum surface through the three-dimensional parameter space. The *global* optimum was obtained by fitting a two-dimensional polynomial to this surface, containing orders of $T^m E_0^n$, with $\max(m + n) = 3$, and determining the minimum of that function. The uncertainties in the parameters were then estimated by standard methods of nonlinear regression. Eventually, the retrieved optimum parameters were $T_{opt} = (19.2 \pm 0.5)$ K, E_{opt} corresponding to an intensity of $(2.3 \pm 0.1) \times 10^{12}$ W/cm^2, and $a_{opt}^{diss} = 0.546 \pm 0.006$.

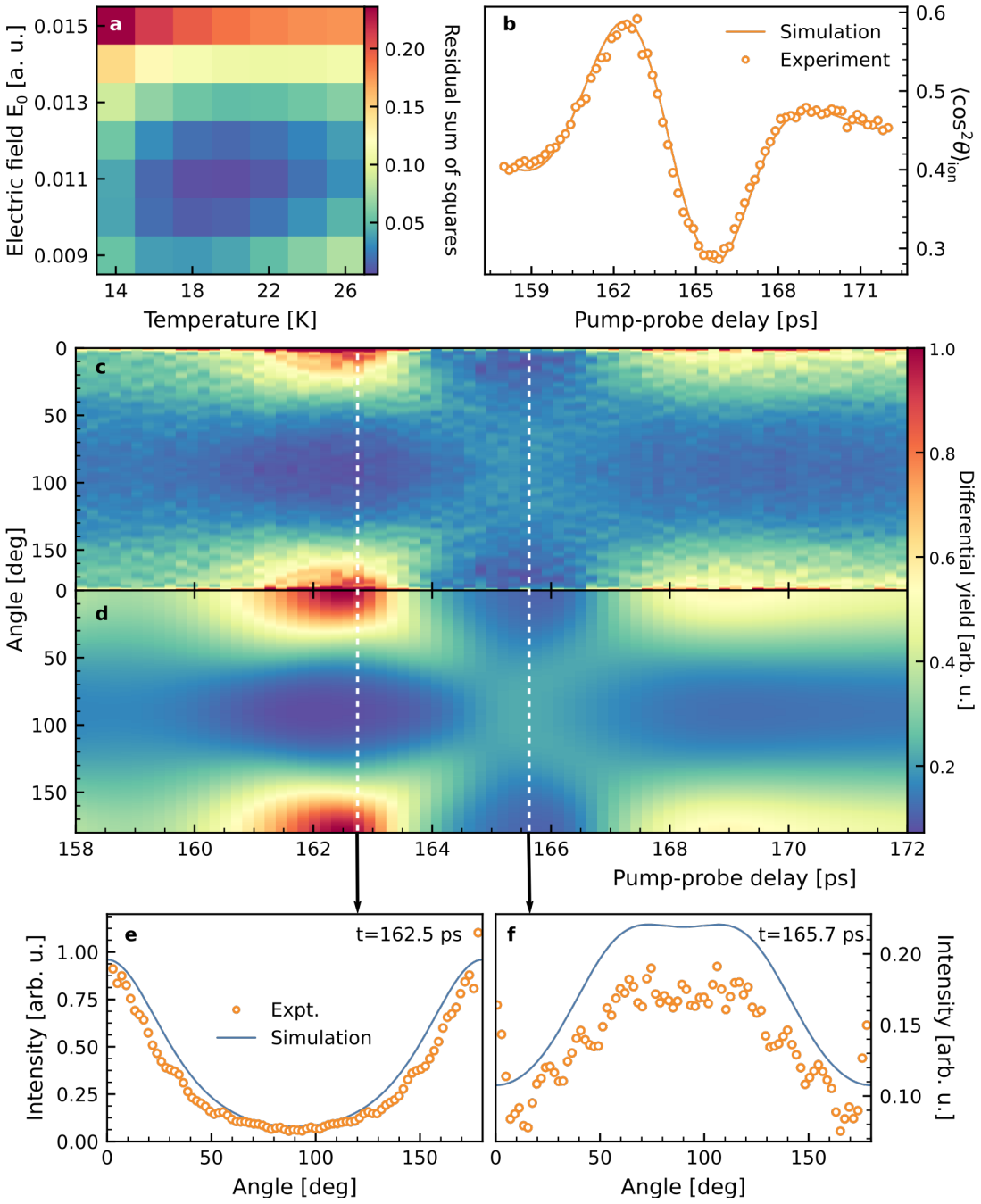

Figure 2.9 Simulation of alignment dynamics and fitting procedure to retrieve the experimental conditions. **a)** Residual sum-of-squares measure between the measured and the simulated evolution of the $\cos^2\theta$ expectation value of the ion distribution, $\langle\cos^2\theta\rangle_{\text{ion}}$, shown as a function of temperature and peak electric field strength, E_0. For every set of (T, E_0) parameters, the anisotropy parameter a^{diss} was optimized individually. **b)** Evolution of $\langle\cos^2\theta\rangle_{\text{ion}}$ for the optimum set of parameters $(T, E_0, a^{\text{diss}})_{\text{opt}}$ (solid line), obtained from the least-squares optimization procedure shown in **a**. The experimental points (open circles) correspond to an average over the integration region B in Fig. 2.7. **c, d)** Evolution of the fragment ion angular distribution through the revival of the rotational wave packet for the experiment **(c)** and the simulation with the optimum parameters **(d)**. **e, f)** Photoion angular distributions, extracted at the indicated pump–probe delays. Note that, for the experimental data, the *inverted* ion angular distribution is obtained for only a single, averaged quadrant of the VMI image, corresponding to a 90° range (see Appendix A). For the visualization in **c**, **e**, and **f**, the data were mirrored. In **e** and **f**, the data were further re-binned into groups of three and the mean of these bins is shown.

What the least-squares surface of Fig. 2.9a emphasizes is that the global optimum in the experimental parameters is – even after introducing the phenomenologically motivated a^{diss} – sharply defined so that we do not find ourselves in a situation, where a broad range of experimental parameters could be made plausible by adjusting a^{diss}. The comparison of the experimentally obtained and the calculated evolution of $\langle \cos^2 \theta \rangle_{\text{ion}}$ in Fig. 2.9b reveals that a very good agreement is achieved. Furthermore, we present the complete extracted photoion angular distribution, integrated over region B in Fig. 2.9c together with the simulated one in panel d of that figure, where again we observe an excellent agreement.

At an even closer look, comparing the photoion angular distributions extracted from both the experiment and the simulation for the pump–probe delay of maximum alignment (Fig. 2.9e), we still find a very good agreement. The same analysis for the pump–probe delay of maximum planar delocalization (Fig. 2.9f) reveals what seems to be a mismatch in amplitude between theory and experiment, although the overall shape of the angular distribution is very similar. As P_{MA} is always normalized to unity, we can at this point only speculate that the functional form we have chosen for P_{ion} cannot fully capture the details of the photofragmentation process, which leads to the observed small deviations.

2.5 Photoelectron spectroscopy with an HHG comb

2.5.1 Experimental data

Right before recording the photoelectron spectra of the aligned molecules, the pump–probe delays for the maximum and minimum of $\langle \cos^2 \theta \rangle_{\text{ion}}$ were determined in a photoion measurement, akin to the one shown in Fig. 2.8. Then, VMI images of the electrons were acquired by reversing the voltages applied to the VMI electrodes and alternating between the corresponding two time delays, recording an image every time. To obtain high-quality data, every image was accumulated over 10 000 laser shots and in total six images were recorded for each delay. Every image was subjected to the usual Abel-inversion routine and radial-distribution extraction individually, and statistical properties of a specific observable, like its mean and standard deviation, were always calculated in the very last step. For brevity, we denote all observables that are associated with the measurement at the alignment peak with a "$\oplus$", and for the planar-delocalization peak with a "$\ominus$".

The resulting, averaged raw and inverted velocity maps are displayed in Fig. 2.10a and b, at the delays corresponding to the alignment and planar delocalization, respectively. Despite being recorded for molecules with distinctly different molecular axis distributions, there is – to the eye – no difference between the two measurements. In both cases, we obtain a congested, weakly structured spectrum that extends to ~1.5 a. u. of electron momentum and that is overall divided into a low-energy and a high-energy region by a signal minimum at ~0.6 a. u. The Abel-inverted images (right halves of Fig. 2.10a and b) reveal that the angular distributions in the low-energy region are more richly structured than those in the high-energy region, which, overall, show a slight asymmetry in form of a preferential ionization along polarization axis.

That the two measurements do, in fact, differ only becomes evident when the *normalized*

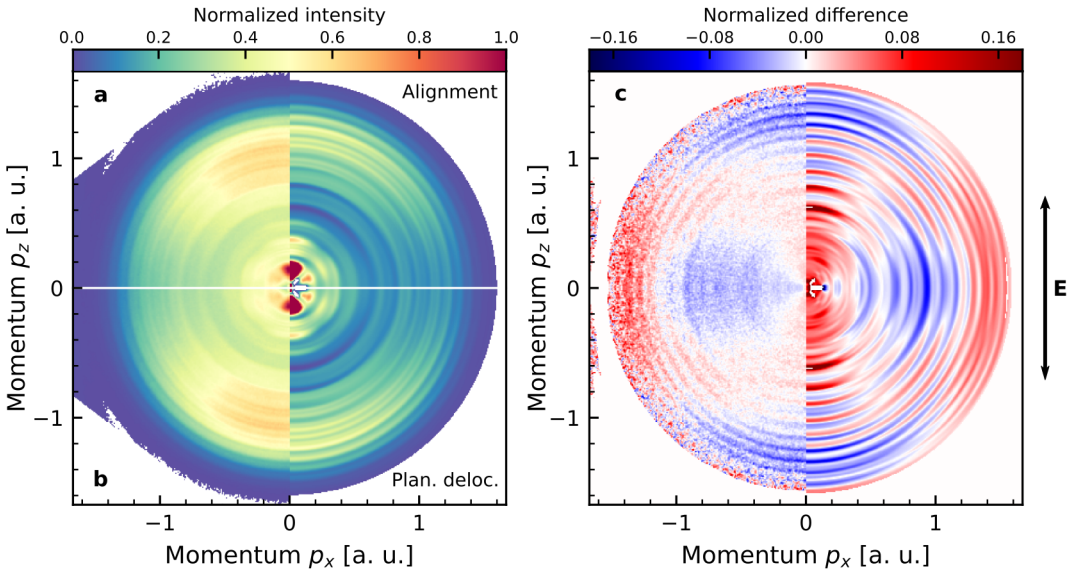

Figure 2.10 2D detector images (left halves) and slices through the 3D velocity distributions (right halves) for the photoionization of pure CF_3I with the whole harmonic comb. **a, b)** Comparison between data recorded at the alignment peak (**a**, $t = 162.5$ ps) and the maximum planar delocalization (**b**, $t = 165.5$ ps). **c)** Normalized difference between **a** and **b**, according to Eq. (2.13). For the visualization, the quadrants were mirrored vertically in **c**.

difference

$$\Delta_N X = \frac{\Delta X}{X^{\oplus} + X^{\ominus}}, \tag{2.13}$$

with

$$\Delta X = X^{\oplus} - X^{\ominus} \tag{2.14}$$

is considered. The normalized differences between the two data sets of Fig. 2.10a and b are shown in panel c of that figure. Here, a clear modulation of the signal intensity by ±5 % on average is revealed. As before, this modulation is best seen in the inverted data, but it is undeniably present in the normalized difference of the raw data, as well, which rules out the possibility of inversion artifacts alone causing this signal difference. Overall, the difference image is structured in two ways: First, there is a concentric ring pattern which must be caused by the various molecular orbitals that contribute with their distinct angular distributions to the overall signal, as well as the fact that several harmonics are involved, which leads to the observed, repetitive ring sequence. Second, a gradual change of the differential angular distributions with increasing absolute photoelectron momentum is observed. The gradual change is most obvious when comparing electrons with $p = 0.8$ a. u., for which emission perpendicular to the polarization direction is suppressed in the normalized-difference image, to those with $p = 1.3$ a. u., for which it is enhanced. Furthermore, the positive lobes in the intermediate-energy region form a characteristic “X shape”, which suggest the presence of higher-order angular-momentum contributions to the angular distributions in the normalized-difference image.

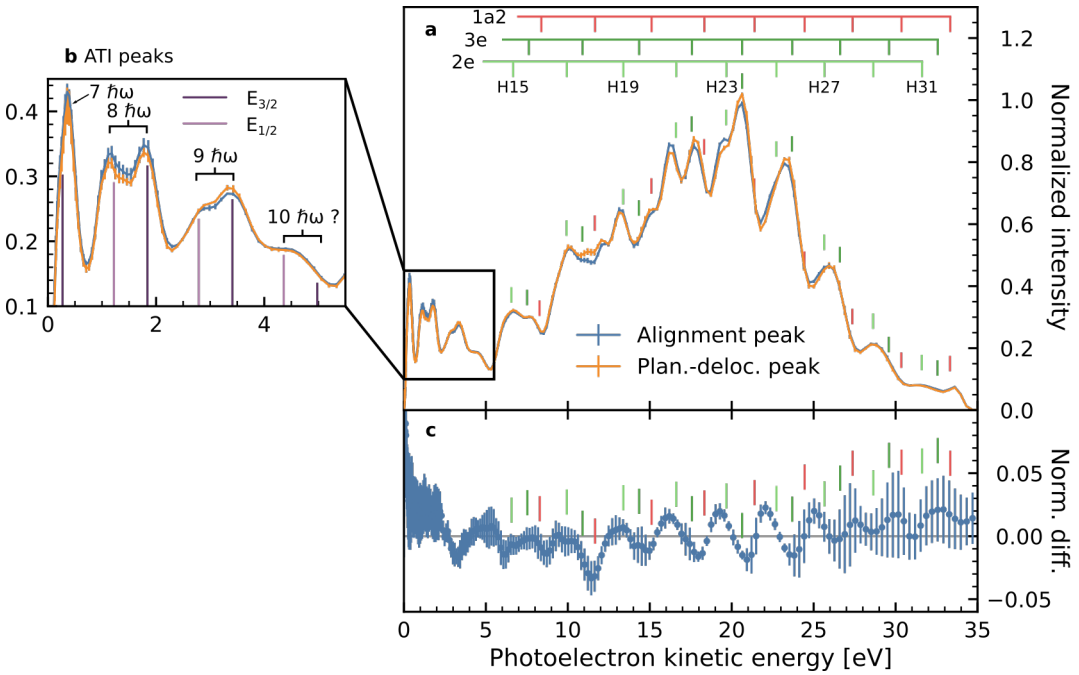

Figure 2.11 Angle-integrated photoelectron spectra. **a)** Radial intensity distributions extracted from the images taken at the alignment peak (blue) and the planar-delocalization peak (orange). The scales at the top indicate the theoretical peak positions for the photoelectron lines, originating from the three indicated orbitals. Small vertical dashes are intended to serve as a guide to the eye. In the inset **b**, the region below 5 eV is expanded, in which multiphoton ionization from the alignment pulse is dominating. Vertical bars indicate the expected peak positions of the n-photon transitions for the lowest spin-orbit ground ($E_{3/2}$) and excited ($E_{1/2}$) states of CF_3I^+, respectively. **c)** Normalized difference between the radial intensity distributions, according to Eq. (2.14). Error bars mark the 95 % confidence interval. Note that the ordinates of **a** and **c** are not to scale with respect to each other.

To quantify the features just described, we first present the angle-integrated photoelectron spectra for the two measurements in Fig. 2.11a. Ideally, one would want to assign the different photolines to the various contributing orbitals. Considering, however, that all harmonics of order 17 and above are able to ionize all of the nine valence levels, there are many more contributions than one can hope to disentangle with the present energy resolution. A closer look at the branching ratios reported by Yates *et al.*,[25] however, reveals that in the photon-energy range of the present experiment, >60 % of the photoelectrons must stem from only three orbitals, namely the group of fluorine 2p lone-pair orbitals: $1a_2$, $3e$, $2e$ (see Fig. 2.1), whereas the other 40 % are coming from the remaining six valence levels. In Fig. 2.11a, we have therefore indicated the expected peak positions for these three states, assuming the photon energies obtained in Section 2.3.2 (harmonic 15 was approximated as $15 \cdot \omega_{\text{eff}}$). As it turns out, many of the protruded features in the photoelectron spectra coincide with these state assignments: in the region from 5 to 20 eV it is the $2e$ orbital that matches well with the observed peak positions, and from 20 to 30 eV, this is true for the $3e$ orbital.

For the region below 5 eV, however, we suspect that the photoelectrons are not only generated by single-photon ionization because here the angular distributions exhibit more than one angular node and hardly change with the alignment distribution. Instead, this

observation can be explained by multiphoton ionization by the NIR alignment pulse. If this was true, it would result in a series of above-threshold-ionization (ATI) peaks, whose kinetic energies, $\epsilon_f^{(n)}$, are given by[44]

$$\epsilon_f^{(n)} = n \cdot \hbar\omega - \mathrm{IP}_f - U_p \,, \tag{2.15}$$

where IP_f is the ionization potential for ionization into the final state f and $U_p = E_0^2/\left(4\omega^2\right)$ is the ponderomotive energy of the photoelectron in the oscillating light field with peak electric field strength E_0. As the probability for above-threshold ionization – to a first approximation – scales exponentially *inverse* with the ionization potential, we take into account as final states f only the two lowest states of CF_3I^+, i. e., the spin-orbit ground and excited state of the non-relativistic ground state, $E_{3/2}$ and $E_{1/2}$, with ionization potentials $\mathrm{IP}_{E_{3/2}} = 10.45\,\mathrm{eV}$ and $\mathrm{IP}_{E_{1/2}} = 11.18\,\mathrm{eV}$. Then, by adjusting U_p guided by visual inspection, an acceptable agreement with the features in the experimental photoelectron spectrum can be achieved for $U_p \cong 180\,\mathrm{meV}$, which is shown in Fig. 2.11b. This ponderomotive potential corresponds to a laser intensity of $\sim 3.1 \times 10^{12}\,\mathrm{W/cm^2}$, which agrees with the result from Section 2.4.3 $(2.3 \pm 0.1) \times 10^{12}\,\mathrm{W/cm^2}$ to within 50 %. This is expected since ionization will mainly proceed at the peak of the laser intensity, whereas the molecular alignment that we have characterized above was averaged over the spatial distribution of the NIR pulse that is probed by the XUV pulse. Therefore, we expect that the ATI peaks will be mainly sensitive to the peak intensity, which is, for a Gaussian pulse, 1.88 times higher than the average intensity in the focus. To summarize, we have to assume that ATI is making a significant contribution to the photoelectron spectrum for n-photon transitions up to order 9 or maybe even 10. As we have to assume that the angular distributions that we measure in this region are strongly affected by ATI photoelectrons, we neglect this part of the spectrum in the following discussion.

To see to what extent the difference between the radial distributions for aligned and planarly delocalized molecules is statistically significant, the normalized difference $\Delta_N Q_0$ of the radial intensity distribution Q_0 (introduced in Eq. (2.1)) is displayed in Fig. 2.11c, together with the point-to-point confidence intervals at the 95 % level. The confidence intervals were calculated from Eq. (2.13) by standard methods of error propagation, this time assuming, for simplicity, that the uncertainties in the measurement follow a Gaussian distribution, which we justify by the fact that the images were accumulated over a large number of laser shots. The confidence interval then spans

$$\mathrm{CI}_{0.95}(\Delta_N Q_0) = \overline{\Delta_N Q_0} \pm 1.96\sqrt{\frac{\sigma_\Delta^2}{m}} \,, \tag{2.16a}$$

where

$$\sigma_\Delta^2 = \left(\overline{\Delta_N Q_0}\right)^2 \left(\frac{\left(\sigma^{\oplus}\right)^2 + \left(\sigma^{\ominus}\right)^2}{\left(\overline{Q_0^{\oplus}} + \overline{Q_0^{\ominus}}\right)^2} + \frac{\left(\sigma^{\oplus}\right)^2 + \left(\sigma^{\ominus}\right)^2}{\left(\overline{Q_0^{\oplus}} - \overline{Q_0^{\ominus}}\right)^2} \right). \tag{2.16b}$$

In these equations, the overscore denotes the mean, $\sigma^{\oplus}$ and $\sigma^{\ominus}$ are the standard deviations of $Q_0^{\oplus}$ and $Q_0^{\ominus}$, respectively, and $m = 6$ is the number of measurements on either side. From Fig. 2.11c it can be seen that the differences between the measurements are, in the region from 10 to 25 eV, significantly different from zero. On the other hand, the maxima

and minima of what seems to be a periodic intensity modulation in this region cannot be unambiguously assigned to any of the three fluorine lone-pair states. We suspect that the exact shape of the difference signal can only be reproduced by averaging over several – maybe all – the involved states.

It turns out that the same observation is true for the extracted radial distributions of the β_l parameters, displayed in Fig. 2.12, which is why have decided not to label any state assignments. Here, we restrict the discussion to β_2 and β_4 because the changes in β_6 and higher are too small to be detected in the present experiment. The general difference between β_2 and β_4 is that, for the randomly oriented molecule, the latter is always zero, whereas the former is generally not. This also becomes evident when comparing panels a and c of Fig. 2.12: as an overall trend, β_2 increases from almost zero at 7 eV to a value of roughly 0.9 at 15 eV, a level on which it remains up to 30 eV. In contrast, the β_4 distributions for molecules in alignment and planar delocalization oscillate around zero in opposite direction for kinetic energies above 7 eV, although the effect is much stronger in alignment than it is in planer delocalization. Only for photoelectrons with lower kinetic energies do the two β_4 distributions converge into one, non-zero distribution, which is again indicative of multiphoton ionization as discussed above.

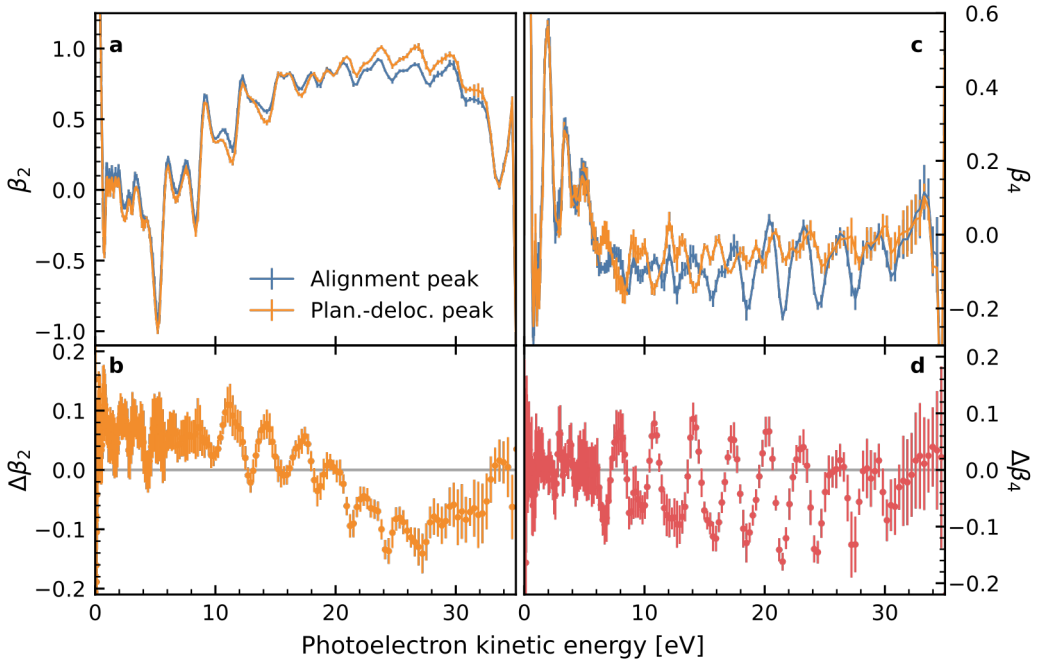

Figure 2.12 Radial distributions of the β_l parameters. **a)** Dependence of β_2 on the electrons' kinetic energy for the data taken at the alignment peak (blue) and the planar-delocalization peak (orange). **b)** Absolute difference, $\Delta\beta_2$, between the two traces shown in **a**. **c, d)** Same as **a** and **b** for the β_4 parameter. Error bars correspond to confidence intervals of 95 % .

Looking at the difference $\Delta\beta_2$, we find an overall downward trend from roughly +0.1 at 11 eV to a little less than −0.1 at 27 eV, on top of which a faster oscillation appears, as we have observed qualitatively in Fig. 2.10c. In comparison, for $\Delta\beta_4$ we observe only a very weak downward trend, if any, but the same pronounced oscillations as a function of kinetic energy,

with an amplitude of $\sim \pm 0.1$.

2.5.2 Computational model

To model the experimental findings from the previous section, the ePolyScat suite of programs was used, in which the electronic structure of the photoionized molecule is treated at the Hartree–Fock (HF) level of theory. As an input, an HF wave function has to be provided, which we did by performing calculations with the GAMESS (US) code. As the calculations with ePolyScat are restricted to the Hartree–Fock level, we decided to employ the largest basis set possible to approach the *exact* Hartree–Fock limit as well as possible. In the first step of an ePolyScat calculation, the basis set and the orbital coefficients are read in, and the orbital wave functions are re-expanded onto a spherical grid by a single-center expansion into a basis set of spherical harmonics. Compared to the actual photoelectron-scattering calculation, this step is fast and therefore increasing the basis-set size does not impose a computational penalty. For all atoms, we took the respective all-electron basis sets of augmented quadruple-ζ quality from the Sapporo family[45,46] of correlation-consistent Gaussian basis sets.[j]

Iodine is a heavy atom and therefore relativistic effects become non-negligible. Common strategies to account for heavy-atom effects are scalar-relativistic correction terms or model-core potentials, in which explicit treatment of the (relativistic) core electrons is avoided by replacing them with an effective potential. However, ePolyScat can neither handle model-core potentials (although scattering codes with this capability have been developed[47]) nor does it incorporate relativistic corrections in the scattering equations. Therefore, all calculations were performed at the non-relativistic (NR) all-electron level, accepting that common relativistic effects, e. g., the uncontraction of the d shell, are not correctly reflected in the input wave function.

As is common in photoionization calculations, we assume for the molecular structure of CF_3I its *experimental* equilibrium geometry. This equilibrium structure is known from microwave-spectroscopy experiments with great precision,[39] and has recently also been reproduced by elaborate electronic-structure calculations.[22] To estimate how much strain is built up in the molecule by *not* choosing the NR-HF equilibrium structure, we have relaxed the molecule at the HF level to the minimum-energy configuration and report the deviations in Table 2.2 together with the experimental geometry from Cox *et al.*.[39] Probably the most important parameter to control the convergence of the photoionization calculation is the maximum angular momentum l_{max}, up to which the molecular orbitals are expanded in the basis set of spherical harmonics. At the same time, l_{max} governs the default expansion sizes for various other variables, e. g., the maximum l in the calculation of the exchange potential and the size of the final scattering matrix. The computation time, however, grows at least quadratically with l_{max}. To determine an acceptable trade-off, photoionization calculations were performed for CF_3I with l_{max} values ranging from 30 to 90 in steps of 10. As the expansion center, typically the center of gravity of the molecule's electron density is chosen. For our CF_3I model, this point is located between the carbon and the iodine atom, at a distance of 1.175 Å away from the carbon. For this point, however, the convergence of the molecular-orbital expansion

j In principle, the Sapporo basis sets are also provided in quintuple-ζ quality, but they contain additional i functions ($l = 6$), whereas the parsing routines of ePolyScat can only handle polarizing functions up to $l = 5$, the h functions.

is very slow because the dense core orbitals of iodine cannot be sufficiently described from this distance. Therefore we have chosen the point at 1.8 Å away from the carbon (or 0.314 Å from iodine), which led to a faster convergence. The two figures of merit for this convergence are the normalization integrals of the re-expanded molecular orbitals and the change in the differential cross section. For the latter, we chose the photoionization of the 4*e* (HOMO) orbital, ejecting photoelectron with a kinetic energy of 5 eV.

Table 2.2 Experimental and calculated equilibrium geometries of CF_3I and corresponding total energies at the HF/AQZP level of theory. Numbers in parentheses are the experimental standard errors.

	Geometry	
	Expt.[a]	HF opt.[b]
C–I [Å]	2.1438(27)	2.1480
C–F [Å]	1.3285(23)	1.3024
∠F–C–F [°]	108.42(23)	108.34
E_{HF} [E_h]	−7254.184 068	−7254.186 213

[a] From Cox *et al.*.[39]
[b] This work.

Ideally, the normalization integral should be 1 after the expansion (as before) and we take its absolute difference from 1 as a measure for the expansion error. In Fig. 2.13a, the expansion error, averaged over all 30 molecular-orbital groups of CF_3I, is plotted against l_{max}. Over the given range, the average expansion error falls from ∼4 % to ∼0.2 %. As an illustration of how the photoelectron angular distributions are affected by the quality of the expansion, we have calculated the photoionization from the 4*e* HOMO orbital for electrons with 5 eV of kinetic energy in the exact-static–exchange (ESE) approximation. For every value of l_{max}, the differential cross section (DCS) for molecules perfectly oriented along the ionizing radiation's polarization axis was calculated, which is displayed in Fig. 2.13b as a function of the angle θ between the polarization axis and the emission direction. We find that the DCSs quickly converge for $l_{max} > 60$. In view of the large number of photoionization transitions that have to be calculated for the experiment with the whole harmonic comb (86 in total), we eventually decided to work with $l_{max} = 70$. For this value, the average expansion error is about 0.5 % and for all valence levels the error is <0.1 %. Judging from Fig. 2.13, we have to accept a convergence error for the DCS that is on the order of 5 % in the perfectly oriented case. Upon averaging over all possible orientations of the molecule, convergence is even faster, so that for the total cross section and the β_2 parameter for the randomly oriented molecule, we find a convergence error <2 %. In relation to the expected fidelity of our computational model, we consider this degree of convergence appropriate.

For the actual calculation, all allowed continuum transitions from the 9 molecular valence orbitals by the harmonics 13 through 31 were evaluated with the full exact-static–exchange-plus-model-correlation–polarization model (ESECP). The photon energies of the harmonics 17 through 31 were taken from the reconstructed spectrum, Fig. 2.5b, and for the harmonics below that, they were estimated as $N \cdot \hbar\omega_{\text{eff}}$. For the construction of the model polarization

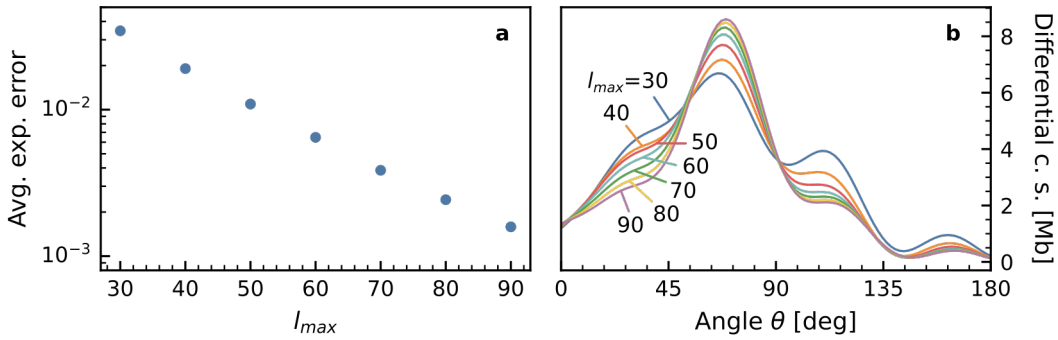

Figure 2.13 Dependence of the average expansion error **(a)** and the differential cross section for the photoionization of the $4e$ (HOMO) orbital, **(b)** on the maximum angular momentum l_{max} in the spherical-harmonics basis employed by ePolyScat. For the details of the calculations in **b**, see the main text.

potential, the polarizability tensor of the molecule has to be provided, for which the same values as in Section 2.4.3 were used (see there and Appendix B for details). For the model correlation potential, the Padial–Norcross functional[48] was employed, which was specifically developed for describing the electron correlation in electron–molecule collisions.

For each orbital, every symmetry-allowed bound–continuum transition is computed individually and afterwards the corresponding matrix elements are collected to evaluate the ionization observables. To understand what transitions are allowed by symmetry, we recall that a dipole-transition integral can be non-zero only if the direct product of the irreducible representations of the initial state, Γ^i, of the final state, Γ^f, and of the dipole operator, Γ^d – along one of the Cartesian axes $d = x, y, z$ – contains the totally symmetric irreducible representation of the point group to which the molecule belongs. In its equilibrium geometry, CF_3I is of C_3v symmetry, and therefore we can write

$$\langle i|d|f\rangle \neq 0 \quad \text{if} \quad \Gamma^i \times \Gamma^d \times \Gamma^f \supset \Gamma^{A_1} . \tag{2.17}$$

For completeness, we give the character table and the product table for the C_3v point group in Table 2.3. From the character table, it is clear that the dipole operator along the z axis transforms like A_1, and along the x and y axes like the doubly degenerate E set. Looking at the product table, one finds that for the ionization out of orbitals of A_1 and A_2 symmetry, a dipole transition along any Cartesian axis couples uniquely to a single symmetry component of the continuum: If the polarization axis is aligned parallel to the principal molecular axis, ionization out of an orbital of A_k ($k = 1, 2$) symmetry can only proceed through the A_k component of the continuum, and if it is aligned perpendicular to the principal axis, the photoelectron wave function will be of pure E symmetry. The photoionization of a degenerate orbital group of E symmetry, however, is a little more involved. For the parallel case, only ionization into the E component of the continuum is symmetry-allowed. In the situation where the polarization axis is aligned perpendicular to the principal molecular axis, however, dipole transitions into all three components of the continuum can make non-vanishing contributions, which can be seen from the product $\Gamma^E \times \Gamma^E$ in the product table.

To benchmark the fidelity of our photoionization calculations, we ideally want to compare them to published data for the randomly oriented molecule. To the best of our knowledge,

Table 2.3 Character table (left) and product table (right) for the C_{3v} point group. The symmetry operations in the head of the character table are the identity operation E, rotations around the threefold axis of symmetry, C_3, and mirroring through the three vertical mirror planes, σ_v.

	E	$2C_3$	$3\sigma_v$	linear fncts. & rotations
A_1	1	1	0	z
A_2	1	1	−1	R_z
E	2	−1	0	(x, y), (R_x, R_y)

	A_1	A_2	E
A_1	A_1	A_2	E
A_2	A_2	A_1	E
E	E	E	$A_1 + A_2 + E$

the only photon-energy dependent, quantitative survey of the photoionization dynamics of CF_3I is the synchrotron study by Yates *et al.*[25] in which only *branching ratios* are reported instead of absolute photoionization cross sections and which does not provide data on the asymmetry parameter, β_2. We recall that the branching ratio, BR_t, for ionization into a final state t at a photon energy $\hbar\omega$ is defined as

$$\mathrm{BR}_t = \frac{\sigma_t(\hbar\omega)}{\sum_f \sigma_f(\hbar\omega)}\,, \tag{2.18}$$

where σ_i is the partial cross section for the final state i and the sum runs over all channels f that are open at the photon energy $\hbar\omega$. Limited by their spectral resolution, Yates *et al.*,[25] were not able to resolve all single-particle states individually, so that in some cases only the BR for the sum of two closely spaced states is reported. From the results of the present calculations, the BRs were formed accordingly from the partial cross sections both in length and velocity gauge, which are displayed together with the experimental values in Fig. 2.14.

Overall, we find a very satisfying agreement between the theory and the experiment of Yates *et al.*.[25] However, we also observe two pronounced differences between the experimental BRs and our simulation: First, for photon energies right above threshold, the calculated BRs for the states $(3e + 1a_2)$, $2e$, and $(2a_1 + 1e)$ are significantly overestimated (panels b, d, and f in Fig. 2.14). Apparently, the ESECP model predicts a strong one-electron resonance for photoelectrons with ∼1 eV of kinetic energy that appears in different channels and that is not observed in the experiment.[k] At the same time, this is the kinetic-energy region where bound states in the continuum, which decay through autoionization, can dominate photoabsorption.[49] This process can only be described through multi-electron resonances, which require the explicit treatment of electron correlation, and is therefore beyond the scope of the applied method. Second, considering the results for the HOMO $4e$ orbital (panel a of Fig. 2.14) we find that – while the general trend is correctly reproduced – the calculated BR is systematically underestimated by almost a factor of two. To some extent, this can possibly explained by the low-energy resonance phenomenon discussed before, which can only become visible at the expense of some other state's contribution being underestimated at the same photon energy (because the BR is a relative measure). It could, on the other hand, also be indicative of a relativistic effect: The fact that the cross section is falling monotonically

k We caution, however, that we do not have reference data for the *exact* same photon energies as in the present experiment, so that there is *in principle* a chance that these narrow resonances are simply not covered by the choice of synchrotron wavelengths.

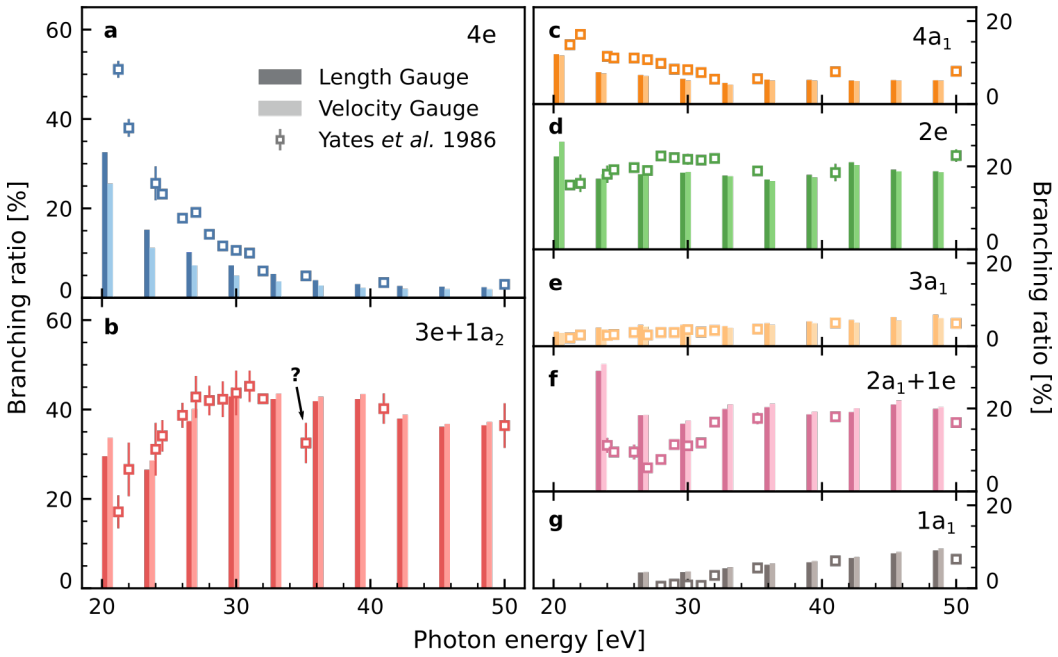

Figure 2.14 Branching ratios for the valence-shell photoionization of CF_3I. Vertical bars show the results from the ePolyScat calculations in length gauge (darker shading) and velocity gauge (lighter shading), respectively. For comparison, experimental values from Yates *et al.*[25] (open squares) are shown together with their reported experimental uncertainty. To emphasize the relative strength of the contributions, all panels are to scale with respect to each other. The point marked as **?** certainly is off due to a misprint in the original publication because the BRs add up to only 90 % at that photon energy, but to the expected 100 % at all others.

suggests that the interaction of the photoelectron with the molecular parent ion is small (which is in line with the notion that the 4*e* orbital has an essentially atomic, outer-valence character) and therefore the cross section is dictated by the dipole overlap between the bound-state and the – essentially unperturbed – continuum wave functions.[49] Now, it is in particular the relativistic shielding of the core electrons and the spin-orbit coupling that affects the radial distribution of the bound electrons. As we neglect relativistic effects in the calculations altogether, and in particular the fact that the ionic state that is associated with the removal of a 4*e* electron is spin-orbit split, we suspect that this leads to the systematic discrepancy between the calculated and the measured BRs.

2.5.3 Connection to the experimental PADs

To be able to compare the results of the photoionization calculations from the previous section to the experimental results presented in Section 2.5.1, we need to simulate photoelectron spectra from the photoionization observables, which requires knowledge of the relative intensities of the harmonics, $I^{(N)}$, the width of each photoline, and its differential cross section, $\mathrm{d}\sigma/\mathrm{d}\theta$, for a given molecular axis distribution, P_{MA}. The relative intensities of the harmonics 17 through 31 are directly taken from the reconstructed spectrum presented in Section 2.3.2. From that spectrum, however, we could not recover the intensities of the harmonics 13 and

15, which are presumably present in this experiment because their photon energies exceed the aluminum filter edge of ~20 eV. Therefore, we use a least-squares fitting procedure, in which they appear as additional fit parameters, to obtain an estimate for them.

The widths of the photolines, on the other hand, are determined by the bandwidth of the individual harmonics, the lifetime of the ionizing species, and the instrumental function of the spectrometer. For a VMI, the instrumental function can take a complicated form and it ideally has to be characterized explicitly for every set of spectrometer voltages. For simplicity, we assume that the resolution of the spectrum is *not* limited by the spectrometer, but by the bandwidth of the harmonics, an approximation that is well justified in our experimental configuration. Further, we assume that all harmonics are of Gaussian shape and that they have the same width, κ, which we treat as a free parameter in the fitting procedure, and which therefore represents the *average* photoline width. Using a single, constant value for the photoline widths may seem like an oversimplification, but it introduces only one additional parameter into the fitting procedure, which makes it more robust.

Now we can write the angle-resolved photoelectron spectrum $F(\epsilon_k, \theta)$ as a function of the *continuous* photoelectron kinetic energy ϵ_k, i. e.,

$$F(\epsilon_k, \theta) = \sum_N \sum_f \left(\mathrm{d}\sigma_f(\epsilon_f^{(N)}) / \mathrm{d}\theta \right) \frac{I^{(N)}}{\kappa} \exp\left\{ \frac{-\left[\epsilon_k - \epsilon_f^{(N)}\right]^2}{2\kappa^2} \right\}, \tag{2.19}$$

where the sums run over all final states f, for which $\epsilon_f^{(N)}$ is positive, and over all harmonics of order N. To calculate the differential cross section, $\mathrm{d}\sigma / \mathrm{d}\theta$, a convolution has to be carried out between the photoemission of a molecule which is fixed in space, and the molecular axis distribution, P_{MA}, of the molecular ensemble. In principle, this can be done analytically by re-expanding P_{MA} in spherical harmonics and applying vector coupling algebra to calculate the product of P_{MA} with the partial-wave dipole matrix elements for photoionization,[50] as was presented in Section 1.3. Here, we have applied the more straightforward, but entirely equivalent approach of integrating the laboratory-frame photoemission numerically over all molecular orientations, weighted by P_{MA}. For a non-linear molecule like CF_3I, this requires an integration over all three rotational degrees of freedom, which we denote by the Euler angles $\mathbf{R} = (\alpha\ \beta\ \gamma)$ (see Section 1.3 for their meaning). The integration over the rotation around the principal molecular axis through the angle γ can, however, be avoided by not working with the differential cross section in the molecular frame, but in the recoil frame. In the latter, a cylindrical averaging around the recoil axis is already implied and we simply require that the recoil axis is identical to the principal molecular axis.

The last bit of complication arises from the fact that in the experiment the emission of the outgoing photoelectron into the solid angle $\mathrm{d}\mathbf{\Omega} = \mathrm{d}\phi \sin\theta\, \mathrm{d}\theta$ of the laboratory frame of reference is measured, in which the polarization axis is fixed while the molecule rotates around it, a problem that was already touched upon at the end of Section 1.3. When calculating differential cross sections in the recoil frame, however, it is conventional to define the direction of photoemission, $\mathrm{d}\mathbf{\Omega'}$, relative to the space-fixed recoil axis. When performing the averaging, the differential cross sections therefore have to be rotated back by the current set of Euler angles to make the polarization axes coincide, which we refer to as the photon frame. This frame transformation is carried out simply by applying the Euler rotation matrices introduced

in Eq. (1.44), which let us write

$$\frac{\mathrm{d}\sigma(\mathbf{R})}{\mathrm{d}\mathbf{\Omega}} = \mathbf{D}(-\alpha, -\beta, \gamma = 0)\frac{\mathrm{d}\sigma(\mathbf{R})}{\mathrm{d}\mathbf{\Omega'}} \,. \tag{2.20}$$

Then, the differential cross section in the laboratory frame is obtained by integrating the (rotated) recoil-frame PAD over all Euler angles, according to

$$\mathrm{d}\sigma_f(\epsilon_f^{(N)})\,/\mathrm{d}\mathbf{\Omega} = \int_0^{\pi}\int_0^{2\pi} P_{\mathrm{MA}}(\beta)\frac{\mathrm{d}\sigma(\mathbf{R})}{\mathrm{d}\mathbf{\Omega}}\,\mathrm{d}\alpha\,\mathrm{d}\beta \,. \tag{2.21}$$

As P_{MA} is, in the present experiment, always cylindrically symmetric, this symmetry is imprinted onto $\mathrm{d}\sigma\,/\mathrm{d}\mathbf{\Omega}$, which renders the differential cross section independent of the azimuthal angle ϕ. This is why we simply use $\mathrm{d}\sigma\,/\mathrm{d}\theta = \frac{1}{2\pi}\,\mathrm{d}\sigma\,/\mathrm{d}\mathbf{\Omega}$ in Eq. (2.19). Eventually, from $F(\epsilon_k, \theta)$ all angular-distribution parameters were calculated in the same way as for the experimental data, which is discussed at the end of Section 2.3.1.

Practically, Eq. (2.21) was integrated on an equidistant grid of 65 points along α and 65 points along the β direction. The parameters were chosen such that when the molecular axis distribution of the randomly oriented ensemble, $P_{\mathrm{MA}}^{iso} = \frac{1}{2}$, was used, the absolute difference between the numerically obtained value of β_2 and the analytical one was always smaller than 5×10^{-3}.

With all quantities of Eq. (2.19) defined, a fitting procedure was used to determine four free parameters: the intensities $I^{(11)}$, $I^{(13)}$, and $I^{(15)}$, and κ. Here, we have included $I^{(11)}$ and all corresponding photoionization transitions, even though we expect the intensity of this harmonic to be very weak after the aluminum filter, as a kind of "sanity check" of our approach.

2.5.4 Comparison between experiment and theory

The fitting procedure was carried out using the PADs recorded at the alignment peak. The distributions of P_{MA} were taken directly from the simulations presented in Section 2.4.3. It may appear most natural to match the simulations to the experiment through the angle-integrated photoelectron spectrum. In Section 2.5.2, however, we have found a good agreement between the calculated and the measured *branching ratios* only, and this does not necessarily imply that the photon-energy dependence of the *absolute* cross section is correctly reproduced. Therefore, the actual optimization was carried out with the radial distribution of the asymmetry parameter, β_2, the results of which are displayed in Fig. 2.15.

Concerning the angle-integrated intensity distribution (Fig. 2.15a), we find that the overall structure of the experimental data is correctly reproduced, but that there is a systematic trend that overestimates the total cross section with increasing photoelectron kinetic energy, which leads to the observation that in the spectra, which are normalized to maximum peak height, the calculated photoelectron spectrum is weaker than the measured one below the normalization point, and more intense above it. For the average asymmetry parameter β_2 that is displayed in Fig. 2.15b, however, which is *by definition* independent of the intensity, we find an almost quantitative agreement between the experimental and the calculated radial β_2 distribution in an kinetic-energy region between 15 and 30 eV. Below this region, the general trend is correctly reproduced, but the detailed structure is washed out in the simulation,

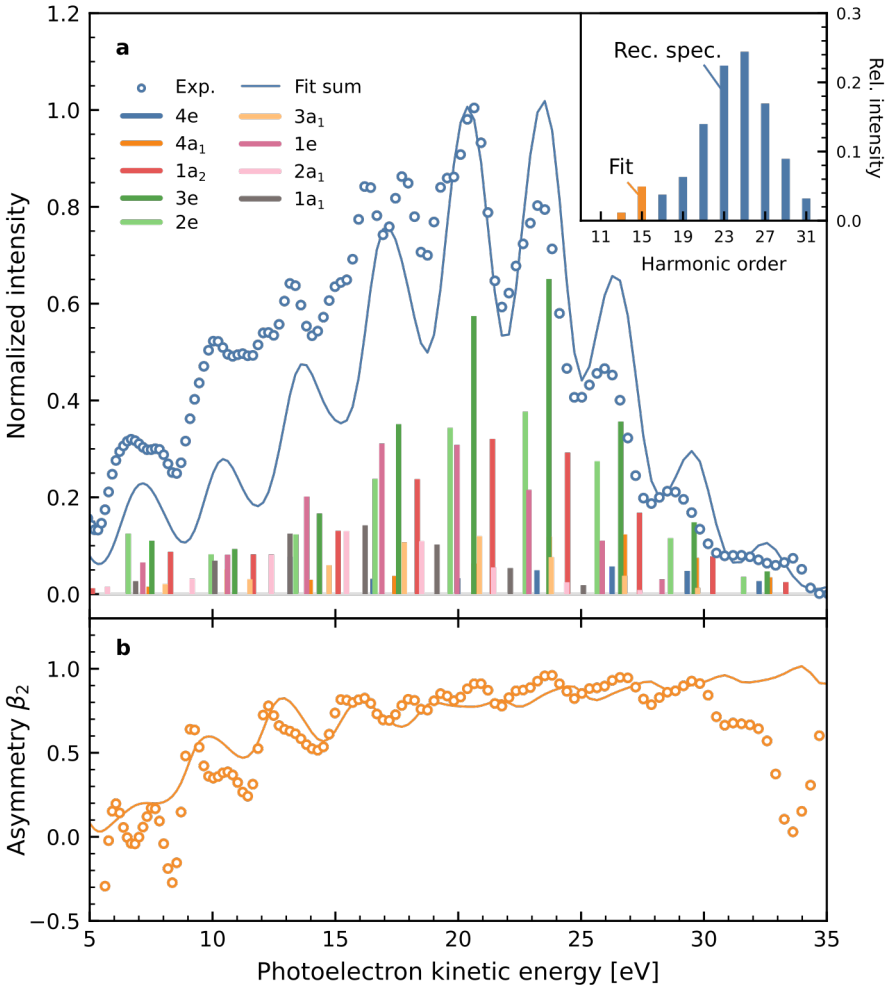

Figure 2.15 Comparison between the experimental photoelectron spectrum (open circles) obtained with the entire harmonics comb and the simulated one (solid line) taking into account the experimentally obtained harmonics spectrum. **a)** Angle-integrated, radial intensity distribution. For the experimental data, the photoelectron data at the alignment peak were used. The simulated spectrum was obtained from Eq. (2.19) after the least-squares fitting procedure described in the main text. A decomposition into the individual contributions is shown as a stick spectrum. The inset shows the complete harmonics spectrum, distinguishing between the harmonics that were obtained from the fit (orange) and those that were obtained from the photoelectron spectrum in helium (blue, see Section 2.3.2). **b)** Same as **a** for the asymmetry parameter β_2.

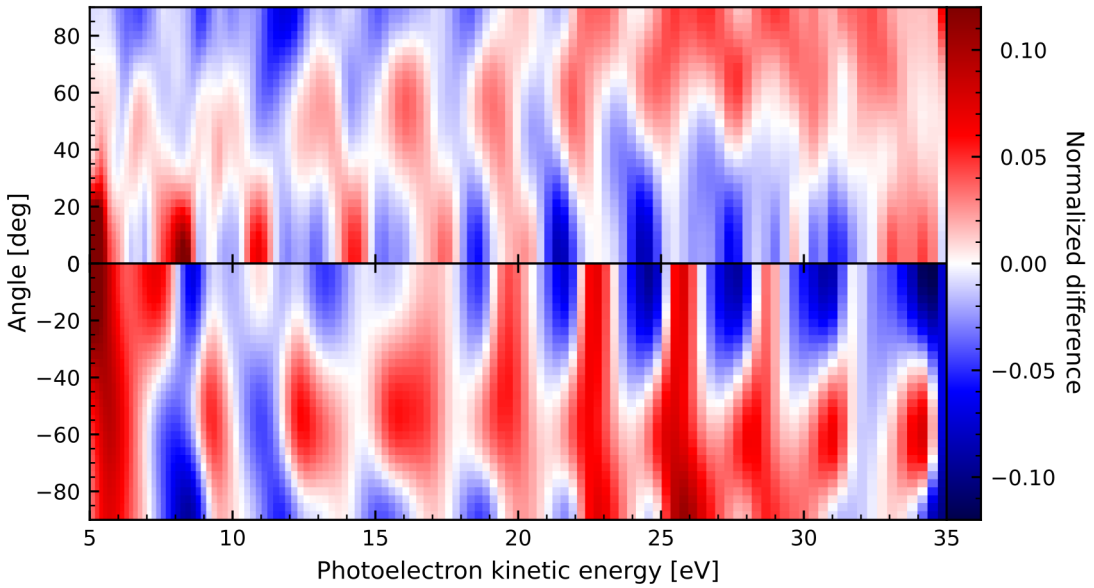

Figure 2.16 Normalized difference of the angle-resolved photoelectron spectrum, $\Delta_N F(\epsilon_k, \theta)$, from the experiment (top) and the simulation (bottom).

which we attribute to the fact that an equal, average peak width was assumed. Above 30 eV, the asymmetry parameter quickly drops to zero in the experiment because in this region the intensity of the photoelectron signal is comparable to (isotropic) background contributions. In the inset of Fig. 2.15a, the relative intensities of the entire harmonics comb are shown, and it appears that the strengths of the fitted harmonics smoothly match the outline of the reconstructed spectrum. In particular, $I^{(11)}$ is estimated to be zero, which seems reasonable from what was said above.

To assess the agreement between the alignment effects in the experimental spectra and the photoionization calculations in a qualitative way, we compare the normalized differences in the angle-resolved spectra $\Delta_N F(\epsilon_k, \theta)$ in Fig. 2.16. Overall, considering the number of approximations and simplifications made, we find that the measurement is very well reproduced by the simulation. In particular, the characteristic, repetitive angular pattern between 15 and 30 eV is almost quantitatively matched, even if in the calculation the strength of the alignment effect is predicted to be stronger than observed in the experiment.

2.5.5 Discussion

Clearly, when facing such a convoluted spectrum as in the present experiment, the appealing advantage of having a simulation that can reproduce the findings to a satisfying degree is that, in the calculation, we can decompose the spectrum into its individual contributions hoping to rationalize the photoionization dynamics. This is done in Fig. 2.17, where the changes in the photoelectron angular distributions between the aligned and planarly delocalized molecules are shown as absolute differences. As expected, the orbital groups that have the highest branching ratios – we recall that this is the group of fluorine $2p$ lone pair orbitals, $1a_2$, $3e$, and $2e$ – are also the ones that dominate the difference spectrum, especially in the region between

15 and 30 eV (panels c, d, and e of Fig. 2.17). Also, for many states, the angular-distribution difference is varying smoothly as a function of photoelectron kinetic energy, for example in panels a, f, and h of Fig. 2.17. What is more striking is that for certain states, at certain energies, the angular distributions change *qualitatively*. This can be seen for the $4a_1$ state (panel b), where a transient dip at small angles appears around ∼25 eV, and for the $3e$ state (panel d), for which the angular-distribution difference is fundamentally different below and above of what appears to be an "inflection point" at ∼15 eV.

We tentatively propose that such drastic changes in the angular-distribution differences are indicative of an underlying one-particle resonance, typically referred to as a "shape resonance". The following qualitative argument shall serve to illustrate this assumption: If no scattering resonance is involved, the photoelectron angular distribution changes smoothly with photoelectron kinetic energy, mostly governed by the energy-dependent Coulomb-phase shift, and this change will be comparable for molecules in all ionization geometries. Therefore, the PAD difference, as shown in Fig. 2.17 should show only a weak dependence on the kinetic energy. With every resonance, on the other hand, a unique resonance continuum wave function is associated that will most likely be highly anisotropic, simply because the potential of the molecule – that causes the transient trapping – is highly anisotropic. Now, if at the resonance position the contribution of this resonance wave function to the overall photoionization dominates, it modulates the PAD of either the aligned, or the planarly delocalized molecule in a characteristic way. This, in turn, will then express itself as a pronounced variation of the angular-distribution difference.

In general, as discussed at the end of Section 1.2, a shape resonance manifests as a sudden jump in the eigenphase sum for the electron scattering off the target ion. In Fig. 2.18a the eigenphase for the $3e$ channel is shown over the energy region of interest, calculated at the ESECP level of theory as above. Notably, not only one, but two steep rises are observed, at energies of ∼10 eV and ∼20 eV, respectively. To quantify them, the eigenphase sum is approximately written as the sum of a constant background phase, δ_0, and the resonance phase shifts, which are represented by arctangent functions, i. e.,

$$\delta(E) = \delta_0 + \frac{A_1}{\pi} \arctan \frac{E - E_1}{\Gamma_1/2} + \frac{A_2}{\pi} \arctan \frac{E - E_2}{\Gamma_2/2}\,, \tag{2.22}$$

where E_i $(i = 1, 2)$ is the center of the phase jump, Γ_i its width, and A_i its step height. Even with this drastically simplified functional form, in which the background phase shift is assumed to be constant, the energy dependence of the eigenphase sum can be reproduced very closely, which is shown in Fig. 2.18a, as well. The obtained resonance parameters are summarized in Table 2.4. What is surprising is that the fact that two resonances seem to be involved is not directly apparent from the (calculated) partial cross section nor the asymmetry parameter β_2 for the randomly oriented molecule, which are shown in Fig. 2.18b and c, respectively. Typically, it is these two observables which are considered when identifying a resonance experimentally because they vary drastically in its proximity.[49]

To characterize the exact shapes of the resonance wave functions and hence their possible impact on the photoelectron angular distributions, they need to be separated from the background scattering wave function, as follows: Formally, shape resonances are defined as poles of the scattering S matrix when its energy dependence is analytically extended into the complex plane.[51,52] To prove that indeed shape resonances are involved, we have carried

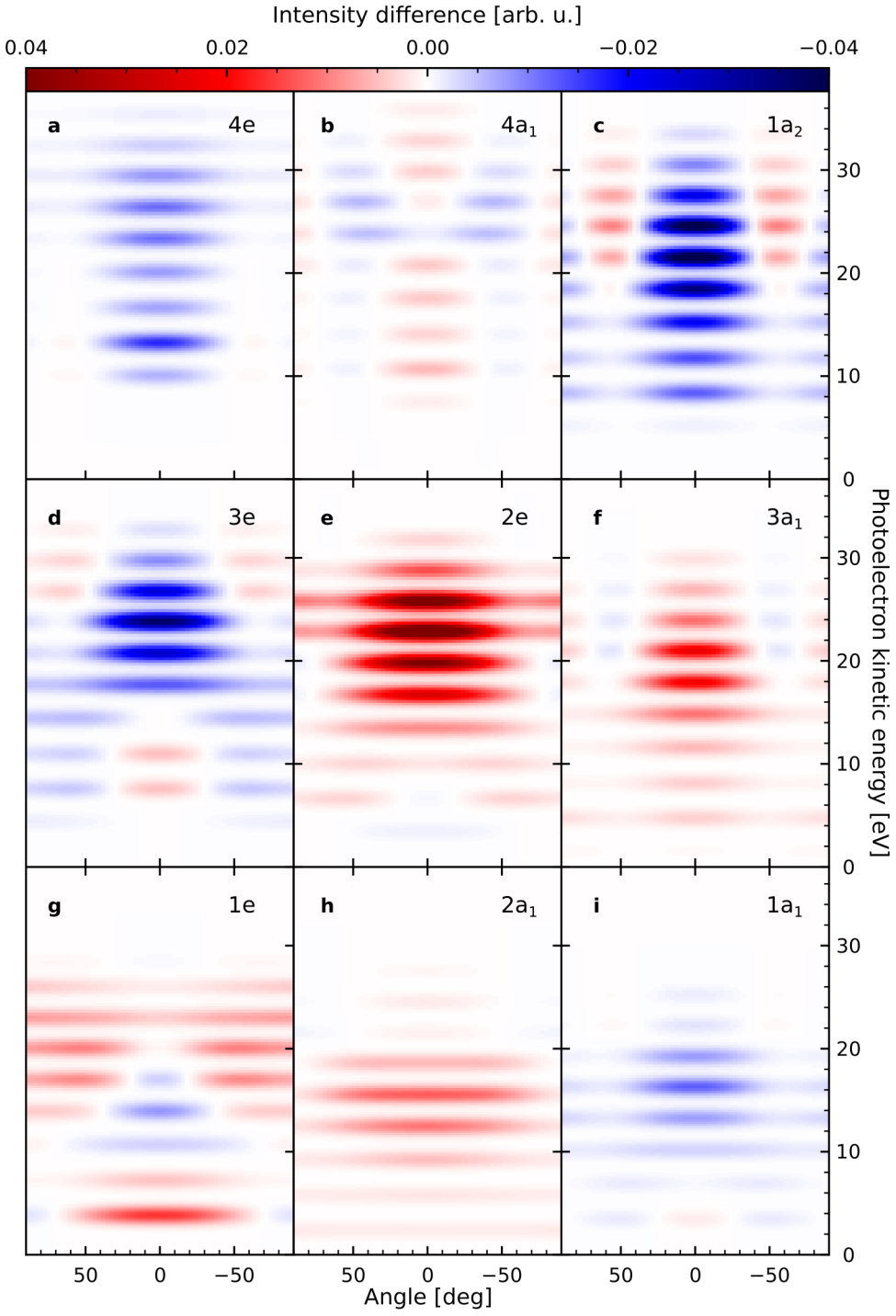

Figure 2.17 Calculated *absolute* differences of the photoelectron angular distributions $\Delta F_f(\epsilon_k, \theta)$, decomposed into the final states f that are indicated in the top right of every panel. The displayed intensity differences are all to scale with respect to each other to emphasize the relative magnitude of the contribution that they make to the difference spectrum shown in the bottom panel of Fig. 2.16.

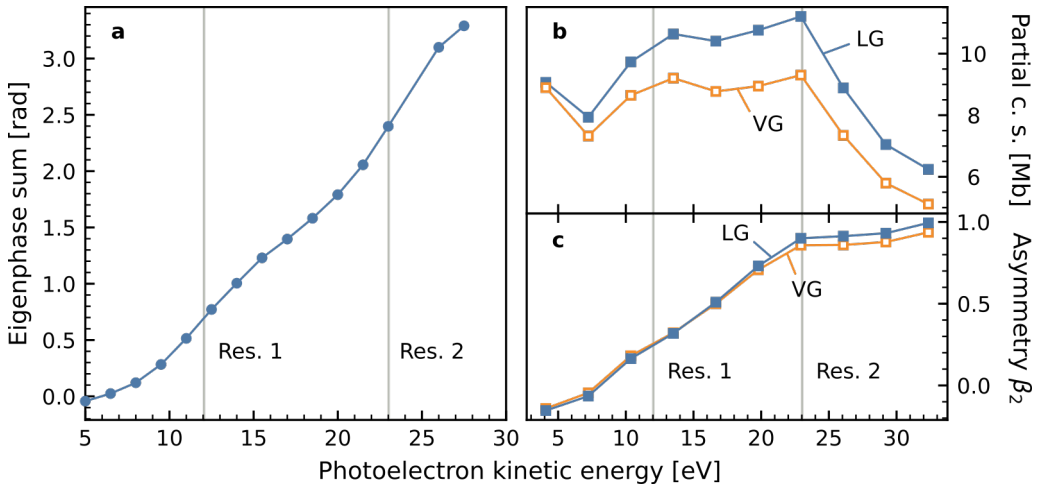

Figure 2.18 Eigenphase sum and photoionization observables for the 3*e* channel of CF_3I. **a)** Eigenphase sum for the electron scattering off CF_3I^+, in which an electron was removed from the 3*e* orbital (dots) and a fit with the function of Eq. (2.22) (solid line). **b, c)** Partial cross section **(b)** and asymmetry parameter **(c)** for the photoionization out of the 3*e* orbital in the randomly oriented molecule.

out pole searches in the complex scattering-energy plane with the algorithm developed by Stratmann & Lucchese[53]. When a resonance is found, the associated scattering wave function can be evaluated at the complex-valued energy which is then equal to the "pure" resonance wave function.

For the resonance search, a simplified, static potential with model exchange is used, which is energy independent, in contrast to the more sophisticated ESECP model introduced above. As its outcome, the algorithm returns a list of extrapolated pole positions at complex-valued energies $E = E_{res} - i\Gamma/2$, where E_{res} is the resonance energy and Γ is the associated resonance width.

Carrying out the resonance search, we were able to identify two poles that correspond closely in energy and width to the phase jumps observed in Fig. 2.18. When more than one pole was found in the corresponding energy region, the one with the smallest imaginary part was chosen because it is this on that has the greatest impact on the eigenphase sum.

The corresponding resonance wave functions are displayed in Fig. 2.19 a through d. From the real-valued wave function (a and b) one can see, how the resonances can be understood in terms of anti-bonding orbitals: In both cases, an f orbital of iodine is involved, that overlaps with what seems to a carbon p orbital in the case of the low-energy resonance, and a d orbital in the other case. From the anti-bonding orbital alone, however, one cannot predict the asymptotic shape of the resonance wave function. It turns out that this shape differs significantly for the two resonances: for the lower one, probability density is concentrated in the direction of the iodine atom. For the higher one, scattering occurs predominantly in the plane perpendicular to the C–I axis.

In the next step we need to verify that these resonances make a significant contribution to the molecular-frame photoelectron angular distribution because, after all, also the background scattering and the dipole selection from the molecular orbital contribute to the final MF-PAD.

To this end, we compare the MF-PAD at harmonic 19 (13.5 eV, Fig. 2.19e) and 25 (22.9 eV,

Table 2.4 Resonance positions and widths of the shape resonances in the photoionization of the 3*e* orbital group, obtained from the fitting of step functions to the eigenphase sum and from the pole-searching algorithm.

	From eigenphase sum			From pole search		
	E_R[eV]	Γ[eV]	ΔΦ[rad]	E_R[eV]	Γ[eV]	Character
Res. 1	12.04	7.62	1.9	11.13	5.30	f on I and p on C
Res. 2	23.42	7.07	2.7	23.06	6.34	f on I and d on C

Fig. 2.19f), which are closest to the determined resonance positions, to the asymptotic shapes of the resonance wave functions. Clearly, there is a striking similarity between the MF-PAD and the retrieved resonance wave functions, which makes us confident that – within the computational results – the two identified resonances do modulate the photoelectron angular distributions significantly.

With the data presented so far, we cannot unambiguously *prove* that it must be these two shape resonances that determine the PADs in the observed way. What we can do, however, is to support this interpretation with an indirect argument: while we cannot simply turn off the existence of shape resonances alone in the simulations, we can turn off the photoelectron–molecular-ion interaction altogether by simply using the Coulomb wave, introduced in Eq. (1.29), instead of the calculated continuum wave functions. To simplify the model further, we come back to the idea once more that the PADs are largely determined by the three most intense contributions, which are associated with the orbitals $1a_2$, $3e$, and $2e$. In what follows, the angular-distribution parameters calculated with the full model (Fig. 2.20) and with the Coulomb waves only (Fig. 2.21) are compared to the experimental results individually to gauge what effect the explicit treatment of photoelectron scattering has on the resulting PADs.

Looking at the comparison between theory and experiment in Fig. 2.20,a pretty good agreement is observed. In particular, qualitatively, the experimental radial distributions are still well reproduced with the 3-state model. Note, however, that the effect size in the individual contributions is up to a factor 3 larger than what is eventually observed after averaging over all contributions.

When the same comparison is made using Coulomb waves instead of the full ePolyScat model, as shown in Fig. 2.21, two striking observations can be made: First, the overall trends in $\Delta\beta_2$ and $\Delta\beta_4$ are not correctly reproduced anymore. In particular, the slow decline and change of sign in $\Delta\beta_2$ is not correctly captured. Second, the rapidly oscillating modulations are still matching the experimental findings very well.

From the above analysis, we conclude that the rapid oscillations are completely determined by the shape of the molecular orbitals: all three orbitals of the 3-state model are fluorine lone-pair orbitals, which are different linear combinations of the fluorine p orbitals. In particular, the spatial filtering that the orbitals cause in the photoionization seems to be exactly opposite for the $2e$ and the $1a_2$ orbitals, whereas ionization from the $3e$ orbital results in a more isotropic PAD.

The overall trends, however, especially that in $\Delta\beta_2$, can only be described to a satisfactory degree when the two shape resonances discussed above are brought in because the precise

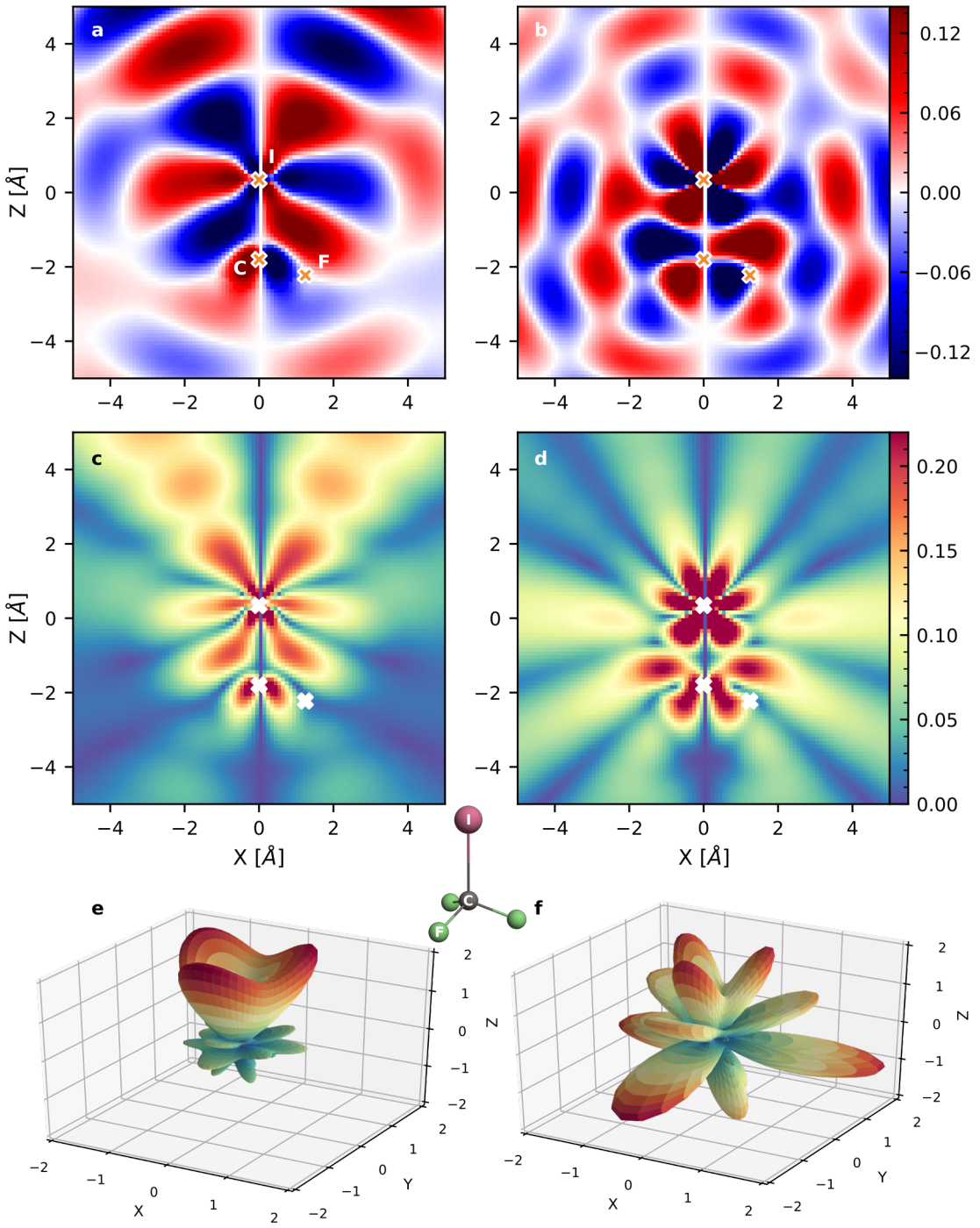

Figure 2.19 Resonance wave functions in the $3e \rightarrow ke$ photoionization of CF_3I. **a, b)** Real part of the resonance wave functions at $E = (11.1 - 2.7\mathrm{i})$ eV **(a)** and $E = (23.1 - 3.2\mathrm{i})$ eV **(b)**, shown as cut through the Cartesian $x - z$ plane that contains the iodine, carbon and one fluorine atom, positions of which are marked by crosses. **c, d)** Same as **a** and **b** but as absolute wave-function value to emphasize the asymptotic behavior of the resonance wave function. **e, f)** Molecular-frame photoelectron angular distributions (in Mb sr^{-1}) for photoionization with harmonic 19, close to the resonance of **a** and **c**, and for harmonic 25, close to the resonance of **b** and **d**.

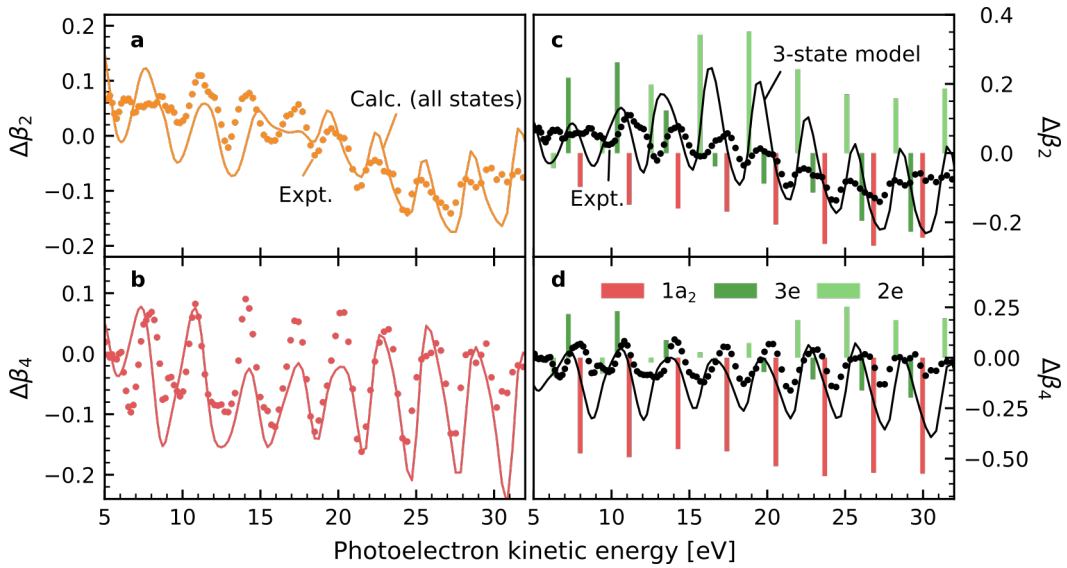

Figure 2.20 Comparison between experimental and theoretical radial distributions of $\Delta\beta_l$. **a, b)** Comparison between experiment (dots) and the full ePolyScat model (solid lines). **c, d)** Same as **a, b**, but only taking into account the three strongest contributing orbitals (note the different ordinates). The vertical bars indicate the individual contributions from the orbitals that are color-coded according to the legend in **d**.

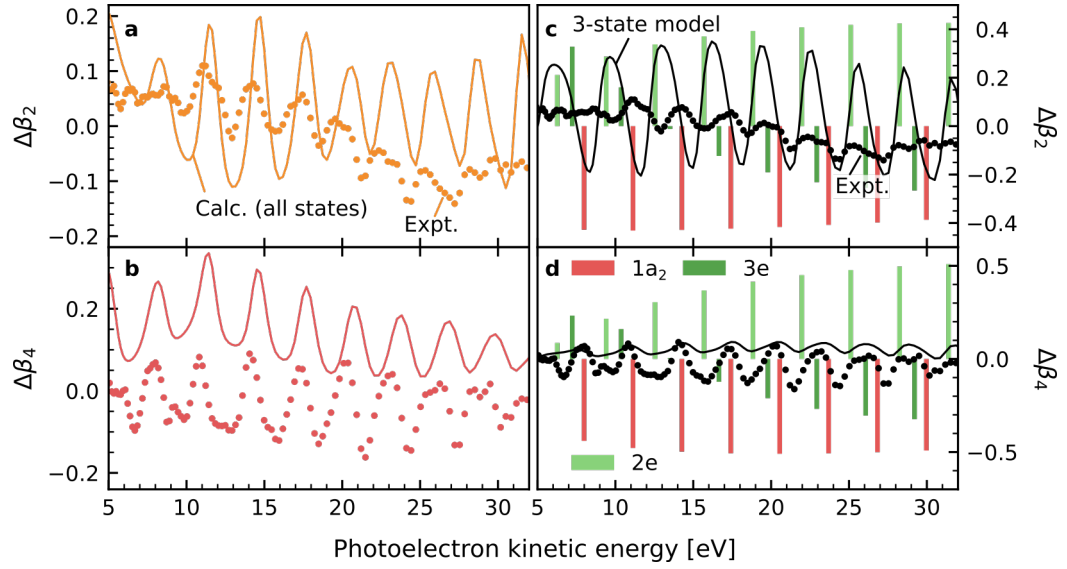

Figure 2.21 Same as Fig. 2.20, but for the calculation with Coulomb waves instead of the full model.

shape of the resonance wave functions is imprinted onto all channels in which these resonances occur.

2.6 Conclusion

In this chapter, we have investigated the effects that molecular alignment has on the photoelectron angular distributions (PADs) in XUV ionization. First, we have quantitatively reconstructed the molecular-axes distribution of the aligned ensemble during the revival of the rotational wave packet. Based on the extracted molecular-axes distributions, the connection between the measured PADs and the calculated ones, which are expressed in the molecular frame, was successfully established through a rotational-averaging procedure. In comparing theory and experiment, we found a convincing agreement within the known limitations of the theoretical model. Furthermore, the detailed analysis of the alignment-dependent changes in the PADs gave strong evidence that these changes can – to a large extent – be understood when considering the contributions from two prominent shape resonances that are not directly apparent in the photoelectron spectra of the randomly aligned ensemble. This interpretation was supported by the observation that the measured trends in the energy dependence of the angular-distribution parameters cannot be reproduced when the photoelectron scattering is turned off completely, which, of course, also eliminates the shape resonances.

References

1. Lucchese, R. R. “A Simple Model for Molecular Frame Photoelectron Angular Distributions”. *J. Electron Spectrosc.* **141,** 201–210 (2004).
2. Dill, D. “Fixed-molecule Photoelectron Angular Distributions”. *J. Chem. Phys.* **65,** 1130–1133 (1976).
3. Dörner, R., Mergel, V., Jagutzki, O., Spielberger, L., Ullrich, J., Moshammer, R. & Schmidt-Böcking, H. “Cold Target Recoil Ion Momentum Spectroscopy: A ‘Momentum Microscope’ to View Atomic Collision Dynamics”. *Phys. Rep.* **330,** 95–192 (2000).
4. Friedrich, B. & Herschbach, D. R. “Spatial Orientation of Molecules in Strong Electric Fields and Evidence for Pendular States”. *Nature* **353,** 353412a0 (1991).
5. Friedrich, B., Pullman, D. P. & Herschbach, D. R. “Alignment and Orientation of Rotationally Cool Molecules”. *J. Phys. Chem.* **95,** 8118–8129 (1991).
6. Fadley, C. S. “Diffraction and Holography with Photoelectrons and Auger Electrons: Some New Directions”. *Surf. Sci. Rep.* **19,** 231–264 (1993).
7. Mikosch, J., Bisgaard, C. Z., Boguslavskiy, A. E., Wilkinson, I. & Stolow, A. “The Quantitative Determination of Laser-Induced Molecular Axis Alignment”. *J. Chem. Phys.* **139,** 024304 (2013).
8. Pavičić, D., Lee, K. F., Rayner, D. M., Corkum, P. B. & Villeneuve, D. M. “Direct Measurement of the Angular Dependence of Ionization for N_2, O_2, and CO_2 in Intense Laser Fields”. *Phys. Rev. Lett.* **98,** 243001 (2007).
9. Thomann, I., Lock, R., Sharma, V., Gagnon, E., Pratt, S. T., Kapteyn, H. C., Murnane, M. M. & Li, W. “Direct Measurement of the Angular Dependence of the Single-Photon Ionization of Aligned N_2 and CO_2”. *J. Phys. Chem. A* **112,** 9382–9386 (2008).

10. Suzuki, Y.-I., Tang, Y. & Suzuki, T. "Time–Energy Mapping of Photoelectron Angular Distribution: Application to Photoionization Stereodynamics of Nitric Oxide". *Phys. Chem. Chem. Phys.* **14,** 7309–7320 (2012).

11. Vozzi, C., Negro, M., Calegari, F., Sansone, G., Nisoli, M., De Silvestri, S. & Stagira, S. "Generalized Molecular Orbital Tomography". *Nat. Phys.* **7,** 822 (2011).

12. Lock, R. M., Ramakrishna, S., Zhou, X., Kapteyn, H. C., Murnane, M. M. & Seideman, T. "Extracting Continuum Electron Dynamics from High Harmonic Emission from Molecules". *Phys. Rev. Lett.* **108,** 133901 (2012).

13. Corkum, P. B. "Plasma Perspective on Strong-Field Multiphoton Ionization". *Phys. Rev. Lett.* **71,** 1994 (1993).

14. McPherson, A., Gibson, G., Jara, H., Johann, U., Luk, T. S., McIntyre, I. A., Boyer, K. & Rhodes, C. K. "Studies of Multiphoton Production of Vacuum-Ultraviolet Radiation in the Rare Gases". *J. Opt. Soc. Am. B* **4,** 595–601 (1987).

15. Paul, P. M., Toma, E. S., Breger, P., Mullot, G., Augé, F., Balcou, P., Muller, H. G. & Agostini, P. "Observation of a Train of Attosecond Pulses from High Harmonic Generation". *Science* **292,** 1689–1692. pmid: 11387467 (2001).

16. Drescher, M., Hentschel, M., Kienberger, R., Uiberacker, M., Yakovlev, V., Scrinzi, A., Westerwalbesloh, T., Kleineberg, U., Heinzmann, U. & Krausz, F. "Time-Resolved Atomic Inner-Shell Spectroscopy". *Nature* **419,** 803–807 (2002).

17. Spielmann, C. "Generation of Coherent X-Rays in the Water Window Using 5-Femtosecond Laser Pulses". *Science* **278,** 661–664 (1997).

18. Popmintchev, T. *et al.* "Bright Coherent Ultrahigh Harmonics in the keV X-Ray Regime from Mid-Infrared Femtosecond Lasers". *Science* **336,** 1287–1291. pmid: 22679093 (2012).

19. Kelkensberg, F., Rouzée, A., Siu, W., Gademann, G., Johnsson, P., Lucchini, M., Lucchese, R. R. & Vrakking, M. J. J. "XUV Ionization of Aligned Molecules". *Phys. Rev. A* **84,** 051404 (2011).

20. Rouzée, A., Kelkensberg, F., Siu, W. K., Gademann, G., Lucchese, R. R. & Vrakking, M. J. J. "Photoelectron Kinetic and Angular Distributions for the Ionization of Aligned Molecules Using a HHG Source". *J. Phys. B: At., Mol. Opt. Phys.* **45,** 074016 (2012).

21. Bisgaard, C. Z., Clarkin, O. J., Wu, G., Lee, A. M. D., Geßner, O., Hayden, C. C. & Stolow, A. "Time-Resolved Molecular Frame Dynamics of Fixed-in-Space CS_2 Molecules". *Science* **323,** 1464–1468. pmid: 19286552 (2009).

22. Alekseyev, A. B., Liebermann, H.-P. & Buenker, R. J. "Potential Energy Surfaces for Ground and Excited Electronic States of the CF_3I Molecule and Their Relevance to Its A-Band Photodissociation". *Phys. Chem. Chem. Phys.* **15,** 6660–6666 (2013).

23. Sutcliffe, L. H. & Walsh, A. D. "Far Ultra-Violet Absorption Spectrum of Trifluoro Methyl Iodide". *T. Faraday Soc.* **57,** 873–883 (1961).

24. Cvitaš, T., Güsten, H., Klasinc, L., Novadj, I. & Vančik, H. "Photoelectron Spectra of Bromo- and Iodotrifluoromethane". *Z. Naturforsch. A* **32,** 1528–1532 (1977).

25. Yates, B. W., Tan, K. H., Bancroft, G. M. & Tse, J. S. "A Variable Energy Photoelectron Study of the Valence Levels and I 4d Core Levels of CF_3I". *J. Chem. Phys.* **85,** 3840 (1986).

26. Gademann, G. *Expanding the Attosecond Toolbox : Demonstration of Novel Experiments, New Light Sources and Detectors* PhD thesis (Radboud University, Nijmegen, 2011).

27. Eppink, A. T. J. B. & Parker, D. H. "Velocity Map Imaging of Ions and Electrons Using Electrostatic Lenses: Application in Photoelectron and Photofragment Ion Imaging of Molecular Oxygen". *Rev. Sci. Instrum.* **68,** 3477–3484 (1997).

28. Jungmann, J. H., Gijsbertsen, A., Visser, J., Visschers, J., Heeren, R. M. A. & Vrakking, M. J. J. "A New Imaging Method for Understanding Chemical Dynamics: Efficient Slice Imaging Using an in-Vacuum Pixel Detector". *Rev. Sci. Instrum.* **81,** 103112 (2010).
29. Kandula, D. Z., Gohle, C., Pinkert, T. J., Ubachs, W. & Eikema, K. S. E. "Extreme Ultraviolet Frequency Comb Metrology". *Phys. Rev. Lett.* **105,** 063001 (2010).
30. Samson, J. A. R. & Stolte, W. C. "Precision Measurements of the Total Photoionization Cross-Sections of He, Ne, Ar, Kr, and Xe". *J. Electron Spectrosc.* **123,** 265–276 (2002).
31. Toma, E. S. & Muller, H. G. "Calculation of Matrix Elements for Mixed Extreme-Ultraviolet–Infrared Two-Photon above-Threshold Ionization of Argon". *J. Phys. B: At., Mol. Opt. Phys.* **35,** 3435 (2002).
32. Aseyev, S. A., Ni, Y., Frasinski, L. J., Muller, H. G. & Vrakking, M. J. J. "Attosecond Angle-Resolved Photoelectron Spectroscopy". *Phys. Rev. Lett.* **91,** 223902 (2003).
33. Zare, R. N. "Photofragment Angular Distributions from Oriented Symmetric-Top Precursor Molecules". *Chem. Phys. Lett.* **156,** 1–6 (1989).
34. Søndergaard, A. A., Shepperson, B. & Stapelfeldt, H. "Nonadiabatic Laser-Induced Alignment of Molecules: Reconstructing $\langle \cos^2 \theta \rangle$ Directly from $\langle \cos^2 \theta_{2D} \rangle$ by Fourier Analysis". *J. Chem. Phys.* **147,** 013905 (2017).
35. Powis, I., Dutuit, O., Richard-Viard, M. & Guyon, P. M. "Photoion Anisotropy in Dissociative Photoionization of CF_3I". *J. Chem. Phys.* **92,** 1643–1652 (1990).
36. Low, K. G., Hampton, P. D. & Powis, I. "Molecule Coordinate Frame Anisotropy in Dissociative Photoionization of CF_3I". *Chem. Phys.* **100,** 401–413 (1985).
37. Eland, J. H. D., Feifel, R. & Hochlaf, M. "Double Photoionization and Dication Fragmentation of CF_3I: Experiment and Theory". *J. Chem. Phys.* **128,** 234303 (2008).
38. Pilcher-Clayton, A. & Eland, J. H. D. "Double Photoionisation Spectra of HI, CH_3I and CF_3I from TOF-PEPECO Measurements". *J. Electron Spectrosc.* **142,** 313–317 (2005).
39. Cox, A. P., Duxbury, G., Hardy, J. A. & Kawashima, Y. "Microwave Spectra of CF_3Br and CF_3I. Structures and Dipole Moments". *J. Chem. Soc., Faraday Trans. 2* **76,** 339–350 (1980).
40. Mikosch, J., Boguslavskiy, A. E., Wilkinson, I., Spanner, M., Patchkovskii, S. & Stolow, A. "Channel- and Angle-Resolved Above Threshold Ionization in the Molecular Frame". *Phys. Rev. Lett.* **110,** 023004 (2013).
41. Zare, R. N. *Angular Momentum: Understanding Spatial Aspects in Chemistry and Physics* (Wiley-Interscience, New York, 1991).
42. Press, W. H., Teukolsky, S. A., Vetterling, W. T. & Flannery, B. P. *Numerical Recipes: The Art of Scientific Computing* 3rd ed. (Cambridge University Press, Cambridge, 2007).
43. Walters, S. W. & Whiffen, D. H. "Rotational Spectrum of Trifluoroidomethane". *J. Chem. Soc., Faraday Trans. 2* **79,** 941–949 (1983).
44. Joachain, C. J., Kylstra, N. J. & Potvliege, R. M. *Atoms in Intense Laser Fields* (Cambridge University Press, Cambridge, 2011).
45. Tatewaki, H. & Koga, T. "Contracted Gaussian-type Basis Functions Revisited". *J. Chem. Phys.* **104,** 8493–8499 (1996).
46. Koga, T., Yamamoto, S., Shimazaki, T. & Tatewaki, H. "Contracted Gaussian-Type Basis Functions Revisited. IV. Atoms Rb to Xe". *Theor. Chem. Acc.* **108,** 41–45 (2002).
47. Bettega, M. H. F., Ferreira, L. G. & Lima, M. A. P. "Transferability of Local-Density Norm-Conserving Pseudopotentials to Electron-Molecule-Collision Calculations". *Phys. Rev. A* **47,** 1111–1118 (1993).

48. Padial, N. T. & Norcross, D. W. "Parameter-Free Model of the Correlation-Polarization Potential for Electron-Molecule Collisions". *Phys. Rev. A* **29,** 1742–1748 (1984).

49. Berkowitz, J. *Photoabsorption, Photoionization, and Photoelectron Spectroscopy* (Academic Press, New York, 1979).

50. Reid, K. L. & Underwood, J. G. "Extracting Molecular Axis Alignment from Photoelectron Angular Distributions". *J. Chem. Phys.* **112,** 3643–3649 (2000).

51. Taylor, J. R. *Scattering Theory: The Quantum Theory of Nonrelativistic Collisions* (Wiley, New York, 1972).

52. Lucchese, R. R. & Gianturco, F. A. "One-Electron Resonances in Electron Scattering from Polyatomic Molecules". *Int. Rev. Phys. Chem.* **15,** 429–466 (1996).

53. Stratmann, R. E. & Lucchese, R. R. "Resonances and the Effects of Interchannel Coupling in the Photoionization of CS_2". *J. Chem. Phys.* **97,** 6384–6395 (1992).

Chapter 3

Imaging Nuclear Wave Packets through Laser-assisted Electron Recollisions in Excited I_2 Molecules

3.1 Introduction

When atoms or molecules are exposed to strong, slowly oscillating laser fields, a great number of fascinating phenomena can be observed. Among them, probably the most notable is the generation of high-order harmonics, a process that was used itself to devise an XUV light source in Chapter 2. We quickly recall that, in the three-step model that is often used to rationalize the high-order harmonic generation (HHG), a valence electron of the atom or molecule is first ionized close to the electric-field peak of the laser field. The liberated electron is then accelerated in the laser field that drives electron away from the parent ion and then back to it, where it recollides with the ion. Now, in HHG, radiative recombination is expected to occur, but the electron could also scatter (either elastically or inelastically) off the parent ion. The experimental technique, in which these rescattered electrons are investigated is referred to as laser-induced electron diffraction (LIED). What is remarkable about the elastic-scattering case is that, if the deflection angle is large, the scattered electron will end up with an asymptotic velocity that is much larger than what it could have gained by acceleration in the field only. Therefore, in the strong-field photoelectron spectrum, the high-energy, backscattering region can typically be cleanly separated and investigated independently.

What is even more appealing is that, under certain circumstances, this rescattering phenomenon can be even further rationalized, using what has become known as the quantitative rescattering (QRS) theory. In this approximation, the returning electron wave packet is approximated as being a plane wave. Consequently, with the help of some side assumptions, the differential scattering cross section (DCS) for the electron–molecular-ion scattering process can be extracted from the measurement and compared to electron-scattering simulations or available experimental data.

Electron scattering experiments are a well-established technique to elucidate the equilibrium structure of molecules.[1] What they require, however, are electrons with de-Broglie wavelengths smaller than the internuclear separations inside the molecule. In particular, for electrons in the keV range, the constituent atoms can be treated as point scatterers, an approximation that is used in the all-classical independent-atom model.[2] Now, in an LIED experiment, the maximum recollision energy (and with it the minimum de-Broglie wavelength), scales linearly with the ponderomotive potential $U_p = E_0^2/\left(4\omega^2\right)$ of the driving laser, where E_0 is the peak field strength and ω is fundamental laser frequency. Obviously, increasing the field strength

will increase U_p, but does not come without risks: if the laser field strength is too high, many other competing processes can occur, like over-the-barrier ionization, which compromise the validity of the QRS approximation. Instead, to reach recollision energies that come close to a regime where the recollisions can be treated classically, increasing the laser wavelength is the more attractive option. Here, we have used optical parametric amplification (OPA) to generate mid-IR pulses at 1.3 μm from a standard 800 nm Ti:Sa laser.

A lot of work has been done to establish and verify the validity of the QRS model, predominantly in noble gas atoms.[3] A notable publication on molecules is the study by Okunishi *et al.*[4] on the N_2 and O_2 molecules, showing that in the extracted DCS, one- and two-particle resonances can be identified, which are in excellent agreement with multi-channel electron-scattering calculations. Recently, Pullen *et al.*[5] have demonstrated that, even in a static LIED measurement, nuclear dynamics in the molecular ion can be revealed by relating the photoelectron spectrum to sub-cycle timing information that was *inferred* from sophisticated models.

What we propose here goes one step further: As the LIED process is extremely fast, it should be possible to image the evolving nuclear structure of a molecule that is e. g., pumped into a dissociative excited state, by comparing the changing signal of the rescattered electrons to scattering calculations in different molecular geometries. As the target system we have chosen the iodine molecule, I_2, for two reasons in particular: First, it exhibits a number of low-lying excited states that can be accessed in the visible region of electromagnetic radiation, and which can be used to prepare dissociating and vibrational wave packets. Second, the total scattering cross section scales with the number of electrons in the target and is therefore much higher for heavy atoms than it is for light ones.

What is more, in two recent experiments it was demonstrated that the evolving nuclear structure of dissociating I_2 molecules could be imaged with ultrafast electron diffraction[6] and x-ray diffraction[7]. In this chapter, we want to investigate to what extent time-resolved LIED experiments can compete with these diffraction techniques or whether LIED experiments can provide complementary insight based on the information that can be extracted from it.

To cover a large range of internuclear distances at which the LIED is sampled, we have, in fact, carried out two experiments: one, in which I_2 is excited into the A state, which leads to photodissociation, and one, in which it is excited into the B state, in which a vibrational wave packet is created that bounces forth and back inside the binding potential well. All important, involved neutral and ion states are given in the scheme Fig. 3.1.[a] The choice of excitation energies was guided by the extensive work of Tellinghuisen[9] on the photoabsorption on I_2 in the visible and infrared region. Based on the transition strengths that he reported for transitions into the *A*, *B*, and *B″* states, 710 nm and 555 nm were chosen for the excitation into the *A* and *B* state, respectively. In the case of the *A* state, this wavelength corresponds to the absorption maximum. For the *B* state, however, the chosen excitation wavelength is red-shifted with respect to the state's absorption maximum to suppress excitation into the dissociative *B″* state, absorption of which is strongest at 490 nm.

In this chapter, we proceed with an approach similar to that of the previous ones: With the photoion measurements, the (typically well understood) wave-packet dynamics are quantified by Coulomb-explosion imaging and the internuclear distance is extracted as a function of

a For a comprehensive overview of the electronic structure of I_2 and I_2^+, we refer to the work of Jong, Visscher & Nieuwpoort,[8] which we consider an invaluable source.

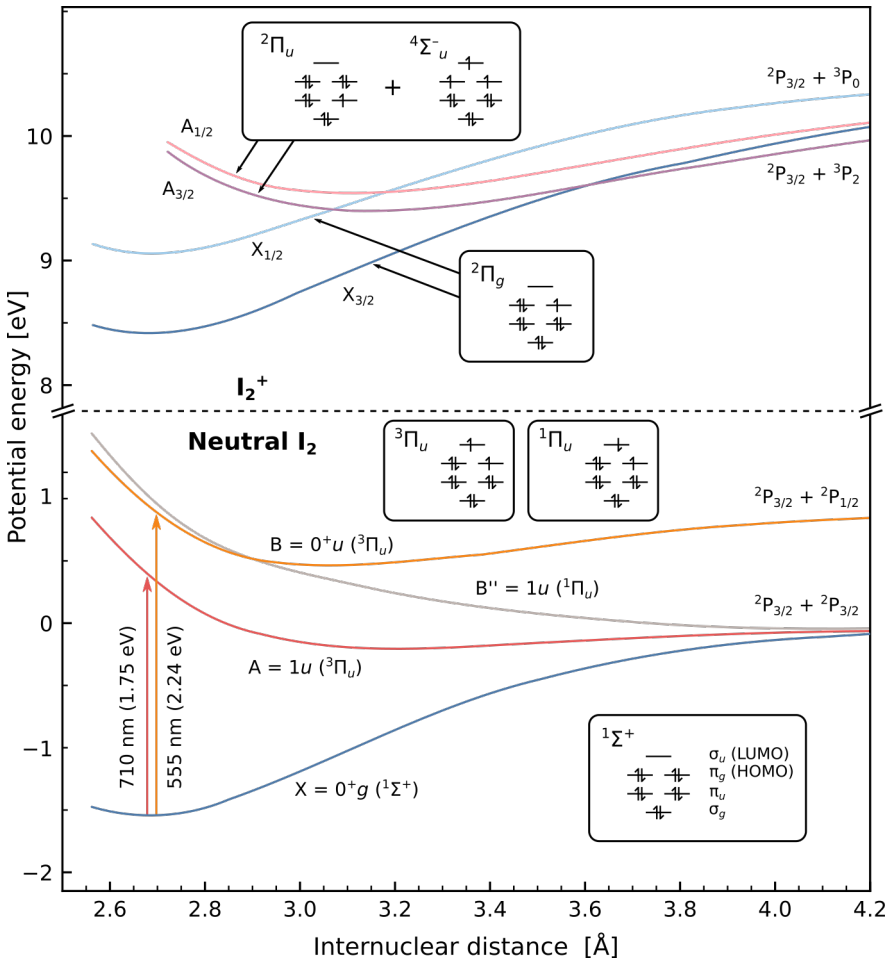

Figure 3.1 Potential energy curves of I_2 and I_2^+ that are relevant for the present set of experiments. All energies are given relative to the $^2P_{3/2} + {}^2P_{3/2}$ dissociation threshold. Inside the boxes, valence-electron configurations are given in terms of a non-relativistic, single-electron picture to illustrate the leading configurations of the indicated term symbols, according to Jong, Visscher & Nieuwpoort[8] (HOMO: highest occupied molecular orbital, LUMO: lowest unoccupied molecular orbital). The dissociative B'' state (gray) is also accessible at 555 nm and population transfer into this state cannot be entirely avoided.

pump–probe delay. Based on these distances, scattering calculations are carried out for I_2^+ in several geometries and the results are compared to the experimental DCS extracted from the time-dependent photoelectron spectra. We find that the observed dynamics can be explained almost completely by considering two strong shape resonances that are involved: the $l = 6$ resonance in I_2 at the equilibrium internuclear distance and the well-known $l = 3$ (or f-wave) resonance in atomic iodine.

3.2 Experimental Setup

For this experiment, laser pulses were generated in a commercial Ti:Sa laser system (Spectra Physics) that provides pulses of 3 mJ pulse energy, 30 fs (FWHM) pulse width centered at

800 nm, at a repetition rate of 1 kHz. Two commercial optical parametric amplifiers (Light Conversion "TOPAS C"), each of which was pumped with 1 mJ of the 800 nm laser output, were operated in parallel to generate the mid-IR and visible light pulses. For the mid-IR arm, pulses of 130 µJ, centered at 1300 nm were generated, which were attenuated with a neutral-density (ND) filter to ~30 µJ. For the *A*-state experiment, 1420 nm pulses were generated in the second OPA, which were then frequency-doubled to give 20 µJ, 710 nm pulses. For the *B*-state experiment, the second OPA was tuned to yield 90 µJ of laser light centered at 555 nm. Reflective ND filters were used to attenuate the visible pump pulses for both the *A*- and *B*-state experiments to ~4 µJ. A remote-controlled shutter was inserted into the beam path to automate the acquisition of probe-only reference data when performing long-running, repetitive delay scans.

Using a 1 : 2 telescope, the beam size of the mid-IR beam was expanded to ensure that the focus size of the (ionizing) mid-IR beam was smaller than that of the visible (pump) beam. The two beams were collinearly overlapped with a dichroic mirror and the combined beams were then focused with a 250 mm focusing lens into the center of a velocity map imaging spectrometer (VMI). The telescope was adjusted to compensate for the difference in divergence of the two beams to overlap the focal spots along the propagation axis. The polarization axes of both beams were adjusted such that they were parallel to each other and parallel to the detector plane to ensure that the recorded images be Abel-invertible.

To prepare a molecular beam, solid I_2 was kept inside a pulsed, heatable Even–Lavie valve. A mixture of I_2 in helium was expanded into vacuum by heating the valve to 45 °C and operating it with 10 bar of helium pressure at a repetition rate of 250 Hz. After a 1 mm skimmer, 20 cm downstream from the valve's nozzle, the molecular beam entered the VMI chamber, where it was crossed with the two laser beams. The charged particles created in the strong-field ionization were projected onto a chevron-paired micro-channel-plate/phosphor-screen assembly (MCP/PH), illumination of which is recorded with a charge-coupled device (CCD) camera. Square-shaped gate pulses were applied to the MCP to select specific iodine-ion charge states for the photoion spectroscopy, and to suppress background electrons when recording photoelectron data.

Typically, a photoion image is accumulated over 2.5×10^3 laser shots, a typical photoelectron image over 1×10^4 laser shots. The VMI images were treated as described in Appendix A, including application of the usual maximum-entropy Abel inversion routine,[10] and extraction of the radial intensity and angular distributions.

The spectrometer was calibrated with a series of ATI peaks recorded in I_2, assuming a spacing of $\hbar\omega = 0.95$ eV. The peak intensity of the 1.3 µm pulse was gauged by estimating the $2\,U_p$ cutoff in the angle-integrated photoelectron spectrum of I_2 (see Section 3.4.1 for the significance of the $2\,U_p$ cutoff). As this cutoff is not sharply defined in the experimental spectrum, but rather appears as a soft knee, we make use of the well-known fact that the power laws with which the photoelectron yield scales before and after that cutoff are distinctly different.[11] Fitting linear functions to the logarithm of the radial intensity distribution in an energy region clearly below and one clearly above the $2\,U_p$ cutoff, an estimate for $2\,U_p$ is obtained as the intersection point between these two lines, which is shown in Fig. 3.2. Applying this procedure to the data presented in this chapter, we always obtain a value of 5.2 eV for $1\,U_p$, which corresponds to a peak intensity of 3.0×10^{13} W/cm^2.

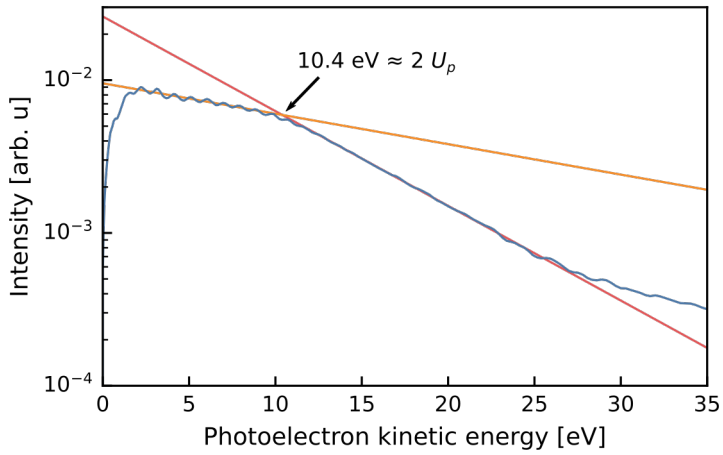

Figure 3.2 Estimation of the experimental laser peak intensity. The $2\,U_p$ cutoff is obtained from the intersection of straight lines fitted to the logarithm of the angle-integrated photoelectron spectrum as explained in the main text. The spectrum shown was obtained from strong-field ionization of ground-state I_2 molecules with the 1.3 µm laser pulse.

3.3 Coulomb-explosion imaging of nuclear wave packets

3.3.1 Static I^+ photoion spectroscopy

When the gas mixture in the molecular beam is irradiated with the 1.3 µm pulse, only $I_2{}^+$ and I^{n+} fragments are observed in the time-of-flight (TOF) spectrum because the ionization potential of helium (25.59 eV) is almost three times as large as that of I_2 (9.31 eV). The pulse energy was attenuated such that the TOF spectrum is dominated by the parent ion and I^+ because, eventually, we want to rationalize the photoelectron spectra in terms of the laser-assisted electron recollisions with the *singly*-charged molecular ion, and a high abundance of higher charge states indicates that more than one electron was removed from the molecule by direct photoionization during the duration of the laser pulse. (Although, to some extent, higher charge states can also be created through impact ionization by the recolliding photoelectrons. Under the present experimental conditions, however, the recollision energies are rather low (<20 eV), which is why we assume that impact ionization does not make a strong contribution.)

In the next step, I^+ fragments were selected for monitoring the molecular dynamics induced by the visible-light pump pulses with the VMI. As a starting point, we first have a look at the static photoion spectra: A typical, static I^+ photoion spectrum for the strong-field ionization with the 1.3 µm pulse is displayed in Fig. 3.3. Overall, the spectrum is composed of four, partially resolved features that are labeled according to their proposed dissociation channels in Fig. 3.3a and b, and which we are going to discuss from highest to lowest fragment kinetic energy. The assignment of the Coulomb channels $I^{n+} + I^{m+}$ with $m, n > 0$ is based on a comparison to the Coulomb repulsion energy of two point charges of charge m and n at the I_2 equilibrium internuclear distance of 2.666 Å, which amounts to $E_C = \frac{1}{2} m\, n\, 5.4$ eV. Here, the factor $\frac{1}{2}$ arises from the fact that, because I_2 is a homonuclear diatomic, every iodine fragment carries exactly *half* the total kinetic energy released.

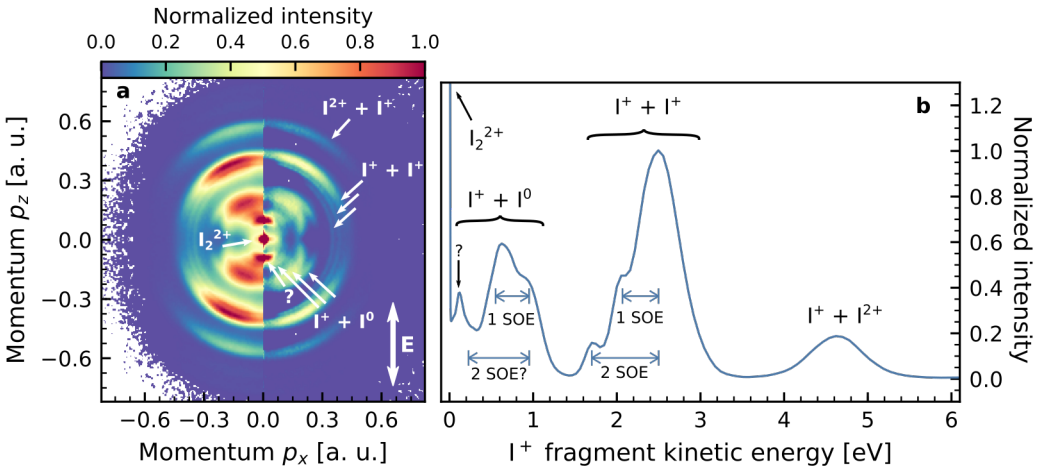

Figure 3.3 Static photoion spectroscopy of I^+ fragments upon irradiation of I_2 with the 1.3 µm pulse only **a)** Projected detector momentum distribution (left half) and slice through the Abel-inverted, three-dimensional ion momentum distribution (right half). **b)** Angle-integrated photoion spectrum with the proposed assignment of its features. The substructure in the peaks is explained by the possibility that one or both of the iodine fragments ends up in a spin-orbit excited state (1 SOE and 2 SOE).

Therefore, the peak at ~4.6 eV can be identified with the $I^+ + I^{2+}$ Coulomb channel, as its fragment energy corresponds to 85 % of the pure Coulomb repulsion energy. The band labeled $I^+ + I^+$ in Fig. 3.3b is actually composed of a large main component at 2.4 eV, which agrees closely to the Coulomb repulsion energy of 2.7 eV and two smaller shoulders at 2.0 and 1.7 eV. We explain this finding by the fact that either one or both of the dissociating I^+ fragments ends up in a spin-orbit excited state (labeled 1 SOE and 2 SOE in Fig. 3.3b, respectively). The energy difference between the ground state of I^+ ($^3P_2$) and the two closely spaced, spin-orbit excited states, $^3P_0$ and $^3P_1$, amounts to 0.799 and 0.878 eV, respectively. Hence, spin-orbit excitation should give rise to an energy loss of ~0.4 eV in the fragment kinetic energy, which agrees very well with our observation.

The substructure of the band that stretches from 0.1 to 1.0 eV must be made up of contributions from the dissociation of I_2^+ molecules. Two rings that are peaked under an angle of ≈40° with respect to the laser polarization axis can be identified in Fig. 3.3a. From Fig. 3.3b, one can see that these features occur at 0.9 and 0.6 eV, respectively. The 0.3 eV spacing between the two *may* indicate that a spin-orbit excitation is involved again, which is supported by the fact that the spin-orbit splitting in the neutral iodine atom (0.94 eV) is comparable to that in the atomic ion. A feature that relates to the 2 SOE channel can *barely* be identified in the Abel-inverted momentum distribution (Fig. 3.3a) and is therefore only tentatively indicated in the photoion spectrum (Fig. 3.3b). Instead, where this channel would be expected to appear, a strong contribution from a channel whose photoion angular distribution is distinctly different, namely peaked along the laser polarization axis, is present in the spectrum. This channel is marked as ? in both panels of Fig. 3.3a, as we were unfortunately not able to assign it.

The most likely origin of the very intense, zero-kinetic energy feature is the formation of stable I_2^{2+} ions, which clearly have no kinetic energy (at least not in the plane of the detector)

and can, therefore, not be distinguished from I^+ ions with the VMI, as the mass-over-charge ratios of these two species are identical.

3.3.2 Photodissociation dynamics (*A* state)

In a delay scan between the 710 nm and the 1.3 µm pulses, I^+ ion VMI images were recorded in time steps of $\Delta t = 45$ fs over the range from −1 to 10 ps. After inversion and extraction of the radial intensity distribution, the mid-IR-only spectrum of Fig. 3.3b was subtracted to emphasize the new contributions that originate from the fragmentation of the excited species, resulting in the two-dimensional map displayed in Fig. 3.4a. In it, the most prominent feature is the curve labeled $X \longrightarrow A$ that appears at time zero with a kinetic energy of 2.5 eV and then quickly drops in kinetic energy with increasing pump–probe delay, converging ever closer to the low-kinetic energy feature at roughly 0.1 eV that is also assigned to the $X \longrightarrow A$ transitions. These two features only differ in the final state that the dissociating wave packet is projected onto, leading to Coulomb explosion in the former and dissociative ionization (or simple atomic ionization at large internuclear separations) in the latter. Asymptotically, the Coulomb-repulsion energy will become so small that the fragment kinetic energies for both states converge to the asymptotic kinetic energy of the *A*-state photodissociation.

Two similar pairs of converging curves are observed with asymptotic kinetic energies of 0.6 and 1.0 eV. For a single-photon transition at 710 nm there are, however, no states that could lead to these dissociation energies. Instead, we propose that two-photon transitions are involved. By energy conservation, the excess energy between two photons of 710 nm (1.75 eV) and the $I_{3/2} + I_{3/2}$ dissociation limit is 1.95 eV, and between two photons and the $I_{1/2} + I_{3/2}$ dissociation limit it is 1.01 eV. Recalling that the measured fragment energy is exactly half the total kinetic energy release, the agreement between this estimation and the observed asymptotic energies is striking. Still, we refrain from making a definitive assignment of the involved states because there are many, closely spaced excited states of I_2 in this region.[8]

At negative pump–probe delays, where the roles of the pump and probe pulses are reversed, the picture changes completely. We follow here the interpretation of Fang & Gibson[12] who have reported their findings for a very similar experiment in I_2. Through strong-field ionization of the mid-IR pulse, vibrational wave packets are prepared in the two lowest ion states of $I_2{}^+$, $X_{3/2}$ and $X_{1/2}$, which are bound and whose equilibrium internuclear distances are slightly *shorter* than that of the neutral ground state. The fast oscillations of these vibrational wave packets are then probed by the 710 nm pulse that projects them onto dissociative states. As the transition probability in the latter step depends on the internuclear separation, an intensity modulation is observed that oscillates with the period of the wave packets.

To quantify the Coulomb-explosion dynamics of the $X \longrightarrow A$ transition, a Gaussian function was fitted to the associated spectral feature at each time delay. To make this procedure more robust, the first fit is carried out at $t = +10$ ps, and then the delay points are treated in reverse order, updating the guess for the central energy after every successful fit.

To predict the fragment kinetic energy as a function of time, we make two simple assumptions: First, the dissociating wave packet is launched on the *A* state at time zero at the equilibrium internuclear distance, $R_{eq} = 2.666$ Å, and is then moving at a constant velocity that is identical to the asymptotic velocity v_0. We justify this assumption by the fact that, on the timescale on which the dissociation is observed, the acceleration of the nuclear wave

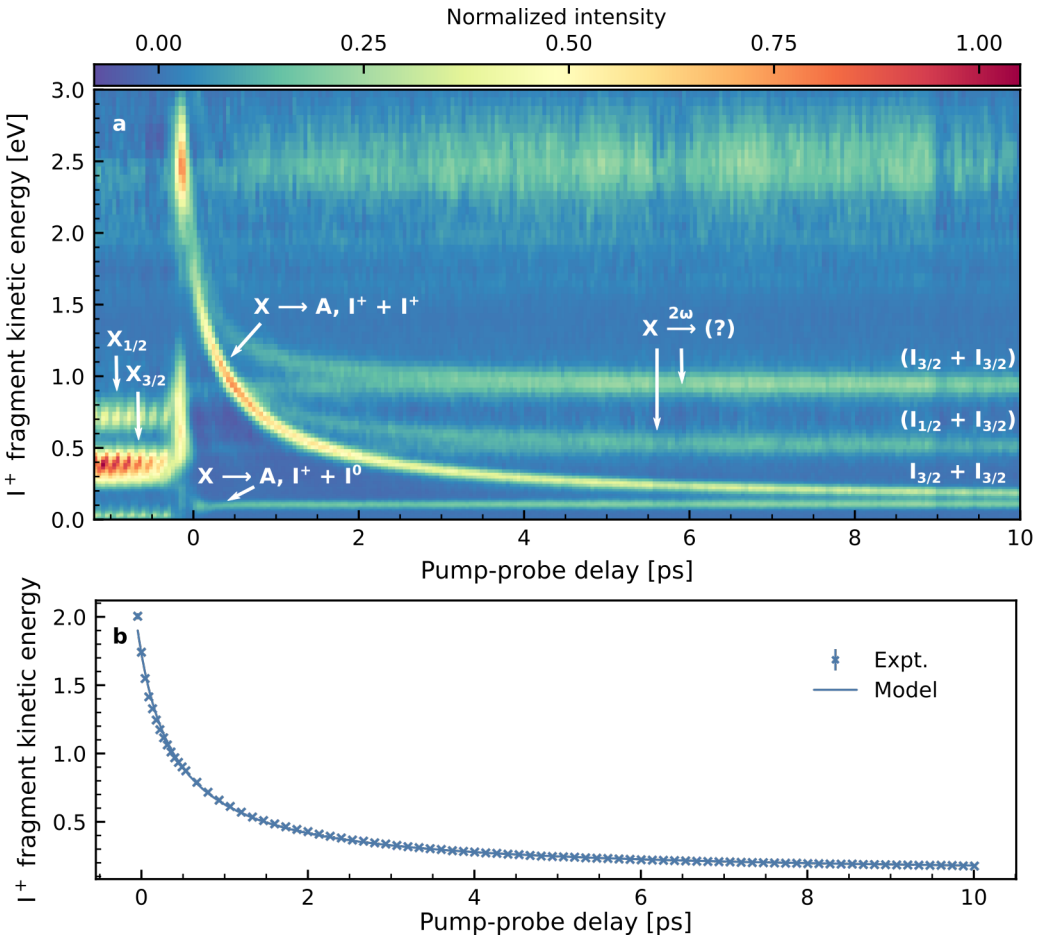

Figure 3.4 Coulomb-explosion imaging of the photodissociation dynamics of I_2 induced by 710 nm excitation. **a)** Time-dependent evolution of the 1.3 µm-only-subtracted I^+ fragment kinetic-energy spectrum. For the $X \longrightarrow A$ transition, both the $I^+ + I^+$ Coulomb channel and the dissociative photoionization channel are observed that converge to the same asymptotic kinetic energy. Also, two weaker contributions from dissociative states are observed, that must have been populated through two-photon absorption. At negative pump–probe delays, the mid-IR pulse *precedes* the visible pulse, so that a vibrational wave packet is formed in each of the two lowest states of $I_2{}^+$, which is then probed by the 710 nm pulse. The broad, noisy feature around 2.5 eV of kinetic energy stems from incomplete subtraction of the mid-IR-only signal. **b)** Comparison between the extracted fragment kinetic energies for the $X \longrightarrow A$ Coulomb channel of **a** and the kinetic energies predicted by the simple model of Eq. (3.2). For clarity, only every third data point is shown for delays >0.5 ps.

packet is fast. Second, the potential energy curve of the Coulomb state that leads to the dissociation into the $I^{m+} + I^{n+}$ fragments can be described by a *shielded* Coulomb potential of the form (cast into convenient units)

$$E_C^{(m,n)}(R) = a_{m,n}\, m\, n \frac{14.4\,\text{eV}\,\text{Å}}{R}\,, \tag{3.1}$$

where R is the internuclear distance and $a_{m,n}$ is a phenomenological shielding constant that is adjusted as a free parameter in a least-squares fitting procedure. Introducing the shielding constant seems to be problematic because asymptotically, $E_C^{(m,n)}(R)$ does not converge to

an unshielded Coulomb potential. We note, however, that the Coulomb energy scales with $1/R$, so that the *absolute* error that is introduced through the shielding constant quickly vanishes. If we, third, assume that the projection from the excited neutral state to the final ionic state occurs instantaneously and that no other, intermediate states are involved, the total kinetic energy can be written as the sum of two terms: the asymptotic kinetic energy of the dissociation, $E_0 = \frac{1}{2} m_{red}\, v_0^2$ (where m_{red} is the reduced mass of the system, which, for a homonuclear diatomic is just half the atom mass), and the Coulomb repulsion energy at the internuclear distance $R = v_0\, t + R_{eq}$,

$$E_{KER}(t) = E_C^{(m,n)}(R = v_0\, t + R_{eq}) + E_0\,. \tag{3.2}$$

Again, keeping in mind that the fragment energy is just $E_{frag} = \frac{1}{2} E_{KER}$, the model function of Eq. (3.2) can be fitted to the time-dependent peak positions, extracted from the data of Fig. 3.4 a, by adjusting only two free parameters, v_0 and $a_{1,1}$. Carrying out this fit results in excellent agreement between the model and the experimental data, as is shown in Fig. 3.4b. In fact, even with our simplistic assumptions, the relative error between the model and the data is never larger than ±2 %. For the shielding constant we obtain a value of $a_{1,1} = 0.86$, which is in very good agreement with the value of 0.80 that Gibson, Coffee & Fang[13] have obtained for modeling their photofragmentation experiments in I_2. The retrieved optimum asymptotic velocity is $v_0 = 8.0\,\text{Å}\,\text{ps}^{-1}$, which is close to the results from a quantum-mechanical wave-packet propagation along the A state potential energy curve carried out by Ritze,[14] who finds a terminal velocity of $8.2\,\text{Å}\,\text{ps}^{-1}$. This implies that already within 1 ps the iodine bond length stretches by a factor of 4, whereas a bond is typically considered broken when the bond length is doubled. Therefore, the interesting dynamics in the LIED are expected to occur within a few hundred femtoseconds of pump–probe delay.

3.3.3 Vibrational wave-packet dynamics (*B* state)

To populate the B state, the I_2 molecules were pumped with a 555 nm pulse and, again, photoionized with the 1.3 µm pulse. The data processing was carried out as described in the previous section on the photodissociation experiment, except that for the time-dependent kinetic-energy spectrum presented in Fig. 3.5a, images were taken in delay steps of $\Delta t = 30$ fs over the range from $t = -0.6$ ps up to +19 ps. For positive pump–probe delays, two fundamentally different dynamics are observed: On one hand, as in the previous experiment, photodissociation manifests as a pair of curves – one of which corresponds to the $I^+ + I^+$ Coulomb explosion channel and one to dissociative photoionization – that converge to a common limit at ~0.45 eV. These two curves can unambiguously be assigned to the $X \rightarrow B''$ transition that was already characterized by Tellinghuisen.[9] Based on the vertical excitation energy of 2.49 eV into that state and the energy of the $I_{3/2} + I_{3/2}$ dissociation limit, 1.556 eV, an asymptotic fragment kinetic energy of 0.47 eV is predicted, which corroborates our assignment. Still, it seems surprising that an excitation at 2.49 eV is possible when the employed laser wavelength corresponds to a photon energy of only 2.24 eV. We note however that the transition at 2.49 eV is covered by the laser bandwidth $\Delta = 60$ m eV, so that we expect the excitation to occur predominantly in the blue part of the laser spectrum.

On the other hand, what is dominating the time-dependent kinetic-energy spectrum are three features with rapidly oscillating fragment kinetic energies, centered at 0.5, 2.0 and

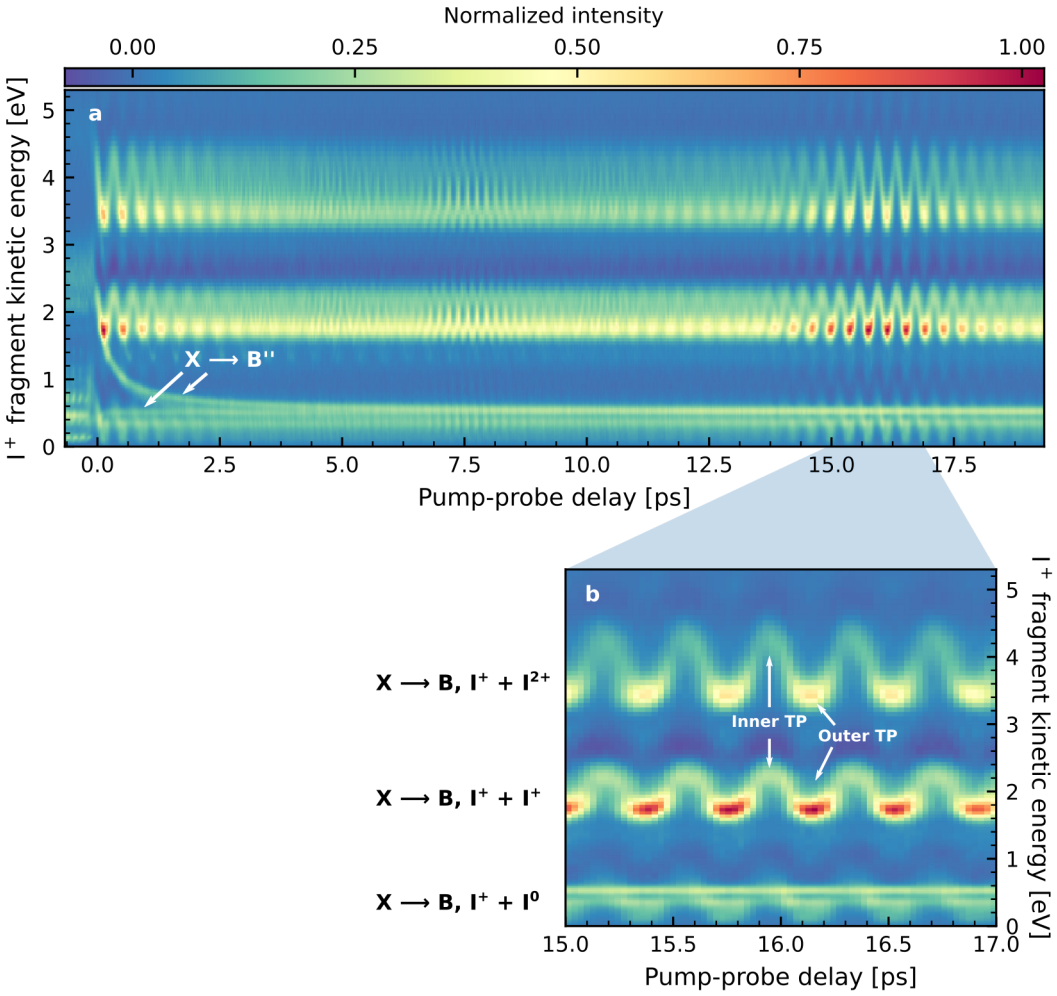

Figure 3.5 Coulomb-explosion imaging of the vibrational wave packet prepared in the B state of I_2 induced by 555 nm excitation. **a)** Time-dependent I^+ kinetic-energy spectrum. At each time delay, the static spectrum of Fig. 3.3b was subtracted. At negative time delays, vibrational dynamics of the ground and spin-orbit excited states of $I_2{}^+$ are observed, similar to what was observed in Fig. 3.3a. **b)** Zoom into the region of the half wave-packet revival, where the wave packet passes through the inner and outer turning points (TPs) can be clearly identified.

3.8 eV, which correspond to the dissociation channels $I^+ + I^0$,$I^+ + I^+$, and $I^+ + I^{2+}$, respectively. All three features are related to the vibrational wave packet prepared in the B state. The wave packet's oscillations can be clearly distinguished from time overlap of the two pulses up to a pump–probe delay of ~3.0 ps, where the wave packet dephases. At certain delays it rephases, which is most prominently seen at the half revival (t = ~16 ps), and less so at the quarter revival (t = ~8 ps).

In Fig. 3.5b, the region at the half revival is enlarged to emphasize the precise wave-packet motion. Here, the inner and outer turning points can clearly be identified. From the kinetic energies at the inner turning points[b] the associated Coulomb and dissociative-photoionization

b Note that the inner turning point is that of *highest* kinetic energy because, again, the Coulomb repulsion scales with $1/R$.

channels can be easily assigned by comparing them to the corresponding channels in the static spectrum of Fig. 3.3b. We note that, in the two Coulomb channels, the signal intensity is significantly increased at the outer turning point compared to the inner one. This finding is probably related to the phenomenon termed "enhanced ionization", which has been observed in several strong-field ionization experiments in I_2 before.[15,16,17]

To predict the evolution of the vibrational wave packet, we need to resort to a more elaborate description of the dynamics compared to our simple model from the previous section. Formally, a vibrational wave packet is defined as the coherent superposition of the vibrational states, $|\nu_e\rangle$, of some electronic state e of the molecule, with vibrational quantum number ν and an associated eigenenergy ϵ_ν. In the present experiment, this wave packet is prepared by an electric dipole transition from the electronic ground state into the B state. Therefore, the time-dependent, field-free evolution of the nuclear wave function $|\chi\rangle$ – after the passing of the laser pulse – can be written as

$$|\chi(t)\rangle = \sum_\nu c_\nu \mathrm{e}^{-\frac{\mathrm{i}}{\hbar}\epsilon_\nu t} |\nu_B\rangle \ , \tag{3.3}$$

where the (real-valued) factors c_ν contain the relative amplitudes of the populated vibrational states. For simplicity, we make use of the Franck–Condon principle to calculate these factors. This implies that the transition probability between a vibrational level of the ground state, $|\nu_0'\rangle$, and the final state, $|\nu_B\rangle$, is given by the overlap integral $\langle\nu_0'|\nu_B\rangle$. Then, the factors c_ν are simply obtained from the product of the Franck–Condon factors and the relative electric field strength of the laser pulse E (in the frequency domain) as

$$c_\nu = \langle\nu_0'|\nu_B\rangle \, \frac{E(\epsilon_\nu/\hbar)}{E_0} \, , \tag{3.4}$$

where E_0 is the peak electric field strength.

To calculate the required quantities of Eq. (3.3), we have used the FORTRAN code of Fischer *et al.*[18] In it, the electronic states are read in on an equidistant grid and Cooley's method[19] is used to iteratively calculate the vibrational eigenvalues and eigenfunctions. To this end, potential energy curves were obtained from the semiclassical Rydberg–Klein–Rees (RKR) procedure, a method that is used to calculate the classical inner and outer turning point of every vibrational level from experimentally determined vibrational and rotational transition energies. The calculations were carried out with the RKR1 program written by Le Roy,[20] which was supplied with high-quality spectroscopic constants for the X and B states of I_2 reported by Gerstenkorn & Luc.[21] The potential energy curves were evaluated on an equidistant grid of 1000 points between 2 and 7 Å.

For the excitation, the electric field envelope was taken to be of Gaussian shape with a flat phase, centered at 2.23 eV with a spectral bandwidth of 60 meV (FWHM), which corresponds to the minimum bandwidth to support a Gaussian 30 fs pulse. From the results of the calculation, the vibrational wave packet is evaluated according to Eq. (3.3). To compare its evolution to the experiment, first the expectation values of the internuclear distance $\langle R\rangle(t) = \langle\chi(t)|R|\chi(t)\rangle$ and of the momentum $\langle p\rangle(t) = \langle\chi(t)|-\mathrm{i}\hbar\frac{\mathrm{d}}{\mathrm{d}R}|\chi(t)\rangle$ are calculated. Making, again, use of the shielded Coulomb potential of Eq. (3.1), the theoretical kinetic energy release is given by

$$E_{KER}(t) = E_C^{(m,n)}(\langle R\rangle(t)) + \frac{\langle p\rangle^2(t)}{2m_{red}} \, . \tag{3.5}$$

From the time-resolved kinetic-energy spectrum the precise time-dependence of the fragment kinetic energies was extracted by fitting a Gaussian function to each of the two Coulomb channels at each time delay. In Fig. 3.6a, we compare the results of this fitting for the $I^+ + I^+$ channel to the predicted time-dependent behavior according to Eq. (3.5). We find that, while the oscillation period is correctly reproduced, the envelope of the full revival is – in the simulation – significantly shifted by 1 ps to longer time delays. In general, the oscillation period and the revival time are closely related to each other, as they are determined by the first and second derivative of ϵ_ν with respect to ν. Therefore, it seems implausible that the period can match when the revival time does not, especially when spectroscopic data are used as a reference that were determined with great precision. Instead, the assumptions that we made about the excitation step must have been incorrect. In particular, we have assumed that the spectral phase of the excitation pulse was flat. Practically, in the OPA process, a significant, positive group delay dispersion (GDD), which is defined as the second derivative of the spectral phase, $D_2 = \frac{\mathrm{d}^2\phi}{\mathrm{d}\omega^2}$, may have been introduced. In fact, we have not attempted to recompress the pulses after the OPA stage. To account for the GDD, we have multiplied the electric field envelope in the frequency domain with a phase term $\exp\{-\mathrm{i}\,\phi(\omega)\}$, where the phase ϕ is given by $\phi(\omega) = D_2(\omega - \omega_0)^2$, with the central frequency ω_0. By adjusting D_2 as a free parameter we can obtain a convincing agreement between theory and experiment for a value of $D_2 = 700\,\mathrm{fs}^2$, both for the $I^+ + I^+$ and the $I^+ + I^{2+}$ channels, which is demonstrated in Fig. 3.6b and c, respectively. With this much of chirp the minimum pulse duration increases from 30 fs to roughly 60 fs.

3.4 Photoelectron spectroscopy

3.4.1 Extraction of the rescattered electrons

All photoelectron spectra were recorded under the same experimental conditions as for the photoion spectra presented in the previous section, having reversed the electrode voltages of the VMI. To capture the weak rescattering signal with sufficient statistics, photoelectron detector images were accumulated over at least 1×10^4 laser shots. In Fig. 3.7a, a representative 1.3 µm-only VMI detector image is displayed on a logarithmic intensity scale. Based on our estimation of the ponderomotive potential (see Section 3.2), the angle-resolved spectrum can generally be divided into three kinetic-energy regions, which are indicated by the dashed circles in Fig. 3.7a: In a purely classical picture of above-threshold ionization (ATI), $2\,U_p$ represents the hard limit for the maximum kinetic energy that *direct* photoelectrons can acquire. When ATI is treated at a quantum-mechanical level, e. g., by solving the time-dependent Schrödinger equation for the photoelectron in the laser field, one finds that this hard limit is slightly softened due to the wave nature of the solution and the fact that electrons are allowed to have a finite initial momentum at the time of birth. As the intensity of the rescattered electrons is roughly two orders of magnitude weaker than that of the direct electrons, this soft cutoff seems to extend well beyond $2U_p$, which can be seen from Fig. 3.7a. Here, we arbitrarily define a limit of $4U_p$ to make sure that all electrons faster than that have undergone a recollision with the parent ion, being deflected under large angles.

In the quantitative rescattering (QRS) approximation, the electron recollision is rationalized by a classical model. Here, we follow the explications of Spanner *et al.*,[22] using atomic units

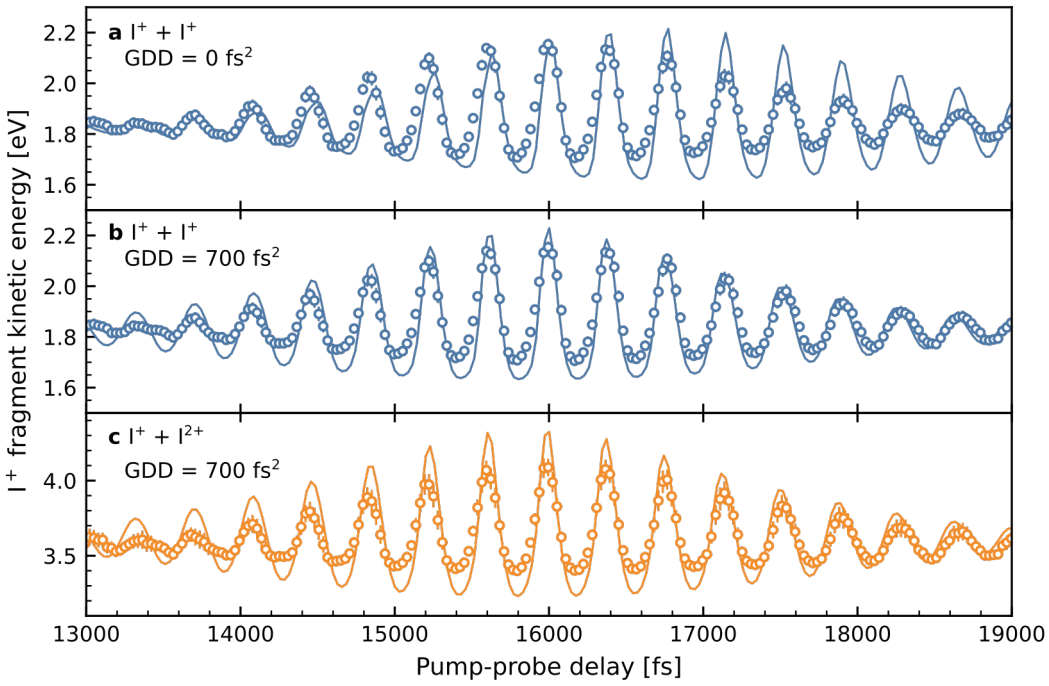

Figure 3.6 Comparison between the fragment kinetic energies of the two Coulomb explosion channels, extracted from the data of Fig. 3.5b and the simulated kinetic energy, according to Eq. (3.5), evaluated by a wave-packet simulation for 555 nm excitation of I_2 into the B state. **a)** $I^+ + I^+$ channel, assuming a flat phase of the 555 nm pulse. **b)** Same as **a**, including a GDD of 700 fs^2. **c)** Same as **b** for the $I^+ + I^{2+}$ channel.

throughout. In the presence of a linearly polarized electric field $E(t) = E_0 \cos(\omega t)$ that is oscillating with frequency ω and where E_0 is the peak electric field strength, photoelectrons can in principle be born at any time t through tunnel ionization (with *some* probability), which we refer to as the time of birth, t_0. A unique electron trajectory for the propagation in the laser field is associated with every t_0. The electron velocity at any time is given by $v(t) = v_0(\sin \omega t_0 - \sin \omega t)$, where v_0 is the velocity connected to the peak vector potential $A_0 = v_0 = E_0/\omega$. To know with what velocity the electron recollides, the relation between the returning time t_r and the time of birth t_0 has to be considered. This means that the equation $x(t_r) = 0$ has to be solved, which leads to

$$\omega(t_r - t_0) \sin \omega t_0 + (\cos \omega t_r - \cos \omega t_0) = 0\,, \tag{3.6}$$

Solving Eq. (3.6) for every t_r yields the time of birth as a function of the returning time, $t_0(t_r)$, from which the recollision velocity $v_r(t_r)$ is calculated. What is measured with the VMI, however, is the *absolute* velocity and after the recollision the photoelectron gains additional momentum parallel to the electric field, equal to the instantaneous vector potential at the returning time, $A_r = -\frac{E_0}{\omega} \sin \omega t_r$. Therefore, elastically scattered electrons with recollision momentum p_i are found in the experimental momentum map on a circle that is shifted away from the origin by the instantaneous vector potential A_r. This is illustrated in Fig. 3.7a for the maximum recollision energy ($\sim 3.2U_p$), the circle of which is shifted by $\sqrt{2 \cdot 2U_p}$. According to

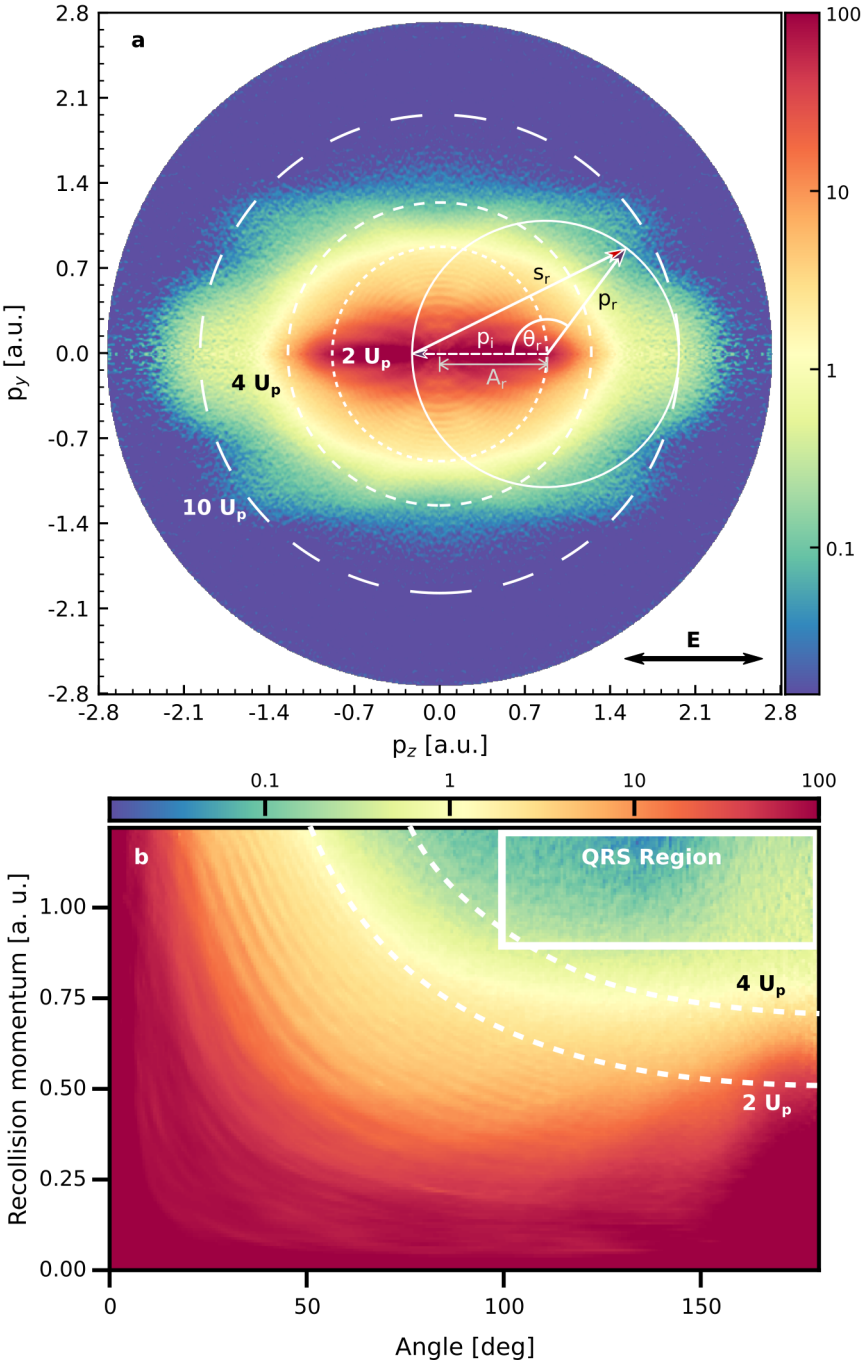

Figure 3.7 Static photoelectron spectrum from the strong-field ionization of I_2 by a 1.3 µm pulse with a peak intensity of 3.0×10^{13} W/cm^2 **a)** Slice through the Abel-inverted, three-dimensional momentum distribution, shown on a logarithmic intensity scale. The dashed circles indicate absolute electron kinetic energies of 2, 4, and 10 U_p. The solid circle represents electrons that have elastically scattered with incoming momentum p_i into the scattering angle θ_r. This circle is shifted by the instantaneous vector potential at the time of recollision, A_r. Note that the image is created from a single, Abel-inverted quadrant through horizontal and vertical mirroring. **b)** Extracted intensity distribution of the rescattered electrons according to Eq. (3.7), as a function of recollision momentum, p_r, and scattering angle θ_r.

the classical recollision model, a maximum kinetic energy, corresponding to $10U_p$, is reached for a scattering angle θ_r of 180°.

Furthermore, we have included a first-order correction to the simple recollision model: Implicit to Eq. (3.6) is the assumption that the position of birth of the electron is zero. To account for a finite birth position, the recollision energy $v_r(t_r)^2/2$ is replaced by the expression $v_r(t_r)^2/-\mathrm{IP}\ \mathrm{d}t_0/\mathrm{d}t_r$,[23] where IP is the ionization potential of the molecule. Consequently, the x and z components of the final (detector) electron momentum (where we take the direction of the electric field to be parallel to the z direction) are given by[22]

$$(v_z - v_0 \sin \omega t_r)^2 + v_x^2 = v_0^2(\sin \omega t_0 - \sin \omega t_r)^2 - 2\,\mathrm{IP}\,\frac{\mathrm{d}t_0}{\mathrm{d}t_r}\,. \tag{3.7}$$

Determining v_x and v_z according to Eq. (3.7) for all $t_0(t_r)$ then yields the mapping between the (detector) photoelectron momentum distribution and the angular distributions of the rescattered electrons as a function of the (corrected) recollision energy.

To extract the differential cross sections (DCSs) of the rescattered electrons, we have calculated $t_0(t_r)$ for 1.3 µm radiation assuming an intensity of $3 \times 10^{13}\,\mathrm{W/cm^2}$ ($U_p = 5.2\,\mathrm{eV}$). The mapping between the recollision momentum and the detector momentum was evaluated from Eq. (3.7), using the IP=9.3 eV for I_2. We find that, under these conditions, the maximum recollision energy is $3.77\,U_p$ (19.6 eV), which shifts the energy cutoff of the photoelectron spectrum to $\sim 10.5\,U_p$. So, while the extension of the cutoff seems very large in the recollision momentum, the maximum photoelectron kinetic energy is only slightly increased and this increase seems to be well supported by the data shown in Fig. 3.7a, in which the photoelectron spectrum extends well beyond the $10U_p$ cutoff. The result of the coordinate transformation from the detector momentum to the recollision momentum is shown in Fig. 3.7b for a single quadrant of the whole image. In the same figure, we also indicate what we will consider the region where the QRS is most appropriate because there is essentially no overlap with the $4U_p$ line, and which we will restrict the discussion to when we extract the differential cross sections from the experiment.

3.4.2 Time-resolved photoelectron spectra

For measuring the time-resolved photoelectron spectra, a small set of pump–probe delays was selected at either excitation wavelength, based on the results from the photoion experiments presented in Section 3.3. For the photodissociation, nine delays between 100 and 700 fs were chosen. Smaller time delays were neglected because at those the two pulses still overlap significantly with each other. The vibrational wave packet, on the other hand, was monitored at ten time delays, distributed over $\sim$ 1.5 oscillation periods in the very center of the half-revival envelope. We note that, in principle, similar dynamics could be observed close to time zero, but here the dissociation of the B'' state might interfere.

In either experiment, the set of delays was scanned in 30 to 50 cycles. A single cycle is made up of one forward and one backward scan, acquiring images over 1×10^4 laser shots at each delay. At the beginning of each cycle, the remote-controlled shutter was closed to obtain a probe-only reference image, which is used to monitor long-term drifts in the laser power or molecular-beam quality.

To assess, whether the molecular dynamics lead to a modulation of the total signal intensity, and to what extent this modulation is different for the rescattered electrons, we used the

following approach: Every image was divided into two regions, one for electrons with kinetic energies lower than $4U_p$ and one for electrons with energies between 4 and $10\,U_p$. Every region was integrated over all angles and energies to obtain its total intensity. Now, within every cycle, the intensities of the images for which both pulses were present were normalized to those of the respective reference images where only the probe pulse was present. We describe the resulting distributions of the relative yields thus obtained by their median and their interquartile range, all of which is displayed in Fig. 3.8 for the *A*-state (photodissociation) experiment.

In general, we observe a clear signature of the excited-state dynamics in these two relative-yield observables. For the photodissociation experiment, looking at the direct electrons (blue squares in Fig. 3.8a), we find that the relative yield is increased by roughly 35 % at the first delay point. This excess quickly decreases with increasing pump–probe delay and the difference with respect to the probe-only signal becomes insignificant around $t = 400$ fs, which is consistent with the result that the I_2 bond length is doubled within ~330 fs. In panels b through g of Fig. 3.8, normalized differences between the raw VMI data at data points that are indicated by the Roman numerals in panel a are displayed, where a label $\mathbf{A} - \mathbf{B}$ suggests a normalized difference of the form $(\mathbf{A} - \mathbf{B})/(\mathbf{A} + \mathbf{B})$. In particular, in the first five normalized-difference images, the time evolution of the excited state is traced by always forming the normalized difference with respect to the probe-only data (i. e., $[\mathbf{A} - \mathbf{0}]/[\mathbf{A} + \mathbf{0}]$). Two remarkable observations can be made: in the first two panels, b and c, the probe-only signal is clearly imprinted in the normalized difference of the direct electrons ($< 4U_p$) as a negative contribution that is narrowly peaked along the laser polarization axis, which, in turn, means that the photoelectron spectrum of the excited-state species must be concentrated more perpendicular to the polarization axis. Then, going from panel d to e, the situation changes qualitatively, in that the imprint of the probe-only signal is split into to two negative bands that are aligned parallel to the laser polarization axis, having an offset with respect to this axis of $p_x \simeq \pm 0.15$ a. u.. We conclude from this observation that the photoelectron spectrum of the excited-state species becomes increasingly peaked *along* the laser polarization axis. In the last panel, g, the normalized difference is formed between the first and last data point of the pump–probe scan, which emphasizes the change in the preferential photoionization direction from perpendicular to parallel even more.

When looking at the rescattered electrons ($> 4U_p$), again going from panel b to f, it appears that there is at first a strong depression at ≈2 a. u. along the laser polarization axis, which later, in panels e and f, corresponding to the completely dissociated iodine molecule, actually turns into a positive contribution. Again, this trend is most obvious from panel g, where the difference between the first and the last data point reveals a strong modulation in the backscattering region

Turning to the *B*-state experiment, we find that the relative-yield measure in the vibrational wave packet (Fig. 3.9a) is at all sampled pump–probe delays enhanced by at least 20 %. Also, the yield reflects the vibrational motion, and reaches its peak at the *outer* turning point at $t = 15.8$ ps, as was already observed in the I^+ fragment signal (see Fig. 3.5b). What is surprising about these results is that the increase in yield of the rescattered electrons is – at all data points and in both experiments – larger than that of the direct electrons, even when the molecule is definitely dissociated. From this we conclude that the rescattering process must be more efficient in the excited state species as well as in the atomic iodine compared to

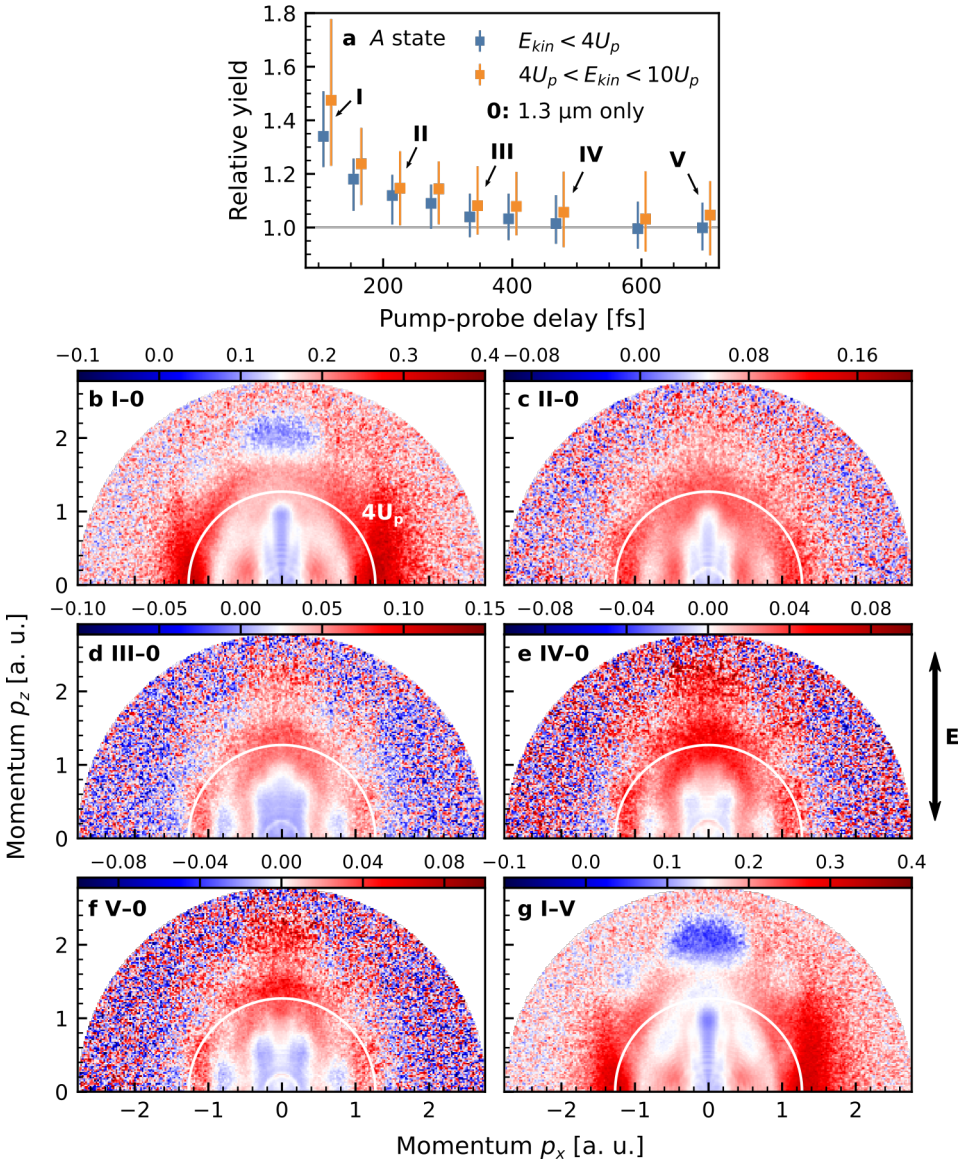

Figure 3.8 Time-resolved photoelectron spectra for the *A*-state (photodissociation) experiment. **a)** Time-dependence of the total intensity relative to that of the 1.3 µm-only measurement, divided approximately into the regions of direct electrons (blue) and rescattered electrons (orange). The error bars mark the interquartile ranges of the intensity distributions collected over all acquisition cycles. For clarity, the data-point pairs are horizontally offset with respect to each other. The Roman numerals mark individual data points, from which the normalized differences in **b–g** are formed, where **0** corresponds to the 1.3 µm-only data (represented by the horizontal gray line in **a**).

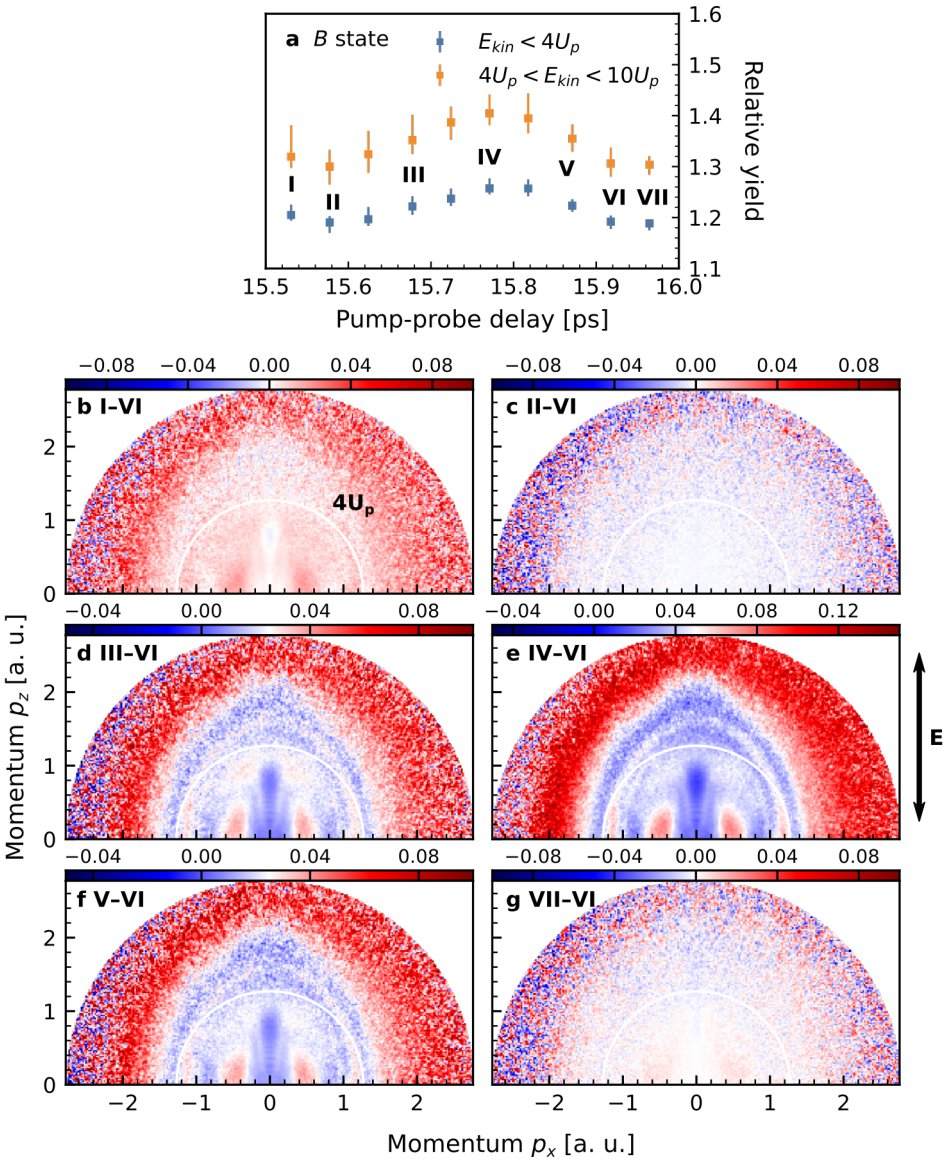

Figure 3.9 Same as Fig. 3.8, but for the *B*-state experiment.

the neutral ground-state molecule.

Again, we have formed the normalized differences for various data points as indicated by the Roman numerals in Fig. 3.9a, this time using point **VI** as the reference point, which corresponds to one of the inner turning points, i. e., differences of the form $(\mathbf{A} - \mathbf{VI})/(\mathbf{A} + \mathbf{VI})$. What makes us confident that the observed changes in the photoelectron spectra are actually related to the proposed wave-packet dynamics is that, when the differences between data taken at or close to two different inner turning points is formed, these differences vanish or become very small, as shown in panels b, c, and g. The greatest contrast is observed for the normalized difference between the inner and outer turning points, as in panel e. Looking at the direct electrons in panel e ($< 4U_p$), it appears that the photoelectron distribution is more perpendicular at the outer turning point than at the inner turning point. The rescattered electron ($> 4U_p$) show a

characteristic intensity modulation with increasing absolute photoelectron momentum. As the molecular bond is stretched, at first – that is, over the first Ångstrom, or so, of increasing bond length – there is a depletion in the backscattering region around ≈2 a. u., which is indicated by the results of Fig. 3.9e as well as that of Fig. 3.8b.[c] After that, when the bond is stretched further until the molecule is completely dissociated, a weak, but clearly distinguishable *overall increase* of the signal in that same region is found with respect to the ground-state molecules, which is what Fig. 3.8e and f suggest. This finding appears puzzling because – naively – one would expect that observables in the photoelectron spectrum develop monotonically along the dissociation coordinate in one direction or the other, growing stronger or weaker, but not that its behavior changes at some point during dissociation. As we will see below, this finding can be explained by considering the scattering dynamics that are directly related to the dissociation.

3.4.3 Computational model

Ultimately, the goal of the modeling efforts is to reproduce and rationalize the angular distributions of the backscattered electrons we have measured as well as the surprising trends in the normalized differences reported in Figs. 3.8 and 3.9. To this end, we devise a model that is composed of several components, based on the approximations and factorizations of the QRS theory. To elaborate on this, we consider first a molecule that is fixed in space. As usual, let the polarization vector of the electric field be aligned parallel to the Cartesian z axis, which we also choose to be the principal axis of a spherical coordinate system with polar angle θ and azimuthal angle ϕ. The orientation of the space-fixed molecule with respect to this axis is measured by the set of Euler angles, $\mathbf{R} = (\alpha, \beta, \gamma = 0)$,[d] where γ is always zero because I_2 is a linear molecule. Upon tunneling ionization, an electron wave packet is launched in the $-z$ direction, which returns after some time from that same direction. In principle, the momentum distribution of the returning wave packet, $W(p_r, \mathbf{R})$ could depend on p_r and $\mathbf{R}$. In the QRS approximation, however, we assume that the imprint of the molecular orbital is washed out during propagation, and therefore that the returning wave packet can be factored into two independent contributions,

$$W(p_r, \mathbf{R}) = w(p_r)\, P_{\text{ion}}(\mathbf{R})\,, \tag{3.8}$$

which means that the returning electron wave packet can be written as the product of a momentum distribution that is independent of $\mathbf{R}$ and an $\mathbf{R}$-dependent differential ionization rate. Then, the rescattered electrons' momentum distribution, $S(p_r, \mathbf{\Omega}, \mathbf{R})$, for the fixed-in-space molecule is given by

$$S(p_r, \mathbf{\Omega}, \mathbf{R}) = w(p_r)\, P_{\text{ion}}(\mathbf{R})\, \frac{\mathrm{d}\sigma(p_r, \mathbf{R})}{\mathrm{d}\mathbf{\Omega}}\,, \tag{3.9}$$

where $\frac{\mathrm{d}\sigma(p_r,\mathbf{R})}{\mathrm{d}\mathbf{\Omega}}$ is the doubly differential scattering cross section for an electron scattering off the molecular ion into the solid angle $\mathrm{d}\mathbf{\Omega} = \mathrm{d}\phi \sin\theta\, \mathrm{d}\theta$. To establish the connection

c Note that, in the case of the photodissociation experiment, data point **I** is not measured at the time overlap of the two pulses, but rather at ≈100 fs, at which point the bond length has already increased by ≈0.8 Å according to the findings of Section 3.3.2.

d Not to be confused with the internuclear distance R.

to what is measured in the experiment, $S(p_r, \mathbf{\Omega}, \mathbf{R})$ has to be integrated over all molecular orientations, possibly taking into account a non-isotropic molecular-axis distribution $P_{\mathrm{MA}}(\mathbf{R})$ if the molecules are aligned in some way,

$$F(p_r, \mathbf{\Omega}) = w(p_r) \int_0^{\pi} \int_0^{2\pi} P_{\mathrm{ion}}(\mathbf{R})\, P_{\mathrm{MA}}(\mathbf{R})\, \frac{\mathrm{d}\sigma(p_r, \mathbf{R})}{\mathrm{d}\mathbf{\Omega}}\, \mathrm{d}\alpha \sin\beta\, \mathrm{d}\beta \ . \tag{3.10}$$

Furthermore, if both $P_{\mathrm{ion}}(\mathbf{R})$ and $P_{\mathrm{MA}}(\mathbf{R})$ are cylindrically symmetric around the polarization axis, which is what we have required the way we devised the experiments, then $F(p_r, \mathbf{\Omega}) = 2\pi\, F(p_r, \theta)$.

Clearly, the crucial quantities that have to be provided for evaluating Eq. (3.10) are the differential scattering cross sections $\mathrm{d}\sigma(p_r, \mathbf{R})\,/\mathrm{d}\mathbf{\Omega}$ (DCS) and the differential ionization yield $P_{\mathrm{ion}}(\mathbf{R})$. (For now, we ignore the treatment of $w(p_r)$ because in Section 3.4.4 we will show how the explicit treatment of this quantity can be avoided by a normalization procedure.) In principle there is no restriction on the level of theory with which each of them is treated. For instance, often the classical independent-atom model is used to predict the DCS, whereas the differential ionization yield is treated with a tunneling approximation. Here, we calculate the DCS with ePolyScat, in which the electron–molecule interaction is treated at the non-relativistic Hartree–Fock (NR-HF) level of theory, and which was already used in Chapter 2 for predicting photoelectron angular distributions in the XUV ionization of aligned CF_3I molecules. At the same time, the frontier orbitals of the NR-HF wave functions are used to calculate the differential ionization rate in the molecular-orbital strong-field approximation (MO-SFA).

We deem it necessary to treat the electron scattering explicitly at a quantum-mechanical level because the recollision energies in our experiment reach only ~20 eV, an impact energy at which electron exchange and quantum-scattering effects, in general, cannot be neglected. We note that, for simplicity, this approach operates in a purely non-relativistic picture, which certainly is its greatest shortcoming.

As a starting point, a restricted closed-shell Hartree–Fock SCF calculation was performed for neutral I_2 in its equilibrium geometry with the GAMESS (US) package. In it, the basis set of augmented-triple-ζ quality from the Sapporo family of basis sets (that ship with GAMESS) was used.[24] From this calculation, a total energy of $E_{\mathrm{HF}}^{eq} = -13\,835.747\,912\,E_{\mathrm{h}}$ was obtained. Then, the internuclear distance was varied both to shorter and longer bond lengths in steps of $\Delta R = 0.2$ Å. As is well known, the breaking of a bond is *never* correctly described in the restricted HF theory.[25] Therefore, a minimal complete active space (CAS) was constructed from four frontier orbitals, the three highest occupied molecular orbitals (HOMO-2, HOMO-1, HOMO) and the lowest unoccupied molecular orbital (LUMO). In the neutral equilibrium ground state these are – in a single-electron picture – occupied as $\sigma_g^2 \pi_u^4 \pi_g^4 \sigma_u^0$ (see the $^1\Sigma^+$ state in Fig. 3.1). Consequently, in the CAS all determinants that can be constructed with an electron occupation of $\sigma_g^p \pi_u^q \pi_g^r \sigma_u^s$ are included, where $p + q + r + s = 10$ for neutral I_2, and $p + q + r + s = 9$ for $I_2{}^+$.

At every internuclear-distance point, multi-configurational self-consistent field (MC-SCF) calculations were performed both for I_2 and $I_2{}^+$. For the neutral species, we recover a correlation energy of $E_{corr} = -11.389\,\mathrm{m}E_{\mathrm{h}}$ at the equilibrium internuclear distance. At infinite distance, the 4 orbitals we have included in the CAS collapse to the degenerate set of $5p$ orbitals on each fragment. Therefore, MC-SCF wave functions were obtained for the atomic iodine species I^0 and I^+, constructing a CAS over the 3 $5p$ orbitals to recover the

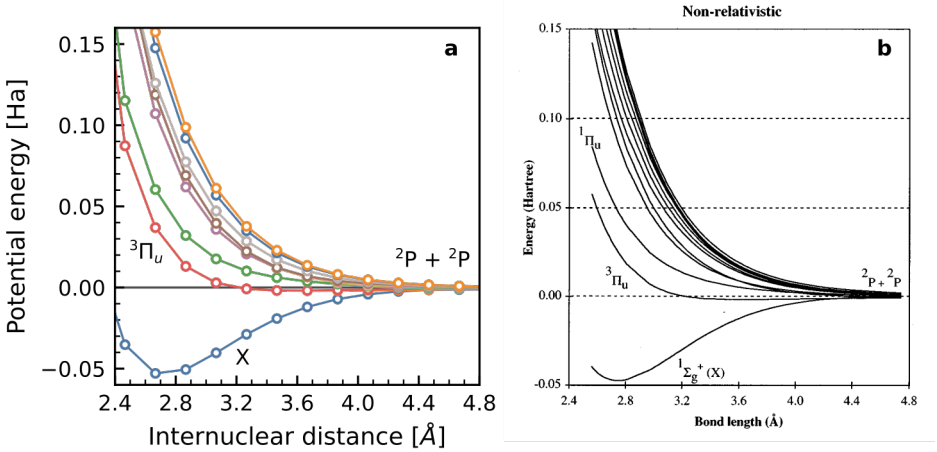

Figure 3.10 Potential energy curves for the ground and the seven lowest, excited states of I_2. **a)** This work. **b)** From Jong, Visscher & Nieuwpoort[8] (Fig. 1, left panel).

energy of the dissociation limit. In Fig. 3.10, we compare the potential energy curves for the neutral I_2 thus obtained to those reported by Jong, Visscher & Nieuwpoort[8], and observe a very close correspondence.

Now, to predict the differential strong-field-ionization yield, we make use of what is known as the molecular-orbital strong-field approximation (MO-SFA),[26,27] which is just an extension of the SFA method as developed for atoms. In this approximation, the potential of the molecular ion is neglected completely and strong-field ionization is thought to occur entirely as a series of n-photon transitions out of a molecular orbital $\phi_i(\mathbf{r})$.[e] Consequently, the differential ionization yield is just the sum of these transitions, i. e.,[28]

$$P_{\text{ion}}(\mathbf{R}) = 2\pi N_e \sum_{n=n_0}^{\infty} |P_n|^2 p_n \,, \tag{3.11}$$

where N_e is the number of electrons in the MO, p_n is the final photoelectron momentum given by $p_n = \sqrt{n\omega - \text{IP}_i - U_p}$ for an ionization potential IP_i associated with the orbital $\phi_i(\mathbf{r})$.

In general, the SFA can be formulated in both the length and velocity gauge. What is particularly appealing about the velocity gauge is that the n-photon ionization probabilities, P_n, can be calculated analytically, as[28]

$$P_n = (U_p - n\omega)\, \tilde{\phi}_i(\mathbf{p}_n)\, J_{-n}\left(\frac{\mathbf{p}_n \cdot \mathbf{A_0}}{\omega}, \frac{U_p}{2\omega}\right), \tag{3.12}$$

where $\tilde{\phi}_i(\mathbf{p}_n)$ is the molecular orbital transformed from position to momentum space, $\mathbf{A_0}$ is the peak vector potential, and $J_n(a, b)$ is a generalized Bessel function that arises from the analytical integration of the time-dependent equation that leads to Eq. (3.12),[29] which was introduced in Section 1.4.

Applying this method to the neutral ground state of I_2 is straightforward because its IP is well-known. As the ionizing orbital we just use the HOMO (π_g). The situation is more

e From here on, we work in atomic units again, unless otherwise noted.

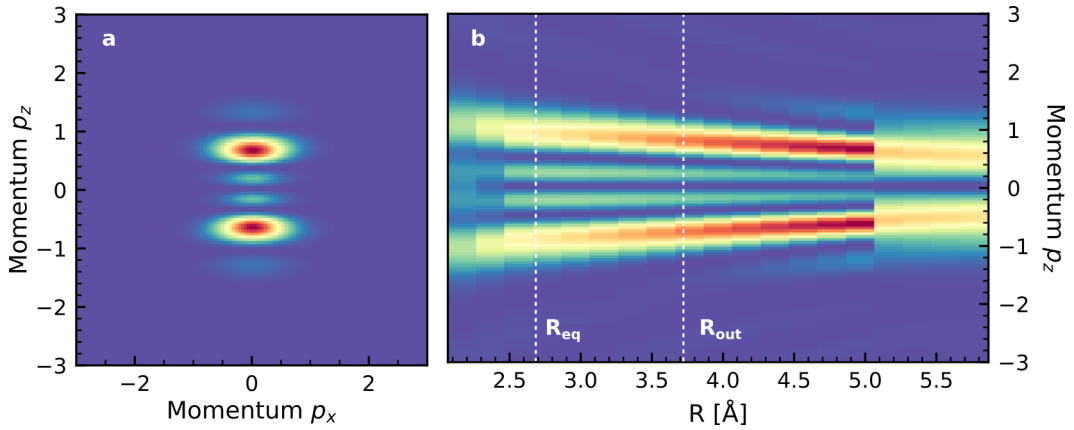

Figure 3.11 Momentum-space LUMO orbitals. **a)** Slice through the LUMO momentum-space orbital at the equilibrium internuclear distance. **b)** Change of the LUMO orbital with increasing internuclear distance. At every R, the x–z slice as shown in **a** was integrated over the p_x coordinate. R_{eq} and R_{out} denote the internuclear distances of the inner and outer turning point, respectively.

complicated for the excited state, which is why we propose a reasoning as follows: In a non-relativistic picture, both the transitions into the A and the B state are described by a single-electron excitation from the HOMO into the LUMO (see again Fig. 3.1). Clearly, this promoted electron is the most weakly bound and, as the total ionization probability scales exponentially (inverse) with the IP, it should dominate the strong-field ionization of the excited-state species. As HOMO and LUMO are of different shapes, P_{ion} is expected to be significantly different for the ground and excited state. Now, as the molecule dissociates, this situation is bound to change: The two orbitals that were the HOMO and LUMO in the ground state will converge in binding energy to a common limit along the dissociation path, and eventually become degenerate.[f] If it is true that the dissociation process can be pictured like this, we need to obtain the momentum-space orbitals for the HOMO and LUMO as a function of internuclear distance together with estimates for their binding energies.

From the MC-SCF calculations, presented in Fig. 3.10, natural orbitals were generated at every bond length, and from these the "natural-orbital" HOMO and LUMO were used for the subsequent calculations. These orbitals are transformed into momentum space *via* Fourier transformation, the result of which is displayed in Fig. 3.11a for the LUMO at R_{eq}. In panel b of that figure, it is demonstrated how the momentum distribution of the LUMO along the bond (z) axis changes with increasing bond length. Clearly, an overall decrease of momentum along this axis can be observed, which is what is expected because the LUMO is an anti-bonding orbital, and – consequently – its repulsive nature vanishes as the bond breaks. We also observe a discontinuity for bond lengths longer than 5 Å, which is probably due to the point of high degeneracy where the involved orbitals become indistinguishable, which often results in unpredictable mixing between equivalent orbitals (which, in turn, changes their spatial orientation). However, as we are – for the moment – only interested in the dynamics between the inner and outer turning points, this discontinuity need not worry us here.

To estimate the binding energies, the energy differences between the neutral $^3\Pi_u$ state and

f In fact, this is strictly true for all four orbitals included in the CAS, but for simplicity we restrict our investigation to the highest two.

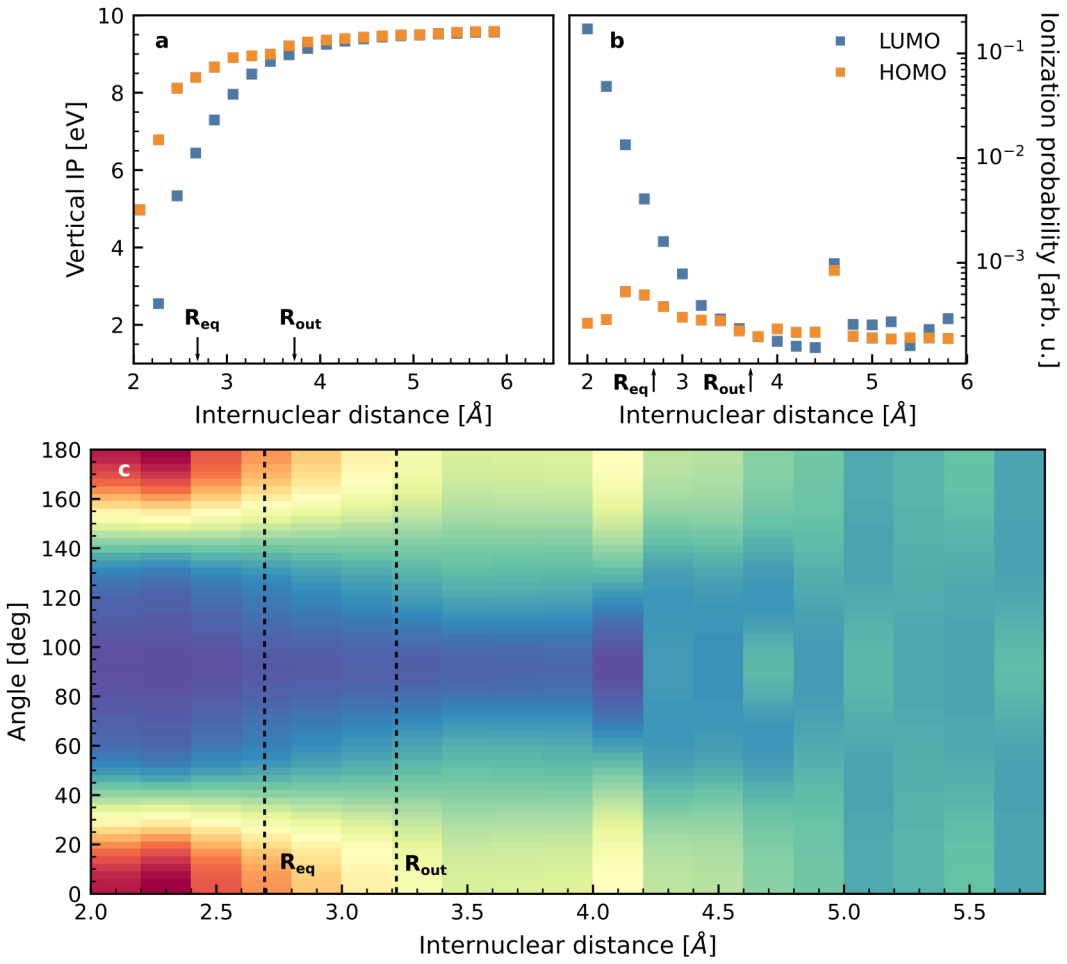

Figure 3.12 Calculation of the differential photoionization yield $P_{\text{ion}}(\beta)$ by the MO-SFA method in the velocity gauge. the **a)** Vertical IPs for ionization from the neutral ground state into the ion ground and first excited states in the non-relativistic CAS model. **b)** Total ionization probabilities for the π_g (HOMO) and σ_u (LUMO) orbitals, using the vertical IPs of **a. c)** Map of the normalized differential photoionization yields $P_{\text{ion}}(\beta)$ associated with the results from **b**, as a function of the internuclear distance and the polar angle β. R_{eq} and R_{out} denote the internuclear distances of the inner and outer turning point of vibrational wave packet prepared in the B state, respectively (see Fig. 3.5).

the two lowest (non-relativistic!) ion states were formed. Referring again to Fig. 3.1, these two states are the $^2\Pi_g$ state, corresponding to ionization out of the σ_u orbital and the $^4\Sigma_u^-$ state, in which an electron was removed from the π_g orbital.

The calculated binding energies are displayed in Fig. 3.12a. At the equilibrium distance, the IP is 6.4 eV for the σ_u (LUMO) orbital and 8.4 eV for the σ_g (HOMO) orbital. For comparison, the experimental ground-state IP is 9.8 eV. As the bond stretches, the binding energies quickly converge to a common limit at 9.6 eV, whereas the experimental IP of I^0 is 10.45 eV. From this we deduce that the vertical IPs are – on average – systematically underestimated by ~1 eV, primarily through the total neglect of relativistic corrections.

Now, we are in the position to calculate P_{ion} from Eq. (3.12), independently for the σ_u and

the π_g orbitals. The resulting total photoionization yield, $P_{tot} = \int_0^{\pi} \int_0^{2\pi} P_{\text{ion}}(\mathbf{\Omega})\, \mathrm{d}\phi \sin\theta\, \mathrm{d}\theta$, is displayed in Fig. 3.12b. As expected, the σ_u orbital dominates photoionization by roughly one order of magnitude at the equilibrium bond length. However, already when the bond is stretched by 0.8 Å the contributions of the two orbitals become comparable in our model.

Eventually, P_{ion} is obtained by summing the two contributions from the σ_u and the π_g orbitals, and normalizing the resulting angular distribution to unit sphere. As I_2 is a linear molecule, P_{ion} must be cylindrically symmetric, and therefore it is sufficient to consider only its dependence on the polar angle β, which is displayed in Fig. 3.12c as a function of the internuclear distance. In line with intuition, the ionization yield is increased when the molecule is aligned parallel to the laser polarization axis. When the internuclear distance is increased, this anisotropy becomes weaker, until it vanishes, which must necessarily be true because, for an unpolarized atom, there can be no angle dependence.

The last quantities we need to compute are the doubly differential DCSs. To this end, we have carried out electron scattering calculations with ePolyScat, making use of the full exact-static–exchange-plus-model-correlation–polarization (ESECP) potential. The Padial–Norcross potential[30] was used as the model-correlation potential and for the atomic polarizability of iodine a value of 5 Å^3 was assumed. The spherical-harmonics basis, in which the molecular orbitals and the scattering wave functions are expressed, was extended up to $l_{max} = 100$. The expansion center was always chosen to be located exactly between the two atoms. As quantum-scattering calculations are computationally demanding, we restricted ourselves to a choice of three representative scattering targets: I_2^+ in the equilibrium geometry of the neutral I_2 (R_{eq}, which we refer to as the "inner turning point", as well), I_2^+ at the outer turning point of the vibrational wave packet ($R_{\text{out}} = 3.72$ Å), and the atomic iodine ion, I^+. For these three targets, restricted-open HF calculations were carried out for the singly charged species to obtain the wave functions, from which the molecular potential is calculated in ePolyScat. In doing so, we imply that, on one hand, the rescattering process is so fast that the returning electron finds its parent ion at the same bond length at which it had left, but that, on the other hand, rescattering is slow enough for the electron density to relax to that of the charged species. All electron scattering calculations were carried out for collision energies between 9 and 24 eV in steps of 1 eV.

In the very last step, the doubly differential DCSs are integrated over all molecular orientations according to Eq. (3.10), including the appropriate P_{ion}, either for the ground state (for comparison to the 1.3 µm-only experiment) or the excited state, as shown in Fig. 3.12c. In addition to that, a molecular-axis distribution $P_{\text{MA}}(\beta) = \sin^2\beta$ was introduced for the photodissociation experiment because the transition into the A state is known to be a perpendicular one. The results of this averaging process are presented in Fig. 3.13a through c, where we compare the predicted scattered-electron angular distributions for the different scattering targets, assuming $w(p_r) = 1$ and including $P_{\text{ion}}(\beta)$ for the excited state at the respective internuclear distance. For the purpose of comparing the computational results to each other, we assume for the moment that $P_{\text{MA}} = 1$, which means that we suppress the effect of molecular alignment. (In Section 3.4.4, we will reintroduce the proper $P_{\text{MA}}(\beta)$ in connection with the actual experimental data.) To facilitate comparison, all three distributions are shown at the same intensity scale. Overall, all three calculations look very similar: All show a pronounced backscattering peak at 180° and a secondary peak at 120°. The backscattering peak is by far the strongest in the atomic iodine, where it peaks at ~17 eV. For I_2^+ at the inner turning

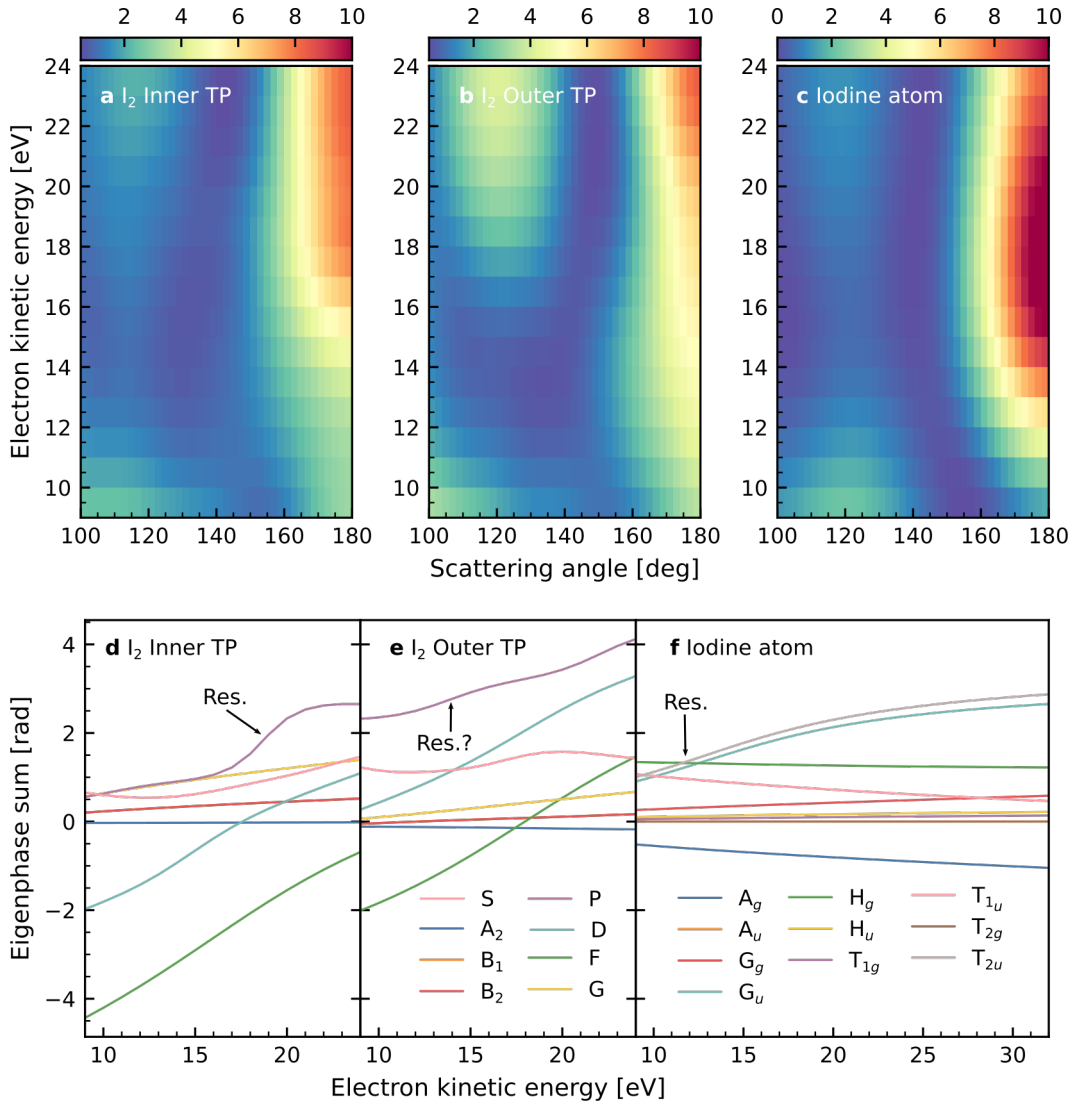

Figure 3.13 Differential electron–ion scattering cross sections **(a–c)** and eigenphase sums **(d–f)** for the electron–ion scattering processes in I_2^+ at the equilibrium internuclear distance (**a** and **d**), I_2^+ at the bond length that corresponds to the outer turning point of the vibrational wave packet (**b** and **e**), and I^+ (**c** and **f**). **a–c** are shown at the same intensity scale. Note that, while the calculations in **d** were carried out in $D_{\infty h}$ symmetry, the results of **e** were obtained in $C_{\infty v}$ because the charge is asymmetrically distributed in the latter case. To facilitate comparison between **d** and **e**, continuum channels of *gerade* and *ungerade* symmetry were added in **e**. As a consequence, **d** and **e** share the same legend.

point (which we take to be identical to the equilibrium bond length) a similar, but weaker backscattering signature is observed. The backscattering feature in I_2^+ at the outer turning point is shifted to lower energies, and seems to appear between 12 and 15 eV.

In general, features in the angular distributions of quantum-scattering calculations are less straightforward to rationalize compared to, e. g., classical scattering models, where two-center interference is encoded in the momentum-transfer cross section and the distance of the two

scatterers is readily retrieved. Okunishi *et al.*[4] have discussed their DCSs for the LIED experiments in O_2 and CO_2 both in terms of a (quantum-scattering) two-center interference and shape resonances. In I_2, electrons with de-Broglie wavelengths that match the distances of inner and outer turning point, must have kinetic energies of 21 and 11 eV, respectively. However, in the calculations, we find little evidence for a two-center interference effect that should manifest as a backscattering peak at these energies. If anything, an energy shift in the onset of the backscattering signal is observed from 16 eV at the inner turning point to 13 eV at the outer turning point.

To investigate whether shape resonances are involved in the results of the present scattering calculations, we looked for sudden jumps in the eigenphase sums of the various scattering channels that are involved, all of which are displayed in Fig. 3.13d through f.[g] Clearly, such a sudden jump can be identified for I_2^+ at the equilibrium bond length in the P channel, centered at ∼19 eV, whereas no comparable phase jump is observed at the outer turning point. In fact, comparing the eigenphase sums of all the other continuum symmetries pairwise between these two calculations, the disappearance of the phase jump in the P channel is the most pronounced difference that is observed. For the iodine atom, Fig. 3.13f, most of the eigenphase-sum curves are rather flat, with the exception of the G_u and T_{2u} channels, which show a steep rise between 9 and 15 eV.

In the next step, the pole-searching algorithm of Stratmann & Lucchese[32] was used that iteratively solves for the positions of poles of the scattering S matrix in the complex-valued scattering-energy plane to locate the positions of shape resonances. With it, we were able to identify two strong poles that are associated with a prominent shape resonance each, one at $E_p = (12.0 - 4.0\mathrm{i})$ eV in the T_{2u} channel of the iodine atom, and one at $E_p = (16.0 - 0.90\mathrm{i})$ eV in the P_g channel of I_2^+ at the inner turning point. While the resonance energy for the shape resonance in the iodine atom agrees well with the phase jump observed in Fig. 3.13f, the position of the resonance for the I_2^+ molecule is ≈2 eV lower than where it appears in Fig. 3.13d. However, we have compared the eigenphase sum that is used internally in the pole-searching algorithm to the one of Fig. 3.13d, and find that it exhibits the same, narrow phase jump, indeed shifted to lower kinetic energies. We recall that for the pole-searching algorithm only an energy-independent model-exchange potential is used, in contrast to the exact treatment of exchange that is accounted for in the results of Fig. 3.13, and attribute this energy shift to the different treatment of the exchange interaction.

To illustrate the nature of these two shape resonances, we have calculated the resonance wave functions at the respective, complex-valued energies, and their real parts are shown in Fig. 3.14. Clearly, the resonance in the iodine atom (panel a) has the shape of an f orbital and, in fact, we find that the amplitude of the resonance wave function is greatest in the $l = 3$ component. This resonance is essentially the same as the famous “giant resonance”

g The various scattering channels arise from the fact that in a general, non-spherical potential-scattering problem not necessarily *all* partial waves are coupled. Instead, if the scattering target exhibits a high degree of symmetry, the continuum wave function can be decomposed according to the irreducible representations of the target.[31] Then, only partial waves that belong to the same irreducible representation are coupled, and each irreducible representation gives rise to a unique scattering channel. The total S matrix therefore becomes block-diagonal, where every block represents an S matrix for a specific channel. For every of these S matrices, the eigenphase sums are obtained individually based on the procedure described in Section 1.2. Note that the various scattering channels for the electron–I^+ scattering arise from the fact that, inside ePolyScat, atoms are always treated in icosahedral symmetry.

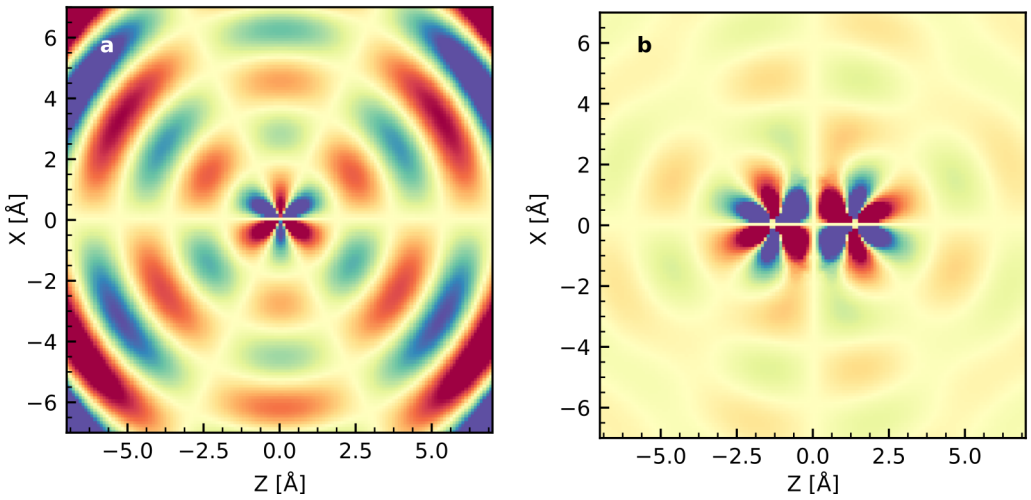

Figure 3.14 Shape resonances in atomic iodine ions **(a)** and I_2^+ at the equilibrium internuclear distance of the neutral I_2 **(b)**. Shown are the real parts of the resonance scattering wave functions. The atom positions are located exactly in the centers of the rosetta-shaped features. **a)** $l = 3$ (f-wave) resonance at $E_R = 12.0\,\text{eV}$, $\Gamma = 8.0\,\text{eV}$. **b)** $l = 6$ resonance at $E_R = 16.0\,\text{eV}$, $\Gamma = 1.8\,\text{eV}$.

in the photoionization of xenon, which is also observed in iodine.[33] If we compare this to the molecular shape resonance (panel b), we find that it can be described by the destructive combination of two such f orbitals, and the resonance therefore appears in the $l = 6$ component. With respect to the results of Fig. 3.13, we interpret this observation as follows: The resonance condition for the $l = 6$ shape resonance, which is met in the kinetic-energy range under investigation at the inner turning point, is detuned when the bond length is increased, so that it disappears completely at the outer turning point. However, the two atoms still polarize each other, so that the atomic shape resonance cannot yet form, for the atomic potential is still too distorted. When the molecule is completely dissociated, however, the atomic shape resonance reappears.

To support this interpretation, we have carried out pole searches in the complex-valued scattering-energy plane for I_2^+ in various intermediate geometries between the inner and outer turning points. The obtained eigenphase curves in the P channel are shown in Fig. 3.15a and corresponding poles in the complex energy plane are displayed in panel b of this figure. We find that the resonance position E_R drops by about 4 eV already within 0.4 Å of increasing bond length, and does not change significantly afterwards (the small deviations that lead to the clustering of the poles in Fig. 3.15b are probably due to numerical instabilities in the pole-searching algorithm). Also the width of the resonance is affected, increasing from $\Gamma \approx 2.0\,\text{eV}$ at R_{eq} to $\Gamma \approx 3.2\,\text{eV}$ at R_{out}. If we trust the results of Fig. 3.15, we can conclude that the position of the molecular shape resonance is very sensitive to small changes of the internuclear distance close to R_{eq}. This means that, when the molecule moves from the inner to the outer turning point, we are in particular sensitive during the first third of this excursion by means of the relaxation dynamics in the molecular shape resonance, where its resonance energy is modulated with a slope of $\approx 10\,\text{eV}\,\text{Å}^{-1}$.

Before we turn to the comparison between experiment and theory, we quickly want to address the question, how the backscattering in the atomic iodine ion, Fig. 3.13c, can look so

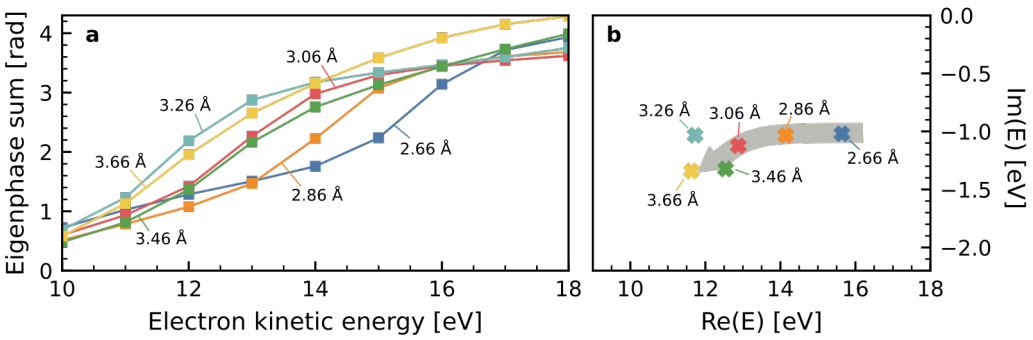

Figure 3.15 Evolution of the molecular shape resonance as a function of the internuclear distance R. **a)** Eigenphase curves for the P channel for I_2^+ in various geometries ranging from R_{eq} to R_{out}. **b)** Same as **a**, but visualized in terms of poles in the complex energy plane of the associated S matrix.

similar to that of the molecular ion at R_{eq}, Fig. 3.13a, even though the shape resonance is shifted by at least 4 eV between these two systems, contradicting the observation that this shift to lower energies is well manifested in the backscattering of the molecular ion at R_{out}, Fig. 3.13b. To give some explanation of how we *suspect* this comes, recall that the atomic ion is a spherically symmetric system, in contrast to the diatomic molecule. As explained at the end of Section 1.2, in the scattering on a spherically symmetric target, there are few partial waves involved in the continuum wave function, but these few partial waves can interfere with each other strongly. In molecular scattering, there are many angular-momentum couplings involved that give rise to many cross terms in the scattering amplitude that may eventually weaken this strong partial-wave interference. From this we conclude *qualitatively* that a shape resonance in molecular scattering is more likely to appear at its actual resonance energy E_R in the backscattering spectrum, whereas in atomic scattering the backscattering can be significantly shifted through partial-wave interference. To support this idea, we have calculated the partial-wave scattering amplitudes f_l according to Eq. (1.26) for the electron–I^+ scattering and compared the different, individual partial-wave DCS, $|f_l|^2$ to each other and to different coherent sums of the f_l, all of which is shown in Fig. 3.16. From panels a, b, and c of this figure, it is clear that the shape resonance manifests in the backscattering region of the f_3, just as one would expect, at the resonance energy of ≈12 eV. When, however, the interference between p, d, and f waves ($l = 1, 2, 3$) is taken into account, the maximum in the backscattering region is shifted up by ≈5 eV as illustrated in Fig. 3.16d. To recover the full DCS, only f_0 and the Coulomb scattering amplitude f_C (see Eq. (1.34)) have to be added, which does not affect the backscattering region, but which is sufficient to almost perfectly reproduce the output of ePolyScat (which also incorporates partial waves of order $l > 3$). Another insight one can gain from this analysis is that the feature at 120° that is observed in all calculations of Fig. 3.13, is related to a contribution from the partial waves of $l = 3$ that is modulated to some extent by partial-wave interference.

3.4.4 Comparison and discussion

We now come back to the experimental results to see whether we can find evidence of the scattering dynamics that are predicted by the calculations. For this purpose, we consider

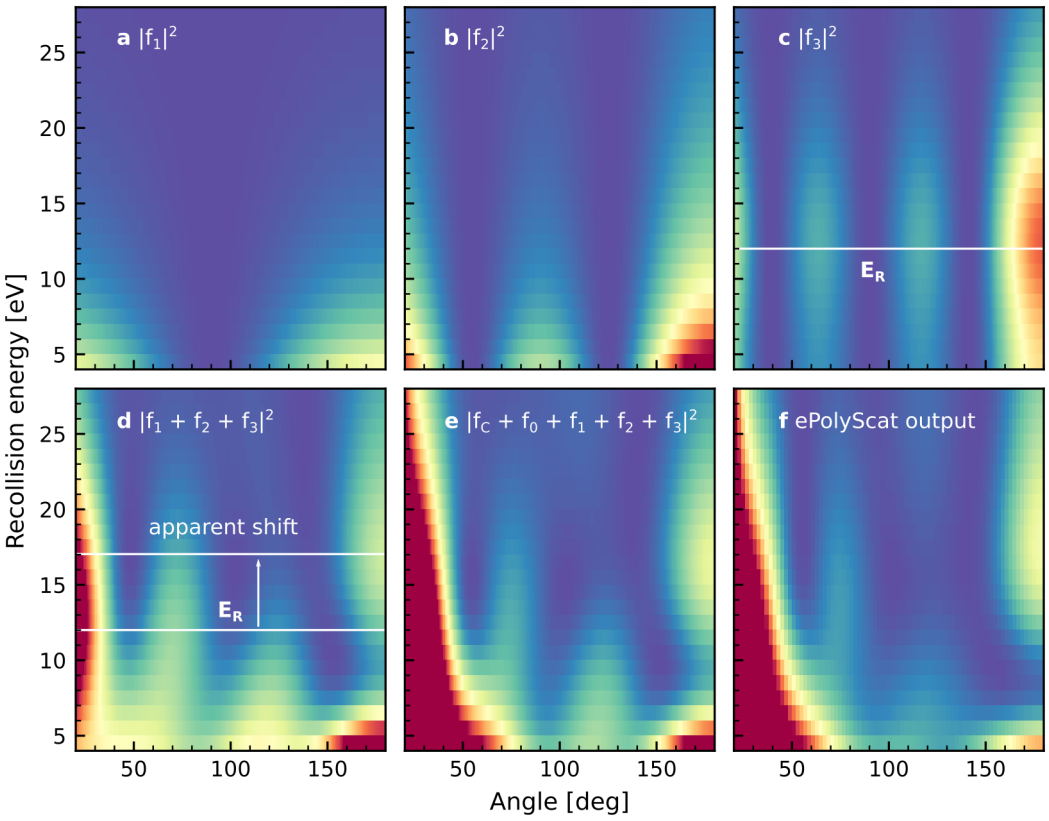

Figure 3.16 Differential scattering cross section for electron–I^+ scattering, decomposed into its partial-wave contributions. f_l are the partial-wave amplitudes of Eq. (1.26) and f_C is the Coulomb scattering amplitude according to Eq. (1.34). The full ePolyScat output **(f)** contains partial waves up to $l = 6$.

first the results of the 1.3 µm-only experiment that were presented in Fig. 3.7. Even though we have extracted the momentum distribution of the rescattered electrons in panel b of that figure, we cannot readily compare them to our calculations because the exact shape of the wave packet in momentum space, $w(p_r)$ in Eq. (3.10), is not known and is difficult to predict reliably.

What Okunishi *et al.*[4] have done to overcome this problem is that they have normalized their experimental angular distributions *to the calculations* at a specific angle, for which they choose one, where the calculated DCS varies the least with kinetic energy. We also apply this procedure, but normalize instead *both* the experimental and the theoretical results at $\theta_{min} = 135°$. We note that, in principle, any angle could be chosen for this procedure, as long as the same one is employed both for the experiment and the theory. In Fig. 3.17 the extracted rescattered-electron angular distributions – normalized at θ_{min} are compared to the respective simulation from the previous chapter for $I_2{}^+$ in its ground state. Overall, considering the many simplifications that we introduced in the model *and* in extracting the scattered electrons, the agreement is very good, and it is even more convincing for the Abel-inverted data (Fig. 3.17b). Here, a clear backscattering peak, centered at 18 eV, can be identified, which we identify with the molecular shape resonance in $I_2{}^+$ at the equilibrium internuclear distance. Also, the

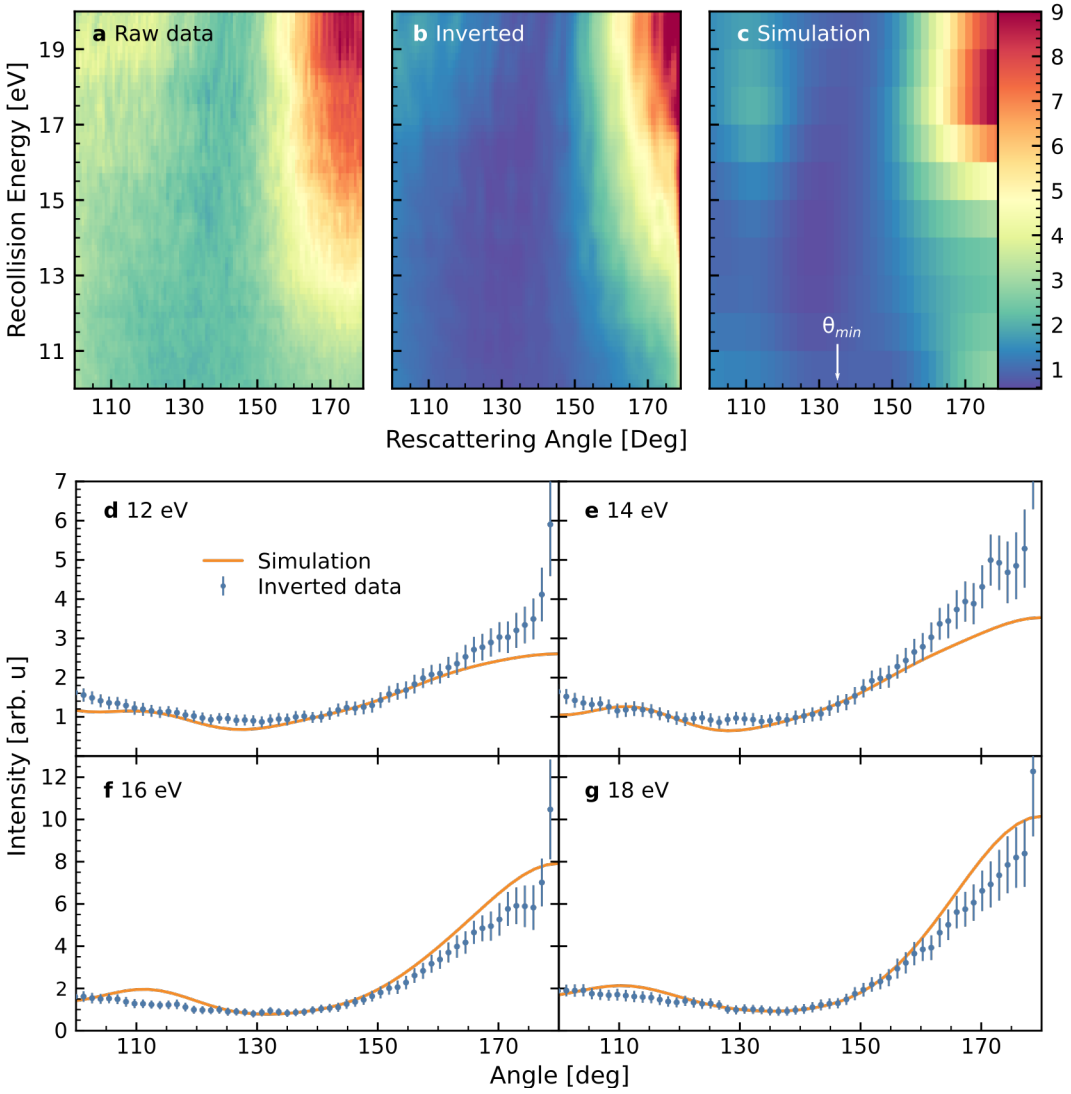

Figure 3.17 Comparison between the experimental and theoretical angular distributions of the rescattered electrons obtained for 1.3 µm ionization of I_2 in the ground state using an intensity of 3×10^{13} W/cm^2. **a–c)** Two-dimensional maps of the extracted rescattered electrons from the raw detector distribution **(a)** and the Abel-inverted slices through the 3D momentum distribution **(b)**, compared to the simulation for strong-field ionization of I_2 in its ground state and at the equilibrium geometry. **d–g)** Angular distributions extracted from **b** and **c** at the indicated electron recollision energies, all normalized at θ_{min}, the position of which is indicated in **c**.

additional structure around an angle of 110° can be identified in the experiment. To show that we can achieve an almost quantitative correspondence between theory and experiment, we have extracted angular distributions at four representative kinetic energies and normalized all traces at θ_{min}, the result of which is displayed in Fig. 3.17d through g.

After these encouraging results we turn to the time-resolved photoelectron spectra. Here, the comparison between theory and experiment is less straightforward because what is

measured is actually always a mixture of ground and excited-state molecules because only a fraction of the molecules will be excited. What is worse is that, although this fraction is constant, its relative contribution to the overall signal may very well change with pump–probe delay, which is what we know from the experiment (Fig. 3.8a and Fig. 3.9a) and also what we expect from the argument outlined in Section 3.4.3 (even though our calculated results differ even qualitatively from the results of the measurement). Our approach to still be able to make a comparison is as follows: For the measurement at each delay, the rescattered electrons are extracted and normalized to the intensities at θ_{min}. If we now take the *absolute* difference of two such normalized spectra, the contribution of the ground-state molecules should identically vanish and the difference between the excited-state fractions should be normalized, as well. We can now compare this difference to the difference between two calculations that were normalized in the same way, which should result in one-to-one correspondence.

Also, we have to form the differences for data points, which we expect to correspond closely to the molecular geometries of the scattering targets that were introduced above. For the photodissociation, we have chosen the very first data point at ∼100 fs (**I** in Fig. 3.8), and the very last one at ∼800 fs (**V** in Fig. 3.8), where the molecule is definitely dissociated, to form the difference spectrum. At the first delay, the molecular bond will already have stretched by ∼0.8 Å. For the simulation, we have therefore taken – on one side – $I_2{}^+$ in the outer-turning-point geometry, R_{out}, and included the $\sin^2$ molecular-axis distribution. On the other side we assume that atomic I^+ can represent the *essentially* dissociated molecule well, and so the difference is formed between the calculations for $I_2{}^+$ at R_{out} and the I^+ atomic ion. We note that, in principle, also the neutral iodine species is present, which could contribute to the scattering signal because the returning wave packet is expected to have a spatial extension that is on the order of a few nanometer.[34] However, the differential scattering cross for the neutral iodine atom is lower by a factor of 3 on average because the Coulomb scattering is what makes the largest contribution to the overall cross section. In Fig. 3.18a through c, we compare the differences thus obtained and observe, again, a very good agreement. The strong negative contribution at 180°, which agrees closely between theory and experiment, can be associated with the strong backscattering in I^+ that was discussed above. Even the peak position of 17 eV seems to match. Also, the negative band under an angle of 120° is observed both in the experiment and the theory, although this feature extends to much lower energies in the calculation. We explain the strong depression in the backscattering signal as an imprint of the *atomic* shape resonance, which was discussed at the end of Section 3.4.3.

For the experiment on the vibrational wave packet, the data points at the inner and outer turning points were taken and subtracted (data points **VI** and **IV** in Fig. 3.9), which is also what was done for the results of the calculation. Here, the molecular-axis distribution was taken to be isotropic because the geometric alignment that is induced by the dipole transition will have long dephased at the full revival of the wave packet.[h] Again, we compare these two differences in Fig. 3.19a through c. Unfortunately, the difference signal is, even with the long-running acquisitions much weaker compared to the photodissociation experiment. Still, we can clearly identify the positive backscattering peak at ≈18 eV and the negative peak at ≈13 eV, which we relate to the molecular shape resonances at the inner and outer turning points, respectively, as discussed in Section 3.4.3. What is more, also all features in the DCS

h At an expected rotational temperature of the ensemble of ≈10 K the alignment that is induced through the dipole transition dephases within ≈2 ps.

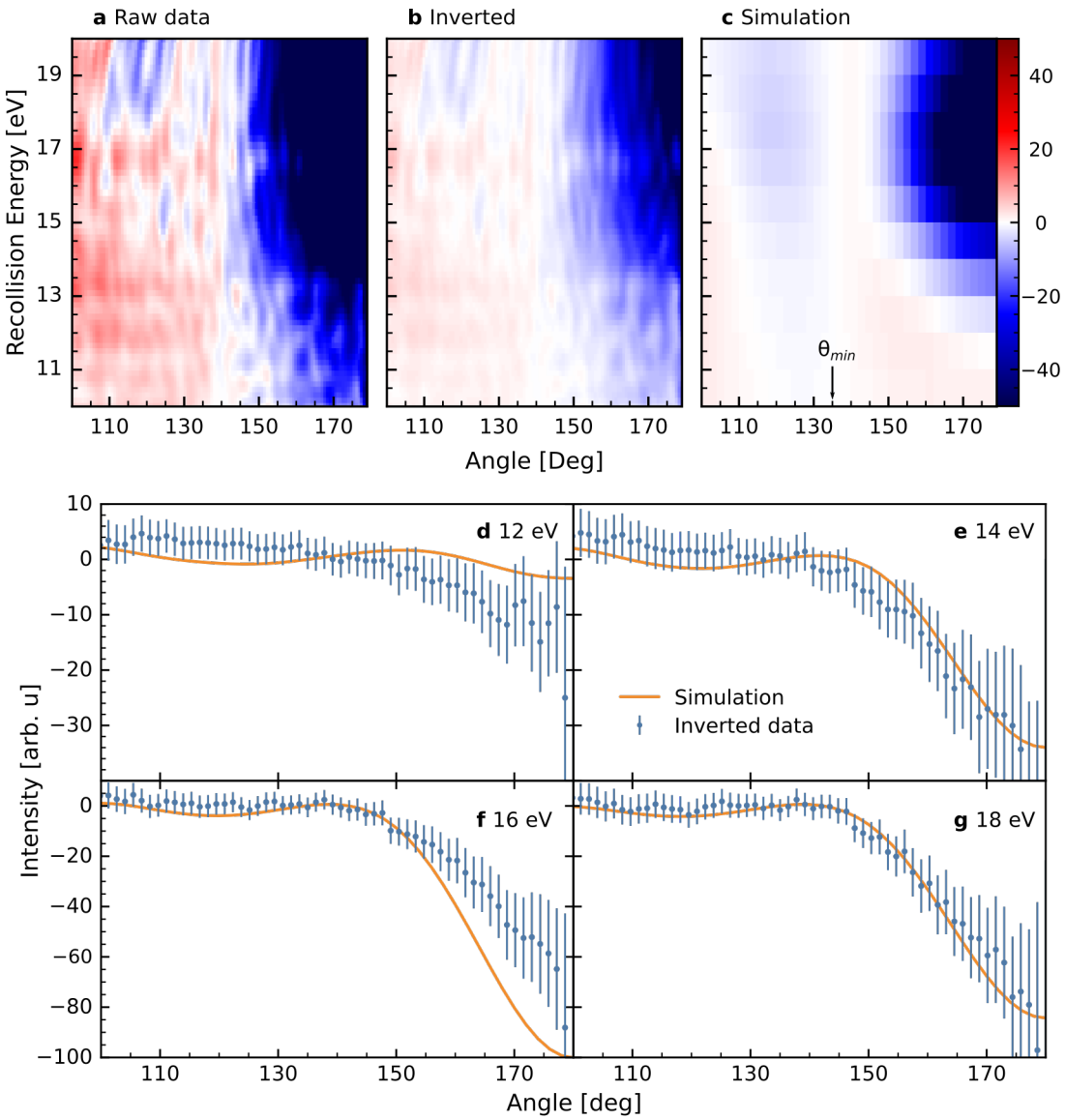

Figure 3.18 Comparison between absolute differences of the rescattered-electron angular distributions for the photodissociation experiment. For the experiment **(a, b)**, the difference **I − V** was formed in terms of the labels given in Fig. 3.8. For the simulation, the difference $I_2(R_{out}) - I^+$ was used to approximate the experimental situation. **d–g)** Angular distributions extracted from **a–c** at the indicated electron recollision energies, all normalized at θ_{min}, the position of which is indicated in **c**. The experimental distributions were scaled by a common, but otherwise arbitrary factor to match them to the calculated ones. Note the different abscissas.

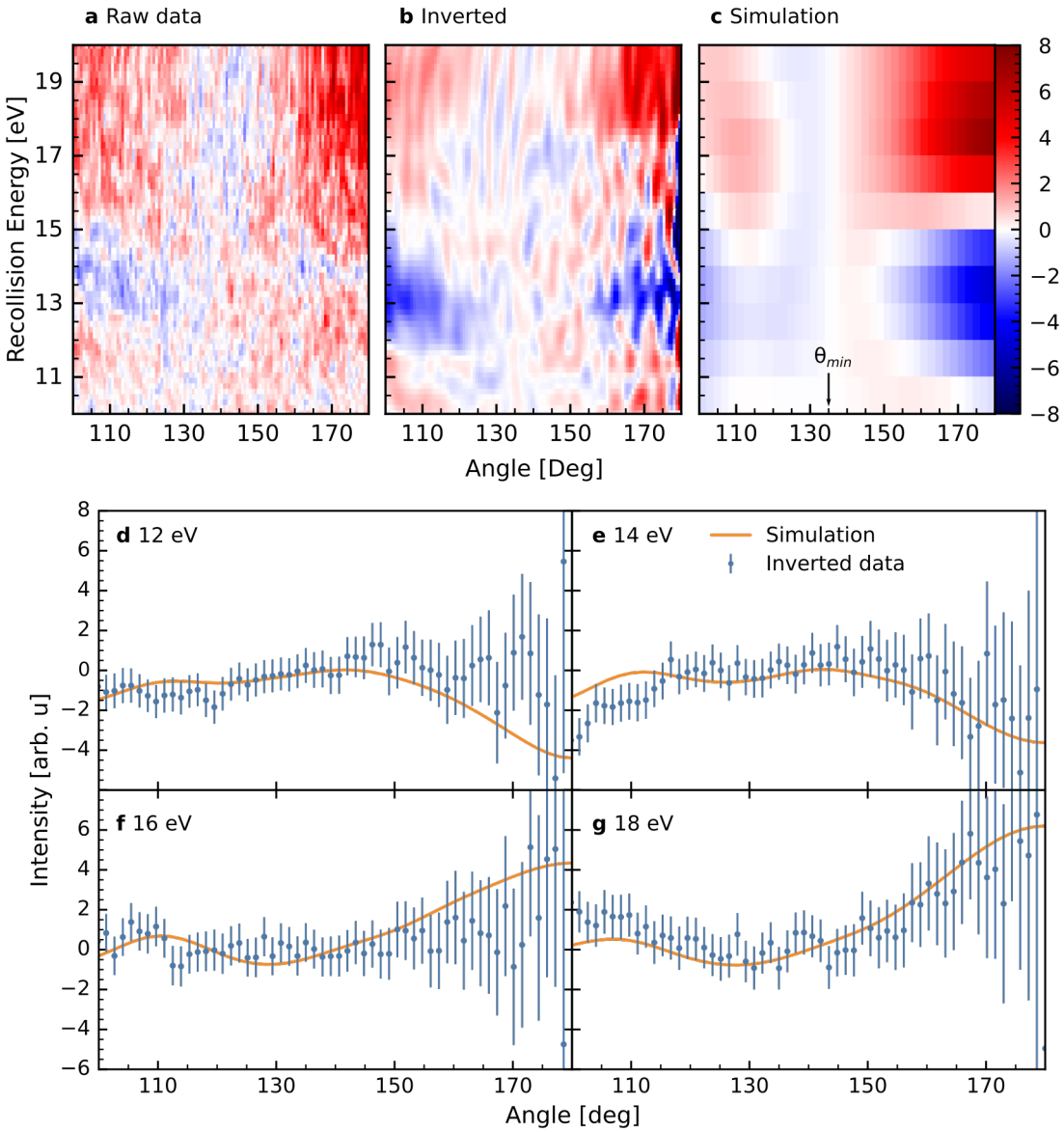

Figure 3.19 Same as Fig. 3.18, but for the *B*-state experiment. Here the difference between the points labeled **VI** and **IV** in Fig. 3.9 is formed, which is compared to the difference between the DCSs for the inner and outer turning in the simulations.

difference for angles $< \theta_{min} = 135°$ are qualitatively in good agreement between theory and experiment. Looking at the extracted angular distributions, Fig. 3.19 d through g, a very good agreement is found although the error bars are significantly larger for this experiment.

3.5 Conclusion

The aim of this chapter was to apply the analysis of laser-assisted electron recollisions in the strong-field ionization of molecules to the excited-state dynamics of I_2 molecules pumped into the *A* or *B* state, triggering photodissociation and the preparation of a vibrational wave packet, respectively. To this end, the molecular dynamics were first quantified by monitoring the $I^+ + I^+$ and $I^+ + I^{2+}$ Coulomb channels in strong-field ionization of I_2. Investigating the associated photoelectron spectra we found a clear modulation in that part of the spectra, to which only rescattered electrons can contribute. In particular, we found a surprising trend in the yield of photoelectrons that are backscattered along the laser polarization axis, in which the intensity first appears to drop with increasing bond length before it increases again.

To understand this, a framework was introduced to extract and rationalize the differential scattering cross sections for the electron–molecular-ion scattering from the associated photoelectron spectra. With the help of scattering calculations we were able to prove that the surprising trend can be explained by the scattering dynamics in the molecule and the atom, respectively: As the bond stretches, the molecular shape resonance is detuned, which causes the drop in backscattering intensity. Asymptotically, as the free iodine atoms emerge, their strong atomic shape resonance dominates the backscattering spectrum, which greatly enhances the intensity in that energy region again.

What we were not able to show is that the exact bond length of the molecule in motion can be extracted as a function of pump–probe delay. Very likely our time resolution of ≈90 fs was simply insufficient to resolve the relaxation of the molecular shape resonance, which occurs already during the first third of the bond stretching in the vibrational wave packet. In general, it appears that in the regime of low-energy electron–molecular-ion scattering, an experiment exploiting laser-assisted electron recollisions is sensitive only to the dynamics of the shape resonances, which are the features that affect the scattering dynamics the strongest. At the same time, this apparent limitation is also the greatest strength of this approach because, as we have shown, shape resonances are extremely sensitive to even the smallest changes in the molecular potential.

References

1. Robiette, A. G. in *Molecular Structure by Diffraction Methods: Volume 1* (eds Sim, G. A. & Sutton, L. E.) 160–198 (The Royal Society of Chemistry, 1973).
2. Srinivasan, R., Lobastov, V. A., Ruan, C.-Y. & Zewail, A. H. "Ultrafast Electron Diffraction (UED)". *Helv. Chim. Acta* **86,** 1761–1799 (2003).
3. Lin, C. D., Le, A.-T., Chen, Z., Morishita, T. & Lucchese, R. "Strong-Field Rescattering Physics—Self-Imaging of a Molecule by Its Own Electrons". *J. Phys. B: At., Mol. Opt. Phys.* **43,** 122001 (2010).
4. Okunishi, M., Niikura, H., Lucchese, R. R., Morishita, T. & Ueda, K. "Extracting Electron-Ion Differential Scattering Cross Sections for Partially Aligned Molecules by Laser-Induced

Rescattering Photoelectron Spectroscopy". *Phys. Rev. Lett.* **106,** 063001 (2011).

5. Pullen, M. G., Wolter, B., Le, A.-T., Baudisch, M., Hemmer, M., Senftleben, A., Schröter, C. D., Ullrich, J., Moshammer, R., Lin, C. D. & Biegert, J. "Imaging an Aligned Polyatomic Molecule with Laser-Induced Electron Diffraction". *Nat. Commun.* **6,** 7262 (2015).
6. Yang, J. *et al.* "Diffractive Imaging of Coherent Nuclear Motion in Isolated Molecules". *Phys. Rev. Lett.* **117,** 153002 (2016).
7. Glownia, J. M., Natan, A., Cryan, J. P., Hartsock, R., Kozina, M., Minitti, M. P., Nelson, S., Robinson, J., Sato, T., van Driel, T., Welch, G., Weninger, C., Zhu, D. & Bucksbaum, P. H. "Self-Referenced Coherent Diffraction X-Ray Movie of Angstrom- and Femtosecond-Scale Atomic Motion". *Phys. Rev. Lett.* **117,** 153003 (2016).
8. Jong, W. A. de, Visscher, L. & Nieuwpoort, W. C. "Relativistic and Correlated Calculations on the Ground, Excited, and Ionized States of Iodine". *J. Chem. Phys.* **107,** 9046–9058 (1997).
9. Tellinghuisen, J. "Transition Strengths in the Visible–Infrared Absorption Spectrum of I_2". *J. Chem. Phys.* **76,** 4736–4744 (1982).
10. Dick, B. "Inverting Ion Images without Abel Inversion: Maximum Entropy Reconstruction of Velocity Maps". *Phys. Chem. Chem. Phys.* **16,** 570–580 (2013).
11. Walker, B., Sheehy, B., DiMauro, L. F., Agostini, P., Schafer, K. J. & Kulander, K. C. "Precision Measurement of Strong Field Double Ionization of Helium". *Phys. Rev. Lett.* **73,** 1227–1230 (1994).
12. Fang, L. & Gibson, G. N. "Strong-Field Induced Vibrational Coherence in the Ground Electronic State of Hot I_2". *Phys. Rev. Lett.* **100,** 103003 (2008).
13. Gibson, G. N., Coffee, R. N. & Fang, L. "Observation of Enhanced Excitation of I_2^{2+} by Strong Laser Fields". *Phys. Rev. A* **73,** 023418 (2006).
14. Ritze, H.-H. *Unpublished Results*
15. Tagliamonti, V., Chen, H. & Gibson, G. N. "Internuclear-Separation-Resolved Asymmetric Dissociation of I_2 in a Two-Color Laser Field". *Phys. Rev. A* **84,** 043424 (2011).
16. Chen, H., Fang, L., Tagliamonti, V. & Gibson, G. N. "Angle-Resolved and Internuclear-Separation-Resolved Measurements of the Ionization Rate of the *B* State of I_2 by Strong Laser Fields". *Phys. Rev. A* **84,** 043427 (2011).
17. Chen, H., Tagliamonti, V. & Gibson, G. N. "Internuclear Separation Dependent Ionization of the Valence Orbitals of I_2 by Strong Laser Fields". *Phys. Rev. Lett.* **109,** 193002 (2012).
18. Fischer, I., Vrakking, M. J. J., Villeneuve, D. M. & Stolow, A. "Femtosecond Time-Resolved Zero Kinetic Energy Photoelectron and Photoionization Spectroscopy Studies of I_2 Wavepacket Dynamics". *Chem. Phys.* **207,** 331–354 (1996).
19. Cooley, J. W. "An Improved Eigenvalue Corrector Formula for Solving the Schrödinger Equation for Central Fields". *Math. Comput.* **15,** 363–374 (1961).
20. Le Roy, R. J. "RKR1: A Computer Program Implementing the First-Order RKR Method for Determining Diatomic Molecule Potential Energy Functions". *J. Quant. Spectrosc. Radiat. Transfer* **186,** 158–166 (2017).
21. Gerstenkorn, S. & Luc, P. "The Iodine Absorption Spectrum around 5915 Å. Calibration and Assignments". *Opt. Commun.* **36,** 322–326 (1981).
22. Spanner, M., Smirnova, O., Corkum, P. B. & Ivanov, M. Y. "Reading Diffraction Images in Strong Field Ionization of Diatomic Molecules". *J. Phys. B: At., Mol. Opt. Phys.* **37,** L243 (2004).
23. Lewenstein, M., Balcou, P., Ivanov, M. Y., L'Huillier, A. & Corkum, P. B. "Theory of High-Harmonic Generation by Low-Frequency Laser Fields". *Phys. Rev. A* **49,** 2117–2132 (1994).

24. Koga, T., Yamamoto, S., Shimazaki, T. & Tatewaki, H. “Contracted Gaussian-Type Basis Functions Revisited. IV. Atoms Rb to Xe”. *Theor. Chem. Acc.* **108,** 41–45 (2002).

25. Szabo, A. & Ostlund, N. *Modern Quantum Chemistry: Introduction to Advanced Electronic Structure Theory* (Dover, Mineola, 1996).

26. Muth-Böhm, J., Becker, A. & Faisal, F. H. M. “Suppressed Molecular Ionization for a Class of Diatomics in Intense Femtosecond Laser Fields”. *Phys. Rev. Lett.* **85,** 2280–2283 (2000).

27. Zhang, B. & Zhao, Z. “Strong-Field Approximation for the Ionization of N_2 and CO_2”. *Phys. Rev. A* **82,** 035401 (2010).

28. Zhang, B. & Zhao, Z. “SLIMP: Strong Laser Interaction Model Package for Atoms and Molecules”. *Comput. Phys. Commun.* **192,** 330–341 (2015).

29. Reiss, H. R. “Effect of an Intense Electromagnetic Field on a Weakly Bound System”. *Phys. Rev. A* **22,** 1786–1813 (1980).

30. Padial, N. T. & Norcross, D. W. “Parameter-Free Model of the Correlation-Polarization Potential for Electron-Molecule Collisions”. *Phys. Rev. A* **29,** 1742–1748 (1984).

31. Gianturco, F. A. & Jain, A. “The Theory of Electron Scattering from Polyatomic Molecules”. *Phys. Rep.* **143,** 347–425 (1986).

32. Stratmann, R. E. & Lucchese, R. R. “Resonances and the Effects of Interchannel Coupling in the Photoionization of CS_2”. *J. Chem. Phys.* **97,** 6384–6395 (1992).

33. Lindle, D. W., Kobrin, P. H., Truesdale, C. M., Ferrett, T. A., Heimann, P. A., Kerkhoff, H. G., Becker, U. & Shirley, D. A. “Inner-Shell Photoemission from the Iodine Atom in CH_3I”. *Phys. Rev. A* **30,** 239–244 (1984).

34. Brabec, T. & Krausz, F. “Intense Few-Cycle Laser Fields: Frontiers of Nonlinear Optics”. *Rev. Mod. Phys.* **72,** 545 (2000).

Chapter 4

Time-Resolved Inner-Shell Photoelectron and Photoion Spectroscopy of Dissociating Methyl Halide Molecules

4.1 Introduction

In this chapter, a series of experiments are presented in which the UV-induced photodissociation of CH_3I[a] and CH_2ICl molecules in the gas phase was investigated by time-resolved core-shell photoelectron and photoion spectroscopy, in experiments that were carried out at the free-electron laser facility in Hamburg (FLASH). The key idea of these experiments is to trace nuclear dynamics in small molecules by ionizing them with soft x-ray photons whose photon energies are well above a core-shell edge of one of the constituent atoms. This has two consequences: firstly, the ionization will be element-specific and, if the chemical environments of like atoms in the molecule differ considerably, also site-specific. Secondly, the atom that is ionized acts as a localized point emitter of electrons, and if the electrons reach de Broglie wavelengths as short as the internuclear distances, diffraction patterns can be observed in the photoelectron angular distributions. In static experiments, e. g., with synchrotron sources, this photoelectron diffraction effect is well-studied and understood.[2,3] The emergence of ultra-fast soft x-ray sources, like free-electron lasers, now opens up the possibility to extend this concept to time-resolved experiments, in which nuclear rearrangements in molecules can be observed by tracing changes in the photoelectron diffraction pattern. Previously, Boll *et al.*[4] have successfully demonstrated that changes in the photoelectron diffraction pattern of laser-aligned molecules can be observed in an experiment using FEL radiation. McFarland *et al.*[5] reported time-resolved measurements of Auger-electron spectra from an FEL experiment. Here, the authors were able to observe shifts in the Auger lines after the photoexcitation of thymine molecules. However, so far, time-resolved effects in the *direct* photoelectrons, which are the most immediate and direct probe of the ongoing nuclear dynamics, have not been observed; this chapter is intended to make a step forward in this direction.

The halomethanes are chosen as target molecules for two reasons: On the one hand, the iodine 4*d* levels possess a binding energy of roughly 60 eV, which makes them accessible to investigation by soft x-ray light sources. On the other hand, the UV dissociation dynamics of the C–I bond, especially in CH_3I, is *exceptionally* well investigated and understood (Alekseyev *et al.*[6] give an account of more than 80 publications as of 2007), making it an ideal model system for a large class of dissociation reactions. At wavelengths between 230 and 300 nm,

a Parts of the results of this chapter, namely the analysis of the photoion and -electron data for CH_3I were published in Braußе *et al.*[1]

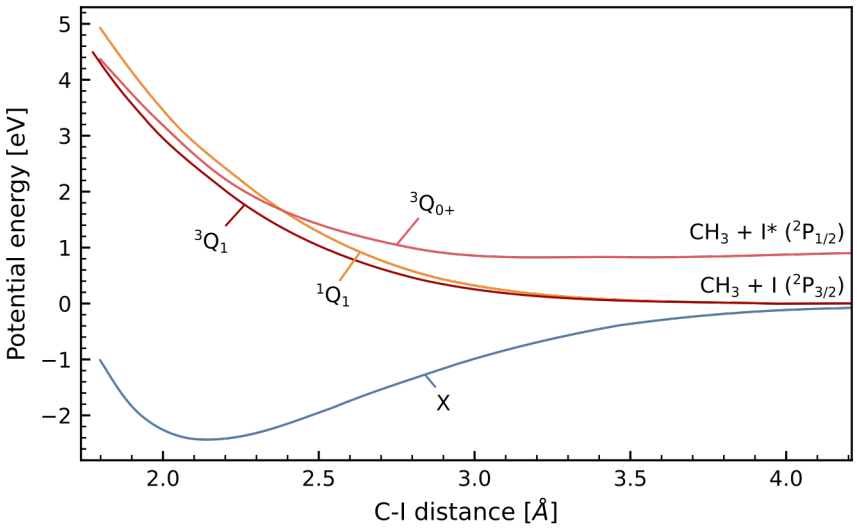

Figure 4.1 Potential-energy curves for CH_3I according to Alekseyev *et al.*[6] The curve labeled *X* represents the (electronic) ground state and the three *Q* states are the main contributors to the excited-state manifold of the *A* band.

CH_3I molecules are excited into an excited state manifold known as the *A* band. This *A* band is composed of three states, called $^3Q_1(E)$, $^3Q_{0^+}(A_1)$ and $^1Q(E)$, where the symbols in parentheses correspond to the irreducible representations of the C_{3v} point group that CH_3I belongs to. All three states are dissociative, but at 266 nm the transition occurs almost exclusively to the $^3Q_{0^+}(A_1)$ state that converges asymptotically to the spin-orbit excited state of iodine, I*($^2P_{1/2}$). However, depending on the exact excitation wavelength, some of the iodine atoms are also found ending up in the spin-orbit ground state, which is caused by a conical intersection that connects the $^3Q_{0^+}(A_1)$ and the $^1Q(E)$ states, with the latter converging to the I($^2P_{3/2}$) ground state.[6] For CH_2ICl, the dissociation dynamics are less well investigated, but a recent comparative study[7] between CH_3I and CH_2ICl, using resonance enhanced multiphoton ionization (REMPI) as a probing technique, suggests that the mechanism is very similar to that of CH_3I.

4.2 Experimental setup

The experiments described here were carried out on the CFEL-ASG multipurpose (CAMP)[8] chamber installed in the focus of beamline BL 1 at the free-electron laser facility in Hamburg (FLASH).[9] This endstation is specifically designed for performing pump–probe experiments in the gas phase, combining the FEL and an optical laser. A schematic overview over both the FLASH facility with its main infrastructure and the CAMP endstation are shown in Fig. 4.2. In this section, following a short introduction of the general FEL operating principle, the details of the CAMP chamber and the pump–probe setup are described and then an account of the diagnostics infrastructure installed at FLASH is given that plays an important role in post-processing the experimental data.

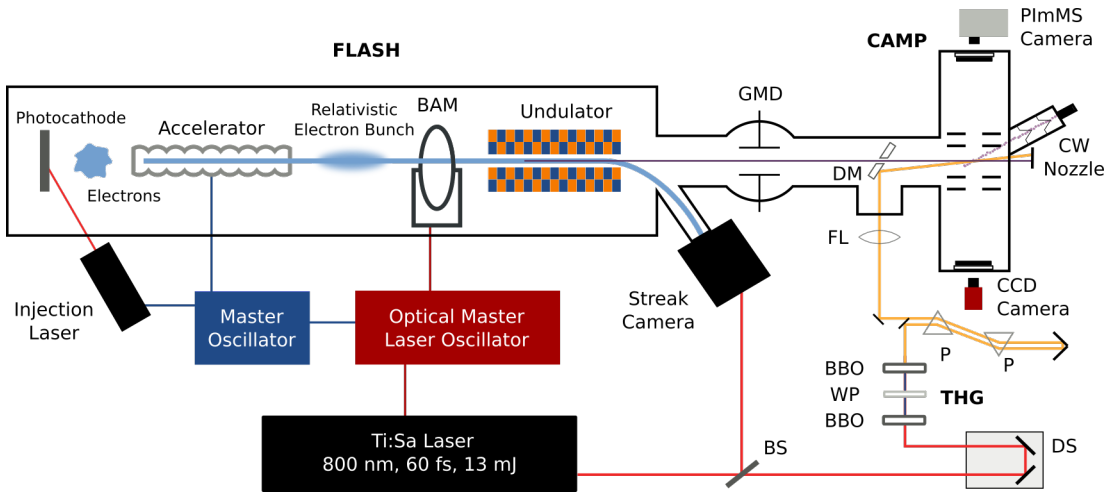

Figure 4.2 Sketch of the free-electron laser (FEL) and the experimental setup. Optical fiber links are shown as dark red lines, electronic (RF) links in dark blue. BAM: Beam-arrival monitor; GMD: gas monitor detector; PImMS camera: Pixel-imaging mass spectrometry camera; DM: drilled mirror; CW nozzle: continuous gas nozzle; FL: focusing lens; P: prism; THG: third-harmonic generation; BBO: β-barium borate crystal; WP: waveplate; DS: delay stage; BS: beam splitter. Based on the sketch in Savelyev *et al.*[10] (Fig. 1).

4.2.1 FLASH free-electron laser

We begin by briefly recalling the operating principle of the FLASH free-electron laser[11] to the extent that it may help understanding the technicalities that will follow: An electron cloud is created on a photocathode by irradiating it with a picosecond laser pulse. This electron bunch is then, in three stages, accelerated in super-conducting, linear accelerators and re-compressed in magnetic chicanes, reaching near-relativistic velocities at the end. Finally, it is sent through the undulator, an array of oppositely poled, permanent magnets. Forced onto quivering trajectories, the electrons spontaneously emit bremsstrahlung, which is amplified in an intricate process, aptly called self-amplification of spontaneous emission (SASE), to eventually yield coherent, short EUV or x-ray pulses, whose central wavelength can be tuned by adjusting the electrons' velocity. Even though SASE FELs have many attractive properties, like the high peak brilliance and photon flux, their spectral properties suffer from the stochastic amplification process that is based on spontaneous emission, leading to a randomized profile in the spectral and temporal domain. Furthermore, it is the SASE process that causes a timing uncertainty in the FEL pulse because the light is generated inside the electron bunch without an external reference. In seeded FELs, in contrast, this timing jitter does not occur.[12]

During the beamtime, FLASH was operated in single-bunch mode[b] to deliver ultrashort pulses of soft x-ray radiation at a central wavelength of 11.6 nm, with an average pulse energy of 115 µJ at a 10 Hz repetition rate. The FEL pulse duration was estimated to be around 120 fs full width at half maximum (FWHM). To reduce multiphoton interactions with the sample to a minimum, the FEL was typically attenuated with either a 400 nm silicon filter or an 800 nm niobium filter, both of which result in a transmission of roughly 3 %.

b As opposed to the multi-bunch mode, in which several closely spaced electron bunches are launched in every trigger cycle.

4.2.2 CAMP station at FLASH

Inside the endstation chamber, the FEL pulse was collinearly overlapped, using a drilled mirror, with a 266 nm pump pulse obtained by third-harmonic generation of the 800 nm output pulse from the Ti:Sapphire pump–probe laser system[13] . A prism compressor installed in the 266 nm beam path was used to partially compress the UV pulses to 100 fs (FWHM). The pulse energy of the UV pulses was typically 35 µJ before the drilled mirror. Both the UV and the FEL pulses were focused and overlapped inside a molecular beam of CH_3I or CH_2ICl molecules seeded in 1 bar helium. The molecular beam was obtained from a CW gas nozzle, followed by two skimmers. Charged fragments created by the interaction of the molecules with the combined UV and FEL pulses were accelerated towards two position sensitive detectors facing each other, using a double-sided velocity map imaging spectrometer (see Fig. 4.2). Electron momentum distributions were recorded using a 75 mm chevron-pair multi-channel plate detector (MCP) followed by a slow phosphor screen (model P20) and a CCD camera, whereas the ion momentum distributions were recorded using a 75 mm chevron-pair MCP detector followed by a fast phosphor screen (model P47) and the Pixel Imaging Mass Spectrometry (PImMS)[14] camera.[c] The PImMS camera allows recording both the hit position and the arrival time of the charged particles. It can operate at a maximum repetition rate of 59 Hz and can store up to 4 impact events per pixel and frame. In the present series of experiments, however, both the PImMS camera and the electron side's CCD camera were synchronized to the repetition rate of the FEL (10 Hz), storing the unique 32-bit bunch ID of the FEL alongside every single frame. Furthermore, we have employed the second, enhanced version of the PImMS camera, which features a significantly enlarged detector array of 324×324 pixels (compared to 72×72 pixels of the first model) with a maximum time resolution of 40 ns. Using the PImMS camera, the momentum distributions of all charged fragments are imaged simultaneously. Both electron and ion momentum distributions were recorded in single-shot acquisition to possibly correct for the inherent shot-to-shot fluctuations of the FEL during post-processing step, details of which are given below.

4.2.3 Diagnostics and synchronization

At FLASH, several tools are set up to monitor and characterize the parameters of the FEL operation on a shot-to-shot basis. Every single shot of the FEL is assigned a unique bunch ID that is stored together with all obtained parameters in the FLASH data acquisition (DAQ) stream. Two devices are particularly important: the gas monitor detector[15] (GMD) and the bunch arrival-time monitor[16] (BAM), both of which are sketched in Fig. 4.2. The GMD is used to measure the shot-to-shot pulse energy of the FEL and is set up between the undulators and the FLASH experimental hall. Essentially, it consists of a vacuum chamber filled with krypton at a pressure of $\sim 1.6 \times 10^{-6}$ mbar. This is low enough to allow a transmission >99 % of the FEL photons, but high enough to create a significant amount of photoelectrons and -ions. These charged particles are accelerated towards two Faraday cups, where they are collected and read out. By calibrating the resulting count rates properly, the single shot pulse energy can be recovered.

c Strictly, this was the second, improved version of the PImMS camera, PImMS2, which is equipped with a significantly larger detector array compared to the first model. For simplicity, we refer to it only as PImMS camera.

The BAM serves a different purpose: A key problem in performing pump–probe experiments between an optical laser and an FEL is the residual timing jitter between the two that arises from variations in the exact velocities of the electron bunches in the linear accelerator. At FLASH, where several stabilizing and feedback-control systems,[17] based on RF[13] and optical links[18], are set up, this jitter is typically reduced to roughly 100 fs (rms). For observing ultra-fast dynamics on a timescale of a few tens of femtoseconds, this is still insufficient. To reduce the timing uncertainty further, different schemes have been proposed. Certainly, the most proficient attempts involve setting up an x-ray–optical cross-correlator[19] behind the interaction region of the experiment, from which the precise delay between the FEL and the optical laser can be retrieved for every shot. With these setups, time resolutions down to 6 fs(rms) have been reported.[20] The main drawback of this approach is, however, that the cross-correlator has to be specifically tailored to every experiment, taking into account the exact geometrical and optical conditions.

Using the BAM, in turn, the timing jitter can be partially corrected without the need for an additional tool at the experiment. In the BAM, an inductive current created by the passing electron bunch is amplified and used to cause an electro-optical modulation of samples of the laser pulses that are generated in the optical master oscillator. The magnitude of this modulation can be related to the arrival-time difference between the electrons and the laser pulse. Strictly speaking, there is not one BAM running at FLASH, but there are several, some of which are part of a feedback loop, that continuously compensates for slow long-term drifts and large, sudden jumps in the timing. In what follows, the BAM we refer to has a dynamic range of 4 ps and can be used for single-shot corrections. Sudden changes in the timing that exceed this range can be identified with a streak camera,[17] that is also shown Fig. 4.2. In contrast to the BAM, the streak camera measures the actual delay between the electron bunch and the optical laser pulse. Its time resolution, however, is not better than 200 fs, and the values fed into the DAQ are updated only at a rate of 1 Hz, preventing single-shot corrections based on its measurements.

Making proper use of the BAM, the uncertainty in the bunch arrival time can be reduced from ≈100 fs to ≈15 fs, which is the standard error of the BAM instrument itself.[16] However, to estimate the *total* residual uncertainty in the timing between the FEL and the optical laser, also the sum of all jitter contributions from all other components in the signal chain have to be taken into account, which is on the order of ≈20 fs.[17] Therefore, the optimum timing precision that can be achieved with the setup described here, is about 27 fs,[10] which is significantly shorter than the cross correlation between the FEL and UV pulses, which is about 160 fs.

4.3 Data analysis

This section is dedicated to the process of analyzing the single-shot data both for electrons and ions, which, in many instances, poses unique challenges to the experimentalist. On the one hand, there is the sheer amount of data that is accumulated when an entire velocity map image is stored for every single shot. A strategy has to be found to compress these data sets, which is necessary for an efficient processing and sorting. On the other hand, a careful investigation of the shot-to-shot FEL parameter fluctuations can guide assessing the sanity and reproducibility of the experiment, which, in turn, helps to decide on the significance of weak,

time-dependent effects. Hence, the analysis is carried out in three stages: pre-processing, synthesis of VMI images after data sorting and selection, and assessment of a time-dependent series of data in terms of the FEL stability and the statistical error.

4.3.1 Pre-processing

Both the electron data, recorded with the CCD camera, and the ion data, captured by the PImMS camera, have to be pre-processed to exploit their full potential with respect to extracting the physically meaningful information content, but in a different fashion and for different reasons. In the case of the electron data, it is the size of the files that hampers straightforward handling. Every image is stored as 1000×1000 8-bit numbers, which, in a typical acquisition of 10 000 shots per delay point, amounts to 16 GiB per file. Now, for a typical pump–probe scan comprising 25 delay points with a $\leq$100 fs step width, data over at least 2.5×10^5 shots is collected. If the data set for every delay step would be treated individually, it would be possible to keep and process it entirely in memory of a work station machine. However, by adding timing-corrections, e. g., through the BAM as shown in Section 4.3.4, the pump–probe delay becomes a quasi-continuous variable, blurring the lines between data sets acquired at discrete delays. In that case, efficient processing can only be performed when the entire time-resolved scan can be held in memory. The best way to achieve this is to run a hit-detection routine over every image that identifies the number and position of all particle impacts and returns them in a tabular form. This corresponds to the complete – physical – information content of the image at the highest degree of data compression, essentially turning 1×10^6 integers, most of which are zero, into $2 \times N$ floating point numbers (due to centroiding), where N is the number of particles in the image. The main problem that can arise in the hit detection of electron data is something that would otherwise be considered a great advantage of the FEL: The high photon flux leads to a large number of charged particles created at every shot. As a consequence, the impacts may form densely clustered regions on the detector, that are not easily disentangled by straightforward routines.

Therefore, a multi-level hit detection was devised to tackle the problem of finding all particles in two consecutive steps: First, a global object-finding algorithm is applied to the image as a whole, using standard procedures from digital image processing.[21] For rates up to 100 counts per shot, this is typically sufficient to identify all impacts. If necessary, a second, local analysis can be carried out for every of the objects found in the first step to decide whether it is made up of one or more impacts and to segment it accordingly. A detailed discussion on the implementation and performance of this algorithm is given in Appendix C. Being able to carry out a hit-finding procedure successfully brings a number of advantages. Not only is the file size drastically reduced – with the current implementation, that is not optimized to this end, it decreases by a factor of 30 – but also the inevitable CCD noise is suppressed. Furthermore, the possibility to count the number of particles explicitly allows to analyze the experimental data in terms of Poissonian statistics, as will be shown in Section 4.3.5.

For the PImMS data, in contrast, the situation is different. The data stream that is read out from the camera already comes in a tabular format. What is reported is a list of the pixels that were lit since the last external trigger event: their x and y position, the time code relative to the trigger, and the register that was filled by recording this event. The latter gives the

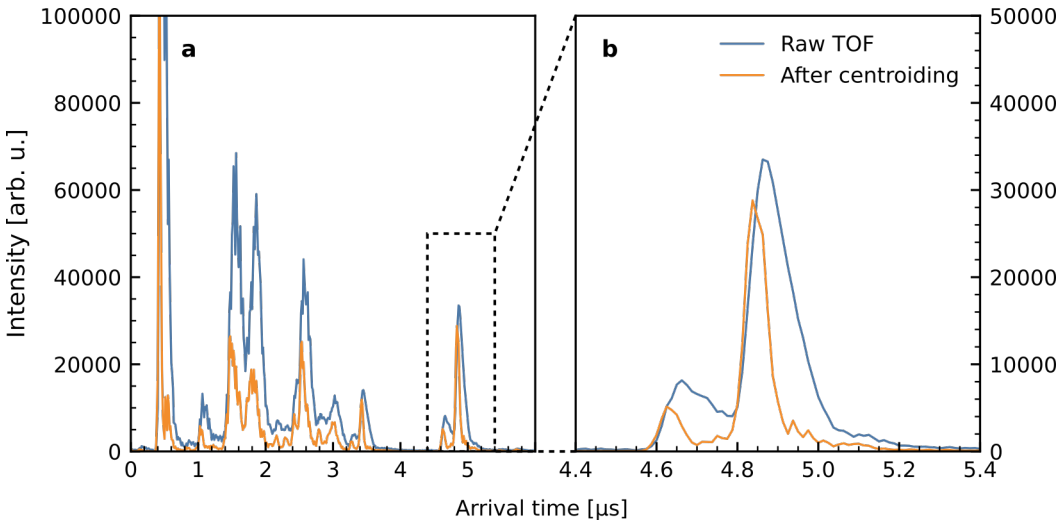

Figure 4.3 Result of the PImMS centroiding procedure. **a)** Comparison between the time-of-flight spectrum reconstructed from the raw PImMS data (blue) to the time-of-flight spectrum reconstructed from the results of the centroiding routine **b)** Zoom on the peak at ≈5 µs.

number of times the pixel was hit, with four being the maximum. Here the pre-processing serves a different purpose. The detector of the PImMS camera is known to suffer from the problem that whenever an impinging particle is detected at one pixel, the surrounding pixels are gradually triggered in the shape of an expanding circle. So, in the spatio-temporal domain, the impact resembles a cone. The problem that this brings is illustrated by the solid blue line in Fig. 4.3a. In the time-of-flight spectra, obtained by projecting the three-dimensional PImMS data onto the arrival-time axis, the individual fragment signals take an asymmetric shape, smeared out towards later arrival times, which, in turn, will unnecessarily deteriorate the time resolution that can be achieved with the PImMS camera.

The above effect is well-known from previous time-resolved particle imaging experiments,[22,23] although the exact reason for it is not understood. To tackle it, the authors of said studies have proposed different centroiding routines. Here we proceed in a straightforward manner: The same object-finding routine that is used for the global analysis of the electron detector images is employed for the PImMS data, but now in three dimensions. This routine identifies contiguous areas in an n-dimensional image of binary data, that is created by adding the entries from the PImMS record as truth values, or hits, to a three-dimensional array of zeros whose axes correspond to the time code, and the x and y position, respectively. Essentially, two pixels of value *true* are considered connected when one of them lies in the 3×3 cube of pixels surrounding the other one. Now, whereas *spatially* the impacts are always contiguous, in the time domain that is not necessarily true. That means that the time codes recorded by adjacent PImMS *detector pixels* can differ by more than one. To account for this fact, the time-code axis is rebinned into groups of the same size to restore the connectivity of the impact events in the above sense, with a group size of three yielding the best results. For every detected object, all the properties of interest are calculated: the center of mass, the total range of time-code units it spans, and the time of impact, which is given by the earliest time code it contains. Consequently, what is considered the actual particle impact

after processing is the center-of-mass x and y positions at that earliest time code. Coming back to Fig. 4.3, the advantage of applying the centroiding routine (orange line) becomes clear, as, in the time-of-flight spectrum, the peaks become narrower and more symmetric, which can be especially well seen in the zoomed section that is Fig. 4.3b.

4.3.2 Analysis of a single delay point

From the pre-processing with the above hit-detection routines, actual particle count rates can be extracted from the raw data. A closer inspection of these count rates reveals that the treatment of the electron data requires special attention because they contain a significant level of background signal. Here, we compare three experimental conditions that were covered during the experiment: first, the complete experiment with the molecular beam, plus the FEL and the UV light (which contains the desired two-color signal); second, experiments with the molecular beam, but with the UV pulse only, and, third, experiments with only the FEL pulses, without molecular beam and UV light. As the photon energy of the FEL surpasses the ionization potential (IP) of every constituent of the background gas, it will create electrons throughout the chamber, even when it is not focused, so that the third, "FEL-only" signal, corresponds to the electrons coming from the background gas. Such an ionization is not possible in the second, "UV-only" case because the 266 nm UV light corresponds to a photon energy of 4.65 eV, and the IPs of the background gases are all certainly > 10 eV.

The UV photon energy is, however, greater than the work function of aluminum, which is what the electrodes of the spectrometer are made of, and stray UV photons can therefore eject electrons from them. In the focus, the intensity of the UV beam is high enough to cause three-photon ionization of the target molecules, which is not strictly a background contribution, but also adds to the UV-only signal as the molecular beam is still present.

The reason for this can be seen in the way these data were acquired: While the FEL-only background signal was recorded in separate acquisitions before or after a pump–probe delay scan, the UV-only contribution is directly contained in the experimental data stream. During most of the beam time, a fast shutter was running that chops the FEL beam at every tenth shot and its status is written to the DAQ stream. Hence, in the analysis step, the shots where the shutter was closed can be separated based on the shutter status. To prove that this works and to assess the overall amount of background signal, the count rates of the different conditions are shown as histograms in Fig. 4.4a. What this shows is that the combined count rates of the "FEL-only" and the "UV-only" signals are on the order of 150 counts per shot, whereas the overall signal of the experiment is only about 260 counts per shot, from which we conclude that only a third of the overall signal can stem from the desired pump–probe photoelectron signal. In the panel beneath the histograms, the correlation between the count rates and the pulse energies reported by the GMD are shown. This reveals two pieces of information: First, there is no correlation between the UV-only signal and the GMD values, which is what is expected, and tells that the sorting based on the shutter data works correctly.

Second, the FEL-only background and the pump–probe signal distributions exhibit a very strong correlation with the GMD and an almost linear dependence on it. This indicates that the bunch IDs for the electron data were correctly recorded and synchronized to the FEL.

After pre-processing, the VMI detector images can be recovered by projecting the x and y positions onto a Cartesian grid of arbitrary size. We note here that, in principle, the methods

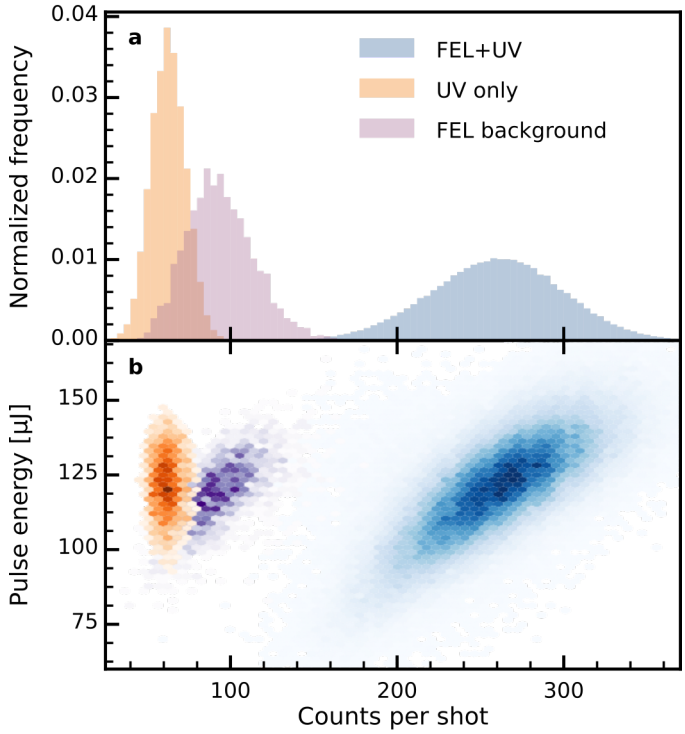

Figure 4.4 Typical electron count rates obtained after hit detection and centroiding. **a)** Normalized histograms of the detected counts per shot for the pump–probe signal (blue, 2.3×10^5 shots), the ionization from the 266 nm pulse (orange, 2×10^4 shots), and FEL background signal without the molecular beam (purple, 1×10^4 shots). **b)** Correlation between the count rates of **a** and the per-pulse energies measured by the GMD.

introduced above provide sub-pixel resolution, so, e. g., for electrons, a grid that is denser than the 1000×1000 pixels of the CCD camera could be used. This is in particular true when Gaussian centroiding is used, as Tremsin *et al.*[24] have shown. Here the limiting factor, however, is the statistics that can be accumulated in the measurement. For the Abel inversion, that represents the last step in the image analysis, an average count of 10 hits per pixel is required[25] to yield a reconstruction of high fidelity. For the electron data, a grid of 601×601 pixels has proven to give a good balance between resolution and per-pixel statistics, whereas for the ions the native grid size of 324×324 pixels of the PImMS2 camera was not changed.

A serious problem that the background contributions cause is that they may not be "Abel-invertible", which deteriorates the outcome of the Abel-inversion process. Therefore, when a VMI detector image for the total experimental signal, which we may call D_{EXP} and which is shown in Fig. 4.5a, is recreated from a selection of shots, the said UV and FEL background contributions, D_{UV} (Fig. 4.5b) and D_{FEL}(Fig. 4.5c), are subtracted from it. Especially, subtracting D_{FEL} is necessary to make the Abel-inversion process more robust, whereas D_{UV} only contains slow photoelectrons which are not expected to strongly affect the reconstruction of the high-energy photoline.

To account for the fact that the FEL-only measurement was not carried out in regular intervals and that its overall signal strength may differ from that during the pump–probe delay scan, D_{FEL} was scaled by a factor f_{BG} (close to one) to avoid over-subtracting the

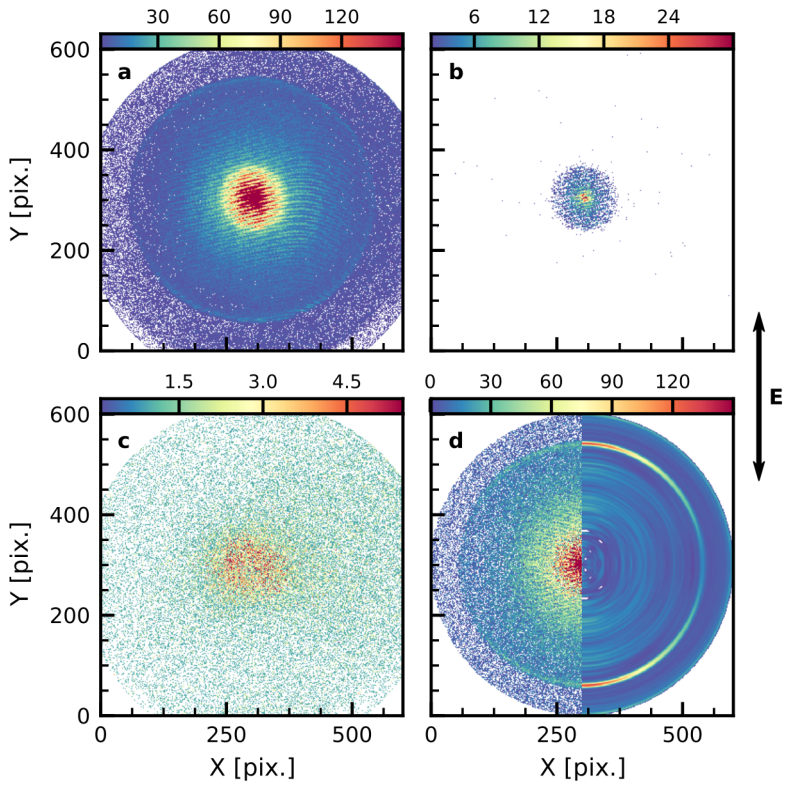

Figure 4.5 VMI detector images reconstructed from fitted hit positions. **a)** FEL+UV pump–probe signal image for a single delay point (shutter open). **b)** UV-only detector image (shutter closed). **c)** FEL background signal without the molecular beam. **d)** Same as **a** after scaling and subtraction of **b** and **c**. Left half: raw detector image; right half: after subsequent Abel inversion.

background contribution, which was judged by the number of negative pixels created. Cast into an equation, the final image D_{corr} is given as

$$D_{\mathrm{corr}} = D_{\mathrm{EXP}} - \frac{N_{\mathrm{EXP}}}{N_{\mathrm{UV}}} D_{\mathrm{UV}} - f_{\mathrm{BG}} \frac{N_{\mathrm{EXP}}}{N_{\mathrm{FEL}}} D_{\mathrm{FEL}}\,, \tag{4.1}$$

where N_i is the respective number of shots for the measurement of the contribution i, which is one of EXP, UV, and FEL; the outcome of this procedure is shown in the left half of Fig. 4.5d. Finally, data beyond a certain maximum radius are set to zero. The image is decomposed into four quadrants, three of which are summed to give the raw data set ready for the Abel inversion (see Appendix A for details). The fourth quadrant could not be used because a sapphire crystal mounted on a linear manipulator, that was used to image the overlap between the FEL and UV beams inside the chamber for alignment purposes, would, even when completely drawn out, interfere with the static field of the VMI so much that the imaging was heavily distorted, especially in the photoline that we intended to investigate. After inversion, the resulting inverted images, and quantities derived from them, like radial distributions, are normalized to the sum of the GMD pulse energies of all shots that contributed to D_{EXP}. Strictly, this procedure is correct only if all detected particles have been created in single-photon processes, for only then the particle yield depends linearly on the FEL intensity.

To test whether the intensity regime of the present experiments can be considered one where single-photon ionization dominates, a static FEL electron measurement comprising 20 000 shots was sorted and binned with respect to the GMD pulse energies; when the analyses of all the bins are collected in the same diagram, they may reveal higher order effects, such as the appearance of a double-ionization peak as a function of intensity. The bins were chosen such as to be of equal *number of shots* and not of equal *energy ranges* because, in the wings of the pulse-energy distribution, there may not be enough shots to yield reliable radial distributions. How the GMD histogram is partitioned into six bins is shown in Fig. 4.6a, whereas the corresponding, radial distributions, normalized to the GMD sum as explained above, are displayed in the panel next to it. If the intensity dependence was linear, all these distributions should now lie on top of each other, and this is generally what we find. Hence, it seems justified to assume a linear dependence of the particle yield on the intensity.

Only for the lowest bins, the peak height is a little lower than expected, which we can only explain by the assumption that the noise is dominating over the signal at these low pulse energies.

4.3.3 Spectrometer calibration

For calibrating the velocity scales in the ion and electron data, different strategies were pursued. Ideally, one just measures a sample for which the binding energies (for photoelectrons) or fragment-ion velocities (for photoions) are reported with great precision in the literature. For the electron side of the spectrometer, helium was measured at full FEL intensity, that is, with all metal filters withdrawn, the result of which is displayed in Fig. 4.7a. At this intensity, three discrete peaks are observed, as shown in the adjacent panel, that are assigned to single-photon ionization leading to He^+ in the ^2S ground state (binding energy 24.587 eV)[26] and, through a shake-up process,[d] in the ^2P first excited state (binding energy 65.44 eV[27]), as well as He^{2+}, that must have been created by a sequential two-photon double ionization, as the observed kinetic energy of the emitted electrons corresponds very well to the second ionization potential of helium, which is known to be 54.417 eV.[28] For the exact FEL photon energy, the values written to the DAQ were used as a reference, which, for this experiment, was reported to be 106.5 eV. With this information, the energy scale of the spectrometer is calibrated according to

$$R_i^2 = c(\hbar\omega - \mathrm{IP}_i)\,, \tag{4.2}$$

where R_i is the radius of one of the three photoelectron peaks introduced above, and IP_i is the corresponding ionization potential. Carrying out the linear regression according to Eq. (4.2), the result of which is shown in the inset of Fig. 4.7b, a calibration constant of $c = (335 \pm 4)\,\mathrm{pix}^2/\mathrm{eV}$ is retrieved, which corresponds to a relative uncertainty of ±1.3 %.

For the ion detector side, no comparable measurement was available. Also, careful investigation of the ion signal of the background gas, primarily made up of molecular nitrogen and water, did not reveal any discrete features that could be used for calibration. Therefore, we resorted to calibrating our ion data with respect to the results of Murillo-Sánchez *et al.*,[7] who report asymptotic fragment kinetic energies for the photodissociation of CH_3I and CH_2ICl at

d In a shake-up ionization, one electron is ejected and a second one is promoted to a bound orbital of higher energy at the same time.

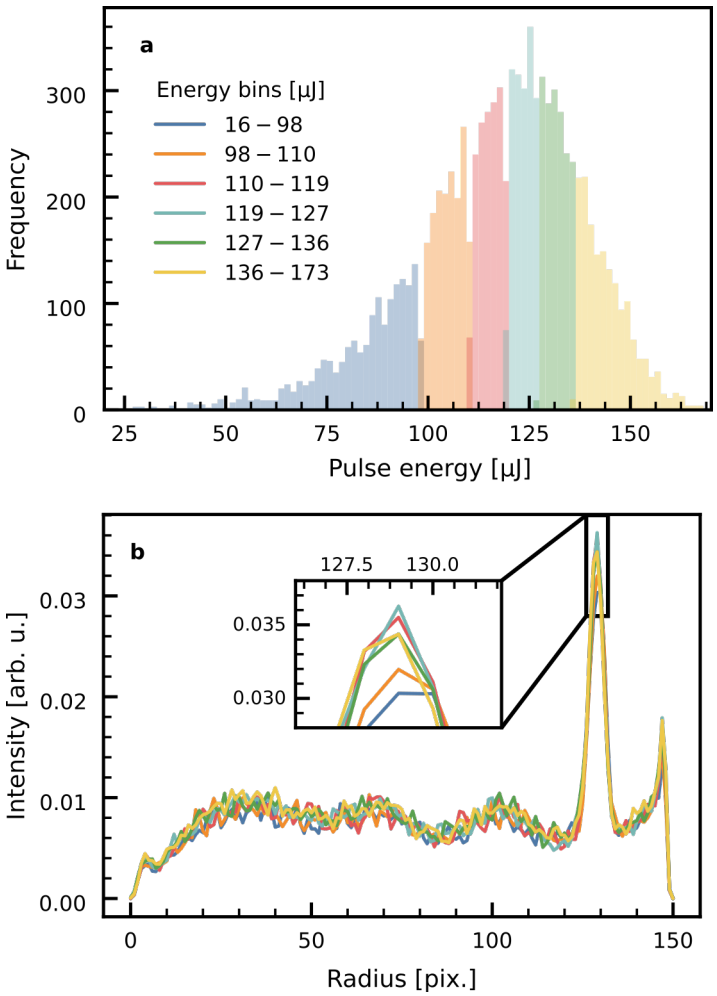

Figure 4.6 Effect of FEL pulse energy sorting and normalization on the photoelectron momentum distribution. **a)** Histogram of the GMD pulse energies for a static FEL measurement over 20 000 shots, binned into six groups with equal numbers of shots. **b)** Angle-integrated momentum distributions for the bins shown in **a** after Abel inversion. The line colors correspond to those given in the legend of **a**. The inset shows the photoline peaks in detail.

266 nm, which is a quantity that is also contained in the present data, as we will discuss in Section 4.4.

4.3.4 Timing diagnostics

As outlined in Section 4.2.3, two devices are used to monitor the pump–probe timing, the streak camera and the BAM. In Fig. 4.8a and b, representative records that show no pathological behavior for an experimental run of 2×10^5 shots are displayed. In the streak-camera data, a slow oscillatory motion with an amplitude of about 200 fs is observed, but, given the limited resolution of this device and the fact that these oscillations were present in all data sets investigated, we assume they can be ignored. The values of the BAM, on the other hand, are scattered around a central value in what seems to be a Gaussian distribution with a full width

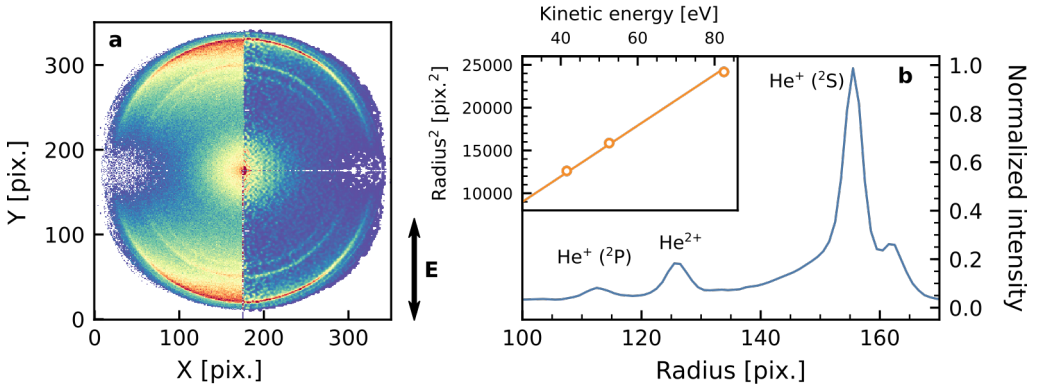

Figure 4.7 Calibration of the electron side of the double-sided spectrometer with helium, irradiated by the 11.6 nm pulse at full intensity. **a)** Left half: raw VMI detector image; right half: after Abel inversion. **b)** Angle-integrated photoelectron momentum distribution of the Abel-inverted measurement. The inset shows the calibration curve for the three peaks marked in the main panel.

at half maximum (FWHM) of about 100 fs.

The delays that were set on the opto-mechanical delay stage can now be corrected by the arrival times reported by the BAM as simple as

$$t_i^{\mathrm{corr}} = t_i^{\mathrm{DS}} - (t_i^{\mathrm{BAM}} - \tilde{t}_{1/2}^{\mathrm{BAM}}), \tag{4.3}$$

where i corresponds to the bunch ID, *DS* stands for delay stage and $\tilde{t}_{1/2}^{BAM}$ is the median of the whole BAM data set. To illustrate the effect of this correction, in Fig. 4.8 both the set delays and the corrected values are plotted on top of each other. Clearly, when the step width is on the order of 100 fs, the corrected delays resemble a quasi-continuous variable, that can now be rebinned into arbitrary shapes and sizes. Furthermore, it becomes possible to use different bin sizes depending on the statistics of the data. Therefore, for the ion data typically a finer binning could be used than for the electrons because the observed time-dependent effects were much more robust in the ions.

Admittedly, one can argue that the BAM correction will not bring any benefits because the time resolution of the experiment, that is limited by the cross correlation between the two laser pulses. Assuming pulse durations (FWHM) of 120 fs for the FEL and 100 fs for the UV pulses, this cross correlation is on the order of 160 fs (FWHM). Therfore, a jitter of 100 fs will hardly deteriorate the achievable time resolution. Nevertheless, we consider the *a posteriori* delay correction and sorting a good practice to guarantee the maximum consistency and reproducibility of the experimental findings and have therefore applied it to all data presented in this chapter.

4.3.5 Sources of systematic and statistical errors

The parameters of the FEL radiation are subject to instabilities both on a short- and a long-term scale. To detect long-term drifts in the FEL performance, the frequency distributions of the reported GMD pulse energies and the central wavelength of the FEL were extracted for each delay and visualized in a so-called violin plot, which shows the smoothed frequency

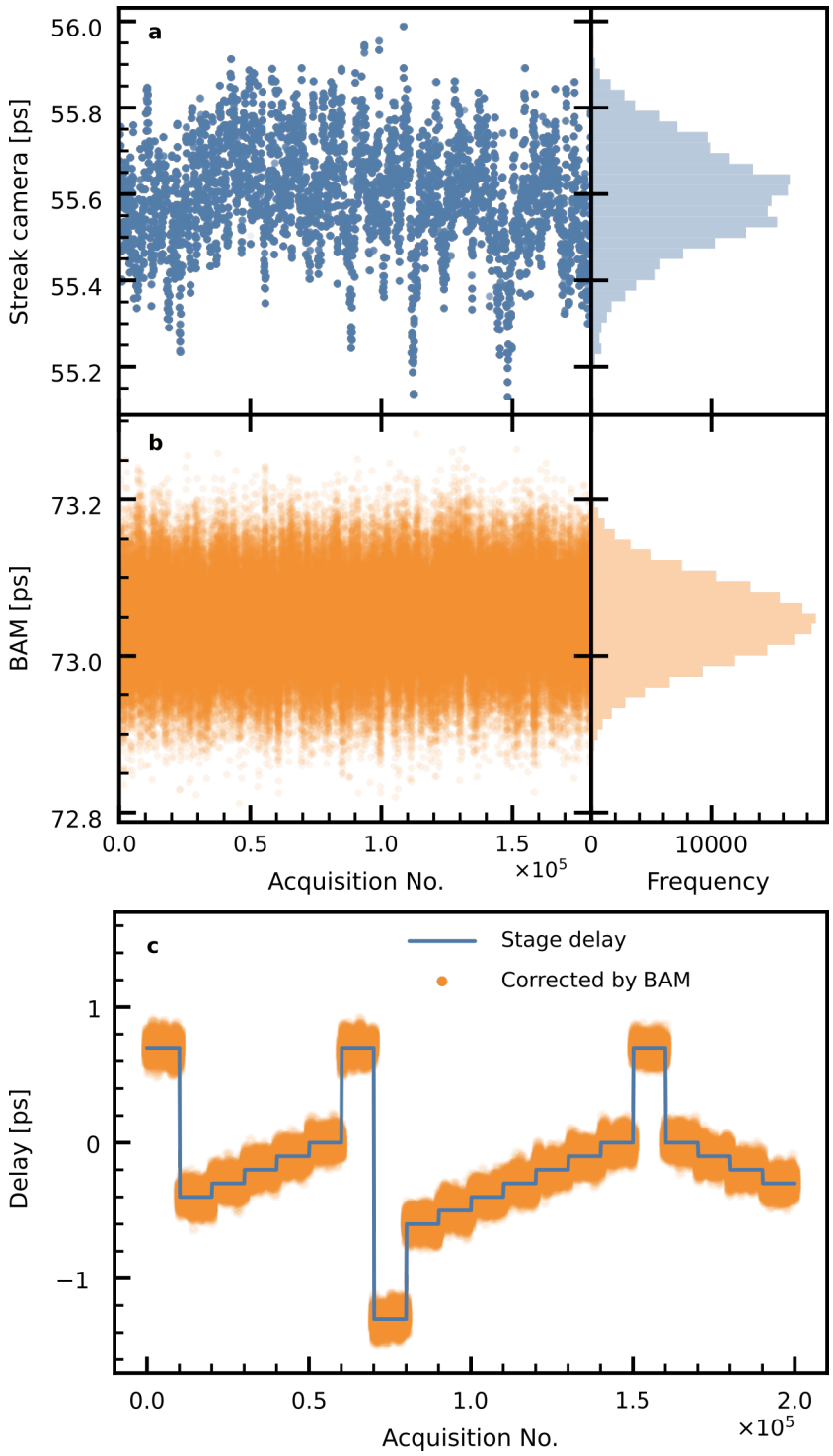

Figure 4.8 Timing diagnostics. **a)** Streak camera measurements and **b)** BAM (fine) values over 2×10^5 shots. The adjacent panels show the histogram over the whole data set. **c)** Delays set on the opto-mechanical delay stage (blue solid line) and corrected delays according to Eq. (4.3) (orange dots) for the same data as in **a** and **b**.

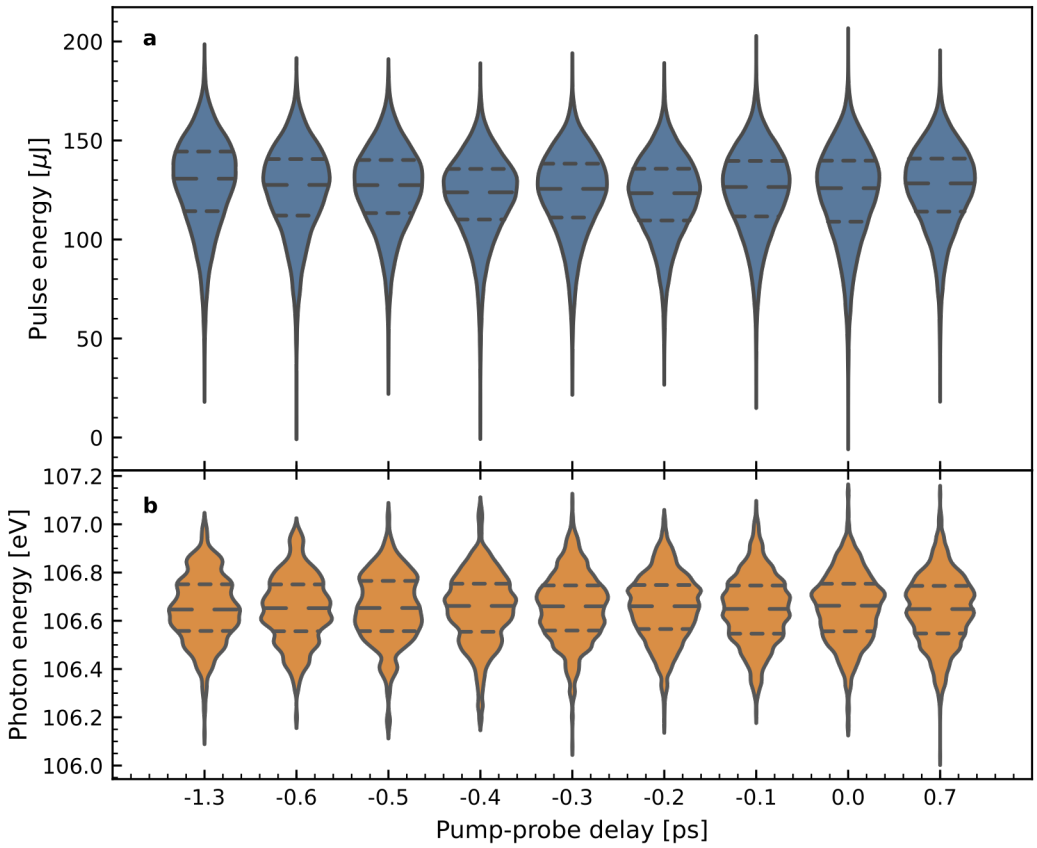

Figure 4.9 Long-term stability of the FEL parameters, shown as violin plots for the pulse energy **(a)** and the central wavelength **(b)** as a function of the delays set on the delay stage. The "violins" are just the smoothed, normalized frequency distributions of the respective parameter at these delays. The fine, broken lines indicate, from bottom to top: the lower quartile, the median, and the upper quartile.

distribution, vertically mirrored, with the lower and upper quartiles and the median indicated by horizontal lines. Looking at the results for the GMD pulse energies, Fig. 4.9a, no anomalies are observed that would give rise to concerns for the duration of this scan, which corresponds to a net acquisition time of roughly 6 hours. At the same time, the data for the photon energy, Fig. 4.9b, are in terms of the median and the quartiles, perfectly stable, but the distributions themselves show a strange, multi-modal structure whose origin is unknown.

Regarding the statistical uncertainties inherent in the experimental results, at least two sources of error have to be considered: First, any particle-detector experiment should follow Poissonian statistics. To verify that this is actually true, a single delay point of an electron pump–probe scan was chosen and, instead of casting the particle hits onto a Cartesian grid, they were binned according to their radial distance from the image center. Now, for every radial bin, a histogram for the number of counts k can be created, which was compared to a Poisson distribution,

$$P(\lambda, k) = \mathrm{e}^{-\lambda} \frac{\lambda^k}{k!}\,, \tag{4.4}$$

in which λ was adjusted as a free parameter. As it turns out, all of these fits show an excellent agreement, with a typical residual of $<1 \times 10^{-3}$; as an example, two such fits are shown in the insets of Fig. 4.10a. Therefore, we conclude that the experimental data indeed follow Poissonian statistics, and consequently the confidence interval of the observed data can be safely assumed to be that of a Poissonian distribution, which, at a confidence level $1 - \alpha$, is given by

$$\frac{1}{2}\chi^2(\alpha/2; 2k) \leq \mu \leq \frac{1}{2}\chi^2(1 - \alpha/2; 2k + 2)\,, \tag{4.5}$$

where $\chi^2(x; i)$ denotes the quantile function of a chi-squared distribution with i degrees of freedom; k is the total frequency after n observations, and $\mu = n\lambda$ its expectation value. The confidence intervals at the 95 % level are displayed in Fig. 4.10a and are typically on the order of ±3 %.

A second source of uncertainties are the errors introduced by the Abel-inversion routine, that, necessarily, always has to be applied to retrieve the physically meaningful information from the raw detector images. Unfortunately, estimating the error that the Abel inversion introduces is not straightforward, and it is not obvious how the above errors propagate into the final inverted results. What can be investigated, however, is the robustness of the inversion routine against statistical fluctuations of the input data. To this end, a bootstrapping procedure was applied, which works as follows:[29] As an outcome of the inversion, not only the inverted image, but also the Abel-projected simulation of the raw detector data are obtained. Subtracting this simulation from the experimental input image gives the pixel-wise residuals. These residuals are collected and a "noise image" is created by drawing residuals from that distribution *with replacement*.[e] The "noise image" is added to the simulation, that sum is subjected to another iteration of the inversion, and its result is saved for later analysis. This process of creating a noise image from the residuals, its addition to the simulation and subsequent inversion is repeated many times and, eventually, the collected results can be statistically analyzed. Note that, while this procedure is *conceptually* simple, it is the hundreds of inversions that make it *computationally* demanding. What is shown in Fig. 4.10b is how the interquartile ranges for the radial intensity distribution, obtained from bootstrapping the data set from the panel above with $N = 400$ iterations, evolve as a function of radius. Comparing the confidence intervals of the raw data, Fig. 4.10a, to the uncertainty that is introduced by the Abel-inversion routine, one can conclude that the Abel-inversion makes a very similar, but still small contribution to the overall uncertainty. When the same analysis is carried out for the sensitivity of the β_2 parameter against statistical noise, a much greater response is found. In particular, only below 50 pix. and around the photoline feature at 250 pix., β_2 values are measured that are *significantly* different from zero, and when we estimate the relative error at the photoline, to be on the order of 20 %.

e This means that the residuals are only copied, but not used up. In other words, at every drawing, all residuals are available and the chance of drawing any of them is always the same, namely $1/N$ for N data points. As a consequence, a given residual can appear in the "noise image" any number of times (including not at all).

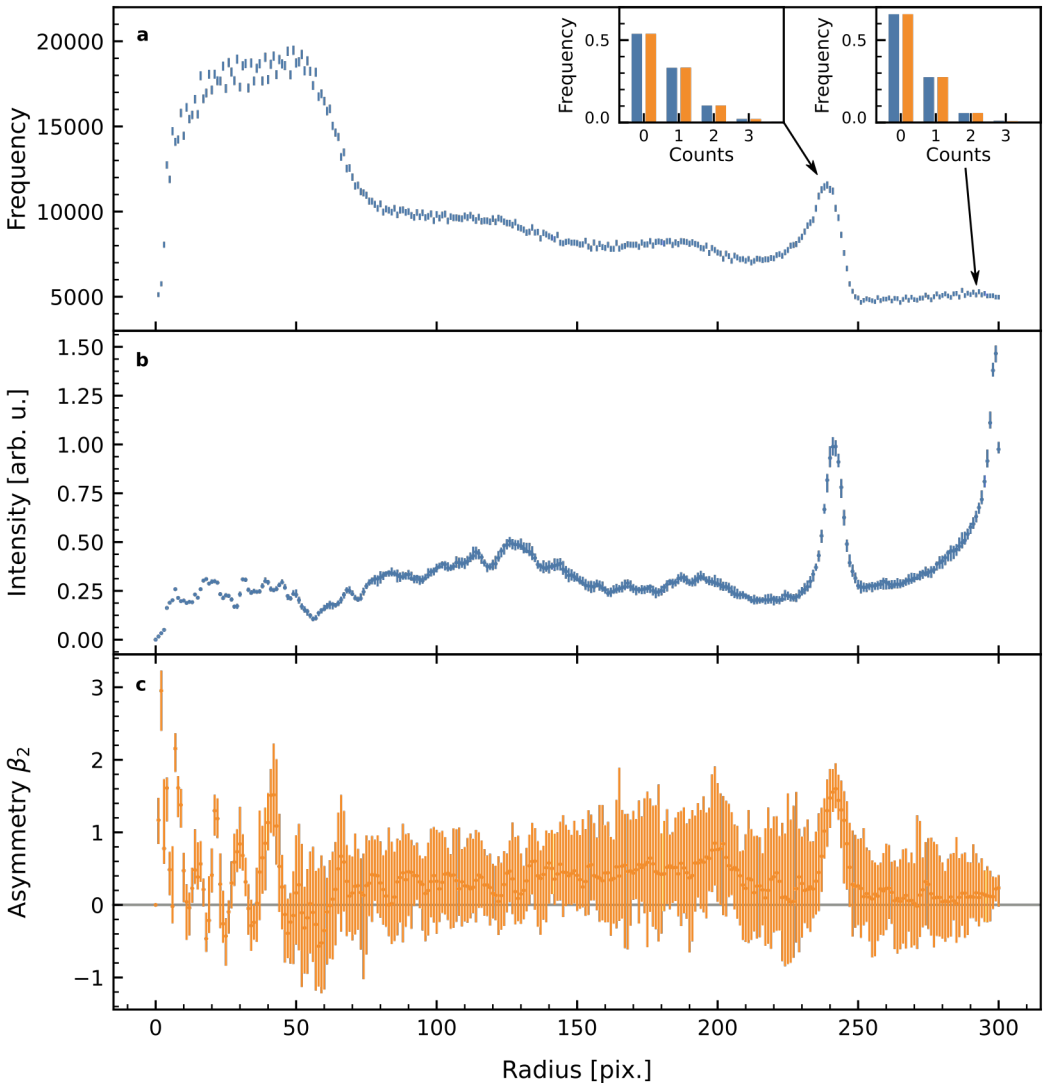

Figure 4.10 Statistical errors of an electron measurement with the VMI. **a)** Confidence intervals at the 95 % level for the radial intensity distribution of the raw electron data after centroiding, assuming the measurement obeys Poissonian statistics. The insets show normalized histograms of the count rates for two selected radial bins (blue) and a fit with a Poissonian distribution (orange). **b, c)** Medians (dots) and interquartile ranges (error bars) for the inversion process obtained from bootstrapping the inversion routine with $N = 400$ for the radial intensity distribution **(b)** and the asymmetry parameter **(c)**.

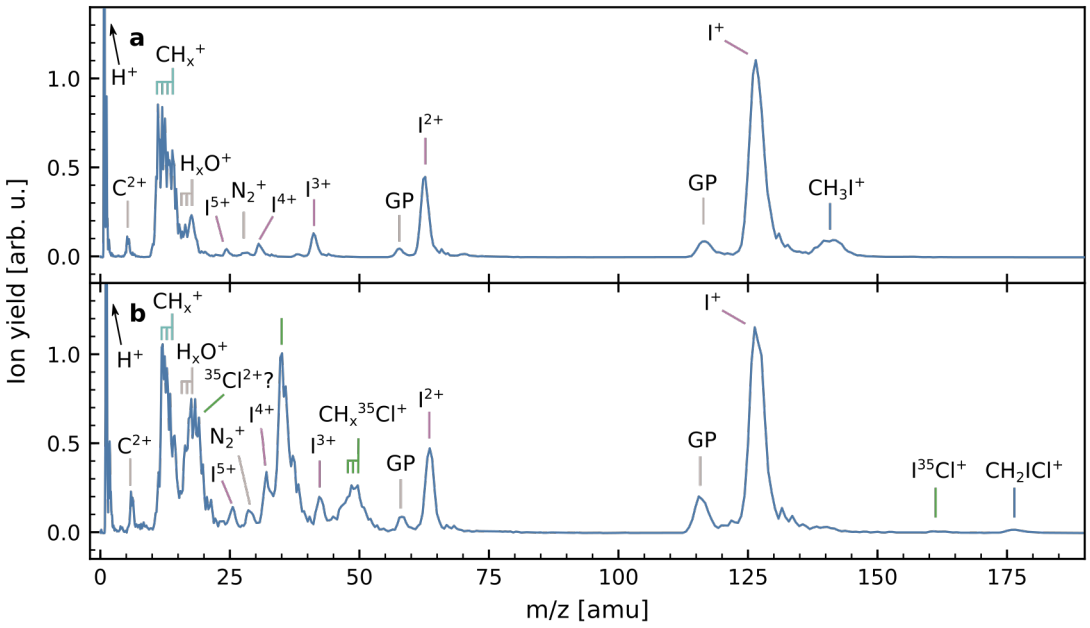

Figure 4.11 Ion time-of-flight spectra recorded in CH_3I **(a)** and CH_2ICl **(b)** upon ionization by an 11.6 nm FEL pulse. In both cases, the spectrum is dominated by I^{n+} and $CH_x{}^+$ fragments. In **b**, additionally, a series of chlorine-containing fragments is observed. The "ghost peaks", labeled as **GP**, eluded assignment.

4.4 Photoion spectroscopy

4.4.1 Time-of-flight spectra

As was outlined in Section 4.3.1, the PImMS camera allows to resolve the particles impinging on the detector in three dimensions, namely an arrival-time and two spatial dimensions. If the resulting data set is summed over the two spatial dimensions, the time-of-flight spectrum of the arriving particles is recovered. Typical time-of-flight spectra for ionization with the 11.6 nm FEL pulse are shown in Fig. 4.11. The mass-over-charge ratios were obtained by calibrating the arrival times of the I^{n+} (n = 1–3) fragments with the Wiley-McLaren formula.[30] For both molecules, the number of parent molecular ions formed is very small and the spectra are mostly composed of I^{n+} fragments and the respective co-fragments $CH_xCl_y{}^+$. In the case of CH_2ICl, also a significant amount of $CH_x{}^+$ and Cl^+ fragments are formed, that could either result from a subsequent fragmentation of the CH_2Cl^+ fragment or a many-body breakup of the parent ion. Furthermore, in both spectra a series of smaller peaks accompanying the I^{n+} signals can be observed, that eluded assignment in terms of meaningful fragment formulas and that are labeled "GP" for "ghost peak" in Fig. 4.11. In his PhD thesis on the technology and application of the PImMS camera, Slater[23] explains the appearance of "ghost peaks" as resulting from a poor choice of parameters for his hit-detection routine. The artifacts he describes appear, however, at arrival times longer than the main peaks, whereas we observe them at shorter arrival times. Furthermore, for the present set of experiments, it was verified that they exist in the raw PImMS data, as well, so that their exact origin remains unclear.

The soft x-ray wavelength of 11.6 nm was chosen to be close to the $\epsilon f \leftarrow 4d$ giant resonance in iodine, that is centered at a photon energy of 94 eV[31], and whose cross section is roughly 10 times larger than that of the valence orbitals. Hence, a vacancy will be preferably created in the iodine $4d$ shell and this core hole relaxes through one or two molecular Auger decays, yielding doubly and triply charged molecular ions. These ions, in turn, fragment after a fast charge redistribution that occurs throughout the molecular ion. The appearance of I^{n+} fragments with charge states higher than three suggests that a small fraction of the ionized species had also absorbed a second photon during the 120 fs duration of the FEL pulse. We conclude this from considering the ionization potentials (IPs) of the iodine $n+$ *atomic* ions because no comparable data is available for the molecules under investigation, but we can assume that the picture is qualitatively similar. According to Fadley *et al.*,[32] the IP for the ionization of I^{n+} to $I^{(n+1)+}$ is approximately $(n+1)\cdot 10$ eV. The binding energy of the $4d$ electrons is 58.3 eV,[33] which is about 48 eV above the first IP (10.4 eV). In other words, the singly charged ion has 48 eV of energy in excess. Judging from the approximate IPs, a single Auger decay (into I^{2+}) requires at least 20 eV of excess energy, and two consecutive decays $\approx 20 + 30$ eV. Therefore, depending on the exact IPs for the molecules, two Auger decays seem to be *just about* energetically accessible after (single) photoionization of the $4d$ shell. If non-sequential photoionization processes would contribute significantly, of course charge states of up to 4+ could in principle be formed at the given photon energy ($10 + 20 + 30 + 40$ eV < 107 eV), but we suspect that the probability for such a mechanism is extremely small. Instead, as mentioned above, we assume that a second photon is absorbed during the duration of the FEL pulse. When this happens, the formation of highly charged iodine ions is even more favorable because the C–I bond tends to stretch after the first ionization step, resulting in a suppression of the charge redistribution efficiency.[34,35]

4.4.2 Photoion spectra

With the help of the above time-of-flight spectra, time windows for the reconstruction of the VMI ion images can be selected. Typically, these windows were chosen to encompass the full width of the ion peak, touching the baseline at both wings. In this way, it was ensured that both early and late ions were collected that are necessary to recover the full Abel-projected Newton sphere. The reconstructed VMI images were subjected to the usual data treatment including Abel inversion, as explained in Appendix A, without any sort of background subtraction.

Ion momentum spectra for selected mass-over-charge ratios are displayed in Fig. 4.12 as a function of the pump–probe delay between the 266 nm and the 11.6 nm pulses, together with the kinetic energy spectra extracted before and after time overlap. We note that the pump–probe delays are only the "lab book delays", which are not properly referenced to a time-overlap signal, which is a problem that we will come back to later in this section. Notably, the kinetic energy spectrum for the singly ionized iodine ion is almost independent of the pump–probe delay for both CH_3I and CH_2ICl, whereas a narrow contribution appears at low kinetic energies in all I^{n+} with $n > 1$, when the UV pulse precedes the FEL pulse (labeled as A in Fig. 4.12).

The yield of this peak increases within a few hundred femtoseconds after time overlap and remains constant thereafter. This feature must originate from the wave packet launched on the dissociative state manifold of CH_3I (CH_2ICl), leading to neutral CH_3 (CH_2Cl) fragments

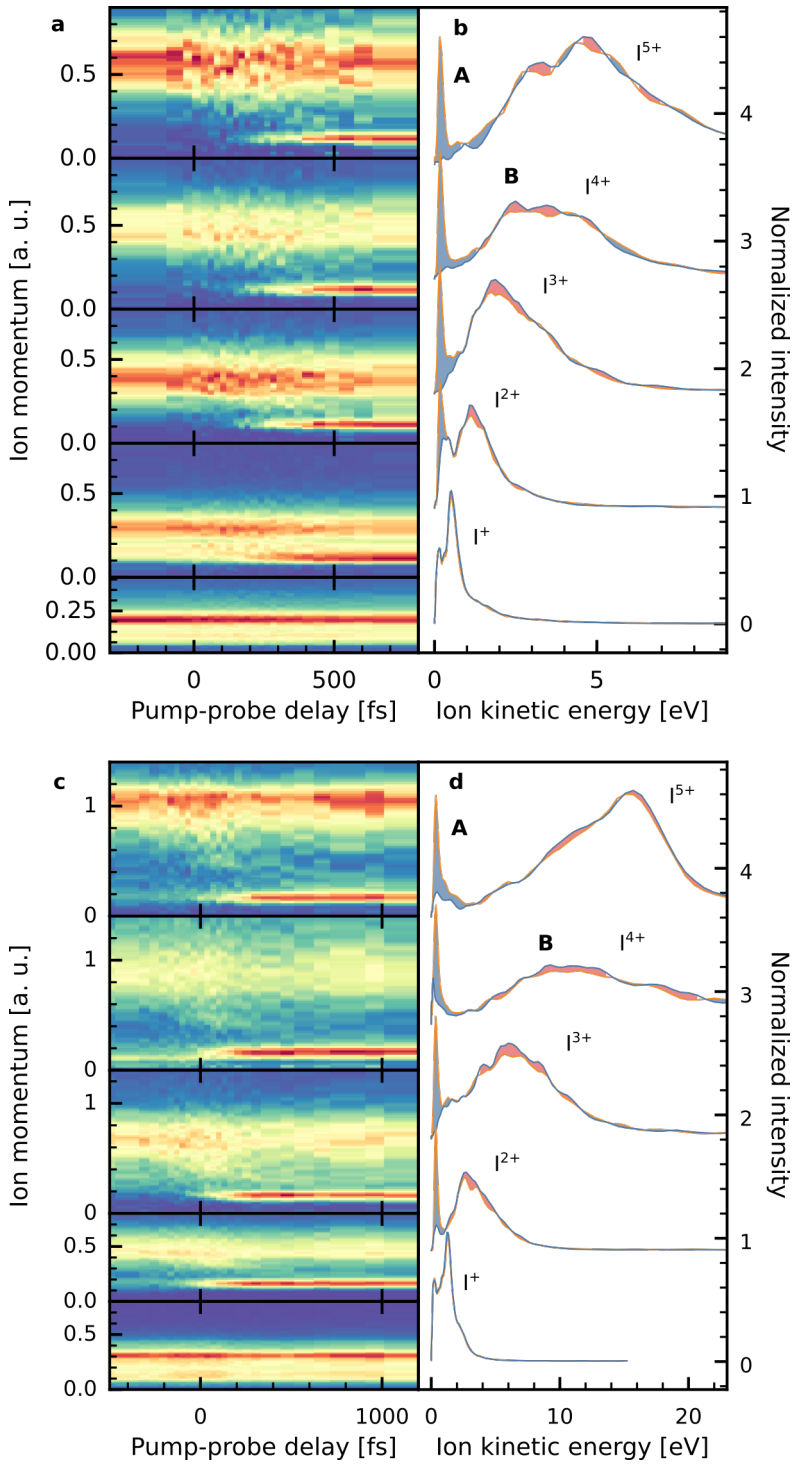

Figure 4.12 Time-dependent I^{n+} ion momentum distributions recorded for CH_3I **(a)** and CH_2ICl **(c)** as a function of the UV pump–FEL probe delay and corresponding kinetic energy spectra (**b** and **d**) for two delays: $t = -1$ ps (blue line), i. e., the FEL pulse comes first; $t = +1$ ps (orange line), i. e., the UV pulse comes first. Shaded areas highlight the increase (blue) and decrease (red) of the signal after time overlap.

and iodine atoms, where the latter are ionized by the FEL pulse. Therefore, this channel's kinetic energy must reflect the asymptotic energy that the iodine fragments acquired during dissociation along the repulsive state potentials. For all I^{n+} fragments, including I^+, broad, high-energy features, labeled B in Fig. 4.12, are observed. These are assigned to the Coulomb explosion of ground state molecules, following core-shell ionization and molecular Auger decay. All of these features show a decrease after time overlap, indicating a depletion of the ground state population.

As discussed above, the delay-dependent channel that appears at low kinetic energies results from ionization following the UV-induced dissociation into neutral fragments. The maximum energy available for the $I(^3P_{3/2})$ and $I^*(^3P_{1/2})$ fragments formed by UV-dissociation is given by

$$E_{av}(I) = \frac{m_{cofrag}}{m_{mol}}\left(\hbar\omega - D_0 - E_{SO}(I) - E_i^{mol}\right), \tag{4.6}$$

where $\hbar\omega$ is the photon energy, D_0 the dissociation energy (2.41 eV and 2.25 eV for CH_3I and CH_2ICl, respectively); E_{SO} is the spin-orbit splitting of 0.946 eV and E_i^{mol} the internal energy of the molecule. The quantity m_{cofrag} is the mass of the co-fragment formed during dissociation, i. e., CH_3 and CH_2Cl for methyl iodide and chloroiodomethane, respectively, and m_{mol} the mass of the parent molecule. The fraction of masses reflects the fact that the lighter co-fragment carries away most of the released kinetic energy, so that, e. g., in the case of CH_3I, only 10 % of the kinetic energy are transferred to the iodine atom. Accordingly, the splitting between the two spin-orbit channels is scaled down by the same factor, so that, given the resolution of our velocity map imaging spectrometer, which we estimate to be about 100 meV below 1 eV, the two dissociative channels of ground and spin-orbit excited iodine will overlap in the final kinetic energy spectrum and cannot be distinguished. In previous work,[7] a quantum yield for I^* formation of 0.75 (0.52) in CH_3I (CH_2ICl) was reported at an excitation wavelength of 266 nm.

In Table 4.1, the measured fragment kinetic energies of the delay-dependent, low-energy channel are compared to values obtained from Eq. (4.6) if the internal energy of the molecules is neglected. Taking into account both the quantum yields for the formation of the two iodine species and the limited energy resolution, a rather good agreement is found for the CH_3I molecule, but a large deviation from the calculated values is observed for the fragment kinetic energy measured in the case of CH_2ICl. We assign this difference to a significant redistribution of the available energy over the rotational and vibrational degrees of freedom of the co-fragment.[7] From our measurement, we can estimate that 36 % of the total available energy is transferred to the internal energy of the co-fragment.

The time for the appearance of the low kinetic-energy feature can be quantified for both molecules by extracting the integrated yield of this feature that appears in all I^{n+} ($n > 1$) channels as a function of pump–probe delay. This is shown in Fig. 4.13, together with the result of a fit to a sigmoidal model function of the form

$$A_{step}(t) = \frac{A_0}{2}\left(1 + \mathrm{erf}\left(\frac{t-\mu}{\sigma}\right)\right) + C\,, \tag{4.7}$$

where $\mathrm{erf}(x)$ denotes the error function, A_0 the height of the step, μ and σ its center and width, respectively, and C is a constant offset that allows for a time-independent baseline.

Table 4.1 Maximum available energy and measured translational kinetic energy for CH_3I and CH_2ICl molecules.

		Fragment kinetic energy [eV]	
		Calc.	Expt.
CH_3I	$I(^3P_{3/2})$	0.13	0.17
	$I^*(^3P_{1/2})$	0.23	
CH_2ICl	$I(^3P_{3/2})$	0.39	0.34
	$I^*(^3P_{1/2})$	0.66	

This particular functional form, using the error function or cumulative Gaussian distribution, is chosen because, if we assume that the appearance is instantaneous, this step-like behavior is broadened by the cross-correlation of the two laser pulses. Technically, the error function arises from the convolution of a Heaviside step function with a Gaussian distribution. By carrying out this convolution analytically, the full width at half-maximum of the Gaussian component takes the form $\mathrm{FWHM} = 2\sqrt{\ln 2}\,\sigma \approx 1.67\sigma$. The center and width parameters retrieved from this fitting procedure are listed in Table 4.2. While, for both molecules, the widths of the step functions are nearly independent of the charge on the iodine, we find a clear increase of the center position with increasing charge state, as is apparent from both Fig. 4.13 and Table 4.2. We note here, however, that the *absolute* zero delay is not known precisely for these experiments as we were not able to observe a signal corresponding to the cross-correlation between UV and FEL pulses in any of the recorded fragments. Still, the trend of increasing appearance times has been observed in previous experiments on the photodissociation of CH_3I molecules ionized at 1.7 nm.[36,37] The authors attribute this charge-state-dependent shift to an intramolecular charge transfer or charge redistribution process that follows the removal of an iodine core-shell electron: As long as the iodine ion is in close proximity to the co-fragment, the highly excited system can relax through ionization of the (chloro-)methyl fragment, which is mediated by the Coulomb attraction of the ion, and which creates another charge, located on the co-fragment. As the two fragments move apart, a potential barrier builds up between them and when this barrier reaches the binding energy of the most weakly bound electrons in the co-fragment, the charge redistribution is suppressed. From this point on, which is referred to as the critical internuclear distance, R_{crit}, the iodine ions undergo atomic Auger decay instead and the additional charge is created in the iodine atom instead. These atomic ions move with the asymptotic kinetic energy release of the photodissociation and are detected as the slow ions under investigation. What this model also implies is that the higher the charge state of the iodine ion, the farther its Coulomb interaction will reach, leading to a longer critical distance and, hence, a later appearance time. This model also explains the absence of this channel in the singly ionized iodine atoms: As the molecule has to carry at least one charge for the charge redistribution to happen, the suppression of this mechanism at R_{crit} will yield at least doubly charged iodine ions. In principle, I^+ could also be formed by valence ionization of the neutral iodine fragments after the dissociation, but probably the cross sections for these channels are so small that, in our experiment, we are not sensitive enough to observe it.

The critical internuclear distance at which the charge transfer is suppressed can be approxi-

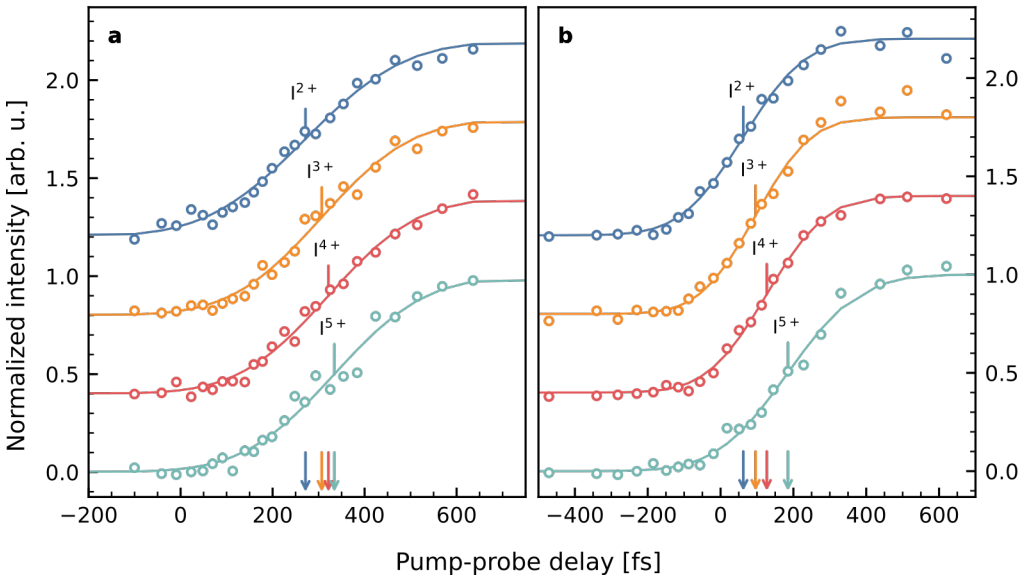

Figure 4.13 Normalized, integrated yield of the low-energy channel as a function of the delay between the UV and the FEL pulse for several low charge states of iodine (circles) together with the corresponding fit according to 4.7 (solid line). Arrows indicate the center positions of the fitted functions. Negative delays correspond to the situation where the FEL pulse arrives first. **a)** CH_3I; **b)** CH_2ICl.

Table 4.2 Experimental center positions (corrected and uncorrected) and widths of the fitted sigmoidal functions (all values in fs) from Fig. 4.13, according to Eq. (4.7). For the sake of comprehensiveness, also the values for the electron measurements are listed, the discussion of which is deferred to Section 4.5.

	CH_3I			CH_2ICl		
	Center μ	μ_{corr}	Width σ	Center μ	μ_{corr}	Width σ
Fragment ion						
I^{2+}	261 ± 9	85	243 ±20	49 ± 7	126	192 ± 14
I^{3+}	290 ± 7	114	211 ±15	74 ± 8	151	177 ± 15
I^{4+}	303 ± 5	127	216 ±10	123 ± 7	200	186 ± 14
I^{5+}	325 ±10	149	219 ±18	182 ±13	259	207 ± 25
Photoelectron contribution						
Molecule	168 ±33	-8	109 ±63	5 ±70	82	153 ±124
Atom	195 ±42	19	125 ±80	4 ±75	81	158 ±132

mated by a classical over-the-barrier model[37] that yields the expression

$$R_{\mathrm{crit}}(p,q) = \frac{(p+1) + 2\sqrt{q(p+1)}}{V_i}\,, \tag{4.8}$$

where q and p are the charge states of the iodine atom and the co-fragment, respectively, and V_i is the vertical ionization potential of the co-fragment. For the present case, p is set to zero, and literature values[38] for the co-fragment IPs are used: 9.86 eV for CH_3 and 8.87 eV for CH_2Cl.

The critical internuclear distance that is obtained from Eq. (4.8) can now be compared to the internuclear distance that would be expected at the center of the step function. For the sake of simplicity, we assume that the two fragments travel at a constant velocity that corresponds to the asymptotic kinetic energy release E_{kin}, neglecting the acceleration at the beginning of the dissociation. In this case, the internuclear distance as a function of time is given by

$$R(t) = R_{eq} + t\sqrt{\frac{2E_{kin}}{m_{red}}}\,, \tag{4.9}$$

where R_{eq} corresponds to the equilibrium internuclear distance and $m_{red} = \frac{m_I \cdot m_{cofrag}}{m_I + m_{cofrag}}$ to the reduced mass, with the iodine atom's mass m_I. The equilibrium distances used were 2.20 Å for CH_3I, which equals the C–I bond distance, and 2.86 Å for CH_2ICl, which is the distance between the iodine atom and the center of mass of the chloromethyl group.[7] The corresponding asymptotic kinetic energy releases were set to 1.286 eV[37] for CH_3I and 1.22 eV for CH_2ICl, which corresponds to the energy release associated with the average fragment kinetic energy measured in this experiment (see Table 4.1).

In Fig. 4.14, the expected internuclear distances according to Eq. (4.9) are compared to the critical internuclear distances for the respective charge state given by Eq. (4.8), revealing a large discrepancy. As mentioned above, however, the shown pump–probe delays are essentially "lab book delays" that may be offset from the actual zero delay by a constant value t_0. Hence, the pump–probe delay t in Eq. (4.9) was replaced with $(t - t_0)$, and t_0 was adjusted in a least-squares fitting procedure as a free parameter. Furthermore, this offset t_0 can differ between experiments, as the data sets for the two different molecules were recorded on different days during the experimental campaign and the exact time overlap between the FEL and the optical laser is known to be subject to long-term drifts. As can be seen from Fig. 4.14, good agreement can be achieved using the fitted values of $t_0 = +176$ fs and -77 fs for CH_3I and CH_2ICl, respectively. The corrected values of the center positions, $\mu_{corr} = \mu - t_0$, are also listed in Table 4.2. On the basis of these values, an overall increase of the appearance times is found for photodissociation of CH_2ICl compared to CH_3I, which is what is expected given the significantly heavier mass of the chlorine atom.

The above analysis demonstrates that the suppression of charge redistribution during the dissociation represents a key ingredient for the appearance of the low kinetic energy channel, even for the lowest of charge states for which it can be observed, $n = 2$. Without doubt, the discussed charge redistribution phenomenon inherently depends on the underlying dissociation dynamics of the neutral, excited species. Disentangling these two interrelated processes in a clean way is, however, a tedious task and will not be pursued here. Instead, we now turn to the investigation of the photoelectrons emitted during the UV dissociation.

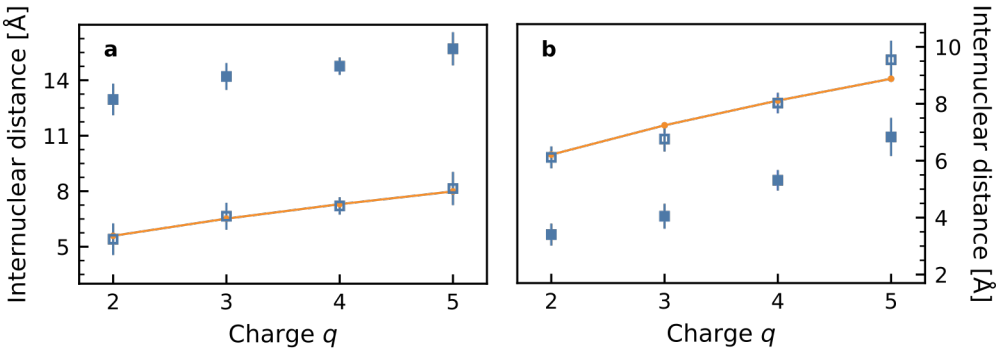

Figure 4.14 Comparison between the critical internuclear distances as a function of the iodine charge state, according to Eq. (4.8) (solid orange line), and the distances retrieved from the experimentally determined step function onsets, assuming fragments traveling at constant velocities as in Eq. (4.9) (filled squares: uncorrected values as in Fig. 4.13; open squares: allowing for an additional time-zero offset t_0 as a free parameter; **a)** CH_3I; **b)** CH_2ICl).

4.5 Time-resolved photoelectron spectroscopy

Slices through the 3D photoelectron momentum distribution recorded in CH_3I and CH_2ICl molecules following soft x-ray ionization are displayed in Fig. 4.15a and b, together with the raw images from the experiment, and the corresponding angle-integrated kinetic energy spectra, Fig. 4.15c. At this photon energy, ionization is dominated by the $\epsilon f \leftarrow 4d$ resonance in iodine and therefore the kinetic energy spectra are mainly composed of the $4d$ photoline close to 57 eV binding energy (region A in Fig. 4.15c). Additional contributions, labeled as B and C in Fig. 4.15c, are assigned to distinct regions of Auger and shake-up electrons which in the case of CH_3I have been observed and described before.[39] The β_2 parameters that were obtained for the photolines in region A are 0.8 ± 0.2 and 1.2 ± 0.2 for CH_3I and CH_2ICl, respectively. Unfortunately, the published reference data by Novak, Benson & Potts[40] and Lindle *et al.*[41], for CH_3I and CH_2ICl, respectively, is only presented in graphical form and not as numerical values, but from what we can tell, the agreement seems to be very good.

The resolution of the velocity map imaging spectrometer at this relatively high kinetic energy is ~1 eV. Combined with the large bandwidth of the FEL (>1 eV), the spin-orbit $4d^{-1}$ core hole state cannot be resolved in the present experiment. We can, nevertheless, resolve a small absolute shift of 0.5 eV in binding energy between CH_3I (peak position 57.1 eV) and CH_2ICl (peak position 57.6 eV). These values are in good agreement with the weighted average of the $4d_{3/2}$ and $4d_{5/2}$ binding energies reported in earlier studies, performed with synchrotron radiation.[33,40]

The changes in the photoelectron spectra (PES) following UV excitation are shown as difference spectra in Fig. 4.16 as a function of pump–probe delay. At each time step, the photoelectron spectrum recorded at a delay of −1 ps (UV late) is subtracted to highlight the delay-dependent changes in the spectra of the excited-state molecules. For both molecules under investigation, the most prominent delay-dependent effect is the appearance of a negative and a positive contribution, labeled as regions I and II in Fig. 4.16, on either side of the photoline. To interpret this observation, we need to distinguish two effects that are expected

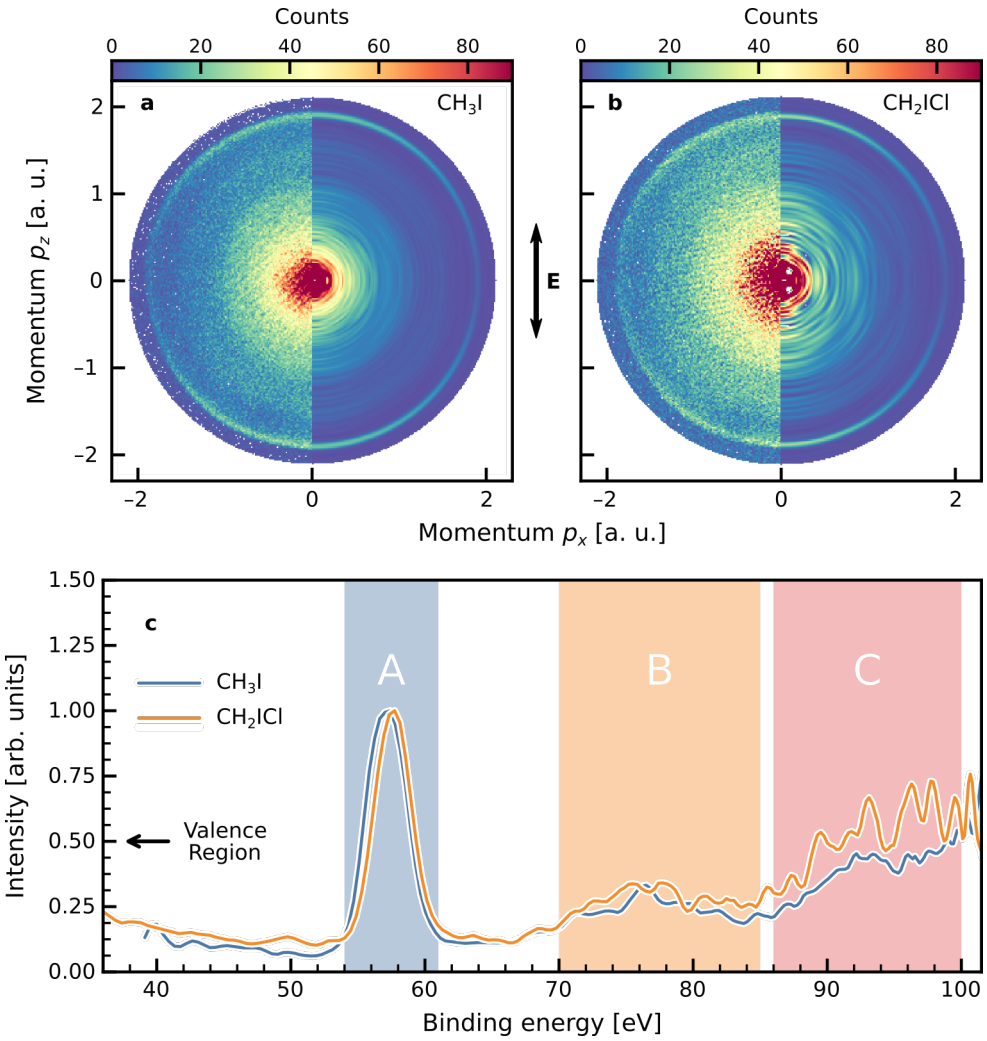

Figure 4.15 Static photoelectron spectroscopy at 11.6 nm. **a)** VMI detector distribution (left half) and slice through the 3D momentum distribution (right half) obtained from Abel-inverting the former for the photoionization of CH_3I. **b)** Same as **a** for CH_2ICl. **c)** Corresponding kinetic energy spectra, shown as a function of binding energy.

to modulate the binding energies of the core-shell electrons during the time-dependent evolution of an excited-state molecule: first, the electronic excitation itself, which is pictured as the promotion of a valence electron into an unoccupied orbital and, second, the so-called chemical shift in the binding energy of the core-shell electrons, which is a consequence of the additional electron density that is presented by the neighboring atoms, which means that the chemical shift is a function of the internuclear separation. As the valence electrons are delocalized throughout the molecule and, compared to the core-shell electrons, only weakly bound, we expect that the first effect, the rearrangement of one these electrons, makes only a small contribution to the time-dependent change in binding energy. Asymptotically, free iodine atoms are formed, which means that the chemical shift, which we introduced as the second effect, will go to zero. We therefore assume that in the time-dependent measurement – to first approximation – the binding energies of the core-shell electrons evolve from the value

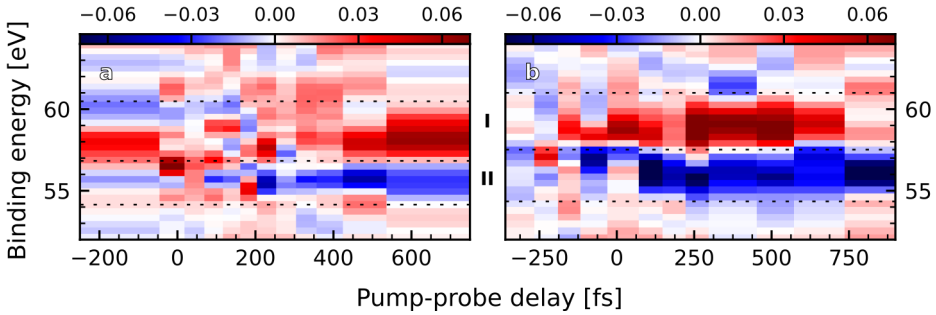

Figure 4.16 Time-dependent photoelectron spectra recorded in CH_3I **(a)** and CH_2ICl **(b)** as a function of pump-probe delay, having subtracted the photoelectron spectrum at a delay of −1 ps (UV late). The dashed lines delimit the regions associated with the depletion of ground-state molecules **(II)** (blue, negative) and the formation of free iodine atoms **(I)** (red, positive).

of the neutral ground-state species to the value of the neutral ground-state atom.

In this picture, which one could call the "excitation-agnostic" picture, the sudden variation of the signal as shown in Fig. 4.16a and b is a direct consequence of the molecules' dissociation: As the two fragments move apart, the chemical shift of the iodine 4*d* levels, which is induced by the (chloro-)methyl group in the bound molecule, is gradually relieved as the electronic structure of the free iodine atom emerges. The 4*d* binding energy of the free iodine atoms is, in either case, higher than that for the bound molecules. Judging from the weighted average of the values reported for the 4*d* core-hole spectroscopy of atomic iodine,[42,43] this difference should amount to 1.0 eV for CH_3I[33] and 0.6 eV for CH_2ICl[40]. Although the resolution of our current experiment does not allow us to resolve the individual spin-orbit states, we are able detect the overall shift of the 4*d* photoline. The drop of the signal in region II can, therefore, be assigned to the depletion of excited state molecules as they dissociate, whereas the rise of the signal in region I is attributed to the ionization of iodine atoms that are formed. Surprisingly, these two features seem to be separated by more than 3 eV rather than the small differences given above, but this deceptively large separation is caused by the ~3 eV width (FWHM) of the photoline feature: A small displacement will result in a large separation in the difference signal, as shown in Fig. 4.16, which means that the largest absolute difference appears in the outermost regions of the peak.

What can also be seen from Fig. 4.16 is that the time-dependent effect is noisy and unstable, and a simple integration of the two regions, similar to the procedure used for the ion data, does not help in quantifying the dynamics observed in the PES. Instead, a fitting procedure is used that works as follows: At each time delay, the broad photoline feature is fitted by a sum of two Gaussian functions. The first Gaussian function reflects the ionization from the molecular iodine's 4*d* levels (of the molecule in the ground state, according to the picture introduces above), whereas the second Gaussian function reflects the ionization from the iodine atom after dissociation. The width of the Gaussian function attached to the molecular contribution is fixed to 3 eV to account for the limited resolution of the velocity map imaging spectrometer and the bandwidth of the FEL pulse, whereas the width of the Gaussian function representing the atomic contribution is used as a free parameter to account for the significant broadening of the free atom's 4*d* photoline due to open-shell couplings.[43] In fact, we find that

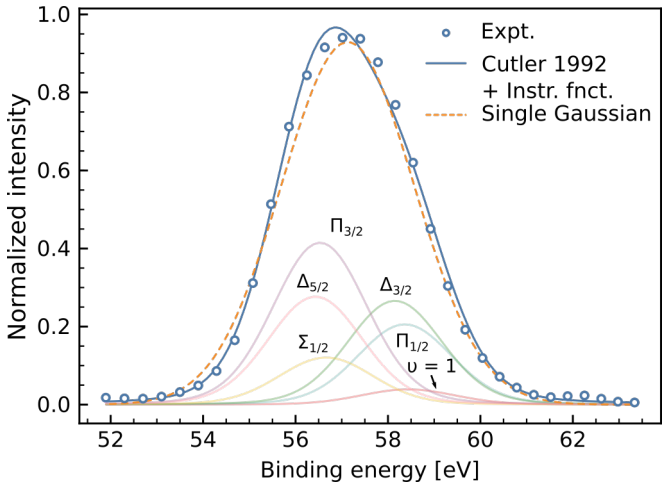

Figure 4.17 Composition of the 4*d* photoline in the photoionization of CH_3I at $\hbar\omega = 90$ eV according to Cutler, Bancroft & Tan[33]. The capital Greek labels on the small peaks denote the substates of the spin-orbit split $4d^{-1}$ core-hole manifold. The label $\nu = 1$ denotes a vibrational excitation in the $\Pi_{1/2}$ state.

the atomic contribution is typically 0.5 eV broader (FWHM) than the molecular photoline. The peak positions of the two Gaussians are fixed to the weighted averages of the known values from synchrotron measurements, i. e., to 57.3 eV for the molecular contribution in CH_3I, 57.7 eV for that in CH_2ICl, and 58.3 eV for the atomic iodine. The amplitudes are used as fitting parameters. Note that this model does not take into account a dynamically shifting component as a function of pump-probe delay since the measurement does not have sufficient temporal nor energy resolution to identify this component reliably.

To justify that a single Gaussian is adequate to represent the photoline under the current experimental conditions, we present the predicted shape of the photoline based on the detailed decomposition reported by Cutler, Bancroft & Tan[33] in Fig. 4.17, convoluted with the experimental resolution, which we estimate to be ≈2.2 eV. Also, in Fig. 4.17 a single-Gaussian fit to this broadened photoline is shown together with the experimental data for the CH_3I photoline. While the agreement between the photoline that is reconstructed from the literature values and the experiment is a little better than that between the experiment and the single Gaussian, we are still convinced that the single Gaussian used in our analysis is a good model because it introduces the smallest number of free parameters.

In Fig. 4.18, we present the results of the fitting procedure, namely, the amplitudes of the above two Gaussian functions (one for the molecular, one for the atomic photoline) as a function of the pump–probe delay. The time-evolution of these two components is, in turn, fitted with a Gaussian cumulative distribution function of the form given in Eq. (4.7). For both molecules, the depletion of the molecular iodine's 4*d* contribution has a decay time close to 120 fs. A slightly longer rising time is observed for the appearance of the atomic 4*d* photoline (see Table 4.2). The dynamics observed in the photoelectron spectrum is 1.7 times faster than the dynamics observed in the I^{n+} fragments for CH_3I and 1.35 times faster for CH_2ICl. This indicates that the photoelectron emitted from core-shell single-photon ionization is directly sensitive to the change of the electronic and nuclear structure of the molecule occurring

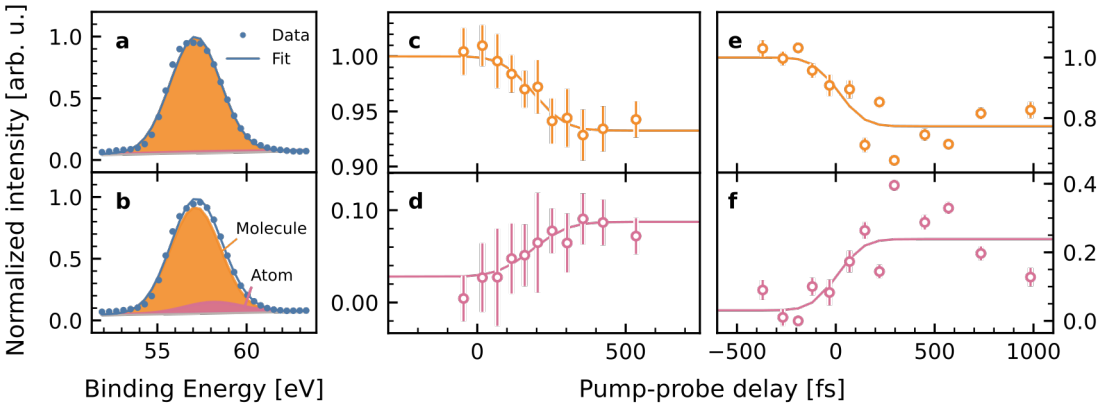

Figure 4.18 Decomposition of the time-resolved photoelectron signal. **a, b)** Illustration of the peak fitting procedure described in the main text, shown for the case of CH_3I at pump-probe delays of −1 ps **(a)** and +1 ps **(b)**. **c–f)** Evolution of the fitted amplitudes of the two Gaussians as a function of pump-probe delay. For CH_3I, the depletion of the molecular photoline is shown in **c** and the rise of the atomic contribution in **d**. **e, f)** Same as **c** and **d** for the case of CH_2ICl.

during neutral dissociation and is not affected by the Auger decays and charge redistribution effects that govern the ion dynamics. Remarkably, we find that the structure of the free atom is established within the 120 fs pulse duration of the FEL and UV pulses. Within the time resolution of our experiment, the rise of the atomic contribution is found at (20 ± 40) fs for CH_3I and (+80 ± 80) fs for CH_2ICl relative to the zero delay that was inferred from the ion measurements. Recently, Drescher *et al.*[44] have reported results on the photodissociation of CH_3I at 266 nm investigated by transient absorption. They find that the formation of the free iodine atom is faster than their time resolution of ≈100 fs, which is essentially what we have also found.

The difference between the dynamics observed in CH_3I and CH_2ICl can be partially attributed to the difference of the reaction times for the UV-induced dissociation of the molecules. For CH_3I, the time required to increase the C−I bond distance by a factor of two can be calculated using two moving fragments at constant velocities (Eq. (4.9)) and is expected to be around 48 fs, whereas this number increases to 55 fs for the CH_2ICl molecule. The main difference arises from the amount of internal energy that is transferred to the CH_3 and CH_2Cl co-fragments during dissociation. While it is negligible in CH_3I, the UV-dissociation of CH_2ICl involves large-amplitude rotational motions of the neutral CH_2Cl radical. On-the-fly adiabatic full-dimension classical trajectory calculations at the *ab initio* complete active space self-consistent field (CAS-SCF) level of theory, performed by Bañares and co-workers,[7] have shown that, due to the rotational motion of the CH_2Cl fragment, the time required to double the equilibrium distance between the iodine atom and the chlorine atom is about 70 fs. As a result, the chlorine atom stays in the vicinity of the iodine atom longer than the prompt C−I bond fission would suggest, which, in turn, affects the dynamics observed in the photoelectron spectra.

Eventually, we want to turn to the discussion of the photoelectron angular distributions and

how these distributions are affected by the molecular dynamics. Here, we have to consider two factors: first, what is the *expected* amplitude of the change in the angular-distribution parameters, which we must compare to, second, the uncertainty in determining these parameters. Based on the findings presented in Fig. 4.10 and the discussion accompanying it, we have to assume that the relative error in β_2 is about five times larger than that in the radial intensity distribution. This is mostly due to the fact that β_2 is obtained from the ratio Q_2/Q_0 (see the discussion at the end of Section 2.3.1 or Appendix A), and it is this division that amplifies the noise from these two experimentally determined quantities. What we have not discussed in Section 4.3.5 is the fact that the relative errors of the β_l grow quickly with increasing l, which can be intuitively understood as a consequence of the fact that, with increasing l, an ever more subtle aspect of the angular distribution is captured. Therefore, we restrict the discussion to β_2 here, which is the angular-distribution parameter we can measure with the greatest precision.

Looking at the literature values for the ground-state molecules we conclude that, for CH_3I, we would not expect β_2 to change *at all* between the bound and the free iodine atom. In fact, Lindle *et al.*[41], using the β_2 values for the photoionization of xenon (as a function of photoelectron kinetic energy) as the reference, found an excellent agreement with the measured β_2 values for CH_3I. This finding can be interpreted such that the CH_3 group acts as such a weak scatterer that its presence hardly modulates the photoelectron angular distributions (at least in the randomly oriented molecule). For CH_2ICl, the situation is different: here the β_2 for the molecule is roughly 1.2 at the present photon energy of ≈100 eV,[40] so that the β_2 will asymptotically drop during the dissociation to ≈ 0.8, which is an effect size we could possibly observe. To investigate this, we have extracted the radial distributions of β_2 in the time-resolved photoelectron measurements, as described in Appendix A, together with an estimate of the errors introduced by the Abel-inversion routine through the bootstrapping procedure described in Section 4.3.5.

The evolution of the β_2 radial distributions for both molecules is shown in the adjacent panels of Fig. 4.19 as the absolute difference with respect to the β_2 radial distributions recorded at −1 ps. For CH_3I, Fig. 4.19a, we can hardly identify any features that are not noise. In the case of CH_2ICl, Fig. 4.19b, we can clearly see a positive contribution rising at a binding energy of ≈59 eV and also a broad, weaker depletion that accompanies it at ≈55 eV. We tentatively assign these two features to an averaging effect between the molecular and the atomic photoline: when the atoms are formed with a more isotropic accompanying photoelectron angular distribution compared to the molecules, the averaging of the two overlapping photolines should depress β_2 at the photoline. In its wings, however, where the angular distribution becomes isotropic rather quickly, the atomic contribution will increase the average β_2 that is observed.

To quantify this effect, we have averaged Fig. 4.19b and the corresponding uncertainties from the bootstrapping over the integration regions of Fig. 4.16b, the result of which is shown in Fig. 4.20. In the atomic contribution we observe a clear step-like behavior. Fitting these data, using once more the error function of Eq. (4.7) , we obtain a center (uncorrected) of $\mu = (27 \pm 55)$ fs and a width of $\sigma = (70 \pm 90)$ fs. While the width is clearly very unreliable, the center position is in good agreement with the data for the intensity evolution of the photolines, collected in Table 4.2. Furthermore, we obtain a step height of 0.11 ± 0.03. Unfortunately, the same fitting failed for the values extracted from the molecular photoline,

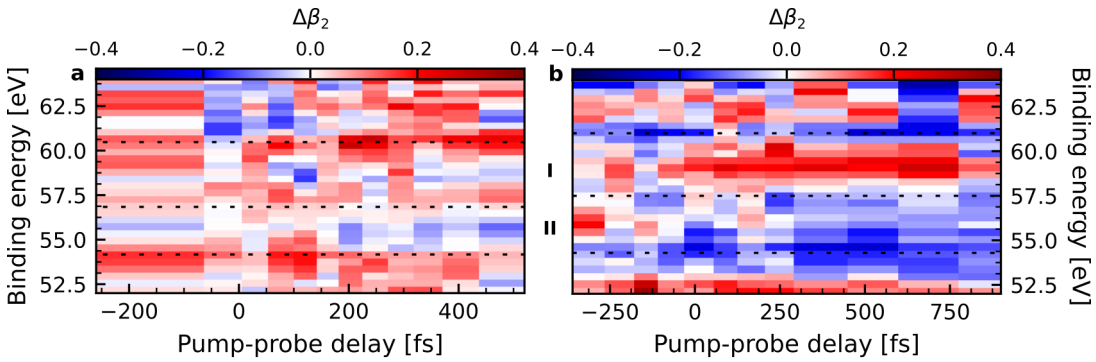

Figure 4.19 Time-dependent change of the asymmetry parameter β_2 as a function of pump–probe delay for CH_3I **(a)** and CH_2ICl **(b)**. At every delay point, the β_2 distribution measured at −1 ps (UV late) was subtracted. The indicated regions are the same as in Fig. 4.16.

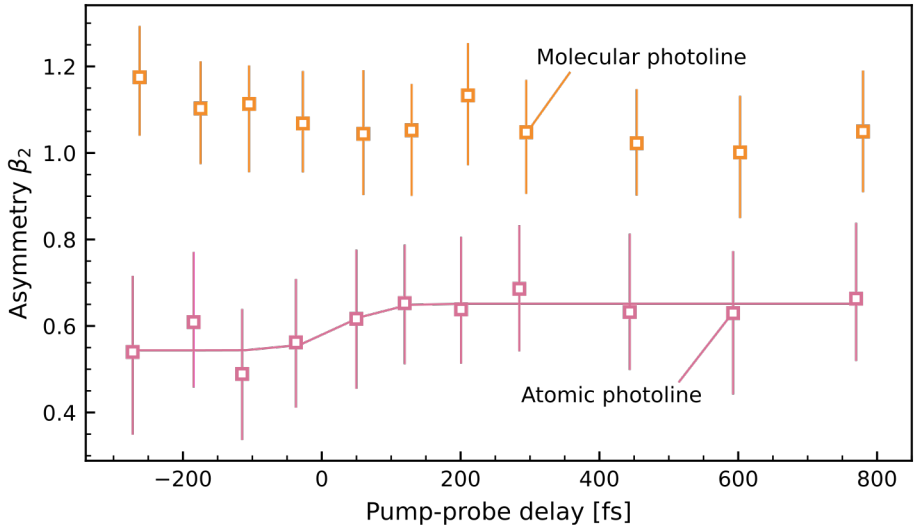

Figure 4.20 Extracted time evolution of the (absolute) β_2 parameter, averaged over the integration regions for the molecular (II) and the atomic (I) photoline, as indicated in Fig. 4.16b. The open squares mark the median values and the error bars the interquartile ranges obtained from the bootstrapping procedure outlined in Section 4.3.5. To the results for the atomic photoline the Gaussian cumulative distribution function of Eq. (4.7) was fitted. For the molecular photoline, this fitting failed.

which do not show a clear step-function behavior.

Still, what is remarkable about this time-evolution analysis is that it can be carried out directly with the experimental data without setting up an additional fitting model, as was done above. What manifests here, we are convinced, is the fact that the angular distribution parameters, even when they are extracted with a greater uncertainty than the angle-integrated photoelectron spectrum as discussed in Section 4.3.5, are less sensitive to statistical fluctuations during the experiment, because the intensity dependence is divided out when calculating the angular-distribution parameters.

4.6 Discussion

First, we want to address the question whether the time-dependent effects presented in this chapter could also be explained by a different excitation mechanism, namely multiphoton ionization caused by the UV light. In principle, the observed dissociation could also be caused by dissociative photoionization, if the molecules end up in a dissociating excited state of the ion after three-photon ionization. However, ionization would lead to shifts in the binding energy of the iodine 4*d* levels that are significantly larger than what is observed (as discussed in Section 4.4.1). According to Fadley *et al.*[32], the shift should be on the order of 10 eV for the iodine atoms. Certainly, a shift that large we should be able to identify and distinguish from the ≈1 eV shift that is observed.

Second, the most striking difference between the ion and electron data is the fact that the time-dependent effect is much more noisy and less reproducible in the electrons. We assume that besides the background level, that was discussed in Section 4.3.2, there is a reason inherent to the spectral properties of the SASE FEL that makes the experiment with direct photoelectrons more challenging: even when the precise spectrum of the FEL pulse fluctuates from shot to shot, the molecules will, after ionization, still end up in the same final electronic states, which will, in turn, hardly affect the kinetics of the subsequent breakup process. Therefore, the ions are always formed with the same kinetic-energy release and give rise to a stable signal. In contrast, the variations in the FEL wavelength are directly imprinted onto the ejected photoelectron; this would also explain why McFarland *et al.*[5] have resorted to measuring Auger electrons. In an Auger process, the kinetic energy of the ejected electron is entirely determined by the energy difference between the initial core-hole and the final valence-hole state. Therefore, the kinetic energy of the Auger electrons is independent of the ionizing radiation, causing a robustness to spectral fluctuations of the FEL similar to what we have proposed for the ions. Similarly, the photoelectron angular distributions should be comparatively insensitive to changes in the spectral shape of the FEL because, by definition, the angular distributions are independent of the intensity. To some extent that is also what we found in our analysis, considering that we observed a quite stable pump–probe effect in the β_2 parameter for CH_2ICl (see Fig. 4.19b) in spite of the fact that the uncertainty should be larger in this quantity compared to the radial intensity distribution.

Third, even if the spectrum of the ionizing radiation was perfectly stable, the results presented in Section 4.5 have revealed the limits of the present experiments in terms of time and energy resolution. As attractive as core-shell photoelectron spectroscopy is as a technique, one has to be aware that the changes in binding energy during a chemical reaction are small compared to the photoelectron energies (in the regime where photoelectron scattering can be treated classically). Applied to the present experiment, this would require an energy resolution better than 500 meV or $\Delta E/E < 1\,\%$. Regarding the spectrometer, this is certainly achievable with a "traditional", one-sided VMI. With the double-sided VMI used in this experiment, this is probably also possible, but note that ions and electrons were measured *simultaneously* here, for which compromises have to be made in terms of the image size and particle focusing on both sides of the spectrometer. However, even with a better spectrometer resolution we would probably be limited by the bandwidth of the FEL, which we estimate to be about 1 eV. The time resolution that is required to resolve the molecular dynamics through the evolution of the binding energies obviously depends on the time scale of these dynamics. Considering the

cross correlation of 160 fs between the FEL and UV pulses, one cannot hope to resolve the dissociation dynamics in CH_3I, but if it is true that the respective dynamics in CH_2ICl happen on a time scale of 70 fs, they could possibly be disentangled by a deconvolution operation. In this sense, we think that the energy resolution is the more severely liming factor.

4.7 Conclusion

In this chapter, two things were established: First, a detailed approach was elaborated to treat the experimental data taken with a double-sided VMI at an FEL facility. In the second step, this method was applied in investigating the *A* band photodissociation of CH_3I and CH_2ICl molecules, probed using core-shell photoionization spectroscopy above the iodine 4*d* edge. It was shown that time-dependent features that are observed in the I^{n+} fragment ions and the direct photoelectrons, respectively, are mediated by fundamentally different processes: the suppression of a molecular Auger type of process on one side, and a quasi-instantaneous photoionization on the other. Unfortunately, we were not able to observe the evolution of the iodine 4*d* binding energy directly. Here, the limiting factors were the low energy resolution of the VMI and the low time resolution due to the relatively long FEL pulses.

The problem that the spectral shape FEL pulses changes from shot to shot is inherent to the way a SASE FEL operates. However, with the development and increasing availability of so-called seeded FELs, in which the light amplification process is not initiated statistically, but seeded by coherent XUV radiation (e. g., from high-order harmonic generation), very stable spectral properties and, moreover, a negligible timing jitter between the FEL and the optical laser can be realized. Recently, Squibb *et al.*[45] have reported time-resolved photoelectron spectroscopy results on the excited state dynamics of acetylacetone, measured with the FERMI FEL at the Elettra facility. Although the aim of this study was to investigate valence-shell ionization at ~20 eV, we note that the FERMI FEL can be tuned to photon energies of up to 300 eV, which opens an exciting perspective for the future of time-resolved core-shell photoelectron spectroscopy.

References

1. Braußе, F. *et al.* “Time-Resolved Inner-Shell Photoelectron Spectroscopy: From a Bound Molecule to an Isolated Atom”. *Phys. Rev. A* **97,** 043429 (2018).
2. Fadley, C. S. “Diffraction and Holography with Photoelectrons and Auger Electrons: Some New Directions”. *Surf. Sci. Rep.* **19,** 231–264 (1993).
3. Woodruff, D. P. & Bradshaw, A. M. “Adsorbate Structure Determination on Surfaces Using Photoelectron Diffraction”. *Rep. Prog. Phys.* **57,** 1029 (1994).
4. Boll, R. *et al.* “Femtosecond Photoelectron Diffraction on Laser-Aligned Molecules: Towards Time-Resolved Imaging of Molecular Structure”. *Phys. Rev. A* **88,** 061402 (2013).
5. McFarland, B. K. *et al.* “Ultrafast X-Ray Auger Probing of Photoexcited Molecular Dynamics”. *Nat. Commun.* **5,** 4235 (2014).
6. Alekseyev, A. B., Liebermann, H.-P., Buenker, R. J. & Yurchenko, S. N. “An Ab Initio Study of the CH_3I Photodissociation. I. Potential Energy Surfaces”. *J. Chem. Phys.* **126,** 234102 (2007).

7. Murillo-Sánchez, M. L., Marggi Poullain, S., González-Vázquez, J., Corrales, M. E., Balerdi, G. & Bañares, L. "Femtosecond Photodissociation Dynamics of chloroiodomethane in the First Absorption Band". *Chem. Phys. Lett.* **683,** 22–28 (2017).
8. Strüder, L. *et al.* "Large-Format, High-Speed, X-Ray pnCCDs Combined with Electron and Ion Imaging Spectrometers in a Multipurpose Chamber for Experiments at 4th Generation Light Sources". *Nucl. Instrum. Methods Phys. Res., Sect. A* **614,** 483–496 (2010).
9. Feldhaus, J. "FLASH—the First Soft x-Ray Free Electron Laser (FEL) User Facility". *J. Phys. B: At., Mol. Opt. Phys.* **43,** 194002 (2010).
10. Savelyev, E. *et al.* "Jitter-Correction for IR/UV-XUV Pump-Probe Experiments at the FLASH Free-Electron Laser". *New J. Phys.* **19,** 043009 (2017).
11. Ackermann, W. *et al.* "Operation of a Free-Electron Laser from the Extreme Ultraviolet to the Water Window". *Nat. Photonics* **1,** 336–342 (2007).
12. Allaria, E., Callegari, C., Cocco, D., Fawley, W. M., Kiskinova, M., Masciovecchio, C. & Parmigiani, F. "The FERMI@Elettra Free-Electron-Laser Source for Coherent x-Ray Physics: Photon Properties, Beam Transport System and Applications". *New J. Phys.* **12,** 075002 (2010).
13. Redlin, H., Al-Shemmary, A., Azima, A., Stojanovic, N., Tavella, F., Will, I. & Düsterer, S. "The FLASH Pump–Probe Laser System: Setup, Characterization and Optical Beamlines". *Nucl. Instrum. Methods Phys. Res., Sect. A* **635,** S88–S93 (2011).
14. Amini, K., Blake, S., Brouard, M., Burt, M. B., Halford, E., Lauer, A., Slater, C. S., Lee, J. W. L. & Vallance, C. "Three-Dimensional Imaging of Carbonyl Sulfide and Ethyl Iodide Photodissociation Using the Pixel Imaging Mass Spectrometry Camera". *Rev. Sci. Instrum.* **86,** 103113 (2015).
15. Tiedtke, K. *et al.* "Gas Detectors for X-Ray Lasers". *J. Appl. Phys.* **103,** 094511 (2008).
16. Löhl, F., Arsov, V., Felber, M., Hacker, K., Jalmuzna, W., Lorbeer, B., Ludwig, F., Matthiesen, K.-H., Schlarb, H., Schmidt, B., Schmüser, P., Schulz, S., Szewinski, J., Winter, A. & Zemella, J. "Electron Bunch Timing with Femtosecond Precision in a Superconducting Free-Electron Laser". *Phys. Rev. Lett.* **104,** 144801 (2010).
17. Schulz, S. *et al.* "Femtosecond All-Optical Synchronization of an X-Ray Free-Electron Laser". *Nat. Commun.* **6,** 5938 (2015).
18. Kim, J., Chen, J., Zhang, Z., Wong, F. N. C., Kärtner, F. X., Loehl, F. & Schlarb, H. "Long-Term Femtosecond Timing Link Stabilization Using a Single-Crystal Balanced Cross Correlator". *Opt. Lett.* **32,** 1044–1046 (2007).
19. Bionta, M. R. *et al.* "Spectral Encoding Method for Measuring the Relative Arrival Time between X-Ray/Optical Pulses". *Rev. Sci. Instrum.* **85,** 083116 (2014).
20. Harmand, M., Coffee, R., Bionta, M. R., Chollet, M., French, D., Zhu, D., Fritz, D. M., Lemke, H. T., Medvedev, N., Ziaja, B., Toleikis, S. & Cammarata, M. "Achieving Few-Femtosecond Time-Sorting at Hard X-Ray Free-Electron Lasers". *Nat. Photonics* **7,** 215–218 (2013).
21. Dougherty, G. *Digital Image Processing for Medical Applications* 1st ed. (Cambridge University Press, Cambridge, 2009).
22. Jungmann, J. H., Gijsbertsen, A., Visser, J., Visschers, J., Heeren, R. M. A. & Vrakking, M. J. J. "A New Imaging Method for Understanding Chemical Dynamics: Efficient Slice Imaging Using an in-Vacuum Pixel Detector". *Rev. Sci. Instrum.* **81,** 103112 (2010).
23. Slater, C. S. *Studies of Photoinduced Molecular Dynamics* phd (University of Oxford, 2013).
24. Tremsin, A. S., Vallerga, J. V., Siegmund, O. H. W. & Hull, J. S. *Centroiding Algorithms and Spatial Resolution of Photon Counting Detectors with Cross-Strip Anodes* in *Proc. SPIE* **5164** (2003), 113–124.

25. Dick, B. “Inverting Ion Images without Abel Inversion: Maximum Entropy Reconstruction of Velocity Maps”. *Phys. Chem. Chem. Phys.* **16,** 570–580 (2013).
26. Kandula, D. Z., Gohle, C., Pinkert, T. J., Ubachs, W. & Eikema, K. S. E. “Extreme Ultraviolet Frequency Comb Metrology”. *Phys. Rev. Lett.* **105,** 063001 (2010).
27. Heimann, P. A., Becker, U., Kerkhoff, H. G., Langer, B., Szostak, D., Wehlitz, R., Lindle, D. W., Ferrett, T. A. & Shirley, D. A. “Helium and Neon Photoelectron Satellites at Threshold”. *Phys. Rev. A* **34,** 3782–3791 (1986).
28. Johnson, W. R. & Soff, G. “The Lamb Shift in Hydrogen-like Atoms, $1 \leq Z \leq 110$”. *Atom. Data Nucl. Data* **33,** 405–446 (1985).
29. Efron, B. “Bootstrap Methods: Another Look at the Jackknife”. *Ann. Stat.* **7,** 1–26 (1979).
30. Wiley, W. C. & McLaren, I. H. “Time-of-Flight Mass Spectrometer with Improved Resolution”. *Rev. Sci. Instrum.* **26,** 1150–1157 (1955).
31. Olney, T. N., Cooper, G. & Brion, C. E. “Quantitative Studies of the Photoabsorption (4.5–488 eV) and Photoionization (9–59.5 eV) of Methyl Iodide Using Dipole Electron Impact Techniques”. *Chem. Phys.* **232,** 211–237 (1998).
32. Fadley, C. S., Hagstrom, S. B. M., Klein, M. P. & Shirley, D. A. “Chemical Effects on Core-Electron Binding Energies in Iodine and Europium”. *J. Chem. Phys.* **48,** 3779–3794 (1968).
33. Cutler, J. N., Bancroft, G. M. & Tan, K. H. “Ligand-field Splittings and Core-level Linewidths in I 4d Photoelectron Spectra of Iodine Molecules”. *J. Chem. Phys.* **97,** 7932–7943 (1992).
34. Hollstein, M., Mertens, K., Gerken, N., Klumpp, S., Palutke, S., Baev, I., Brenner, G., Dziarzhytski, S., Wurth, W., Pfannkuche, D. & Martins, M. “Ultrafast Charge Redistribution in Small Iodine Containing Molecules”. arXiv: `1605.09317 [physics]` (2016).
35. Mertens, K., Gerken, N., Klumpp, S., Braune, M. & Martins, M. “Soft X-Ray Multiphoton Excitation of Small Iodine Methane Derivatives”. *J. Mod. Opt.* **63,** 383–389 (2016).
36. Erk, B. *et al.* “Imaging Charge Transfer in Iodomethane upon X-Ray Photoabsorption”. *Science* **345,** 288–291. pmid: `25035485` (2014).
37. Boll, R. *et al.* “Charge Transfer in Dissociating Iodomethane and Fluoromethane Molecules Ionized by Intense Femtosecond X-Ray Pulses”. *Struct. Dyn.* **3,** 043207 (2016).
38. Andrews, L., Dyke, J. M., Jonathan, N., Keddar, N. & Morris, A. “Photoelectron Spectroscopic Study of the Ground States of CH_2Cl^+, $CHCl_2^+$, and $CHFCl^+$”. *J. Am. Chem. Soc.* **106,** 299–303 (1984).
39. Holland, D. M. P., Powis, I., Öhrwall, G., Karlsson, L. & von Niessen, W. “A Study of the Photoionisation Dynamics of Chloromethane and Iodomethane”. *Chem. Phys.* **326,** 535–550 (2006).
40. Novak, I., Benson, J. M. & Potts, A. W. “UV Angle-Resolved Photoelectron Spectra of Mixed Methylene Dihalides Using Synchrotron Radiation”. *Chem. Phys.* **107,** 129–138 (1986).
41. Lindle, D. W., Kobrin, P. H., Truesdale, C. M., Ferrett, T. A., Heimann, P. A., Kerkhoff, H. G., Becker, U. & Shirley, D. A. “Inner-Shell Photoemission from the Iodine Atom in CH_3I”. *Phys. Rev. A* **30,** 239–244 (1984).
42. Tremblay, J., Larzilliere, M., Combet-Farnoux, F. & Morin, P. “Photoelectron Spectroscopy of Atomic Iodine Produced by Laser Photodissociation”. *Phys. Rev. A* **38,** 3804–3807 (1988).
43. Nahon, L., Svensson, A. & Morin, P. “Experimental Study of the 4d Ionization Continuum in Atomic Iodine by Photoelectron and Photoion Spectroscopy”. *Phys. Rev. A* **43,** 2328–2337 (1991).

44. Drescher, L., Galbraith, M. C. E., Reitsma, G., Dura, J., Zhavoronkov, N., Patchkovskii, S., Vrakking, M. J. J. & Mikosch, J. "Communication: XUV Transient Absorption Spectroscopy of Iodomethane and Iodobenzene Photodissociation". *J. Chem. Phys.* **145,** 011101 (2016).

45. Squibb, R. J. *et al.* "Acetylacetone Photodynamics at a Seeded Free-Electron Laser". *Nat. Commun.* **9,** 63 (2018).

Summary and Outlook

With the work that is collected in this thesis, a great deal of progress has been made in establishing the measurement, analysis, and interpretation of photoelectron angular distributions (PADs) as a powerful technique in time-resolved photoionization experiments to reveal details about the electron–parent-ion interactions that are elusive when considering only angle-integrated quantities, paying special attention to the role that shape resonances play in this context. In order of appearance, the aspects of this progress are threefold: first, in Chapter 2, we have demonstrated to what extent the amount of information that can be retrieved from the photoelectron angular distributions can be enhanced by laser-induced molecular alignment for the case of XUV ionization of CF_3I molecules. In particular, we uncovered that the rather structureless energy dependence of the photoionization observables for randomly oriented molecules is in fact composed of overlapping contributions from two distinctly different shape resonances, each of which contributes to the angular-distribution parameters of the aligned ensemble with essentially opposite sign, which allowed their discrimination and assignment in the experimental data.

Second, in Chapter 3, we have carried out the analysis of time-dependent PADs for an experiment, in which actual molecular dynamics are involved, namely photodissociation and vibrational wave-packet dynamics in I_2 molecules, induced by transitions at 710 nm and 555 nm, respectively. Here, instead of single-photon XUV ionization, multi-photon ionization in an intense mid-IR laser field was used as the probe mechanism, which has the advantage that, experimentally, such a laser setup operates typically more stable than an HHG source. The drawback is that the analysis of the electron data is rather involved and this treatment is based on many side assumptions, whose appropriateness has to be guaranteed. In the best case, however, from such a measurement the differential scattering cross sections for the electron–molecular-ion scattering can be extracted which can be directly compared to calculations and genuine electron-scattering measurements.

The key result of Chapter 3 is that we were able to reproduce changes in the angular distributions of the rescattered electrons for both the photodissociation and the vibrational wave-packet experiments quantitatively by electron-scattering calculations. Furthermore, we developed an interpretation of the observed changes in terms of a molecular shape resonance that very sensitively depends on the internuclear distance between the iodine atoms and an atomic shape resonance in I^+ that appears when the molecule is completely dissociated. To the best of our knowledge, the notion that a shape resonance could be extremely sensitive to small changes in molecular structure has been discussed theoretically,[1] but not explored experimentally so far.

As hinted above, the insight into the photoelectron dynamics, which ultimately enabled the interpretation of the findings of Chapters 2 and 3, was obtained by the ability to reproduce and rationalize PADs for electrons with kinetic energies ≤ 30 eV with the help of calculations carried out with ePolyScat. It is important to stress that, on one hand, this is a kinetic-energy

region in which classical models of the electron–parent-ion interactions are inappropriate, but, on the other hand, the application of a quantum-scattering model alone does not guarantee success. In fact, there are many examples in the literature where the agreement between experiment and theory is not even qualitatively convincing, but – then again – photoionization of molecules is notoriously difficult to treat theoretically.

To overcome this complication, the idea behind the experiments presented in Chapter 4 was to use radiation in the soft x-ray regime, both to probe a quasi-atomic core-shell level in the molecule and to reach photoelectron kinetic energies, where the photoelectron scattering can be treated classically. Then, these two factors combined would lead to a particularly simple interpretation of the photoelectron angular distribution in terms of an outgoing photoelectron wave ejected by a point emitter that rescatters from the other atoms in the molecule like on point-like scatterers. While we were able to detect the signature of the molecular photodissociation of CH_3I and CH_2ICl at 266 nm in the iodine 4*d* photoline, which is in itself an important, albeit technical, breakthrough, we could not – even with the most sophisticated data treatment – determine changes in the PAD of the photoline significant enough that they would have prompted further analysis and modeling.

Naturally, the amount of progress that a thesis can achieve in its field must always be incremental, but this progress is at the same time highly specific. So with the results that we have collected up this point and the insight we have gained, we can envisage some directions, along which these experimental approaches can be further developed. First, apart from the remarks that were made regarding the technical limitations of the FEL experiments in Chapter 4, we want to address once more the expected effect sizes in the change of the photoelectron angular distributions. In Section 4.5, we have stated that the β_2 parameter is expected not to change when going from the bound molecule to the free atom. This statement, however, is strictly true only for the randomly oriented molecule. Even if the CH_3 group is a weak scatterer, its presence breaks the spherical symmetry of the molecular potential, which inevitably changes the partial-wave interference in the outgoing photoelectron wave function, an effect that was discussed in this thesis in Section 3.4.3 in connection with electron–ion scattering, but, more specifically, already in relation to the 4*d* ionization of CH_3I by Powis.[2] Since we have already demonstrated in Chapter 2 how molecular alignment can bring out unexpected details of the photoelectron scattering dynamics, we assume that in a measurement using an aligned ensemble, a greater sensitivity of the PADs to the photodissociation could be detected.

Second, as we have repeatedly stated, the central message of this thesis is that shape resonances are ubiquitous in low-energy (photo-)electron scattering and they easily dominate the electron–parent-ion scattering spectra. While this may hamper an intuitive interpretation of the scattering dynamics without relying on sophisticated calculations, we have also shown, in particular in Section 3.4.4, how sensitive the positions and widths of the resonances are to the *exact* shape of the molecular potential. This, in turn, means that the rescattering of photoelectrons should not only be sensitive to the nuclear structure of the molecule, as developed in Chapter 3, but even to the electronic structure. This becomes important when electronic states are coupled, as it happens close to conical intersections. In fact, Han & Yarkony[3] have recently developed the theoretical framework to treat electron scattering when non-adiabatic dynamics are involved. Of course, the transition through a conical intersection happens on a time scale much faster than anything we have discussed in this thesis, but the

analysis that we have presented in Section 3.4 can in principle be applied to arbitrarily short, few-cycle laser pulses.

References

1. Stratmann, R. E. & Lucchese, R. R. "Resonances and the Effects of Interchannel Coupling in the Photoionization of CS_2". *J. Chem. Phys.* **97,** 6384–6395 (1992).
2. Powis, I. "A Theoretical CMS-Xα Treatment of CH_3I Photoionization Dynamics: Outer Valence Shell and Iodine 4*d* Levels". *Chem. Phys.* **201,** 189–201 (1995).
3. Han, S. & Yarkony, D. R. "Determining Partial Differential Cross Sections for Low-Energy Electron Photodetachment Involving Conical Intersections Using the Solution of a Lippmann-Schwinger Equation Constructed with Standard Electronic Structure Techniques". *J. Chem. Phys.* **134,** 174104 (2011).

Appendix A

VMI Data Processing

In general, a tomographic reconstruction is necessary to retrieve the original 3D velocity distribution from the "line-of-sight" projection that a VMI causes as illustrated in Fig. 2.3, which requires sampling the velocity distribution in this way under many angles.[1] If, however, the 3D distribution is cylindrically symmetric around some axis and this axis is aligned parallel to the detector plane, a single projected image that is captured by the VMI contains all information necessary for the inversion.

Mathematically, the special case including rotational symmetry can be described by the so-called Abel transformation. Let $P_v(v, \theta, \phi)$ denote a 3D velocity distribution that is expressed in spherical coordinates; here, v is a radial coordinate that is proportional to the particle's velocity, θ and ϕ are the polar and azimuthal angle, respectively. As stated above, we require that the distribution be cylindrically symmetric around the principal axis, which we let coincide with the z axis. This renders $P_v(v, \theta, \phi)$ independent of ϕ, and hence we can simply work with $f(v, \theta) = P_v(v, \theta, 0)$, which corresponds to a two-dimensional (2D) slice through the 3D distribution. Clearly, we could also express the velocity distribution $f(v, \theta)$ in cylindrical coordinates as $f(z, \rho)$ by a standard coordinate transformation, where ρ measures the perpendicular distance from the z axis.[a] We now want to express the projection of $f(z, \rho)$ onto an image $F(z, x)$, which is easily identified with the detector image that is captured by the camera. This relation is given by[2]

$$F(z, x) = 2 \int_x^\infty \frac{\rho f(z, \rho)}{\sqrt{\rho^2 - x^2}} \, \mathrm{d}\rho \ . \tag{A.1}$$

What is remarkable about Eq. (A.1) is that it generates the projection "line-by-line" because the integration is independent of z. This observation follows directly from the projection–slice theorem,[3] from which one can also derive the finding that the Abel projection can be inverted by the consecutive application of a Fourier and an inverse Hankel transformation onto a line of the image. This so-called Fourier–Hankel method probably is the most straightforward way to perform an Abel inversion, but in practice it suffers from a great sensitivity towards experimental noise. Therefore, a number of inversion techniques have been developed over the years to overcome this problem. Among these, certainly the most popular methods now are those, in which the Abel projection is precomputed for a basis set that is supposed to represent $f(z, \rho)$ well, and the projected basis set is then fitted to the experimental image. Applying the fit results to the "original" basis set yields $f(z, \rho)$. These methods are best

a It is an unfortunate fact of life that so many coordinate systems are involved in describing a VMI experiment. Cartesian and cylindrical coordinates are, however, most natural in describing the image acquisition and Abel inversion, whereas the physically significant information content is best described in spherical coordinates.

known under their acronyms like BASEX[4] or pBASEX,[5], which differ only by the choice of the employed basis functions. These basis-set based approaches, however, typically perform a least-squares fitting of the given basis sets to the data, by which the experimental error is inherently assumed to be Gaussian in nature. For particle-counting experiments carried out with a VMI, Poissonian statistics have to be assumed for the error term instead. Therefore, we have used – throughout this thesis – an algorithm based on the so-called maximum-entropy method (MEM). The MEM approach was developed by Burch, Gull & Skilling[6] in the 1980's as a general technique for image restorations, but it was only recently that it was incorporated into an Abel-inversion routine by Dick.[2] This routine offers the possibility to choose between different error terms and has, in the author's experience, proven to give the most faithful reconstructions compared to other methods, especially for images with very small total count numbers.

In any case, the application of an Abel-inversion routine yields, as its central result, the inverted map $f(v,\theta)$ (possibly after a coordinate transformation of $f(z,\rho)$ if that is what the employed method returns). As the angular dependence of the velocity map can always be expanded into a Legendre series, $f(v,\theta)$ can be written as a sum of radial velocity distributions, $Q_l(v)$, with increasing angular momentum l, like

$$f(v,\theta) = \frac{1}{v^2}\sum_{l=0}^{L} Q_l(v)\, P_l(\cos\theta)\,, \tag{A.2}$$

where $P_l(x)$ are the usual Legendre polynomials and L denotes the highest angular momentum to include (which can, for example, be predicted by Yang's theorem[7]). The $Q_l(v)$ distributions are formally obtained from a Legendre expansion as

$$Q_l(v) = v^2(2l+1)\int_0^{\pi} f(v,\theta)\, P_l(\cos\theta)\sin\theta\,\mathrm{d}\theta \tag{A.3}$$

where the factor v^2 is part of the volume element of the spherical coordinate system, which has to be included for the peak heights and areas to scale correctly. While $Q_0(v)$ clearly corresponds to the angle-integrated radial velocity distribution, the *beta* parameters, $\beta_l(v)$, from Eq. (1.39) are simply given by

$$\beta_l(v) = \frac{Q_l(v)}{Q_0(v)}\,. \tag{A.4}$$

Obviously, these $\beta_l(v)$ are smooth functions of the radial coordinate, so that when we discuss the angular distribution's properties of a specific feature in the photoelectron or -ion spectrum, we will indicate a region over which this distribution was integrated.

In practice, treating an experimental VMI image proceeds as follows: First, the image is interpolated by a fast 2D cubic spline routine. Before evaluating the cubic splines on a square Cartesian grid, they can be rotated and shifted, to center the image and align its symmetry axes with the horizontal and vertical axis of the image. When working with linearly polarized light, the up—down symmetry of the VMI image is not broken, so that all four quadrants of the image should contain the same information. Therefore, we check the quality of the centering by extracting the radial intensity distribution of the *raw* image for all four quadrants and

tweak the centering offsets in the z and x directions such that all four distributions perfectly overlap.[b]

Eventually, the optimized image is evaluated on a $N \times N$ Cartesian grid, where N is always odd and chosen to be close to the original image size. Then, all four quadrants of this transformed image are summed up to give the maximum signal-to-noise ratio for the inversion routine, unless the quality of certain quadrants is deteriorated, e. g., due to a detector damage, in which case they are discarded. This sum-of-quadrants is eventually subjected to the MEM Abel-inversion routine. The inverted map that this routine returns is then again interpolated with the 2D cubic spline method, from which it is cast into polar coordinates. For a quadrant of $N \times N$ pixels, we typically choose a polar grid of N radial pixels and $M = 1025$ polar pixels for the transformed image $\mathbf{P}$. This image corresponds to a discretized version of the slice through the momentum distribution, $P_{ij} = f(v_i, \theta_j)$, where i and j are indices that run over the N and M radial and polar pixels, respectively. To extract the radial distributions, we do not integrate Eq. (A.3) numerically, but evaluate the Legendre polynomials in the Vandermonde matrix, $\mathbf{V}$, with matrix elements $V_{jl} = P_l(\cos\theta_j)$ and solve the system of linear equations,

$$\mathbf{V}\,\mathbf{Q} = \mathbf{P}^\top \tag{A.5}$$

for the matrix of radial distributions $\mathbf{Q}$, containing the matrix elements $Q_{li} = Q_l(v_i)$. From these, both the radial intensity distribution and the corresponding $\beta_l(v_i)$ are extracted as described above.

Another way that Eq. (A.3) can be read is that the Q_l distributions up to the maximum angular momentum L contain all physically meaningful information of the measurement. Therefore, we typically present the inverted images in the re-expanded, or *Legendre-filtered* form, Eq. (A.3), unless N is very large or convergence of the expansion is slow.

References

1. Wollenhaupt, M., Krug, M., Köhler, J., Bayer, T., Sarpe-Tudoran, C. & Baumert, T. “Three-Dimensional Tomographic Reconstruction of Ultrashort Free Electron Wave Packets”. *Appl. Phys. B* **95,** 647–651 (2009).
2. Dick, B. “Inverting Ion Images without Abel Inversion: Maximum Entropy Reconstruction of Velocity Maps”. *Phys. Chem. Chem. Phys.* **16,** 570–580 (2013).
3. Montgomery Smith, L., Keefer, D. R. & Sudharsanan, S. I. “Abel Inversion Using Transform Techniques”. *J. Quant. Spectrosc. Radiat. Transfer* **39,** 367–373 (1988).
4. Dribinski, V., Ossadtchi, A., Mandelshtam, V. A. & Reisler, H. “Reconstruction of Abel-Transformable Images: The Gaussian Basis-Set Expansion Abel Transform Method”. *Rev. Sci. Instrum.* **73,** 2634–2642 (2002).
5. Garcia, G. A., Nahon, L. & Powis, I. “Two-Dimensional Charged Particle Image Inversion Using a Polar Basis Function Expansion”. *Rev. Sci. Instrum.* **75,** 4989–4996 (2004).

b In principle, this procedure can be automated by an optimization routine if a figure of merit is calculated to quantify the agreement between the four radial distributions. In fact, different algorithms for the centering of VMI images have been proposed in the literature, e. g., the one by Bordas *et al.*[8] that is based on the autocorrelation of the image. In our experience, these algorithms often end up in local minima instead of the global one, and therefore their outcome always has to be carefully checked.

6. Burch, S. F., Gull, S. F. & Skilling, J. “Image Restoration by a Powerful Maximum Entropy Method”. *Computer Vision, Graphics, and Image Processing* **23,** 113–128 (1983).
7. Yang, C. N. “On the Angular Distribution in Nuclear Reactions and Coincidence Measurements”. *Phys. Rev.* **74,** 764–772 (1948).
8. Bordas, C., Paulig, F., Helm, H. & Huestis, D. L. “Photoelectron Imaging Spectrometry: Principle and Inversion Method”. *Rev. Sci. Instrum.* **67,** 2257–2268 (1996).

Appendix B

Calculation of the polarizability tensor of CF_3I

The molecular polarizability is required as a parameter in both the simulations of the impulsive molecular alignment as well as in the the expression for the model correlation-plus-polarization potential in the ePolyScat calculations. As there seem to be no published data on the polarizability of CF_3I in the literature, neither experimental nor theoretical, we made an attempt to calculate this property ourselves. The static polarizability is one of many properties that are derived from the response of a molecule to the application of an external, static field $\boldsymbol{\epsilon} = \begin{pmatrix}\varepsilon_x & \varepsilon_y & \varepsilon_z\end{pmatrix}$. The total energy of the molecule, E, in the presence of the field can be expanded in the Taylor series

$$E(\boldsymbol{\epsilon}) = E(0) - \sum_i \mu_i \varepsilon_i - \frac{1}{2!}\sum_{ij} \alpha_{ij}\varepsilon_i\varepsilon_j - \frac{1}{3!}\sum_{ijk}\beta_{ijk}\varepsilon_i\varepsilon_j\varepsilon_k - \dots , \tag{B.1}$$

where i, j and k refer to one of the Cartesian axes, μ is the permanent dipole moment of the molecule, α the molecule's polarizability, and β its (first) hyperpolarizability. If the molecule is further aligned with its principal axis along one of the Cartesian axes, the off-diagonal elements of α_{ij} vanish.[1] Consequently, to predict the response properties of CF_3I we carried out *ab initio* calculations with the GAMESS (US) package, applying a static field along one of the Cartesian axes in equidistant steps.

As a starting point, a reference wave function was obtained in a Hartree–Fock calculation for CF_3I in its experimental equilibrium geometry, assuming C_{3v} symmetry and using a model-core-potential basis set of augmented triple-ζ quality.[2] In this basis set, the 1s shells of carbon and fluorine, and all shells of iodine except for the 4d, 5s and 5p shells are replaced by model potentials, removing a total of 44 core electrons and just as many nuclear charges, effectively. The calculated total energy for these input parameters was $E_{\mathrm{HF}} = -189.386\,904\,E_{\mathrm{h}}$. From this reference wave function – by means of a coupled-cluster singles-and-doubles calculation with variational estimation of the triples contribution, commonly known as CCSD(T)[3] – a correlation energy of $E_{\mathrm{corr}} = -1.113\,275\,E_{\mathrm{h}}$ was recovered.

This calculation was then repeated, varying a static electric field along one Cartesian axis at a time, in steps of $\Delta\varepsilon_i = 1 \times 10^{-2}$ a. u. $= 5.14 \times 10^7\,\mathrm{V\,cm^{-1}}$ in both negative and positive directions. Here we follow the convention of choosing the molecule to be oriented along the z axis, with the iodine site pointing in the $+z$ direction. Special attention must be paid if the field is pointing along the x or y axes because, in this case, the field breaks the molecular symmetry and the calculations are prone to converge slowly or not at all. From seven points the permanent dipole moment μ_i and the polarizability tensor components α_{ii} were approximated by sixth-order finite difference formulas[4] for the first and second derivative, respectively. A graphical representation of this procedure is displayed in Fig. B.1, whereas the extracted

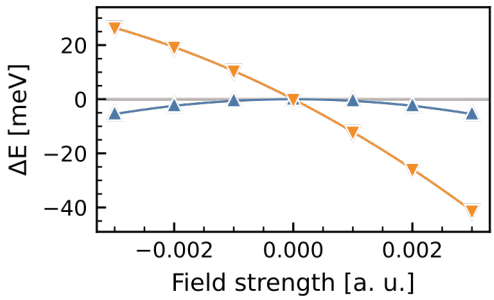

Figure B.1 Change of the total energy of CF_3I at the CCSD(T)/MCP-ATZP level of theory with an electric field applied along the x axis (blue triangles) and the z axis (orange triangles), respectively. The solid lines correspond to the quadratic approximation.

values are listed in Table B.1. Also in Table B.1, we compare our results to values we were able to find in the literature. The dipole moment of CF_3I is, in fact, known with good precision from microwave spectroscopy, where it is obtained from Stark-effect measurements, and our result deviates by only +0.6 % from the measurement of Cox *et al.*[5], which is even within the range of two standard errors they report for their results. For the polarizability, however, there are no reliable numbers reported. Marienfeld *et al.*[6] have extrapolated an isotropic polarizability of 8.9 Å^3 from comparing the trends in the series of CH_3X and CF_3X molecules, for X = H, F, Cl, Br, I. Morris[7] assumes a value of 8.32 Å^3, but does not give any explanation of its origin, whatsoever.

Table B.1 Values calculated for the components of the dipole moment, μ_i, and the polarizability tensor, α_{ii}.

	μ_z [D]	μ_x [D]	α_{zz} [Å^3]	$\alpha_{xx} = \alpha_{yy}$ [Å^3]	$\langle\alpha\rangle$ [Å^3]
This work	1.0540	0.000[a]	9.04	6.67	7.46
Reference	1.048 ± 0.003[b]				8.90[c]

[a] As required by symmetry.
[b] Experimental value by Cox *et al.*.[5]
[c] Value extrapolated by Marienfeld *et al.*.[6] from the series of CF_3X molecules, with X = H, F, Cl, Br, I.

References

1. Kurtz, H. A., Stewart, J. J. P. & Dieter, K. M. “Calculation of the Nonlinear Optical Properties of Molecules”. *J. Comput. Chem.* **11,** 82–87 (1990).
2. Sakai, Y., Miyoshi, E., Klobukowski, M. & Huzinaga, S. “Model Potentials for Main Group Elements Li through Rn”. *J. Chem. Phys.* **106,** 8084–8092 (1997).
3. Bartlett, R. J. in *Modern Electronic Structure Theory* (ed Yarkony, D. R.) 1047–1131 (World Scientific Publishing Company, Singapore, 1995).
4. Fornberg, B. “Generation of Finite Difference Formulas on Arbitrarily Spaced Grids”. *Math. Comput.* **51,** 699–706 (1988).
5. Cox, A. P., Duxbury, G., Hardy, J. A. & Kawashima, Y. “Microwave Spectra of CF_3Br and CF_3I. Structures and Dipole Moments”. *J. Chem. Soc., Faraday Trans. 2* **76,** 339–350 (1980).

6. Marienfeld, S., Fabrikant, I. I., Braun, M., Ruf, M.-W. & Hotop, H. "High Resolution Low-Energy Electron Attachment to CF_3I". *J. Phys. B: At., Mol. Opt. Phys.* **39,** 105 (2006).
7. Morris, R. A. "Gas-phase Reactions of Oxide and Superoxide Anions with CF_4, CF_3Cl, CF_3Br, CF_3I, and C_2F_4 at 298 and 500 K". *J. Chem. Phys.* **97,** 2372–2381 (1992).

Appendix C

Multi-Level Hit-Detection Algorithm

In the first step, before the actual hit finding is applied, an attempt is made to normalize the raw images to account for a varying sensitivity across the detector, which would otherwise hamper the quality of the hit detection in dimmer areas. Therefore, for every pixel of the camera, the maximum intensity value observed is determined over an entire data set, as shown in Fig. C.1b for an electron image set of 10 000 acquisitions. Afterwards, a moving-window rank filter at the 95 % level and a 70 × 70 window is applied to this maximum-value image to smooth out bright features, which yields the reference for normalization, that every single-shot image is normalized to, corresponding to Fig. C.1c.

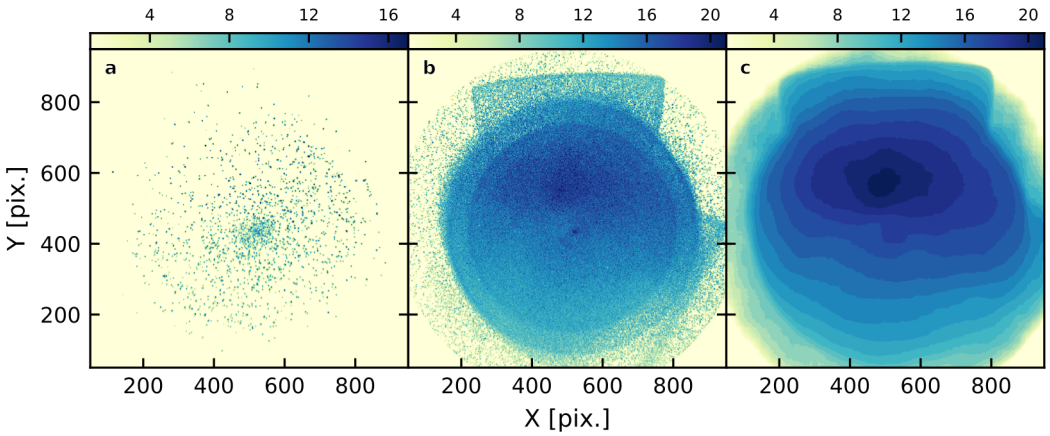

Figure C.1 Normalization of electron images. **a)** Typical electron single-shot image. Note the low overall intensity given as 8-bit integers (max. 255). **b)** Maximum values of the electron images over 10 000 shots. **c)** Same as **b** after application of a moving-window rank filter.

Now that each pixel value falls between zero and one, a sigmoidal histogram-stretching function is applied to the gray levels, which has the form

$$I_{out} = \left(1 + \mathrm{e}^{-\frac{I_{in}-\beta}{\alpha}}\right)^{-1}, \tag{C.1}$$

where I_{in} and I_{out} are the input and output gray levels, respectively, β is the midpoint of stretching and α its strength. For the data presented in Section 4.5, $\beta = 0.2$ and $\alpha = 20$ were found to give good results, in that the contrast of weak hits was considerably increased, as shown in Fig. C.2b. The last step in the global analysis concerns the selection of the threshold, above which a pixel in the image is considered belonging to an object. For this purpose, Otsu's method[1] was employed, which seeks to determine an optimum discrimination value

between the two distinct gray-level distributions, one of which is that of the objects, scattered around one, and the other one that of the background, scattered around zero. When all the gray levels after histogram stretching are sorted into a common, normalized histogram, this histogram can be partitioned by a trial threshold t into two classes, for each of which the class probability $\omega_{0,1}(t)$, which is just the sum of all contained probabilities, and the class variance $\sigma^2_{0,1}(t)$ can be calculated. Then, the optimum threshold t_{Otsu} is the one that minimizes the intra-class variance

$$\sigma^2_{intra} = \omega_0(t)\sigma^2_0 + \omega_1(t)\sigma^2_1 \,. \tag{C.2}$$

The optimized threshold according to this procedure is determined once per data set and typically has a value of ≈ 0.8. By applying this threshold, a binary image is created from the grayscale one, that is then subjected to the object identification and labeling routine, that was also utilized for the PImMS data, as discussed in Section 4.3.1. From Fig. C.2c it can be seen how the image is partitioned into separate objects and that, in regions with few impacts, the routine performs well in distinguishing individual hits.

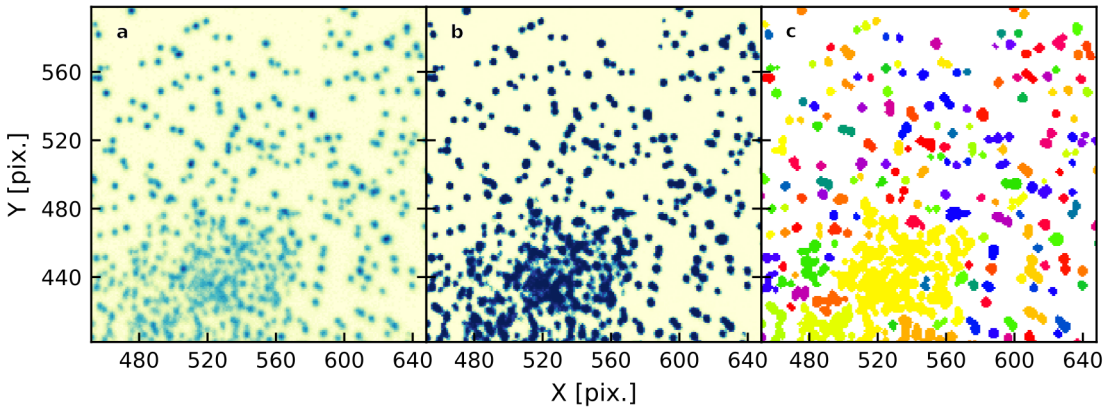

Figure C.2 Global analysis of the electron images. **a)** Detail of the sample image, Fig. C.1a, around the center. **b)** Same as **a** after normalization with respect to Fig. C.1c and application of the gray-level stretching. **c)** Color-coded representation of all objects identified above the threshold calculated by Otsu's method.

If, like in Fig. C.2c, it is clear that a single threshold is insufficient to disentangle larger aggregations of particle hits, the local analysis is applied to every object that was found on the global level, individually. In it, the normalized values before gray-level stretching are extracted from the image for a rectangular section that completely encompasses the considered object. An equidistant scale of gray levels is created and the selected region is thresholded at every one of those levels. Walking from top to bottom, on every layer, all the contained objects are identified with the above binary object-detection routine. At every step it is checked if every detected object entirely covers one and only one such object from the layer above. If it contains two previously found objects, this means that the two peaks have merged and their sizes and positions from the previous layer are stored for further analysis. The advantage of this – rather laborious – procedure is that the complete shape of the peak can be sampled up to the point where it overlaps with a neighboring one, as can be seen from Fig. C.3a. In this way, it is ensured that as many values as possible are fed into the subsequent Gaussian centroiding routine, to make it as robust as possible.

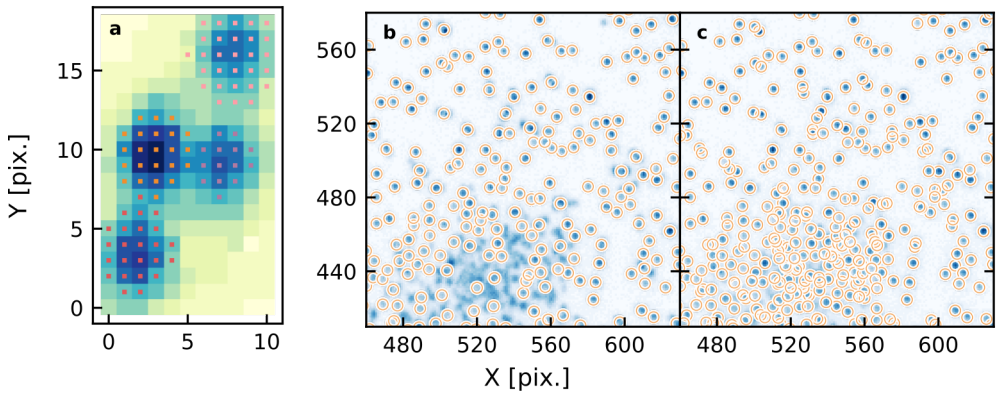

Figure C.3 Local analysis of the objects identified in the global routine. **a)** Decomposition of a single object into four peaks after slicing it in the z-direction along eleven equidistant levels. **b, c)** Comparison of the results from the single- and multi-level detection. Orange circles mark the positions of the identified hits. **b)** Thresholding at a single level, optimized by hand, and subsequent center-of-mass centroiding. **c)** Outcome of the fully automatic multi-level detection routine with Gaussian centroiding.

The centroiding itself is carried out with a standard linear-algebraic approach. The goal is to find a set of parameters for the product of Gaussian functions,

$$G(x,y) = G_0\, \mathrm{e}^{-\left[\left(\frac{x-\mu_x}{\sigma_x}\right)^2+\left(\frac{y-\mu_y}{\sigma_y}\right)^2\right]}, \tag{C.3}$$

that represents the best fit to the measured intensities in a least-squares sense. This model function contains five independent parameters: the centers and widths, each in x and y direction, and the overall amplitude; hence, at least five pixel values have to be supplied or the centroiding routine fails. In particular, as a welcome side effect, it will always fail for CCD noise and other single-pixel artifacts that are surrounded by zeros because all values must be non-zero, which will become clear from Eq. (C.4) below.

First, the intensity values g_i of the peak, that was singled out in the previous step, are re-shaped into a one-dimensional vector and the Vandermonde matrix $\mathbf{V}$ is constructed; that means

$$\mathbf{g} = \begin{pmatrix} g_1(x_1,y_1) \\ g_2(x_2,y_2) \\ \vdots \\ g_n(x_n,y_n) \end{pmatrix} \quad \text{and} \quad \mathbf{V} = \begin{pmatrix} 1 & x_1 & x_1^2 & y_1 & y_1^2 \\ 1 & x_2 & x_2^2 & y_2 & y_2^2 \\ \vdots & \vdots & \vdots & \vdots & \vdots \\ 1 & x_n & x_n^2 & y_n & y_n^2 \end{pmatrix}.$$

Eventually, the system of linear equations for the element-wise logarithm of $\mathbf{g}$,

$$\ln \mathbf{g} = \mathbf{V}\mathbf{c}\,, \tag{C.4}$$

is solved by a standard least-squares solver to yield the vector of coefficients $\mathbf{c}$, from which the parameters of Eq. (C.3) can be recovered by simple algebra. Compared to the relatively slow local analysis, the centroiding comes at almost no additional computation time and is therefore always performed.

In Fig. C.3b and c, hit detection at a single and multiple levels are compared. For the single threshold, instead of using t_{Otsu}, the threshold was tweaked by hand to give the best possible

object discrimination, judged upon inspection. In comparison the multi-level method, that works practically without such intervention, can be seen to give much more accurate results, especially in the central region of the image. To further assess how faithful the Gaussian centroiding works, the functions of the form of Eq. (C.3) were re-evaluated with the fitted parameters on a Cartesian grid of the same size as the original image, and both are displayed side by side in Fig. C.4.

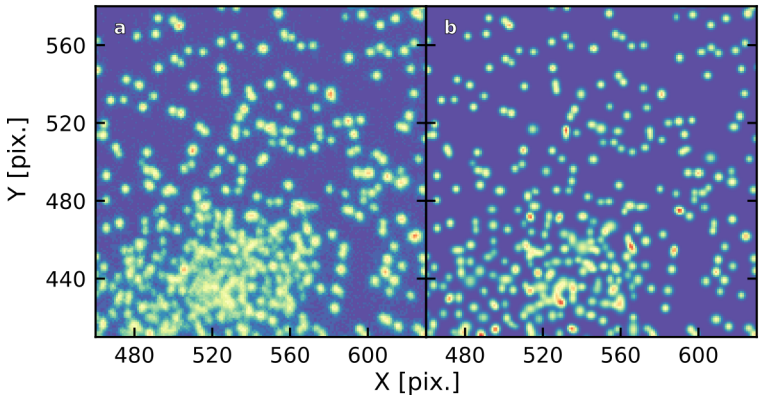

Figure C.4 Two-dimensional Gaussian centroiding. a) Detail of the sample image as in Fig. C.2a, just on a different color scale. b) Re-evaluation of the Gaussian peaks fitted in the hit detection step.

In this section, the application of the multi-level hit detection was shown for a sample image with about 400 particles. The algorithm was, however, also applied to data taken at full FEL intensity, where it successfully coped with up to 2500 hits per image. As the local analysis is the limiting factor, the computation time scales roughly linear with the total number of counts. For the present example of 400 hits, the routine takes pretty much 1 sec per image. As there is no interdependence between the analysis results of individual images, the process is trivially parallelized, so that an electron data set of 10 000 shots can be processed on 12 cores in 15 min. We are convinced that the additional time spent in pre-processing is definitely compensated for by the savings in the subsequent analysis.

References

1. Otsu, N. “A Threshold Selection Method from Gray-Level Histograms”. *IEEE Trans. Syst., Man, Cybern.* **9,** 62–66 (1979).

List of Publications

- Braußе, F., Bach, F., Rouzée, A. & Vrakking, M. J. J. “Imaging nuclear wave packets through laser-assisted electron recollisions in excited I_2 molecules”. In preparation.
- Braußе, F., Rouzée, A. & Vrakking, M. J. J. “Photoelectron angular distributions from the XUV ionization of aligned CF_3I molecules”. In preparation.
- Allum, F. *et al.* “Coulomb-explosion Imaging of CH_3I and CH_2ClI Photodissociation Dynamics”. *J. Chem. Phys.* Accepted.
- Krečinić, F., Wopperer, P., Frusteri, B., Braußе, F., Brisset, J.-G., De Giovannini, U., Rubio, A., Rouzée, A. & Vrakking, M. J. J. “Multiple orbital effects in laser-induced electron diffraction of aligned molecules”. *Phys. Rev. A.* Accepted.
- Braußе, F. *et al.* “Time-Resolved Inner-Shell Photoelectron Spectroscopy: From a Bound Molecule to an Isolated Atom”. *Phys. Rev. A* **97,** 043429 (2018).
- Amini, K. *et al.* “Photodissociation of Aligned CH_3I and $C_6H_3F_2I$ Molecules Probed with Time-Resolved Coulomb Explosion Imaging by Site-Selective Extreme Ultraviolet Ionization”. *Struct. Dyn.* **5,** 014301 (2018).
- Burt, M. *et al.* “Coulomb-explosion imaging of concurrent CH_2BrI photodissociation dynamics”. *Phys. Rev. A* **96,** 043415 (4 2017).
- Amini, K. *et al.* “Alignment, Orientation, and Coulomb Explosion of Difluoroiodobenzene Studied with the Pixel Imaging Mass Spectrometry (PImMS) Camera”. *J. Chem. Phys.* **147,** 013933 (2017).
- Savelyev, E. *et al.* “Jitter-Correction for IR/UV-XUV Pump-Probe Experiments at the FLASH Free-Electron Laser”. *New J. Phys.* **19,** 043009 (2017).

Danksagung

Wie letztlich vielleicht jedes größere Vorhaben wäre diese Dissertation ohne die Unterstützung, den Zuspruch und ganz besonders die Geduld unzähliger Menschen nie zustandegekommen. Daher wünsche ich mir, dass sich alle angesprochen fühlen, die dazu beigetragen haben, aber an dieser Stelle nicht namentlich erwähnt werden. Zuerst möchte ich Marc Vrakking danken, und zwar zum einen dafür, dass er mir die Möglichkeit gegeben hat, die vorliegende Arbeit anzufertigen, und zum anderen für die Freiheiten und Spielräume, die er mir in dieser Zeit gewährt hat, und die ich sehr genossen habe. Auch danke ich ihm für das Vertrauen, das er in meine Fähigkeiten gesetzt hat, entgegen mancher Zweifel (einschließlich meiner eigenen). Natürlich möchte ich mich auch bei Markus Gühr bedanken, der sich ohne Zögern bereit erklärt hat, das Zweitgutachten zu übernehmen. Außerdem danke ich Arnaud Rouzée, der diese Arbeit geduldig über die vielen Jahre begleitet hat. Ohne Zweifel hat er getan, was er konnte, um dieser Promotion zum Gelingen zu verhelfen. Mein ganz besonderer Dank gilt Oleg Kornilov, der gerade in der Abschlussphase, wenn die Laune einmal nicht so gut war, mit wohldosiertem “entertainment”, wie er es nennt, dafür gesorgt hat, dass es weitergeht.
An dieser Stelle möchte ich die Gelegenheit nutzen allen Kollegen und Kooperationspartnern zu danken, die geholfen haben, die Experimente, die in dieser Arbeit zusammengetragen sind, zum Erfolg zu führen. Stellvertretend für die Vielen, die an der Kollaboration für die FLASH-Experimente beteiligt waren, möchte ich mich bei Daniel Rolles, Rebecca Boll, Tatiana Marchenko und Mark Brouard für die konstruktive Zusammenarbeit bedanken. Mein besonderer Dank gilt dabei Dave Holland und Gildas Goldsztejn, die mich auch vor Ort am MBI unterstützt haben. Ebenso konnte ich mich hier am Institut auf die Hilfe und Unterstützung meiner Kollegen in den Laboren verlassen, insbesondere auf die von Song-Hee, Faruk, Florian, Johan, Geert und Jochen. Viele Erkenntnisse dieser Arbeit hätte ich nie gewinnen können, hätten nicht Robert Lucchese seinen ePolyScat-Code und Bernhard Dick seine MEM-Abelinversion mit mir geteilt. Auch dafür vielen Dank! Natürlich gab es neben all der Mühe auch viele heitere Nachmittage. Dafür möchte ich mich bei Sascha, Nils, Lorenz, Katrin und Martin bedanken.
Aber gerade außerhalb des MBIs haben viele Menschen geholfen mich aufzurichten, wenn ich einmal ein bisschen schief lag. Das waren einerseits die Cats vom Jazzorchester und natürlich Justin, der es *immer* geschafft hat, mich auf andere Gedanken zu bringen. Andererseits waren das meine Freunde Gregor, Ria und Martha, die mich schon seit so vielen Jahren begleiten. Ich möchte mich auch bei Jutta bedanken, der ich den Abschluss dieser Arbeit versprochen habe, und den ich ihr schuldig bin, auch wenn sie das fertige Dokument gar nicht mehr gelesen hat. Mein ausgesprochener (und viel zu oft unausgesprochener) Dank gilt meiner Familie, ganz besonders meinen Eltern, die mich, solange ich denken kann, in allen meinen Vorhaben bedingungslos unterstützen und bestärken. Nicht zuletzt danke ich Schnapula (meiner Muse!). Ohne Dich hätte ich bestimmt schon tausendmal aufgegeben. Du und ich, wir bilden eine Einheit!

Selbständigkeitserklärung

Hiermit versichere ich, dass ich die vorliegende Dissertation selbständig und nur unter Verwendung der angegebenen Literatur und Hilfsmittel verfasst habe. Diese Arbeit ist weder in einem früheren Promotionsverfahren angenommen noch als ungenügend beurteilt worden.

Berlin, den 26. September 2018 Felix Braußе